Hydroelastic Response of Surface-Effect Ship Bow Seals: Large-Scale Experiments and Post-Buckling Analysis

by

Andrew D. Wiggins

A dissertation submitted in partial fulfillment
of the requirements for the degree of
Doctor of Philosophy
(Naval Architecture and Marine Engineering)
in The University of Michigan
2014

Doctoral Committee:

Professor Marc Perlin, Co-Chair
Research Scientist Steven F. Zalek, Co-Chair
Professor Silas D. Alben
Professor Steven L. Ceccio
Professor Yin Lu Young

Vitruvius says that small models are of no avail for ascertaining the effects of large ones; and I here propose to prove that this conclusion is a false one.

— Leonardo Da Vinci[a]

[a] Notebooks (Da Vinci, 2008, pg. 82)

to Virgil and Jillian

Acknowledgments

The large-scale experiments described in this thesis would not have been possible without the hard work, creativity and tenacity of the entire multidisciplinary University of Michigan team. I am deeply indebted to Richard Mooney, Matt Van Eck, Dave Parsons, Kyle Tobias, Matt Kramer, Simo Makiharju, Robert Dellsy, Winston Moy, Schuyler Cohen and Brent Cragin. Each made a significant contribution to the development of the large-scale testing platform; handling the stress of the testing environment with aplomb. I would also like to recognize the administrative staff at the Marine Hydrodynamics Lab for their assistance procuring the many puzzle pieces that comprise the large-scale testing platform. I would like to recognize the hard work and patience of the machinists at RETD Manufacturing, in Jackson, Michigan; who, in addition to excellent work, graciously allowed us access to their facility work bay, utilities and overhead crane for construction of the test platform. I would like to thank Rob Cole and Gloria Hogue at NSWC Panama City for the design and construction of the initial set of finger seals employed during the experiments. I would like to thank Dave Newborn of Oregon State University for his expert videography and willingness to pitch-in with the set-up of the large-scale experiments. A relatively latecomer to the surface-effect ship experiments, I would like to thank Michael Wright for his expert help in conducting the small-scale experiments.

I would like to thank co-chairs Drs. Steve Zalek and Marc Perlin excellent mentorship *and* hard manual labor in Memphis. I am fortunate to have worked with exceptionally patient and available advisors who afforded me the opportunity and resources to explore a number of solution paths.

I would like to acknowledge my committee, Drs. Steve Ceccio, Yin Lu Young and Silas Alben for their feedback and support as the project progressed from rough sketches and proposals to a complex 10-metric-ton behemoth (both figuratively and literally).

I was lucky enough to interact with a number of distinguished mentors outside the University of Michigan on this project. Professor Larry Doctors of the University of New South Wales has been an invaluable resource throughout this project and has taught me a lot on how to ask good scientific (and computer-related) questions. I would like to thank Bob Wilson, retired engineer from Naval Surface Warfare Center for the many colorful discussions of surface-effect ship testing and historical insights. The extensive testing and innovation by Bob and his contemporaries in the in the 1960's and 1970's laid the foundation for this thesis.

There isn't enough room here to properly thank my parents. In particular, thank you for helping instill the grit necessary to face the many challenges of this project. Finally, I would like to thank my beautiful wife Jillian for her patience as I proceeded to destroy a significant portion of my "good good" clothes while conducting experiments at the U.S. Navy's Large Cavitation Channel. Without her unwavering support, this project would not have been possible. The thesis is co-dedicated to my grandfather Virgil, scientist and perpetual "young man", who passed near the beginning of my doctoral studies.

The research was generously sponsored by the Office of Naval Research under grant N00014-10-1-0302, by Ms. Kelly B. Cooper, program manager. The advanced motion capture instrumentation employed during the large-scale experiments was acquired through the Defense University Research Instrumentation Program under grant N00014-11-1-0877.

Table of Contents

List of Figures

Figure

List of Tables

Table

List of Appendices

Appendix

Nomenclature

Symbols

$()_{m,f}$	subscripts denote (m)odel and (f)ull-scale
α	wave angle with respect seal axis, $\alpha = \theta_{face} - \beta$
$\bar{h}$	mean seal elevation
β	seal angle in tail region, w.r.t. horizontal
Δ	non-dimensional relative compression ($\Delta = \frac{S}{L}$)
δ_c	cushion depression, based on Doctors (2012) nomenclature
δ_h	effective hinge height above seal tip (proxy for local immersion)
δ_s	seal immersion, based on Doctors (2012) nomenclature
$\eta_{\rho g}$	non-dimensional system size relative to hydrostatic buckling length, $\eta_{\rho g} = \frac{L}{L_{\rho g}}$
γ_{PV}	specific heat ratio
κ	curvature, where subscripts $()_{1,2}$ refer to principal directions
κ_G	Gaussian curvature
λ_0	buckling wavelength at initial bifurcation
$\lambda_{\rho g}$	hydrostatic buckling wavelength

λ_e effective buckling wavelength

λ_{SF} scale factor

λ_w free-surface wavelength

ν Poisson's ratio

Π_D bending or strain energy

Π_K potential energy of foundation

Π_{PE} total potential energy

Π_T total work

ρ_a density of air

$\rho_w(\rho)$ density of water

σ_T surface tension

θ_0, θ_{face} leading angle of seal face with respect to horizontal

ζ free-surface elevation

A_{33} added mass ratio in heave

C_b cushion compliance

D bending rigidity, given by $\frac{Et^3}{12(1-\nu^2)}$ for a linearly elastic material

$D_{\overline{XY}}$ bending rigidity, average of warp (X) and weft (Y) directions

D_x, D_y bending rigidity in the warp (x) and weft(y)

E_c tensile modulus of elasticity for seal fabric coating

E_r tensile modulus of elasticity of seal fabric reinforcement

E_t tensile modulus of elasticity for total composite

F force (often compressive)

F_c critical buckling load

fn Froude number, $fn = \dfrac{U}{\sqrt{gL}}$

fn_c Froude number based on cushion length

fn_H water depth (H) based Froude number

g acceleration due to gravity

h seal elevation relative to mean

h_f finger height

h_{gap} daylight or leakage gap

K_{f_e} effective foundation stiffness

L generic characteristic length scale, taken as the arc-length for later chapters

$L_{\rho g}$ hydrostatic buckling length

L_c cushion length

L_e effective buckling length

L_f, L_m characteristic length, (f)ull and (m)odel scale

L_n natural buckling length

L_w wetted length

m, n mode number/number of half-wavelengths

p_c cushion pressure

Q flow rate

Q_{out} leakage flow rate

R_f Seal radius

T tension

t_c thickness of coating

T_f, T_m absolute temperature, model and full scale

t_r thickness of reinforcement

t_t thickness of total composite

U velocity

V_c cushion volume

w_f finger width

X_G, Y_G, Z_G global coordinate system

X_h, Y_h, Z_h reference frame based at seal hinge

$X_{IVC}, Y_{IVC}, Z_{IVC}$ reference from for IVC-3D linescan camera

X_S, Y_S, Z_S fixed reference frame based at seal tip

Terms

ACV Air Cushion Vehicle

BHC British Hovercraft Corporation

BoF Beam on foundation

FSI Fluid Structure Interaction

HDL Hovercraft Design Limitted

HN Hypalon/Nylon composite material(Type 1)

LCAC U.S. Navy's Landing Craft Air Cushion vehicle

LCC U.S. Navy's Large Cavitation Channel

NN Nitrile/Nylon composite material(Type 0)

NSWC Naval Surface Warface Center

NSWCCD Naval Surface Warfare Center Carderock Division

PMD Photonic Mixer Device, a type of time-of-flight camera developed by PMD Gmbh

SERT Seal Environmental Response Tester

SES Surface-Effect Ship

SSC Ship-to-Shore Connector

T-CRAFT Transformable craft

ToF Time-of-Flight, as in Time-of-Flight camera

TSL Techno-Superliner

Abstract

Bow seals are critical components on advanced marine vehicles that rely on aerostatic support to reduce drag. They consist of a series of open-ended fabric cylinders ("fingers") that contact the free surface and, when inflated, form a compliant pressure barrier. Bow seals are unique in that, unlike a majority of structures in civil and mechanical engineering, bow seals operate in a buckled state.

The response characteristics of these structures are of practical interest due to unacceptable wear rates on seal components and difficulties in predicting seal performance. Despite this, the hydroelastic response of the seal system, particularly basic information on seal vibration modes and the mechanisms responsible for seal wear, remains largely unknown. Similarly, estimates of the hydrodynamic loads on the seal system are inaccurate and based on heuristic scaling of data from small-scale experiments, where similitude is challenging to maintain. Thus, a large-scale test system is necessary to obtain accurate estimates of bow seal response.

The work is comprised of three parts. Part one presents detailed observations of bow seal response acquired using a large-scale test platform developed as part of the present study. These high-resolution observations, the first of their kind, show bow seal response to be characterized by complex post-buckling behavior. Part two proposes an analytical framework for interpreting the wide range of behavior observed at large scale. Using this framework, key parameters driving seal conformation and stability are identified. It is found that, due to their buckled state, bow seals are highly susceptible to a mode switching instability, which may be a potential mechanism responsible for the damaging vibrations.

In part three, a benchtop experiment is used to demonstrate that the scalings identified in this study hold across a wide range of bending rigidities. This work has implications for improving drag and wear characteristics in future bow seal designs. In addition, the scaling parameters identified in this study may govern buckling in other physical systems, such as ice sheets and biological membranes.

Chapter 1
Introduction

Motivation

Bow seals are critical components of advanced marine vehicles such as Surface-Effect Ships (SESs) and Air-Cushion Vehicles (ACVs) which rely on aerostatic support to reduce vessel draft and drag. Future development of this class of vessels, which offer significant advantages in terms of motions and transport efficiency at high speeds, is contingent on reducing risk associated with the seal system. Problems with bow seals include rapid degradation of the seals in the marine environment which contributes significantly to life-cycle costs of SES. In addition, difficulties in predicting seal loads at the design stage adds risk to prime-mover selection: this is especially problematic as SES are weight sensitive.

Despite these problems, the hydroelastic response of the seal system, particularly basic information on the seal vibration modes and the physical mechanisms responsible for seal wear remains unknown. Similarly, estimates of the hydrodynamic loads on the seal system are notoriously inaccurate and based on heuristic scaling of small-scale test data. The utility of these small geometrically-similar experimental studies is limited as the system features a number of structural, aerodynamic and hydrodynamic scales making similitude challenging to maintain.

The SES bow seal system is a complex fluid-structure interaction problem. The problem is unique in that, unlike a majority of structures in civil and mechanical engineering, seals operate in a buckled state. In response to external forces, seals reconfigure and adapt, undergoing large structural displacements. As such, these structures pose significant modeling

challenges. State-of-the-art seal models, such as those proposed by Doctors (2012) neglect the three-dimensional finger seal shape, seal material properties (Graham et al., 1983) and real fluid effects (Ryken, 1978). In the absence of systematic data on bow seal performance, it is not clear as to the validity and implications of these modeling assumptions. Therefore, in order to further develop these tools, and more importantly, to reduce risk associated with the design of SES seals, there is a demonstrated need to provide modelers high-quality reference data for validation studies.

The overall goal of this research is to investigate the physics of SES finger seals under calm water conditions through physical experiments and mathematical modeling. The work seeks to understand how seals respond under the action of hydrodynamic forces and to the identify the physical mechanisms responsible for seal vibration. The work not only provides much needed data for validation studies, but provides an analytical framework within which to view seal conformation. The bow seal problem is found to have parallels in a number of fields, particularly in the emerging field of soft matter which concerns the configuration of highly-compliant structures.

The work is comprised of three parts. Part one presents detailed observations of bow seal response acquired using a large-scale test platform developed as part of the present study. The large scale of the test platform is required to overcome limitations of previous studies and is necessary to obtain accurate estimates of bow seal response. The high-resolution observations made with the large-scale test platform, the first of their kind, show bow seal response to be characterized by complex post-buckling behavior. Part two proposes an analytical framework for interpreting the wide range of behavior observed at large scale. Using this framework, key parameters driving seal conformation and stability are identified. It is found that, due to their buckled state, bow seals are highly susceptible to a mode switching instability, which may be a potential mechanism responsible for the damaging vibrations. In part three, a benchtop experiment is used to demonstrate that the scalings identified in this study hold across a wide range of bending rigidities. This work has implications for

improving drag and wear characteristics in future bow seal design, which may ultimately enable more widespread adoption of SES technology. In addition, the scaling parameters identified in this study have application in other fields and may govern buckling in physical systems diverse as ice sheets and biological membranes. The work highlights the rich statics and dynamics of a buckled structure subject to fluid loading.

Chapter 2
Background

This section provides background information on surface-effect ship (SES) seal physics and highlights significant research questions addressed by the thesis. It also illustrates difficulties confronted by experimentalists in the SES seal area, which motivates the large-scale experimental approach described in Chapter 3. The chapter closes with an overview of the three studies carried out as part of this dissertation.

2.1 SES concept and bow seals

This section describes the primary components of SESs, introducing the bow seal that is the focus of the thesis. A typical layout for a surface-effect ship is shown in Figure 2.1. Rigid sidehulls and flexible bow and stern seals bound a pressurized air cushion that is fed by lift fans. Unlike conventional displacement hulls, where vessel weight is supported entirely by displaced fluid, in cushion-borne operations, SES rely on aerostatic and hydrodynamic support. The pressurized air cushion supports around 60-85% of the SES's weight, with the remainder supported by sidehull lift and buoyancy. By raising the sidewalls almost entirely out of the water, a considerable reduction in the wetted surface and drag of the vessel can be realized. Flexible seals and attendant lift systems on SESs represent critical and complex systems absent in conventional craft.

SESs offer key advantages in terms of transport efficiency, scalability and motions, particularly for missions that require high-speed and shallow draft (Butler, 1985; Steen, 2004). Because of their unique capabilities, SESs are rediscovered periodically by naval architects

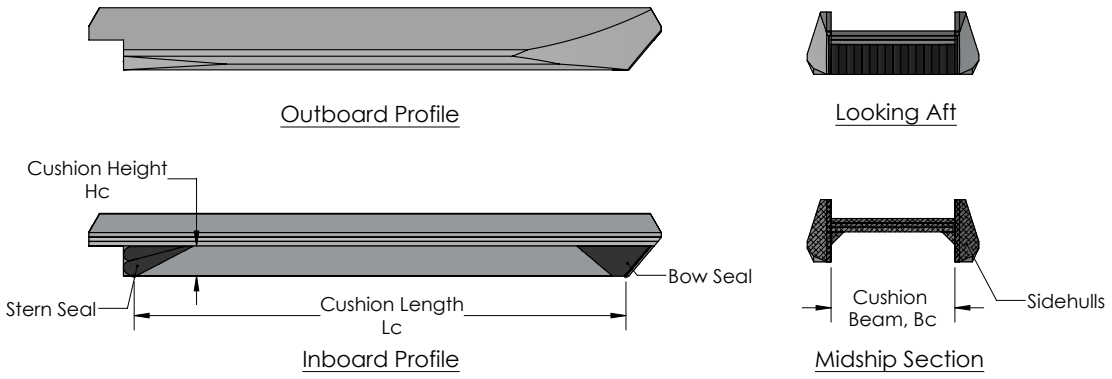

Figure 2.1 Layout of transformable craft (TCRAFT) surface-effect ship (SES). Drawing courtesy of Rob Cole, NSWC Panama City Division.

seeking to fulfill demanding requirements for next-generation naval platforms. However, because of high fuel costs, complexity, and risks of SESs and associated systems (e.g. bow seals), SESs have not met the promise of the 1970s when, on the heels of the successful U.S. Navy's 92 knot (47 m/s) SES 100B test craft program, SESs were touted as a vital part of U.S. national naval strategy. Since their invention, over 2000 SESs and Air-Cushion Vehicles (ACVs[1]) have been constructed world-wide and deployed for a variety of military and civil missions, finding application as minesweepers, patrol craft, and high-speed ferries. Modern examples of SESs include the Japanese Ogasawara Techno-Superliner (TSL) and the Norwegian Royal Navy's Skjold class patrol boats. A profile of the TSL underway is shown in Figure 2.2. The U.S. Navy's Landing Craft Air Cushion (LCAC) class and proposed Ship-to-Shore Connector (SSC) are examples of modern ACVs. In fact, this thesis is done in conjunction with the Naval Surface Warfare Center (NSWC), Panama City, which is the test facility for the U.S. Navy's LCAC program.

[1]Definitions per Yun and Bliault (2000) are adopted in this document. The term SES is refers to an air-supported vehicle with rigid sidewalls and flexible seals fore and aft. The term Air-Cushion Vehicle (ACV) refers to an amphibious air-supported vehicle with flexible seals around the entire periphery. ACVs are also known as hovercraft. Particularly in the ACV literature, the term "seal" is used interchangeably with the term "skirt". These terms both refer to the same structure, and aside from minor difference in mounting, the insights to be gained via this thesis are equally applicable to SESs and the bow seals on ACVs.

Figure 2.2 Ogasawara Techno-Superliner (TSL), largest surface-effect ship (SES) built to date, 140 m in length.

2.2 Bow Seals

Flexible seals are a critical structural element that enable SESs and ACVs to efficiently traverse obstacles. Their development constituted a major breakthrough in the practical application of air cushion technology.

To illustrate the advantage of flexible seals, consider the lift power required for the simplified ACV shown in Figure 2.3. This arrangement is similar to a plenum-type ACV of the late 1950's. The weight of the ACV W_{ACV} is supported entirely by an air-cushion of pressure p_c acting on a wetdeck of area A_{wd}. Using conservation of energy, the volume flowrate Q_{out} per length ds along the periphery of the craft, as a function of hovering height h_{gap}, is estimated as:

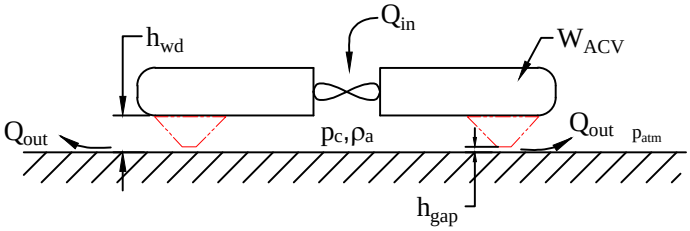

Figure 2.3 Air-cushion vehicle (ACV) without seals.

$$\frac{Q_{out}}{ds} \approx \sqrt{\frac{2p_c}{\rho_a}} h_{gap}, \tag{2.1}$$

where losses due to friction at the exit and elsewhere are ignored. Integrating around the air-cushion, it is seen that required power density (P) increases linearly with hovering height

h_{gap} and that for a given weight (W_{ACV}) a larger planform (A_{wd}) is more efficient,

$$P = p_c Q_{out} \sim (\frac{W_{ACV}}{A_{wd}})^{\frac{3}{2}} (\frac{2}{\rho_a})^{\frac{1}{2}} h_{gap}. \tag{2.2}$$

Due to the power densities achievable, early ACV's without seals ($h_{wd} = h_{gap}$) were limited to hovering heights h_{gap} of around 300mm (Crago, 1968). This small hovering height severely limited the operational environments of seal-less ACVs to calm water conditions where the wave amplitudes $A \ll h_{gap}$ or to relatively small, inefficient sizes where the cushion length $L_c \ll \lambda_w$, where λ_w is the free surface wavelength. Even in calm water conditions, a small wet deck clearance limits the ability of an ACV to "take-off" and reach cruising speeds, as significant drag will occur due contact between the wave system generated by the air cushion and the wet deck and stern seals. At primary hump speed, linear theory predicts that the wave amplitude A_{hump} generated by the air cushion approaches $A_{hump} = \frac{4p_c}{\rho_w g}$ (Yun and Bliault, 2000). The size of this vessel-generated wave sets a fairly stringent requirement for the wet deck clearance, particularly for vessels with the high cushion pressures characteristic of early ACV designs. It is not surprising that seal-less ACVs were noted for their inability to reliably accelerate to cruising speed (Yun and Bliault, 2000). Without large wet deck clearance, ACVs and SESs would have been relegated to a novelty, unsuitable for real-world application.

The purpose of a bow seal is to decouple the wet deck clearance (h_{wd}) of an ACV or SES from the leakage gap (h_{gap}). This is accomplished with a flexible structure mounted to the wet deck that locally deforms in the presence of obstacles.

The exact form of the modern bow seal was the result of an intense "cut and try" effort (Crewe, 1971), evidenced by over 350 patents for various bow seal designs between 1960 and today. A few of the candidate designs are shown in Figure 2.4. Even as late as the SES 200 program in the 1980s, there were a number of competing forms of bow seals, notably finger seals, planing seals, and transverse stiffened membrane seals (Yamakita, 1985). Due

to communalities between seal types, this thesis, which looks at the behavior of a flexible body at the air/water interface, has broad application to other types of bow seals.

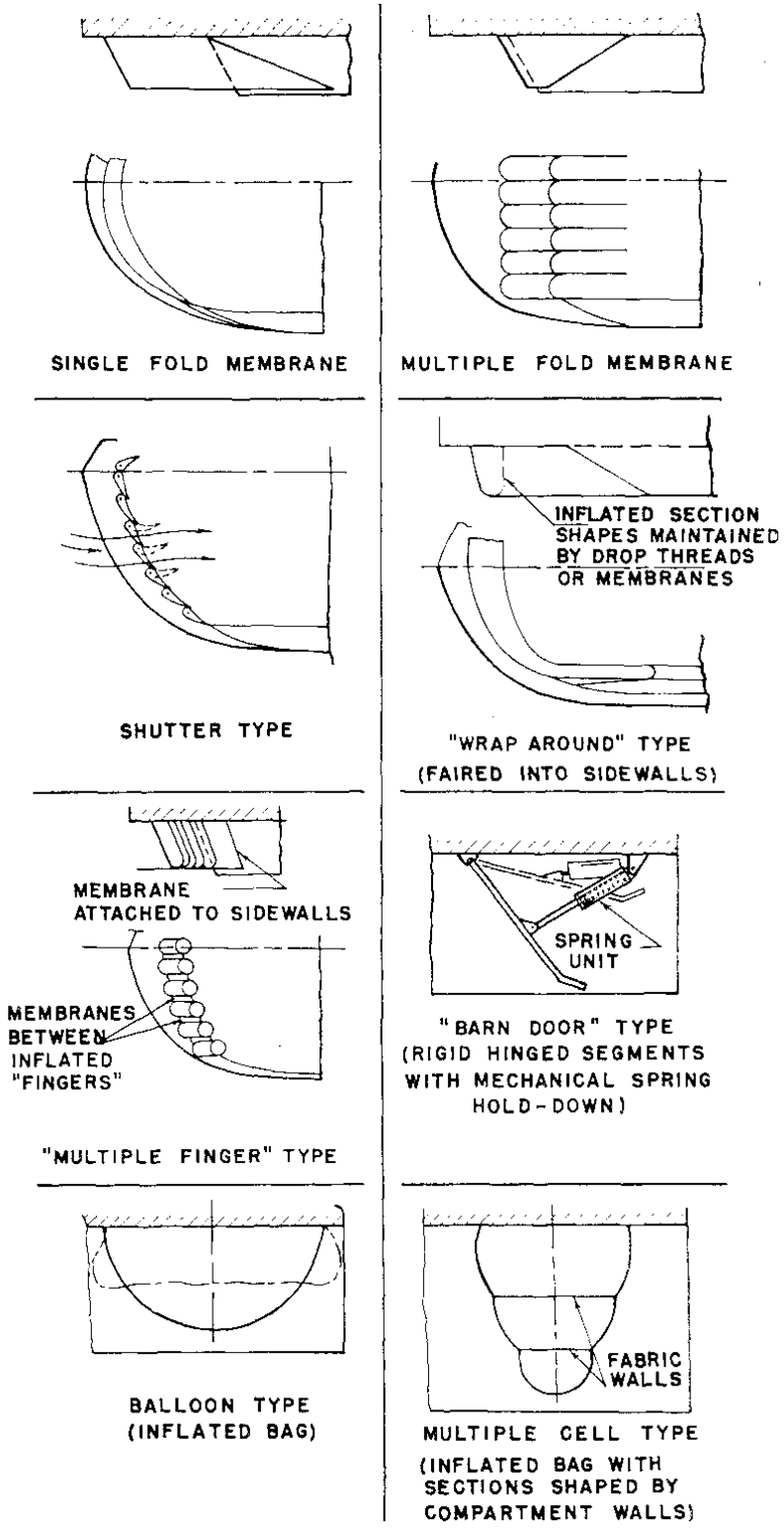

Figure 2.4 Early bow seal concepts (Waldo, 1968).

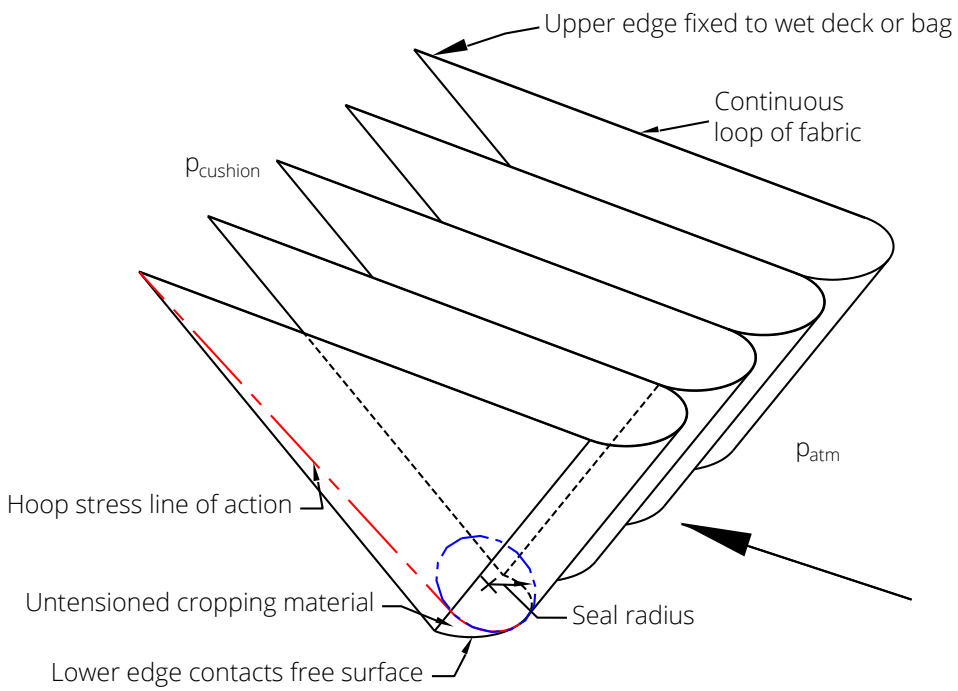

Figure 2.5 Finger seal arrangement.

2.2.1 Finger Seals

The predominant type of bow seal currently in service is the finger seal, which is the focus of this thesis. Building on earlier work by Latimer-Needham at the British Hovercraft Corporation (BHC), the finger-type bow seal was developed by Denys Bliss at Hovercraft Design Limited (HDL) in the 1960's (Bliss, 1969). A finger-type bow seal system consists of continuous loops of flexible material arranged in series as shown in Figure 2.5. When inflated, the individual fingers seal against one another to form a flexible curtain that bounds the air cushion. The upper edge of the seal design is either hard-mounted to the wet-deck structure, which is adopted in modern SESs, or to a flexible bag. The flexible bag arrangement is favored in ACV design, as it serves as fail-stop should the vessel experience "plough-in", a bow-down moment caused by drag on the bow seals. Under optimal running conditions, the lower edge of the fingers graze the free surface resulting in minimal drag. However, in other conditions, such as at lower speeds, in waves, or when the vessel is

trimmed, a substantial portion of the fingers are "immersed" and contact the free-surface, contributing significantly to the overall drag of the SES.

Finger seals offered significant advantages over competing designs, such as peripheral jets and monolithic seals, including:

1. Independence: The fingers are independent and able to conform to complex shapes such as the free-surface of the ocean. The small "daylight" or leakage gap of finger seals dramatically reduces the power requirements for the lift fan system (Bliss, 1969).

2. Redundance: Finger seals provide a level of redundancy, as the gap-created loss of a single finger will be largely filled by the expansion of neighboring segments.

3. Serviceability: Due to wear problems endemic to all forms of bow seals, they inevitably require replacement before regular dry dock maintenance. The mechanical simplicity of the finger seal leads to fairly straightforward maintenance that can be performed by service boats or divers. Later finger designs often feature removable cuffs whereby the wear-prone lower section of the seal can be replaced without removing the entire seal (Butler, 1985).

4. Lower drag: The flexibility of the finger seals results in significantly lower drag than earlier designs, such as peripheral-jet type seals which feature rigid mechanical fasteners and down-stops. Lower drag leads to greatly improved performance (Crewe, 1971). ACVs equipped with finger seals are noted for their "take-off" ability and are less susceptible to plough-in than their peripheral jet outfitted counterparts.

The geometry of a typical finger seal is listed in Table 2.1 and shown in Figure 2.6. The forward rake of the seal is driven by the need for static hovering stability, which is particularly important for ACVs (Crewe, 1971) and also to prevent seal buckling (or "tuck-under") due to hydrodynamic loads (Chapin, 1977). Work performed in Japan indicates that the seal rake also has significant impact on seal wear with the ideal leading angle (θ_{face}) being

between 40-50 deg (Yamakita and Itoh, 1998). Ideally, the aftmost point of the top edge is selected such that the line of action of the primary hoop stress is supported to the seal tip.

In practice, the top length/included angle is often truncated due to mounting constraints. Presently, there is limited engineering guidance on the hydrodynamic impact of decreasing the top length (L_{top}), thereby unloading the seal tip. Seals are "cropped", which provides untensioned material between the seal tip and the tangency line between fingers. Cropping decreases the air leakage between seals, with the undesirable side-effect of increased wetted surface and drag. The values in Table 2.1 are based on Type A seals used on the U.S. Navy's modern Landing Craft Air Cushion class (LCAC), which were provided by the Naval Surface Warfare Center (NSWC) Panama City. Rather surprisingly, the dimensions of LCAC finger seals are largely unchanged from the original patents (Bliss, 1969). The design likely reflects that the parent hull form for the LCAC (1984) is the BHC SR.N5, an earlier British design.

2.2.2 Materials used for finger seals

Materials used on bow seals are subject to an extremely harsh operating environment requiring flexibility, impermeability, high tensile strength and fatigue resistance. Like the

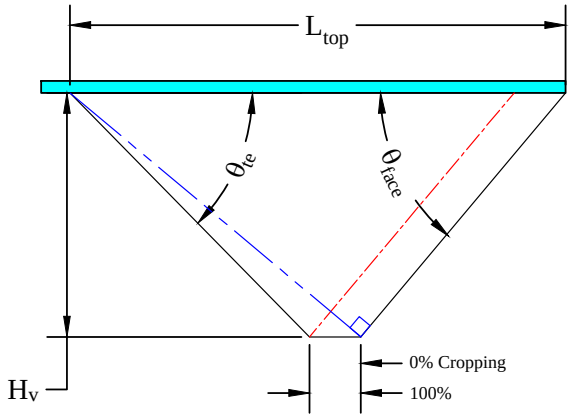

Face Angle, θ_{face}[a]	50.0	deg
Cropping	100	%
Finger Height, H_v	0.940	m
Finger Width, w_f	0.303	m
Finger Radius, R_f	0.151	m
Finger Top Lengh, L_{top}	1.908	

Table 2.1 Finger seal principal characteristics (as tested).

[a] θ_0 in Doctors nomenclature

Figure 2.6 Finger seal geometry (as tested).

finger seal design, materials used on modern ACVs such as the LCAC can be traced to earlier British efforts (Swallow et al., 1971). This research has led to seal materials that are laminates in the form of a woven base fabric embedded in an elastomer matrix. The predominant base fabric is nylon 66, which offers excellent fatigue properties and relatively low water absorption. High twist yarns are used in open weave patterns, resulting in a flexible base fabric with small gaps that permit the coating to bond with itself (Inch et al., 1989). The coating is applied to the base fabric via a calendering process in order to make the material impermeable. The coating used on the LCAC seals is a natural rubber and polybutadiene blend, not unlike the materials used in automobile tires or conveyor belts. Natural rubber is preferred due to its crack resistance and relatively low hysteresis which resists thermal breakdown during vibration. Neoprene coated fabrics have also been used extensively as they offer superior chemical and ultraviolet light resistance. The areal weights for the coated fabrics used in past designs vary considerably, 7between 1.35 and 3.25 kg/m^2, depending on the size of the vehicle. Due to tensile strength requirements, seals on large SES concepts such as proposed by the U.S.Navy's 3KSES (Chapin, 1977) and T-CRAFT programs require heavier fabrics and extrapolation outside the range of past experience. The choice of fabric weight/fabric thickness is based on tensile load requirements and reflects two competing seal design philosophies. The BHC skirt design philosophy, stated in Crewe (1971) and Swallow et al. (1971), holds that the improved wear properties of heavier skirt materials outweighs the increased drag and lightship weight. Other designers, such as Vosper Thornycroft maintain that seal materials should be as light and flexible as possible to reduce drag and minimize delamination-type seal failure (Dyke, 1976). The thesis provides information that designers can use to begin to make an informed material selection process.

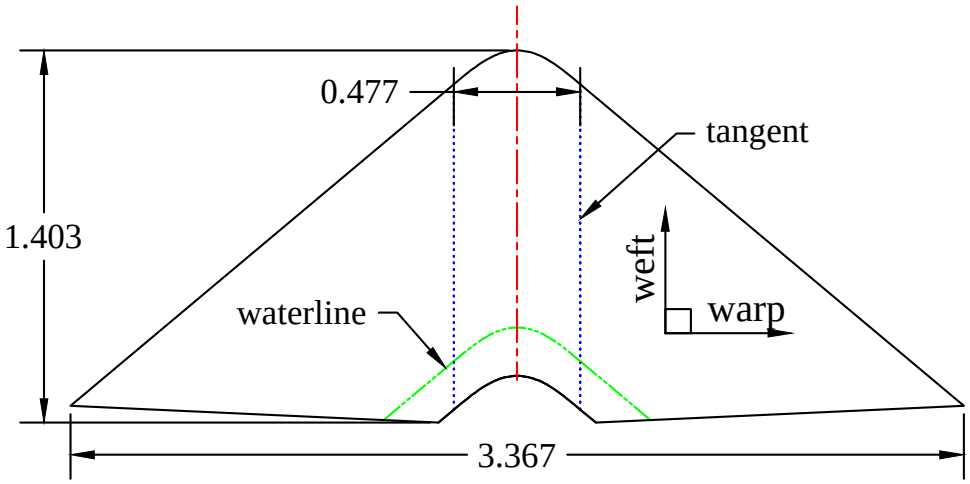

Figure 2.7 Lofted finger seal (as tested) with fabric direction shown. See Appendix D for details on the seal geometry. All dimensions are in meters.

2.3 Sea trial data for SES

> [Bow seal wear] is far and away the most expensive maintenance item on the craft and immediately one asks what is being done to reduce it. Very little indeed! Here then is a priority one task for the experts, for unless an answer can be found the future for operators of the SRN 4 is going to be difficult (Colquhoun, 1971).

Bow seals operate at a violent unsteady air/water interface and are routinely subject to large structural displacements, buckling and high-frequency vibrations. For a variety of reasons that will be discussed in later sections, the primary method of evaluating seal designs and materials remains full-scale trials. To investigate SES and ACV and associated technologies, test craft programs were established in the U.S. (Wellman, 1981), Great Britain, Japan and elsewhere. These programs yielded a wealth of qualitative information on bow seal performance as well as illustrated some of the benefits of controlled experiments. Seal-specific trial information largely takes the form of direct observations made with periscopes and access ports, and postmortem reports of seal damage. Quantitative information on seal performance derived from sea trials is limited. Important contributions in this challenging area include data from systematic seal exchanges and wear measurements on the BHC SR.N5 (Swallow et al., 1971) and Vosper Thornycroft VT-1 (Dyke, 1976), and

efforts to instrument fingers and measure seal response with load cells and strain gauges (Crewe, 1971), accelerometers (Ryken, 1978; Yamakita and Itoh, 1998), and high-speed cameras (Tsutsumi and Naito, 1991).

The design life of a modern finger seal system is between 400 and 1000 hours (Lavis, 2009), which is nearly two orders of magnitude less than the regular dry docking interval of a naval vessel, leading them to be viewed as expensive consumables. A typical failure mode of finger seals is shown in Figure 2.8. The extensive seal damage accumulated in less than 100 hrs on the first generation LCAC deep-skirt (1998) and is believed to be due to fatigue (Lavis, 2009). Later design iterations were able to achieve satisfactory seal life and drag for this design. Very little is known about the physical mechanisms responsible for wear patterns such as that seen in Figure 2.8 (NMAB, 1978).

Rather than look solely at postmortem measurements of seal damage, there have been a few attempts to try to understand the excitations that may result in seal wear. Field measurements of finger seal accelerations reveal extremely high accelerations in the neighborhood of the seal tip. During the U.S Navy's SES 100B (1976) trials, reproduced in Malakhoff and Davis (1981), the maximum acceleration two inches from the seal tip was nearly 1000 g. Subsequent large-scale tow tank tests (Ryken, 1978) and trials with the Japanese Meguro-2 (1998) test craft (Yamakita and Itoh, 1998) suggest that the accelerations from the SES-100B trials likely would have been even higher had there not been mass loading from the large piezoresistive accelerometers. Smaller single-axis accelerometers used on the Meguro-2 trials showed maximum accelerations of nearly 7450 g and a fairly broadband response (Yamakita and Itoh, 1998). Like the SES 100B trials, Yamakita and Itoh showed that the mean spectral frequency and standard deviation of seal motion varies linearly with speed, reaching a maximum of around 150 hz at 38 knots.

In response to artifacts and instrument failures associated with contact measurements of seal motions, there has been at least one effort to acquire seal motions in a non-contact manner. This was accomplished through high-speed optical tracking of markers located

(a) Delamination of first generation LCAC deep-skirt after 100 hours (Lavis, 2009).

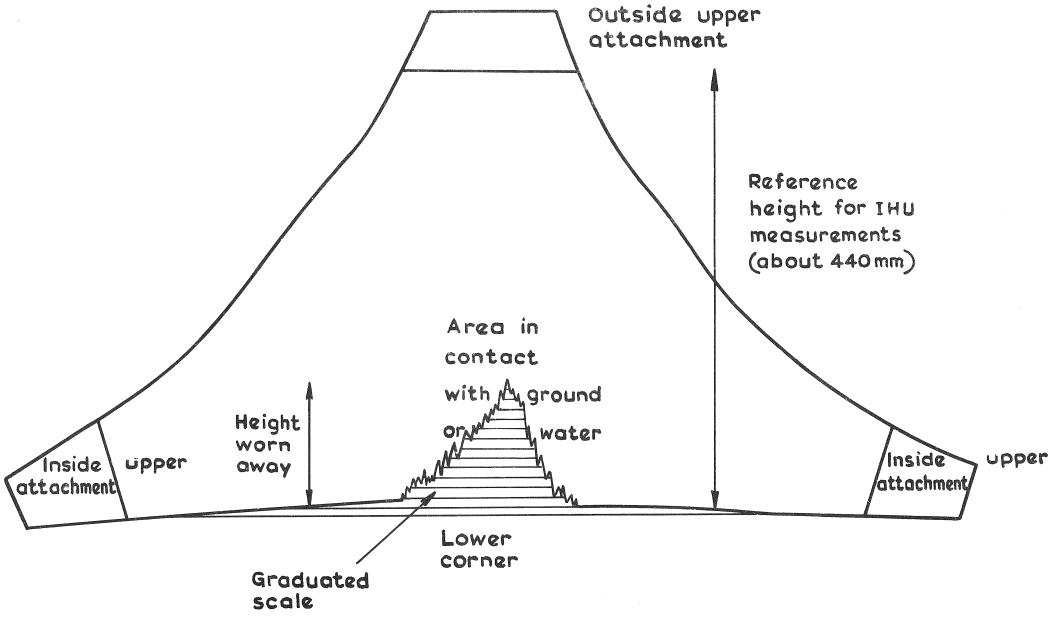

(b) Typical seal wear during BHC SN.5 trials (Swallow et al., 1971).

Figure 2.8 Seal wear patterns.

along the centerline of a finger seal (Tsutsumi and Naito, 1991). Carried out at lower speeds (10-30 knots) than the SES 100B and Meguro-2 trials, these tests observed maximum vertical accelerations on the order of 70 g at a frequency of 60 Hz. The increase in seal accelerations near the tip reported by Yamakita and Itoh (1998) and Malakhoff and Davis (1981) is not as pronounced for the optically derived results (Tsutsumi and Naito, 1991). This may be due to limitations with the measurement method, which may be sensitive to spray and sample rate limitations near the seal tip.

Sea trials on ACVs and SESs indicate that seal wear is a persistent and unresolved problem. The trials also illustrate the many challenges in conducting large-scale trials on these structures, namely the harsh testing environment and the wide-bandwidth required to resolve motions of the seal tip.

2.4 Physical model tests of SES bow seals

Generally taking the form of small Froude-scaled physical model tests, a number of experimental test programs have been undertaken. Despite their limitations, these tests provide insight into the physical mechanisms responsible for seal drag and flagellation as well as guidance as to the experimental approach required to advance our understanding of seal physics. Utilizing segmented models, whereby the loads on the bow and stern seal system can be isolated, small-scale calm water studies performed by Heber (1977), Fridsma and Van Dyck (1979) and Yamakita (1985) showed that SES seal drag is significant at lower Froude numbers ($fn_c < 0.75$), particularly in the subhump ($fn_c \approx 0.35$) regime. At subhump velocities, Heber reported that seal drag (bow and stern) comprised nearly 50% of total drag (likely an overestimate due to unrealistically thin sidewalls). As velocity is increased, SESs exhibit more favorable trim angles and the contribution of the seal to the total drag decreases as sidehull frictional and aerodynamic drag begins to dominate.

The physical mechanism responsible for increased seal drag at sub-hump speeds is believed to be a local increase in seal immersion caused by the presence of cushion-generated waves at both the bow and stern seals, and vessel pitch. The dependence of seal drag on vessel trim/seal immersion has also been noticed by other researchers. On non-segmented models, seal drag performance is often studied indirectly through measuring the sensitivity of the total drag to trim (Klichko, 1991).

As pointed out by Ryken (1978), the small-scale results of Heber contain a few anomalies, particularly for the fixed trim case that is directly comparable to results from the present

study. Surprisingly, Heber shows that there is a negligible increase in finger seal drag for a 1 degree change in trim, which corresponds to a 40% change in seal immersion. This and suspiciously low drag coefficients at higher speeds, leads Yun and Bliault (2000) to recommend applying large safety factors when extrapolating drag data for seals. These large safety factors are somewhat paradoxical, considering that at small-scale the seal materials are too stiff (Section 2.5.1), which would tend to suggest that the seal drag measurements at small-scale are too high.

The efforts of Heber and others show that there is significant uncertainty inherent in hydrodynamic forces derived from a small-scale approach. As will be investigated in Section 2.5.1, seals used on small-scale models are too stiff and do not buckle or vibrate in a manner representative of behavior observed during sea trials. Therefore, another experimental approach must be taken that is able to reproduce the full-scale relationship between the seal structure and the environment. Examples of large-scale bow seal experiments using full-scale seals include those conducted at the Naval Surface Warfare Center Carderock Division (NSWCCD) using the Seal Environmental Response Tester (SERT) (reviewed in Malakhoff and Davis (1981) and recently by Doctors and Zalek (2010). These tests represent important starting points for the experimental approach adopted for the present study.

The Seal Environmental Response Tester (SERT) was developed at NSWCCD to support the SES 100B test craft program. Capable of velocities to 50 knots and supporting partial-height finger seals from the SES 100B, two series of experiments were carried out with SERT (Besch, 1976; Ryken, 1978). The test rig is shown in Figure 2.9; it consists of a simplified SES with thin rigid aluminum sidewalls, a segmented planing-type stern seal and a force balance to measure the gross loads on the seal system.

Using high-speed photography (Besch, 1976) made some of the first laboratory observations of finger seal behavior. Besch identifies a number of instability types present in seal response. At shallow immersions ($\frac{\delta_s}{R_f} < 0.19$), where δ_s is the immersion and R_f is the seal radius, Besch describes travelling waves emanating from the seal centerline, a phenomenon

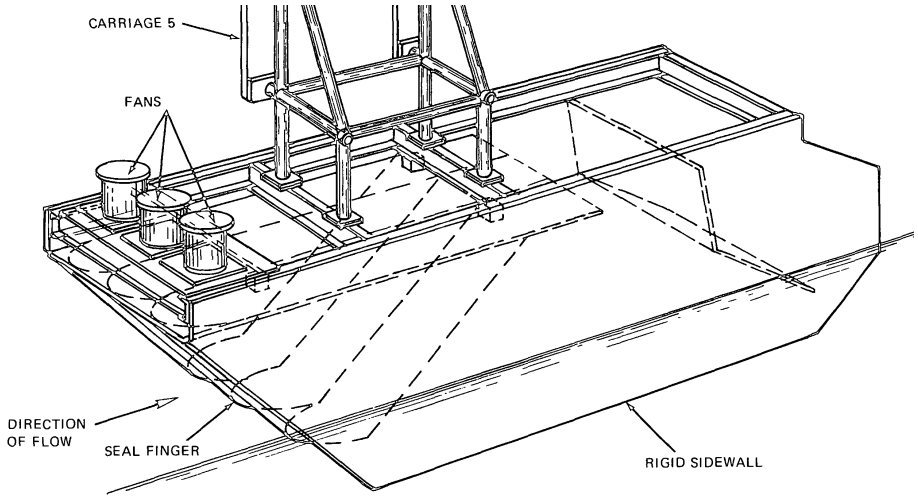

Figure 2.9 Seal Environmental Response Tester (SERT) (Besch, 1976; Ryken, 1978).

the author terms "buckle cycling." At deeper immersions ($\frac{\delta_s}{R_f} \geq 0.19$), Besch observes both random ("buffeting") and high-frequency periodic ("flutter") type instabilities. Besch (1976) also reports that the cross-flow buckling mode number seems to change with seal immersion, with finger seals generally favoring buckling patterns symmetric about the seal centerline. Figure 2.10 shows a typical seal shape from Besch (1976) at an immersion $\delta_s = 63.5$ mm. The SERT experiments also pioneered the use of finger-mounted accelerometers, which were employed to measure accelerations at a number of points along the seal.

Later tests by Ryken (1978) refined the acceleration and drag measurement techniques on SERT. Acceleration measurements taken by Ryken (1978) show that flagellation for the SES 100B finger seals occurs above a critical velocity of around 20 knots, with acceleration magnitude increasing with cushion pressure. Ryken (1978) also presents a simplified seal drag model, taking into account the change in wetted surface that occurs when the seal is folded at higher immersions, and explores whether panel flutter might explain the observed behavior. Doctors and Zalek (2010) developed a test rig similar to SERT but with a lobed stern seal and a 2-dimensional membrane seal. Measurements are made of the deformed seal shape using optical methods and string potentiometers. The results are then compared with numerical results for a compliant planing surface.

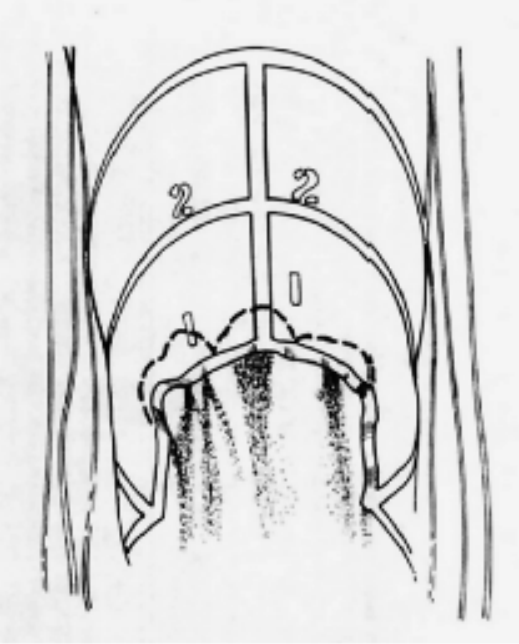

Figure 2.10 Mode shape at immersion $\delta_s = 63.5$ mm, based on high-speed footage from the Seal Environmental Response Tester (Besch, 1976; Ryken, 1978).

2.5 Scaling in SES physical model experiments

To motivate the large-scale experimental approach developed as part of this thesis, physical arguments are used in this section to identify dimensionless groups of importance for the bow seal problem and to explain why it is difficult to capture the relevant physics in the small-scale experiments that have typified past work.

2.5.1 Model experiments

An established technique in the field of Naval Architecture, scaled model experiment's aim is to investigate full-scale phenomena through experiments conducted at a smaller scale. The physical lengths between small and full-scale are related via a scale-factor $\lambda_{SF} = \dfrac{L_f}{L_m}$, where L_f and L_m are physical lengths at (f)ull-scale and (m)odel. The small-scale experiment must also be dynamically similar to full-scale; that is, the ratios of the dominant forces in the problem must be maintained under the change in physical length.

Due to the presence of the free-surface, which sets the wave drag and boundary con-

ditions for the finger seals, the balance of inertial forces to gravitational forces, or Froude number ($fn = \frac{U}{\sqrt{gL}}$), where L is a characteristic length, and U a characteristic velocity, is expected to play a dominant role, and must be maintained between model and full-scale.

Typical of Froude-scaled experiments in hydrodynamics, achieving Froude similitude for $\lambda_{SF} \gg 1$, leads to distortions in the balance of viscous and inertial forces (Reynolds number, *R*e) and in the balance of surface tension to inertial forces (Weber number, *We*) (Newman, 1977).

$$fn = \frac{U}{\sqrt{gL}} \tag{2.3}$$

$$Re = \frac{UL}{\nu_{visc}} \tag{2.4}$$

$$We = \frac{\rho_w U^2}{\sigma_T}. \tag{2.5}$$

These distortions are expected to manifest themselves in a variety of ways in the bow seal problem. In particular, as will be discussed in Chapter 5, Reynolds numbers differences between small and full-scale lead to dissimilar flow-induced tensions in the seal fabric.

In the case of bow seals, the compliance of the air cushion and flexible seal system of an SES adds further complexity to the execution of Froude-scaled physical model tests. Balances of dominant aerodynamic and structural forces must also be maintained. It will be shown, that when the most important of these additional forces are included, dynamic similitude is also physically unrealizable at smaller model length scales.

Engineers involved in the initial development of the finger seal were well aware of these limitations (Lavis et al., 1974; Sullivan and Graham, 1989; Benya, 1971) and developed a series of tests and analytical techniques in order to isolate the relevant physics, including the use of skirt boxes for seal shaping studies and air/water jet flagellators to perform endurance testing of materials candidates.

Cushion compliance scaling

The compliance of the air cushion, $C_b = \dfrac{dV_c}{dp_c}$, where V_c is total cushion volume and p_c the absolute cushion pressure, plays a significant role in the response of an SES to disturbances (Lavis et al., 1974; Moulijn, 2000). The difficulty arises for small-scale geometrically-similar experiments, in that the cushion is too stiff by a lenth-scale factor of approximately λ_{SF}. For the calm-water bow seal problem, this leads to a uniform pressure resonant frequency that is too high by a factor of λ_{SF} and a restoring force resisting seal motion due to the cushion compression that is also too high. Experiments by Kapsenberg and Compton (1996) on geometrically-similar SES models of two different lengths has shown that in seakeeping experiments, the cushion compliance distortion manifests itself as incorrect heave natural frequencies, under-prediction of low-frequency vessel motions, and added resistance in waves. The distortion is particularly problematic when large scale factors are adopted, such as required for large target vessels due to model basin space restrictions. For example, for the U.S. Navy's T-CRAFT target vessel, $\lambda_{SF} = 30$ was chosen. A number of experimental techniques have been proposed for conducting small-scale experiments with minimal distortion, including changing the atmospheric pressure and adding flexible diaphragms, but each of these proposed techniques have significant limitations[2].

To illustrate how the cushion stiffness distortion arises and to show that altering the atmospheric pressure alone does not fully remedy the problem, the cushion stiffness scaling for a Froude-scaled SES experiment with geometric scale factor $\dfrac{L_f}{L_m} = \lambda_{SF}$ is examined. Subscripts indicate (m)odel and (f)ull-scale.

The following non-dimensionalization is adopted, velocities (U) are scaled as

$$U^* = \frac{U}{\sqrt{gL}} \tag{2.6}$$

where L is a characteristic length scale, typically taken to be the cushion length and g is the

[2]For instance, designing of the flexible diaphragm with a particular frequency response poses it's own challenges (Moulijn, 2000).

acceleration due to gravity. In the case of the bow seal, the cushion depression, $\delta_c = \frac{p_c}{\rho_w g_m}$ (ρ_w is the water density) or the wetted length l_w may be more appropriate length scales.

Forces (F) and time (t) are non-dimensionalized as

$$F^* = \frac{F}{\rho g L^3}, \tag{2.7}$$

$$t^* = \frac{t}{\sqrt{\frac{L}{g}}}. \tag{2.8}$$

Consistent with this scaling, the non-dimensional cushion compliance $\left(\frac{dV_c}{dp_c}\right)^*$ is given by

$$\left(\frac{dV_c}{dp_c}\right)^* = \frac{(\frac{dV_c}{dp_c})\rho_a g}{L^2}. \tag{2.9}$$

In order to satisfy dynamic similitude $(\frac{dV_c}{dp_c})^*_m = (\frac{dV}{dp_c})^*_f$, where ρ_a is the density of air:

$$(\frac{dV_c}{dp_c})_m = (\frac{dV_c}{dp_c})_f \frac{\rho_{a_f} g_f}{\rho_{a_m} g_m \lambda^2_{SF}} \tag{2.10}$$

The difficulty in achieving similitude for $\frac{dV_c}{dp_c}$ is due to the equation of state for air. Starting with conservation of mass for the cushion and assuming isentropic conditions, it can be shown (Moulijn, 2000) that linearized about a given cushion volume V_c

$$\frac{dV_c}{dp_c} \approx \frac{V_c}{\gamma_{PV}(\tilde{p}_c + p_a)}, \tag{2.11}$$

where $\tilde{p_c}$ is the gage or perturbation pressure, p_a is the atmospheric pressure and γ_{PV} is the heat capacity ratio. Substituting this expression into Equation 2.10, it is seen that generally for dynamic similitude,

$$\frac{V_{c_m}\gamma_{PV_f}(\tilde{p}_{c_f} + p_{a_f})}{V_{c_f}\gamma_{PV_m}(\tilde{p}_{c_m} + p_{a_m})} = \frac{\rho_{a_f} g_f}{\rho_{a_m} g_m \lambda^2_{SF}}. \tag{2.12}$$

For a geometrically similar model, Equation 2.12 can be simplified by substituting ($V_{c_m}/V_{c_f} = \frac{1}{\lambda_{SF}^3}$) , and if gravity and the gas is unchanged, $g_f = g_m$ and $\gamma_{PV_m} = \gamma_{PV_f}$. In general, at model scale the cushion pressure $\tilde{p}_{c_m} \ll p_{a_m}$ so $(\tilde{p}_{c_m} + p_{a_m}) \sim p_{a_m}$, leading to the conclusion that cushion stiffness similitude can only be maintained if

$$\frac{p_{a_m}\rho_{a_m}}{\rho_{a_f}(\tilde{p}_{c_f} + p_{a_f})} = \frac{1}{\lambda_{SF}} \tag{2.13}$$

or with a considerable reduction in the ambient pressure. Recalling Equation 2.1, it is desirable to maintain $\rho_{a_m} = \rho_{a_f}$ in order to maintain similitude for the air leakage velocity, which is likely important for understanding the role of cushion pressure on seal motions. In this case, returning to the equation of state ($\frac{p_a}{\rho_a} = RT$), achieving a reduction in ambient pressure without changing the air density requires a reduction in absolute temperature (T_f,T_m) as well as ambient pressure leading to

$$\frac{T_m}{T_f} = 1/\lambda_{SF}. \tag{2.14}$$

Practically it is not possible to realize this reduction in absolute temperature when studying the interaction of an SES with a free-surface as the water would freeze.

Other methods of achieving similitude for the cushion compliance have been proposed, these include augmenting the cushion volume such that ($V_{c_m} = V_{c_{mgeom}}\lambda_{SF}$) (Rijken et al., 2010), adding a flexible diaphragm to augment the cushion stiffness (Sullivan and Graham, 1989; Moulijn, 2000), or even utilizing a rotating arm of radius R_{arm}s to change the acceleration due to gravity at model scale $g_m = g_f\lambda_{SF}$, where $g_m = {V_{c_m}}^2/R_{arm}$. While novel, these techniques these experimental likely introduce additional complexity and uncertainty to the small-scale experiment.

In summary, it is very challenging to maintain similitude for the cushion compliance between model and full-scale experiment. Generally, as model size increases, the cushion becomes softer and the cushion dynamics approach those of full-scale. For the experimental approach described in Section 3 softening of the cushion is accomplished by making the

cushion as large as possible, and through the addition of a passive back pressure control system, which can be used to further reduce dp_c/dV_c and suppress other acoustic modes, allowing results to be compared to very large SES.

Fabric property scaling

The interaction of the flexible bow seal with the environment adds another challenging element to scaling of SES experiments. In particular, bending rigidity and fabric mass, and their relation to aerodynamic and hydrostatic/hydrodynamic forces are expected to play a critical role. For the unsteady problem, viscoelastic properties of the seal coating are also likely to have a significant impact (Sullivan et al., 1985).

Fabric property scaling: mass

The mass of the fabric m is usually specified per unit area, which for a homogenous material $m = \rho_{fabric} t_t$, where ρ_{fabric} is the material density and t_t is the fabric thickness. Fabric mass may be non-dimensionalized as $m_r^* = \dfrac{m_r}{\rho_w t_t}$ which leads to the conclusion that fabric mass should be reduced by the scale ratio $m_{r_m} = \dfrac{m_{r_f}}{\lambda_{SF}}$. Due to the density of the coating which comprise most of the seal volume, the mass ratio of seal materials m_r^* is typically close to one, with specific gravities of 0.94 for natural rubber to 1.2 for neoprene. Because of the low mass ratio, it is expected that added mass will have a dominant effect in the unsteady seal response when there is free-surface contact. To show why this is the case, treat a section of the seal as a half-submerged rigid plate vibrating at infinite frequency (to eliminate the effect of the free-surface (Kármán, 1929)). The added mass is estimated as $A_{33} = \pi \rho_w w^2/2$, half the added mass of a fully submerged flat plate with width w. The mass of a section of seal of the same width is given by $m = m_r^* \rho_w w t_t$. The added mass ratio is then $A_{33}/m = \dfrac{\pi}{2}\dfrac{w}{t_t}$. For the seal materials considered in this thesis, the added mass ratio is greater than 200, indicating that the material mass can likely be neglected when hydrodynamic forces dominate. However, in the case of seal vibration, which can occur at

low immersions where the seals may be largely out of the water and significant air leakage is present, material mass will likely need to be taken into account.

Where the seal is not contacting the free-surface, an important ratio governing seal shaping and buckling is that of the gravitational moment (due to material mass) to the elastic bending moment, given by $\frac{mgL^3}{D}$, where D is the bending rigidity, m is the areal density of the fabric and L is a characteristic length (Wang, 1984). If the bending rigidity D satisfies Froude similarity, then this balance is implicitly satisfied; however as is discussed in the next section, the bending rigidity of fabrics used for small-scale experiments is generally too high, leading to distortions.

Fabric property scaling: bending stiffness

Adopting the Froude-scaled non-dimensionalization of Section 2.5.1, where $F^* = \frac{F}{\rho g L^3}$ bending rigidity is non-dimensionalized as

$$D^* = \frac{D}{\rho g L^4} \tag{2.15}$$

where ρ is the density of water (or air) and L is a length scale. When ρ_w is used, D^* can be thought of as a ratio of bending (strain) energy, Π_D to the potential energy, Π_K of a hydrostatic foundation where $\Pi_D = \frac{1}{2} D \int \kappa^2 dA \approx \frac{1}{2} D \int (\nabla^2 h)^2 dA \sim \frac{Dh^2}{L^2}$ and $\Pi_K = \frac{1}{2}\rho_w g \int h^2 dA \sim \rho_w g h^2 L^2$, h is the vertical displacement of the material and dA is the area of a patch of the seal material. This interpretation of D^* as a ratio of energies will prove useful in Chapter 5, where this scaling is examined further. It will be shown that maintaining D^* is equivalent to matching the seal buckling behavior at zero speed, and due to Reynolds number distortions, does not ensure similitude at speed.

To understand why it is difficult to achieve bending rigidity similitude, even at zero speed, the materials used for SES seals are examined. The materials used for SES seals are composites comprised of a nylon fabric reinforcement and an elastomer coating. This

creates a material with a combination of low bending rigidity, impermeability and high tensile modulus. At typical seal tensions the materials can often be treated as inextensible (see Section 5.2).

Materials testing conducted as part of the present study (see Appendix A) shows that the bending rigidity of a full-scale seal material is largely set by the elastic modulus of the coating, while the effective tensile modulus is dominated by properties of the reinforcement. To see why this is the case, consider three linearly elastic layers bonded together to form a single-ply laminate of total thickness t_t and a reinforcement thickness t_r centered about the neutral axis of the laminate. This idealization is shown in Figure 2.11. For the purposes of this analysis, the orthotropic properties of the reinforcement are ignored. 4 If the modulus of the coating is given by E_c, and the modulus of the reinforcement E_r, an upper limit of the bending rigidity (D_1) of a single-ply composite can be approximated via lamination theory (Vinson, 2005). The bending rigidity of a laminate with three layers (k=3) is approximated by Equations 2.16 and 2.17 which assume no slip between layers and no shear deformation. Poisson's ratio for the reinforcement ν_r is taken to be roughly the same as for the coating $\nu_c \approx \nu_r \approx 0.5$.

$$\begin{aligned} D_1 &= \frac{1}{3}\sum_{k=1}^{3}\frac{E_k}{1-\nu_k^2}(y_k^3 - y_{k-1}^3) \\ &= \frac{1}{3}\frac{E_c}{1-\nu_c^2}((-\frac{t_r}{2})^3 - (-\frac{t_t}{2})^3) + \frac{1}{3}\frac{E_r}{1-\nu_r^2}((\frac{t_r}{2})^3 - (-\frac{t_r}{2})^3) \\ &\quad + \frac{1}{3}\frac{E_c}{1-\nu_c^2}((\frac{t_t}{2})^3 - (-\frac{t_r}{2})^3) \end{aligned} \tag{2.16}$$

$$D_1 = \frac{E_c t_t^3}{12(1-\nu_c^2)}\left(1 + \left(\frac{t_r}{t_t}\right)^3\left(\frac{E_r}{E_c}\right)\left(\frac{1-\nu_c^2}{1-\nu_r^2}\right)\right) \tag{2.17}$$

For full-scale seal materials, such as the Type 0 (NN) used during the experiments (see Appendix A) $\frac{t_r}{t_t}$, is of order 10^{-1} and E_r/E_c is of order 10^1 which leads to an approximation for the bending rigidity $D \sim t_t^3 E_c$.

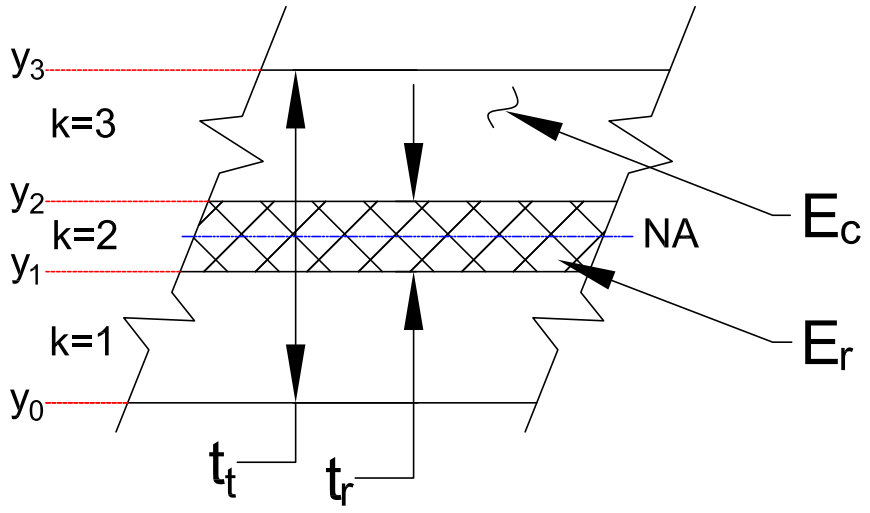

Figure 2.11 Laminate representation of seal material.Seal material treated as three (k=3) linearly elastic layers bonded together to form a single-ply laminate of total thickness t_t and reinforcement thickness t_r centered about the neutral axis (NA) of the laminate. The modulus of the coating is E_c. The modulus of the reinforcement is E_r.

Achieving bending rigidity similitude at model scale therefore requires altering the elastic modulus of the coating and material thickness. The required elastic modulus at model scale is

$$E_{c_m} = \frac{E_{c_f} t_{t_f}^3}{\lambda_{SF}^4 t_{t_m}^3}. \tag{2.18}$$

Since materials used for model seals are similar in density to the full scale materials, in order to match material mass ratio, $t_{t_m} \approx \frac{t_{t_f}}{\lambda_{SF}}$. In practice Yun and Bliault (2000) has found that for correctly scaled fabric mass, model seals are generally thicker than the scale ratio would suggest. Assuming that the fabric thicknesses are indeed scaled properly, a reduction in the coating modulus of elasticity, $E_{c_m} = \frac{E_{c_f}}{\lambda_{SF}}$, is required to set $D_m^* = D_f^*$.

Realizing a significant reduction in E_c while maintaining Froude similitude for the material mass and geometric similarity for the strain ($\varepsilon \lll 1$) is very difficult and significant concessions are generally made in fabric selection. A survey of suitable commercially available coated fabrics has shown that, in general, $E_{c_m} \geqq E_{c_f}$ (Yun and Bliault, 2000), which when combined with the thickness distortions results in model fabrics that are too stiff by a factor of at least λ_{SF}. There are a couple plausible explanations for these distortions,

one is that the coating materials, natural rubber and butidiene are formulated for maximum flexibility and effecting a significant change of E_c puts the fabric selection choice outside the range of commercially available materials. Also, the ratio of the thicknesses $\frac{t_r}{t_t}$ needs to be roughly the same at model and full-scale or the modulus of the reinforcement may dominate the bending rigidity and will need to be scaled as well.

An example of how the thickness ratio $\frac{t_r}{t_t}$ alters the properties of a composite can be seen in the case of the materials used for the large-scale experiments described in Chapter 3. The tensile elastic modulus for the Type-1 material (HN), the lightest sample tested (similar to a fabric that might be used for a small scale test), is three times greater than the thicker, full-scale like Type-0 material (NN). Examining the HN fabric, the ratios of the thicknesses for the component layers is different than the NN fabric, $t_t \sim t_r$ which suggests[3], owing to the thinner coating, the reinforcement comprised of yarns of nylon 6/6 (E= $2 - 3.6 \cdot 10^9$ Pa) strongly influences the tensile modulus and bending rigidity. Comparing the mass, the effective scale ratio is $\lambda_{SF_{mass}} \approx 6$ while the scale ratio based on D is $\lambda_{SF_D} \approx 3$, showing the difficult in matching both mass and bending rigidity and achieving large scale ratios.

Given these challenges, at least one author has proposed selecting the most flexible fabric available that meets the hoop stress requirements, and ballasting the fabric with discrete weights to get closer to the desired stiffness (Prokhorov, 1981).

In summary, to procuring materials achieving similitude for the bending rigidity would involve developing new coating materials and fabrics, a prospect, which even if feasible, would likely distort the nonlinear and orthotropic properties which may play an important role in seal behavior.

[3]This can be shown via the "rule of mixtures" Vinson (2005) $E_t = \frac{E_c(t_t - t_r)}{t_t} + \frac{E_r(t_r)}{t_t}$, which, assuming equal strains in the layers, relates the effective total modulus of elasticity E_t to the thicknesses t_t, t_r and moduli E_c, E_r of the layers.

Fabric property scaling: nonlinearities

As both the reinforcement and coating are constructed of polymers, which exhibit complex constitutive properties including nonlinear stress-strain behavior, hysteresis and viscoelasticity (Graham et al., 1983; Hertzberg et al., 1975), nonlinear behavior is expected to play a role in the behavior of SES seals. An example of the viscoelastic behavior found in SES seal materials is seen in Figure 2.12. This shows that as strain rate is increased in the tensile mode, the seal material become more "glassy" or rigid, resulting in a 10 fold increase in elastic modulus. Seal materials are composites which may possess different glass transition frequencies for the reinforcement and coating. When the material is excited in tension, the transition frequency may be set by the reinforcement while in bending the transition frequency may be dependent on properties of the coating.

In addition, the presence of the woven fabric reinforcement adds a degree of orthotropy, with the fabric possessing principal directions due to the weaving process (Hu, 2004). This nonlinear behavior is specific to particular base fabrics and coating formulations and likely cannot be scaled without significant distortion. Appendix A shows that for the Type-1 (HN) material employed during the large-scale experiment, there are significant differences in the bending rigidities measured in the warp (D_X) and weft directions (D_Y) with $\frac{D_X}{D_Y} \approx 2$. Along

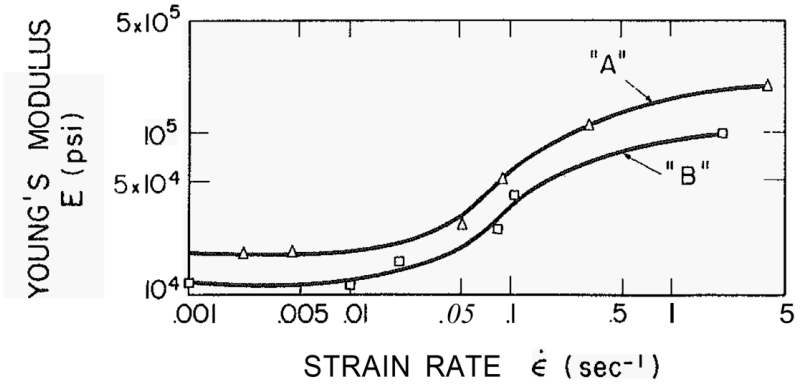

Figure 2.12 Effect of strain rate on elastic modulus of two elastomer-fabric composites. Material A is a sample taken from an ACV skirt, while material B is a commercially available neoprene-coated nylon fabric not specifically designed for ACV use (Graham et al., 1983).

the bias, or a direction between the warp and weft, the bending rigidity may be even lower depending on the fabric structure (Hu, 2004). To date, very little attention has been devoted to the constitutive modeling of seal materials. An approach that can test the performance of these complex materials under real world loading is highly advantageous, as it is difficult to know a priori the significance of these nonlinearities.

2.6 Summary of previous work

Despite extensive full-scale trials and physical model testing, the hydroelastic response of the seal system, particularly basic information on the seal modes and the physical mechanisms responsible for wear patterns such as Figure 2.8b remains largely unknown. Significant questions such as the stability of seal configurations to disturbances cannot be answered at this time. Similarly, estimates of the hydrodynamic loads on the seal system are notoriously inaccurate and are based on heuristic scaling of small-scale test data. The utility of these small geometrically similar experimental studies is limited, as the system features a number of structural, aerodynamic and hydrodynamic scales, making similitude difficult to maintain at small scale. In particular, achieving similitude quantities such as air cushion compliance and the bending rigidity of the seal fabric lead to a physically unrealizable small-scale model design.

Underlying both questions on seal wear and seal drag is a basic need to understand how finger seals deform under the influence of hydrodynamic and aerodynamic forces. There is also a parallel need to develop testing capabilities such that bow seal response can be observed at a relevant physical scale. The large-scale studies conducted by Besch (1976) are an example of a fruitful approach for designing physical experiments on bow seals, and represent an important starting point for the present study. Besch (1976) provides detailed descriptions of the types of seal response, as well as acceleration data which show the measurement bandwidth required to characterize bow seal response and the advantages

of a non-contact measurement system. Besch (1976) also shows the challenges in data reduction and interpretation once finger seal data are acquired, and the need for a framework to interpret the wide range of seal behavior.

2.7 Present Study

The thesis is composed of three studies:

Study 1

Utilizing a large-scale experimental approach, Study 1 documents the hydroelastic response of a surface-effect ship finger seal system under calm water conditions. The study seeks to isolate the effects of cushion pressure and seal immersion on seal configuration. The study contrasts the behavior of finger seals constructed of materials with markedly different material properties. Study 1 contains three parts: The first part, Chapter 3, describes the large-scale experimental approach. It provides detail on the test geometry and highlights the specialized measurement systems used to characterize the test platform configuration and 3-dimensional seal shape. The second part, Chapter 4, presents results from experiments conducted at the U.S. Navy's Large Cavitation Channel utilizing the new test capability. The results focus on quantitative descriptions of the cross-flow profiles and boundary conditions. Lastly, the study synthesizes imagery and shape data to identify dominant response regimes and potential stability boundaries. Study 1 shows the hydroelastic response of bow seals to be characterized by striking stable and unstable post-buckling behavior. Bending rigidity is found to have a significant influence on seal response.

Study 2

The second study, contained in Chapter 5, examines the dramatic changes in configuration observed in the experiments through the lens of post-buckling theory and scaling arguments.

Study 2 seeks to identify physical mechanisms and dimensionless parameters driving the cross-flow conformation of bow seals.

First, Study 2 proposes a decomposition of the seal into three regions based on the balance of stretching and bending forces. The remainder of Study 2 focuses on the "tail" region where the seal lies parallel to the free-surface. Second, motivated by the large-scale data, Study 2 analyzes the kinematics of seal compression and proposes a mechanical model of seal confinement. Third, Study 2 introduces a model, based on a geometrically-nonlinear beam on an elastic foundation, for cross-flow buckling in the Tail region. The study then employs this analogy to investigate the influence of bending rigidity and boundary conditions on seal mode shape and stability. Lastly, Study 2 employs scaling arguments to estimate hydrodynamic terms in the model and to ultimately derive scaling laws describing how the cross-flow profile of a finger seal changes with velocity, pressure, and immersion.

Study 3

The third study, contained in Chapter 6, verifies the the zero-speed scaling laws introduced in Study 2 through a small-scale experiment. The approach allows explicit control of the material compression and system size.

Lastly, in Chapter 7, there is a recap of contributions of the work. An extensive list of recommendations for future work is provided in Chapter 8.

2.7.1 Study limitations

The present study is subject to a number of limitations which are discussed briefly below. Detailed discussions of specific limitations are contained within the individual Chapters. Methods for reducing these many of these limitation are proposed in the Future Work, Chapter 8.

Limitation in scope

The experimental observations presented in Study 1 are limited strictly to a single finger seal geometry at a single heading. Due to a dearth of finger seal validation data, any generalization of the results to finger seals with different geometries or configuration should be approached with caution. Significantly changing the face angle or seal cropping could result in very different responses.

The present study is limited in scope to the post-buckling analysis of the finger seals. The results presented in Study 1 represent a small subset of the data collected during the large-scale experiment. Data types presented are intentionally limited to those relevant to the modeling efforts of Study 2, and consist primarily of information on seal shape and boundary conditions. Conspicuous omissions from Study 1 include information on the frequency-content of seal vibration and estimates of hydrodynamic loads. These data will be presented in future reports.

Limitations of the experimental approach

There are a number of limitations to the present study due to the experimental approach. First, there are limitations associated with free-surface operations at the Large-Cavitation Channel. Due to problems associated with air entrainment, the large-scale data presented in Study 1 are limited to a narrow velocity range, corresponding to a variation of 0.07 in cushion-length based Froude number (fn_c). To capture the range of wave slopes typically encountered by an SES may require a Froude number(fn_c) range of 1.5. Because of this, hypotheses on the influence of velocity on seal shape, such as contained in Study 2, cannot be tested. Similarly, the reproducibility of the large-scale experiment is limited as compared to conventional tow tanks tests. Final running level and velocity at the LCC is dependent on a nonlinear relationship between tunnel rotation rate, gate angle and initial fill level. Because of this, small differences in inflow velocity and running level exist between conditions, limiting the ability to make direct comparison between runs. The large-scale data were also

affected by unsteadiness in the inflow velocity and free-surface elevation. These effects were a function both of the velocity tested and the time on-condition. This impacts seal buckling, as the instabilities responsible for folding are known to be highly sensitive to imperfections and disturbances.

Second, as is the case with any measurement, there are Nyquist related resolution limitations and uncertainty. The 3-dimensional Time-of-Flight measurements used to capture seal shape are particularly sensitive as they are not intended for imaging moving targets or a free surface. In addition, as discussed in the Future Work, calibration and registration of these cameras within the global coordinate system is an ongoing research area. In general, derived quantities that compare absolute positions of ToF imagery to an absolute position of another sensor (ultrasonic probe) should be interpreted with caution.

Lastly, the results of the benchtop experiments are subject to a number of limitations. Two-dimensionality is not realized during the experiment. The experiment is sensitive to misalignment; this manifests itself in spanwise variation in the buckling profiles. In addition, opportunities for direct comparison between the large-scale experiments and the small-scale experiment are limited. The large cross-flow displacement observed in the experiments could not be sustained at small-scale without detachment of the free-surface.

Limitations of the analytical approach

The qualitative models introduced in Study 2 have very significant limitations and should be viewed as tools to aid interpretation of the data. Limitations of these and other modeling approaches are discussed in light of the full-scale data in Section 5.1.

The analytic modeling limitations fall into a number of categories. First, a 2-dimensional model is used to model a fundamentally 3-dimensional structure. This simplification is partially justified by the region decomposition proposed in Study 2, however there is not a 2-dimensional analogue of the Gaussian curvature. Second, the model considers solely quasi-static behavior of the seals. Third, complexities in the constitutive properties of the

seal materials are ignored in favor of a linearly elastic isotropic material.

Chapter 3
Large-scale experimental approach

As part of Study 1, a large-scale experimental approach is described which overcomes many of the scaling problems that have limited previous SES experimental studies and enables the high-fidelity measurements required to characterize the complex response of bow seals. Development of this unique testing capability is described in Section 3.1. The experimental approach leverages recent advances in non-contact measurement techniques to acquire time-resolved, high-resolution 3-dimensional measurements of seal shape. Implementation of this system is described in Section 3.2.

An outline of the test plan and procedures executed during the experiments at the U.S. Navy's Large Cavitation Channel is provided in Section 3.3. Post-processing methods are briefly described in Section 3.4, including information on the processing stream for the motion capture data. Additional information on the experimental setup can be found in the appendices. Appendix C contains details on the load cell calibration method. Appendix D provides additional details on the geometry of the large-scale test platform. The first two sections of this chapter were previously published as Wiggins et al. (2013).

3.1 Development of a large-scale seal testing platform

3.1.1 Platform Design

An inboard profile of the SES seal test platform located in the test section along with the free-surface forming gate is shown in Figure 3.1. A survey of free-surface running condi-

tions at the Large Cavitation Channel (LCC) was performed in 2010. These preliminary experiments determined that at supercritical velocities (depth-based Froude numbers (fn_H) greater than unity) and high initial fill levels (the initial static water level in the test section roughly 90 % full), stable free surface conditions could be generated. The resulting free surface was found to be fairly 2-dimensional (mean spanwise variations on the order of 5 mm over a span of 3.3 meters) with water depths downstream of gate between 1.0 m and 2.1 m, depending on the angle imposed by the free surface forming gate. Between the vena contracta and the hydraulic jump in the diffuser, typically corresponding to a streamwise distance of nearly 10 m, the mean free surface level generally varied less than 15 mm.

Per the 2010 survey, the test platform is positioned downstream of the gate such that the free surface is fully developed prior to contact with the bow seals and the hydraulic jump that returns the flow to sub-critical depth is located downstream of the stern seal (Figure 3.1). As installed, the test platform is nominally 7.9 m long, 1.52 m wide and 2.0 m tall (much of which is not immersed during tunnel operation) and is of welded and bolted steel construction. The mass of the platform is roughly 8.4 metric tons, not including support structure. The air cushion is bounded by the flexible seal system at the bow, thin rigid sidewalls, port and starboard, and a rigid segmented stern seal. The platform structure extends 1.5 m forward of the bow seals. This extension provides a rigid sheltered area for flow visualization equipment. Additionally, there is a system of turnbuckles which lash the platform to the top of the test section and prevent yaw (not shown in Figure 3.1).

The large size offers a number of advantages. First, the large size and robust seal mounting system provides the ability to install multiple full-scale or truncated seals and expose them to controlled "full scale" pressures and significant environmental loadings. Installing multiple seals is advantageous as it reduces testing artifacts due to finite-width effects. Second, as discussed in Section 2.5, the large air volume enclosed by the platform decreases the stiffness of the air cushion. This allows comparisons to be made to bow seals of relatively large SES type craft. The compliance of the air cushion is further augmented by

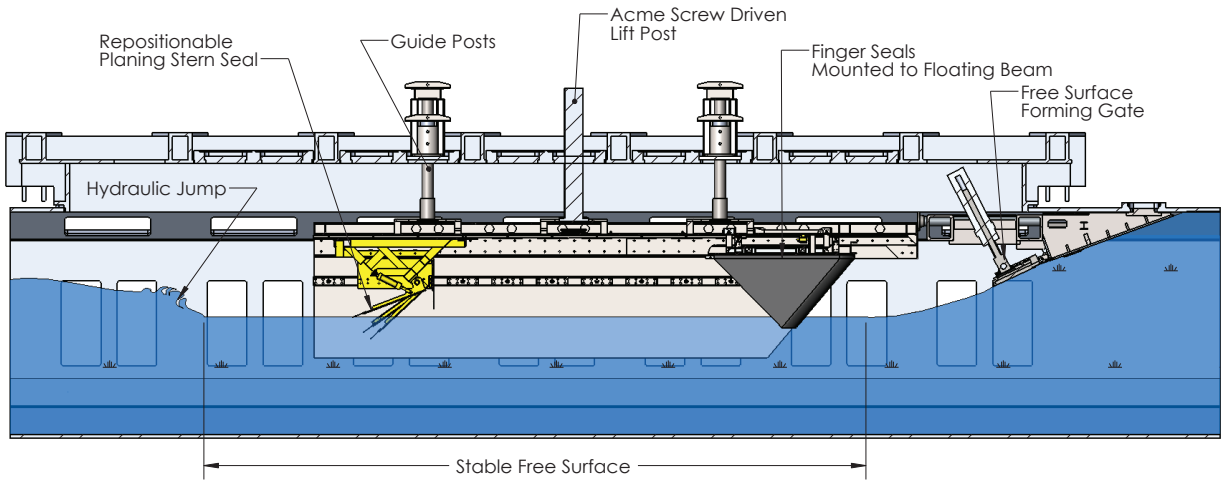

Figure 3.1 Profile of seal test platform in the Large Cavitation Channel (LCC) test section.

a pressure control system utilizing sensitive back-pressure regulators. A one-line diagram of the pressure control system is provided in Appendix D.

During normal operations, the platform is fixed in heave. Offline, after freeing the turnbuckles and guide posts used to secure the platform within the test section, the platform can be repositioned via a lift post. Four guide posts extend vertically from the platform and integrate with the top of the LCC test section. The guide posts provide additional rigidity and also provide the cushion air conduit to the platform. The position of the seals relative to the free surface can be controlled by changing the angle of the free surface forming gate or by changing the shaft location of the bow seal mounting plate. As installed, the test platform is positioned to accommodate testing seals at a local draft (also known as immersion) of 0 to 300 mm. A summary of the test platform properties is provided in Table 3.1.

3.1.2 Bow seal system

The platform is outfitted with five finger seals. The seals were fabricated by the Naval Surface Warfare Center, Panama City Division and sized similar to Type-A seals on the U.S. Navy's Landing Craft Air Cushion (LCAC) class. The geometry of the finger seals is given in Table 2.1. The mounting system for the finger seals is shown in Figure 3.2. In

Length overall	7.90	m
Mass of test platform alone	8.4	mt
Length of cushion, L_C	3.1-6.5	m
Length of cushion (nominal), L_C	5.88	m
Breadth of cushion, B_C	1.52	m
Sidewall depth	1.68	m
Sidewall draft at zero immersion	0.42	m
Channel width	3.05	m
Maximum design pressure	3000	Pa
Maximum flow speed	8.0	m/s
# of Fingers	5	
Finger height	1.00	m
Finger width	0.31	m
Finger seal leading angle	50.00	deg

Table 3.1 Test platform properties (see Appendix D for additional test platform dimensions).

order to decouple the global vertical and horizontal forces, a floating-beam arrangement is employed. The main bow seal plate is hung below the fixed platform structure via four control arms, which are linked to permit only a single degree-of-freedom. The main plate is restrained by a single high accuracy tension/compression load cell (Cooper LRCN 710, 4450N capacity). When properly aligned, friction and off-axis loading are minimal and a majority of the global horizontal force is transferred to the tension/compression load cell, whereas the weight of the plate and vertical component of the pressure force are carried by the control arms through their bearings.

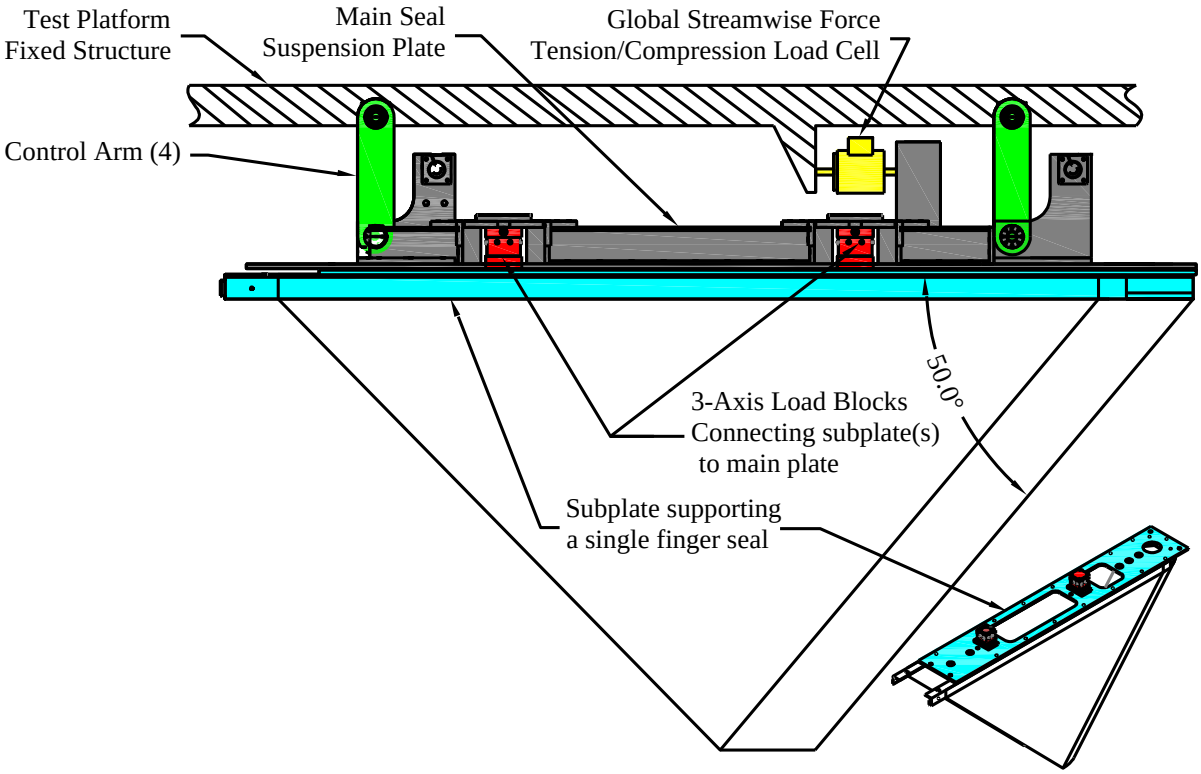

Figure 3.2 Floating beam force measurement system.

Pull tests on the main plate using a traceable standard showed that the global horizontal load measurement system has virtually no mechanical loss. Typical calibration curves for the system are shown in Figure 3.3. Decay tests of the main plate without the load cell or finger seals reveal the system damping ratio to be around 3% of critical. In order to reduce friction between the sidewall and the inflated finger seals, the inner face of the sidewall is lined with a low-friction Teflon® sheet.

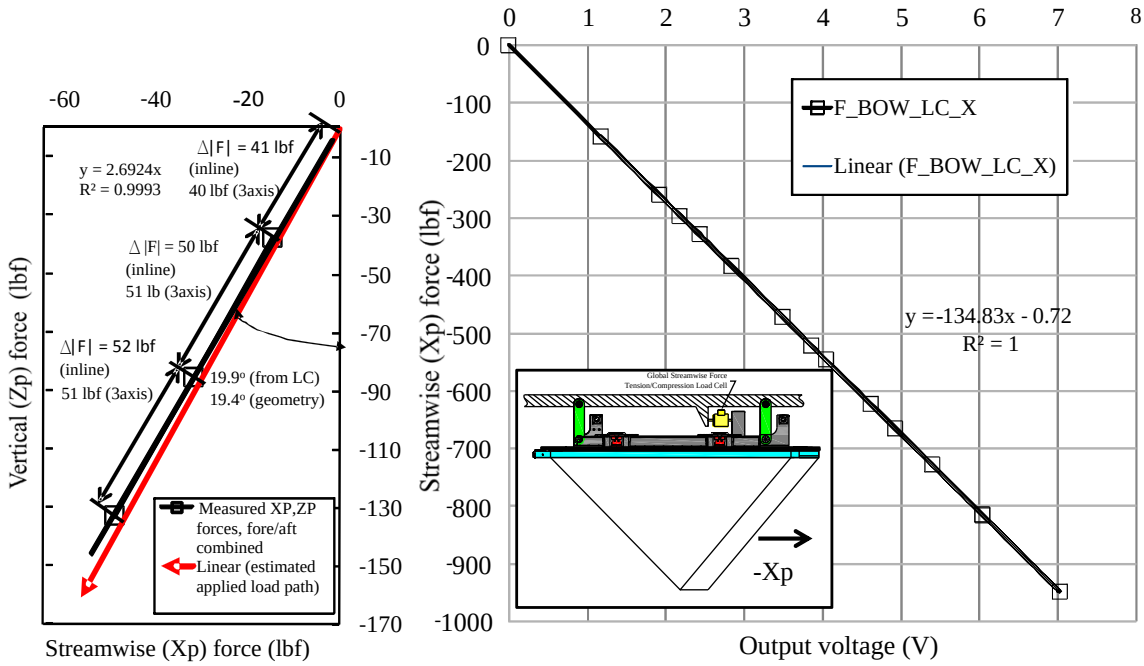

(a) 3-axis load cell calibration

(b) Single axis load cell calibration

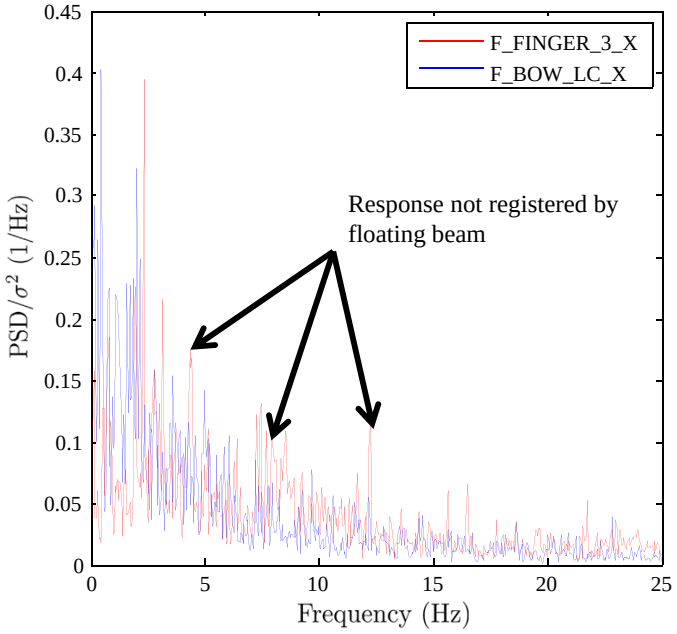

(c) Frequency response comparison

Figure 3.3 System characterization of floating beam and 3-axis load cell systems. a) 3-axis load cell calibration, force vector compared with geometry. b) Floating beam calibration curve. c) Frequency response comparison, 3-axis load cell and floating beam system. Power spectral density is derived from typical streamwise force measurement. Spectral density is normalized by the variance (σ^2).

Figure 3.2 shows the individual finger seal attachment method. Individual finger seals are clamped to an aluminum structure which runs along the perimeter of the mounting plate. These mounting plates rigidly connect to the main plate at two locations. This arrangement facilitates measurement of the vertical and horizontal loads on an individual finger seal via two three-axis load blocks (FUTEK MTA400) installed at the two support points. For the commissioning experiments (2011), only Seal 3 (center), furthest from the influence of either sidewall, is instrumented in this manner. In the second phase of experiments, completed July 2012, two seals were instrumented in this manner. On the non-instrumented seals, dummy blocks are used instead of load cells, but they could also be instrumented in the same manner. Measurement of local loads on an individual finger in a seal system offers some key advantages over previous seal force measurement approaches such as those employed by Heber (1977) and Besch (1976), including:

- Reduced sidewall/seal interaction forces.
- Direct measurement of the total forces, with essentially no mechanical losses.
- Wider bandwidth measurement. The rigidly mounted load cell and subplate system have a higher stiffness and lower mass than the large floating beam, resulting in a wider measurement bandwidth. This can be seen in the right inset in Figure 3.3
- Pitch moment measurement. At sub-hump and hump speeds, vertical forces on the seals are significant (Heber, 1977; Yamakita and Itoh, 1998). The vertical force measurement and the derived pitch moment allow us to understand how these quantities change with Froude number.

3.2 3-dimensional motion capture system

The shape of the flexible bow seals is captured through a non-contact 3-dimensional motion capture system. The measurement approach leverages recent advances in range imaging

cameras, permitting the configuration of the seal to be captured in a high-resolution, time-resolved manner. The non-contact approach avoids the artifacts due to mass-loading that are inherent in accelerometers and other contact-based measurement approaches.

Bow seal hydroelastic response features a range of time and length scales. In calm water conditions, previous work suggests the shape of the cylindrical and knuckle regions is largely static and is three-dimensional. In the Tail region, previous work suggests that seal response features buckling at high mode numbers (short wavelength) and under certain conditions, high-frequency vibration (maximum 90 Hz for the velocities achievable at the LCC) may occur. To adequately resolve seal motion in this critical region, requires both high frame-rates and spatial resolution.

Figures 3.4 and 3.5 show the motion capture system as installed for the July 2012 experiments. Based on proof-of-concept experiments carried out in 2011, time-of-flight (ToF) cameras were chosen as the primary seal displacement measurement method. Benefits of the ToF cameras include compact size, robustness and comparatively high frame rates (up to 120 frames per second). ToF cameras based on PMDtec's Photonic Mixer Device (PMD) sensor were selected.

The principle of operation for the PMD ToF camera is shown in Figure 3.6. PMD cameras use a bank of infrared (IR) LEDs to actively illuminate the seal with an amplitude-modulated signal of frequency f_{mod} (typically around 20 MHz). The time required for light to travel from the emitter to the target and return, or "time-of-flight" (t_{oF}) is given by $t_{oF} = 2\frac{Z}{c}$, where c is the speed of light, and Z is the distance to the target. In the case of an amplitude modulated source, the source will have shifted a phase ϕ_{ToF} relative to the reflection in time t_{oF}. Provided that the frequency of modulation f_{mod} is chosen such that the phase does not wrap (exceed 2π) for a given target, the distance Z can be estimated from the phase shift,

$$Z = \frac{c}{2f_{mod}} \frac{\phi_{ToF}}{2\pi}. \tag{3.1}$$

The PMD camera estimates the phase shift ϕ_{ToF} on a pixel-by-pixel basis. This is accom-

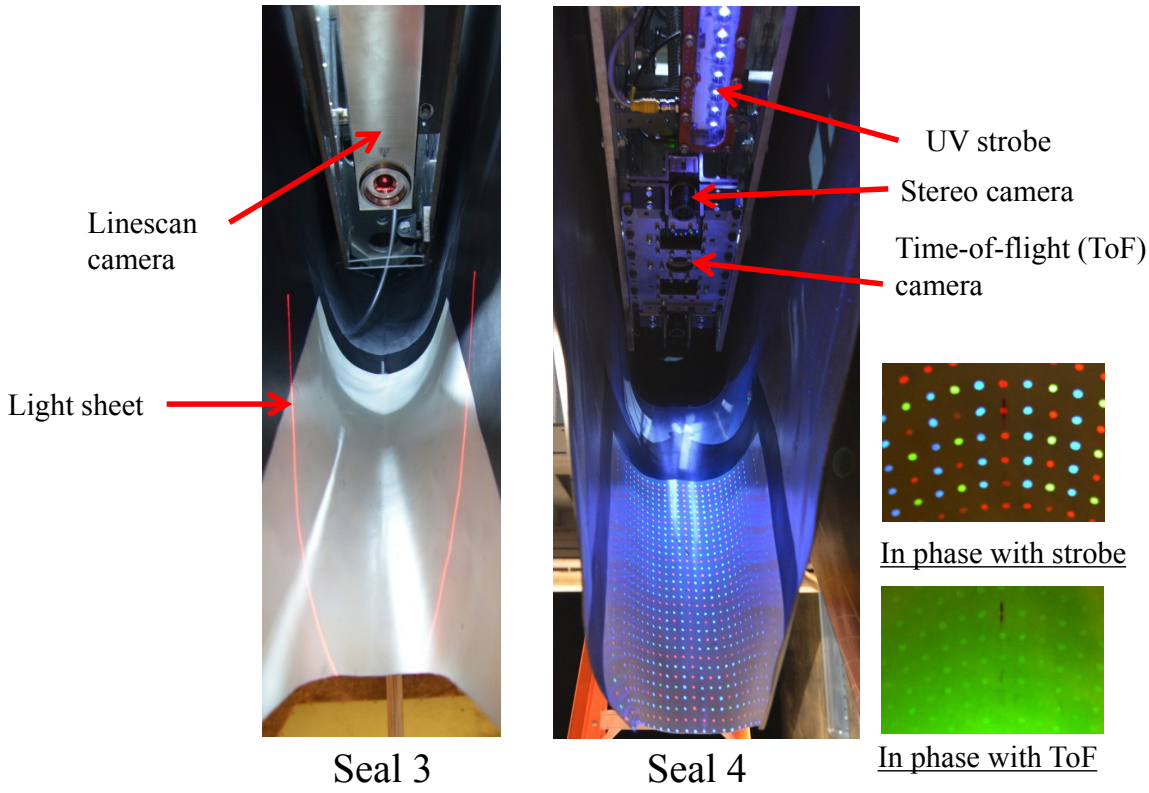

Figure 3.4 Seal motion capture system, including reference channels, as installed, Summer 2012.

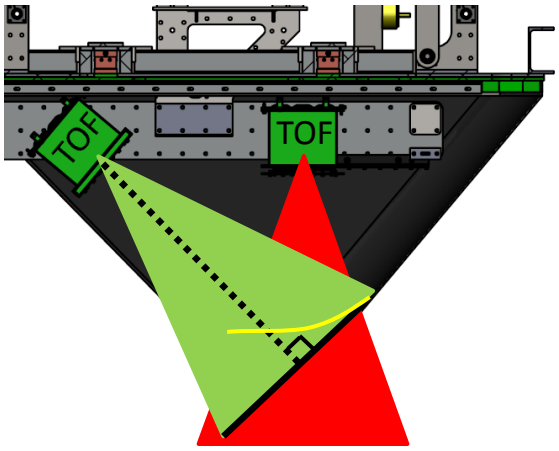

Figure 3.5 Time-of-flight camera arrangement, interior of Seal 4.

plished through specialized pixels that gate (shutter) at very high frequencies in phase with the light source. Each "phase image" I_p samples the scene at phase ϕ with respect to the source signal. These samples can be combined, using a 4-shift algorithm, to demodulate the

signal and estimate the phase shift,

$$\phi_{ToF} = tan^{-1}\left(\frac{I_p(3\pi/2) - I_p(\pi/2)}{I_p(\pi) - I_p(0)}\right). \tag{3.2}$$

Mathematically, the phase image I_p represents a convolution of the reference signal and the reflection. The limits of the convolution integral are set by the integration time T_i an important parameter that is manually tuned to the target properties. T_i is akin to the exposure time for an intensity camera. The control software provided by the manufacturer permits setting different integration times for each of the four samples. Per the manufacturers an integration sequence close to $T_{1:4} = [0.25, 0.02, 0.02, 0.25]$ msec was adopted for the majority of the experiments, which corresponds to an exposure time of $\Delta(T_{1:4}) = max(\phi_i/(2\pi f_{mod}) + T_i) \approx 0.25$ msec per frame. Due to onboard processing and throughput limitations, the frame rate is significantly lower than the integration time suggests, generally around 100 Hz.

Two compact PMD cameras are located inside Seal 4 with overlapping fields of view. A single PMD camera is installed in Seal 3. The overlapping fields of view are required in order to eliminate occlusions created by folds in the seal material and to optimize return

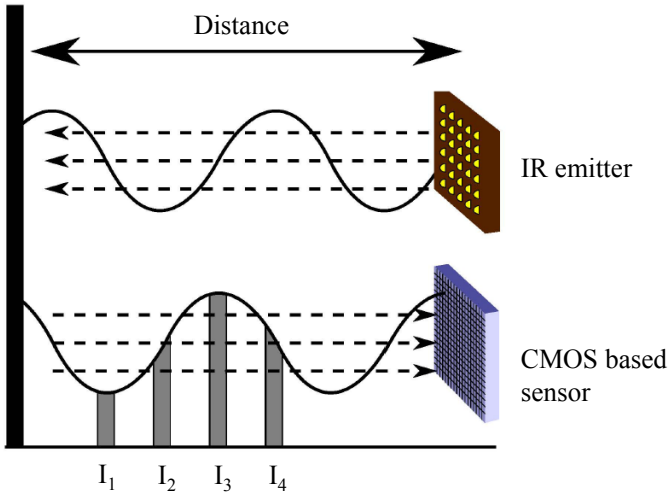

Figure 3.6 Time-of-flight camera principle of operation. I_1, I_2, I_3 and I_4 correspond to a sequence of phase images used to demodulate the signal and measure phase between IR transmission and return (Figure modified from Foix et al. (2011)).

signal strength. The reference frames used for the ToF cameras ($X_{ToF}, Y_{ToF}, Z_{ToF}$) are shown in Figure 3.7. To reduce possible interference between the sensors, each uses a different modulation frequency. The two cameras provide real-time distance information at 80,000 points on the lower third of seal, corresponding to a spatial resolution of around 5 mm at a typical object distance of 1 m. The uncertainty in the distance information returned by these cameras is typically better than 4 mm near the image center. However due to their principle of operation, uncertainty can vary considerable depending on the strength of the return signal. Experiments performed at the University of Michigan have shown that the reflectance values and the quality of the return is dramatically improved when the interior of black Type-0 (NN) seals have been painted with a very thin coat of white flexible paint.

Current generation ToF cameras are not capable of resolving the high-frequency vibrations characteristic of the Tail region due to insufficient spatial resolution and inter-frame motion-related artifacts. To augment the ToF camera system in this region, a high-speed reference channel is employed on the centerline seal (SICK IVC-3D 200, 0.2 mm resolution (typical) , 5000 lps). The SICK IVC-3D integrates a high-speed CMOS linescan camera with a light-sheet generator in a single housing. The camera can be seen in Seal 3 of Figure 3.4. The reference frame for the linescan camera (X_{IVC}, Z_{IVC}) is shown along with the ToF cameras in Figure 3.7. In order to capture the buckled seal shape, the camera is oriented such that the light sheet is projected on the seal in the cross-flow direction. Triangulation and factory-provided camera calibration information are used to estimate the seal profile. The measurement is made at a fixed streamwise distance ${}^{s}X_{IVC}$ from the undeflected seal tip. Data from the linescan camera is used extensively in Chapter 4.

Another significant limitation of the ToF measurement method is the Eulerian nature of the point-clouds. Without additional visual cues, ambiguity exists in determining the location of features such as the seal centerline or seal edge. To identify these features, the reflectance amplitude image is segmented. There is significant uncertainty in this processing step. For instance, in test conditions with an agitated free surface it may difficult to

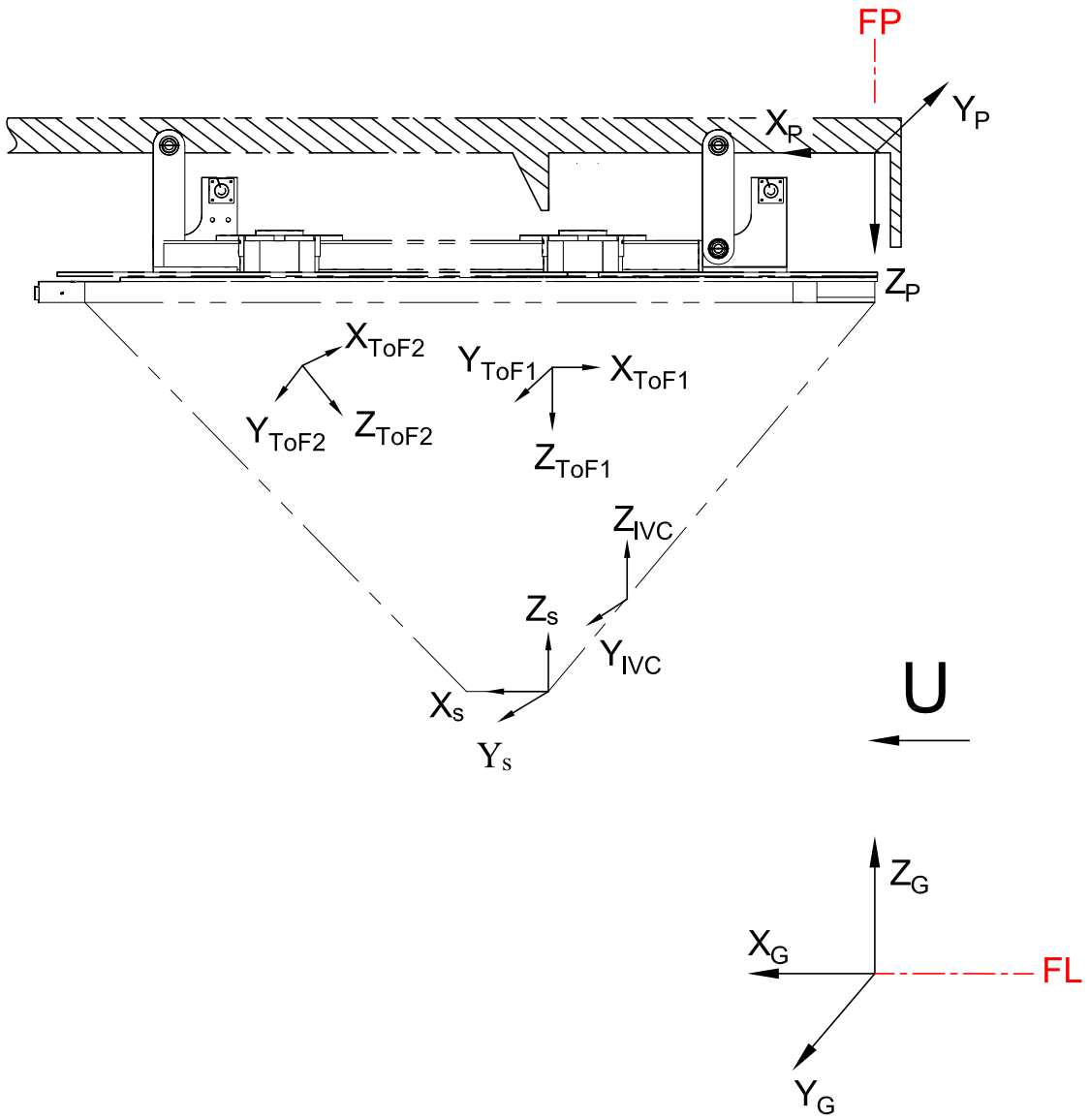

Figure 3.7 Coordinate frames used by measurement subsystems (list what they are).

distinguish the seal edge from the free-surface.

To improve these estimates, an optical tracking reference channel was developed. A challenge of adding an optical tracking system in parallel with a ToF system is that tracking requires the addition of active or passive markers to an otherwise uniform seal face. The presence of these markers significantly degrades the quality of ToF measurement, which is a function of the surface reflectivity. This limitation was overcome through the development of a novel passive marker system. Ultraviolet (UV) sensitive paint (DAYGLO Phantom)

was applied to the seal at known locations. Under normal lighting conditions, the markers are transparent to the ToF camera. However, under the action of an UV strobe, the markers can be triggered in/out-of phase with the ToF system. Using off-the shelf CMOS machine vision cameras, the resulting images can be easily segmented and registered. An example sample images taken in/out-of phase with an UV strobe is shown in the lower right corner of Figure 3.4. To integrate images from the various sources custom image acquisition software was developed in C++ and LabView.

3.3 Execution of large-scale experiments

Experiments using the test platform developed as part of Study 1 were conducted in the Summer 2011 and Summer 2012. The test plan is given in Table 3.2. Two sets of finger seals were tested based on the geometry supplied by the NSWC Panama City (Figure 2.6). The seals were constructed of two markedly different materials: a relatively stiff nitrile/nylon (NN) seal material (Type-0) similar to the fabric used on current ACVs and a lighter and more compliant hypalon/nylon (HN) material (Type-1), which was the lightest fabric that could be located and was suitable for hydrodynamic testing. The estimated material properties of the two different finger seal materials are given in Table 3.3. Additional information on the constitutive properties of the two materials is presented in Appendix A, obtained to support finite element modeling and the post-buckling analysis carried out as part of Study 2.

The study primarily seeks to isolate the effects of cushion pressure and seal immersion on seal configuration. Immersion is the local draft of the seal and is depicted in Figure 3.9. The nominal immersion is δ_s and is measured from the undisturbed waterline. δ_c is the static cushion depression, defined as

$$\delta_c = \frac{p_c}{\rho g}. \tag{3.3}$$

For each seal type, a dense test matrix was executed that fully covered the range of

Seal type	finger	seal
Seal material types	2	#
Seal depth immersions, δ_s	0-300	mm
Cushion pressure, p_c	0-3000	Pa
Cushion depression, $\delta_c = \frac{P_c}{\rho_w g}$	0-300	mm
Free stream velocity, U	5-8	m/s
Water depth, H	$Z_{G_{tip}} + \delta_s$	
	1.45-1.75	m

Table 3.2 Finger seal test plan.

Materials		Nitrile\Nylon	
		Hypalon\Nylon	
Areal density	ρ_f	1.76	kg/m^2
		0.23	kg/m^2
Fabric thickness	t_t	1.57	mm
		0.23	mm
Water density	ρ_w	998	kg/m^3
Bending rigidity, avg warp(X)/weft(Y)	$D_{\overline{XY}}$	$3.8 \cdot 10^{-3}$	Nm
		$4.8 \cdot 10^{-5}$	Nm
Tensile modulus, avg warp(X)/weft(Y)	E_t	$1.79 \cdot 10^9$	Pa
		$5.28 \cdot 10^9$	Pa
Poisson's ratio	ν	0.49	

Table 3.3 Estimated seal properties. See Appendix A for additional details.

conditions achievable with the test platform and free-surface forming gate. The range of steady state conditions achieved with the stiff Type-0 (NN) and compliant Type-1 (HN) finger seals is shown in Figure 3.8. In dimensional terms, cushion pressures (p_c) to 3500 Pa were tested at nominal immersions (δ_s) to 300 mm. The cushion pressure (p_c) corresponds to a maximum cushion depression, $\delta_c = 358$ mm.

The test matrix covers a narrow speed range of 5.5-8.0 m/s, with the majority of the measurements acquired between 5.5-6.6 m/s. At velocities above 6 m/s, air entrainment became problematic and test durations had to be limited due to free surface and velocity fluctuations. In dimensionless terms, the velocity range corresponds to a cushion-length based Froude number (fn_c) of 0.75-0.85. The maximum non-dimensional immersion $\delta_s/R_f = 1.5$. It should be noted that in the top inset of Figure 3.8, there is a slight decrease in velocity

with increased seal immersion. This is a byproduct of the experimental approach, and is a consequence of conservation of mass. During the experiment, fine control over bow seal immersion could be achieved by altering the upstream gate angle. However, unless the impeller rate and gate angle were changed in parallel, changes to the gate angle had the undesirable effect of altering both the running level and the velocity in the test section. This represents one of the challenges of performing free surface experiments in a water tunnel as compared to a tow tank.

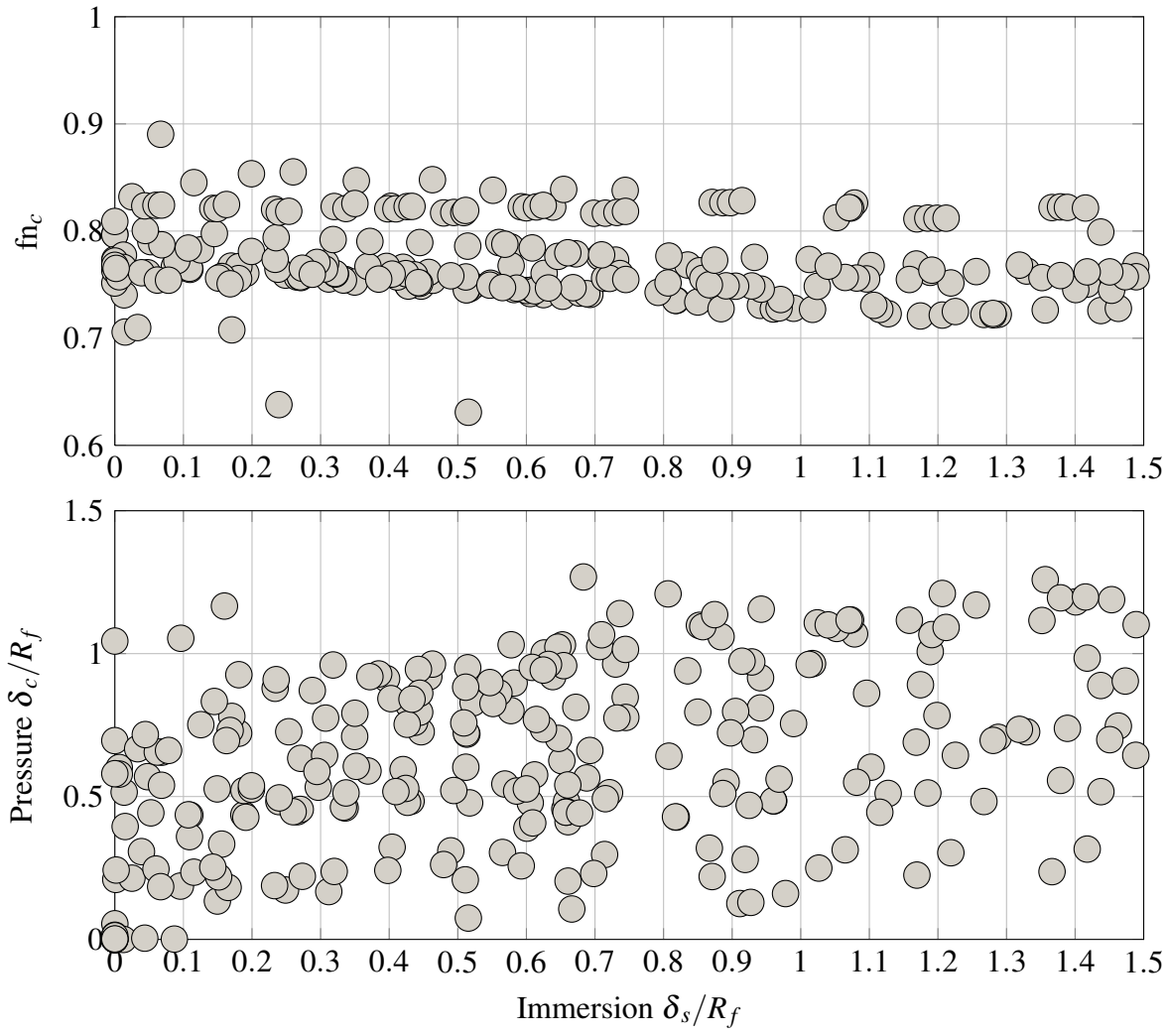

Figure 3.8 Range of steady experimental conditions (Summer 2012), Type-0 and Type-1 and finger seals. Froude number (fn_c) and pressure (p_c) as a function of immersion (δ_s) is shown.

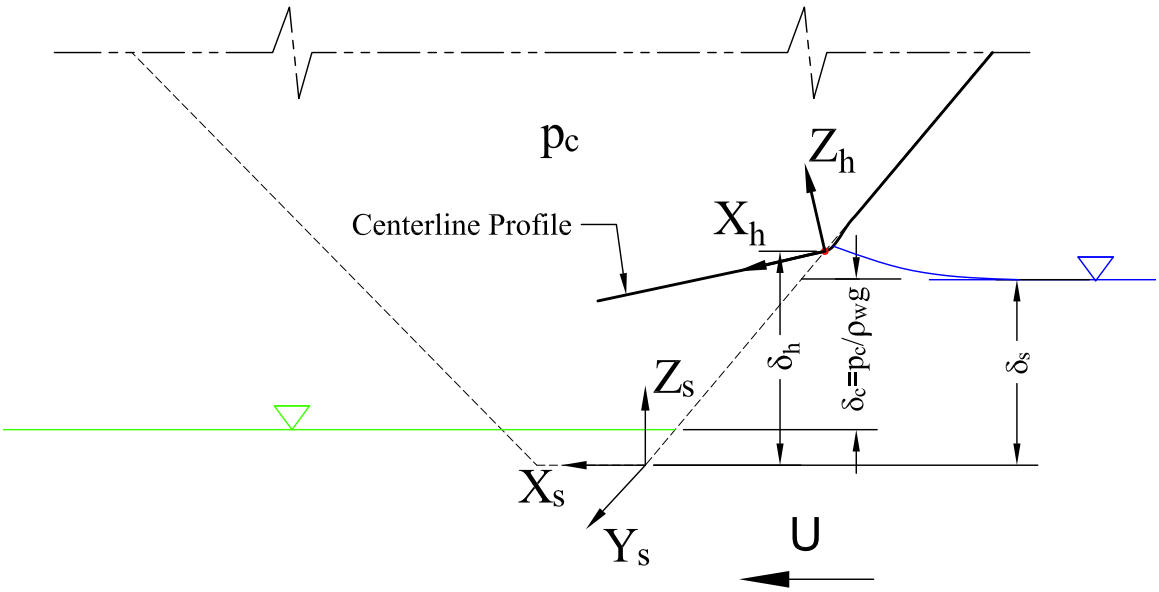

Figure 3.9 Definition of immersion δ_s, cushion depression $\delta_c = \frac{p_c}{\rho_w g}$, and hinge elevation δ_h. Nominal hinge location taken to be intersection of Tail (see Figure 4.4) and seal face tangents.

3.3.1 Experiment Execution

During the commissioning experiments, a number of different types of tests were conducted. These tests were performed not only to fulfill the main mission of the experiments – to characterize the steady response of the seals, but also to characterize the test platform itself and build some intuition as to the unsteady behavior of the seals. Due to the presence of the free-surface forming gate, test procedures had to be developed during the start-up and shutdown process to ensure that a free surface could be achieved without damage to the instruments or the test platform. The following is a brief description of typical test procedures and the start-up/shutdown process.

Zeroing the instrumentation

Prior to filling the tunnel a series of measurements are recorded to verify the offsets of the ultrasonic rangefinders, cushion pressure sensors and load cells.

Fill/pressure tests

Once the offsets are acquired with the empty test section, water is allowed to enter the test section. Water level is monitored using a sight glass mounted outside the test section. Mäkiharju and Elbing (2013) found that running conditions in the test section with the free-surface forming gate may be set by filling the tunnel to a prescribed level and setting the impeller rotation rate and gate angle appropriately. Data are acquired during the filling process to check that the water level derived from the ultrasonic probes is consistent.

When the water level reaches the base of the bow seal, filling is momentarily stopped and offsets are acquired on the wet/wet pressure transducers and the pitot rake that was located upstream in order to measure speed over depth. The stern seal is then brought forward and the pressure control system set to pressurize the cushion to around 500 Pa. This is done to apply a known pressure on the bow seal system in the absence of hydrodynamics forces. These data is later used to estimate projected areas and pressure tares required to derive the hydrodynamics forces from the gross loads registered on the load cells.

At selected points during the fill test, the fill is stopped momentarily and forced oscillation tests are conducted. These tests consisted of pulsing the fan rotation rate at a known frequency. In the absence of hydrodynamic forces, the projected area can be estimated from the inner product of the excitation as measured by a pressure transducer and the force registered by the load cell. See Appendix C for details on the analysis of fill tests.

For the final stage of the fill, the fan rotation rate is set to the maximum (105 Hz) to create a pocket to protect the instruments mounted to the test platform wetdeck during start-up. The ultimate static water level corresponds to filling around 90% of the test section.

Test start-up

To minimize the length of time with the test platform submerged, the impeller is started almost immediately after the fill level is reached and the bulk slowly accelerated to the desired velocity. The gate angle is set such that the resulting free surface elevation will

be at the desired level. Due to the large volume of water in the LCC, about 5 minutes is required until the velocity is sufficiently high that supercritical flow is established in the test section. The establishment of the supercritical flow is marked by the presence of an unsteady hydraulic jump in the test section. The jump starts at the trailing edge of the gate and moves downstream. To reduce the blockage in the tunnel and reduce the time that the hydraulic bore is churning in the test section, the stern seals, which had been lowered to help create the pressurized protective pocket, are raised.

Steady

With the free surface established at the desired level and testing, testing can begin. The stern seal is lowered to contact the free surface and the fans and backpressure regulators are set to achieve the desired pressure. Each steady-state run generally lasted around five minutes. During the test, the time-of-flight system and the video observation system is triggered along with the analog data acquisition system. At each nominal bow seal immersion, three to five steady runs are acquired, each corresponding to a different cushion pressure. The free surface elevation at the windows are measured via scales. The reference velocity from the LDV system is added to the test log.

Ramps

Between steady state conditions, intermediate steps or ramps are recorded as well. The pressure and bow seal immersion is varied slowly between setpoints. The ramp tests are around 5 minutes in duration for changes in pressure and 10 minutes in duration for changes in bow seal immersion.

Shutdown

To shutdown the test platform, the stern seal is lowered and the fans set to the maximum frequency. Once the flow has slowed sufficiently, draining is commenced almost immediately

to minimize the length of time the platform is submerged. If testing is to be resumed soon or additional static pressurization test performed, the tunnel is left half full with the water level below the instruments; otherwise the tunnel is drained to the floor of the test section. Offsets are again taken with the tunnel test section empty.

3.4 Analysis methods

3.4.1 Time series

Extraction of steady state conditions

Data were often acquired in the form of extended runs each containing a number of discrete steady state conditions. Unfortunately, due to feedback between the unsteady closure of the cushion at the stern seal, the stern seal position, and the pressure control system, fairly significant pressure fluctuations existed in the cavity even for relatively constant input conditions. Therefore, an algorithm had to be developed to identify the stationary segments within a given file. Once the stationary segments of the files were identified and extracted, additional post-processing steps, such as averaging and deriving new channels, could be reliably performed. The criteria set to qualify a portion of the time series as stationary was as follows:

- Minimum test duration of 20 s
- Relative pressure fluctuations less than 3% of the mean
- Free stream velocity fluctuations less than 2% of the mean
- Constant free-surface forming gate position (related to water level)
- Constant stern seal flap position (five flaps).

To assist in determining the start and stop times of the stationary segments in the presence of noise, each of the channels used as indicators were filtered using a piecewise constant denoising filter (Little and Jones, 2011). An advantage of this approach, as opposed to a typical low pass filter, is that it preserves the step changes in the signals, allowing us to maximize the length of the windowed runs.

Free-Surface Profiles

Time series of the raw airgap is recorded at each of the free-surface measurement locations shown in Figure 3.10. The coordinates of the airgap measurements relative to the global coordinate system (see Figure 3.7) are contained in Appendix D. Airgaps along with the other analog channels is acquired at a base rate of 250 Hz using an 16 bit-A/D converter and LabView®software. To minimize interference between sensors, the firing of each ultrasonic sensor was staggered, leading to an effective reduction in the data rate to a minimum of 50 Hz. Reference airgap data were acquired with the test section empty before and after each day's runs. As expected, these tests confirmed the known distance from the emitter to the test section bottom. Initially data from the reference wave probe, whose data were contaminated with reflections of the hard structure of the camera traverse supports; after relocating the sensor to a more favorable position, the remaining mean shifts and glitches had to be removed in post-processing. The mean shifts and other glitches were removed by thresholding the data based on the excursions from a zero-phase, low-pass filtered version of the time-series. The erroneous measurements were excluded from the sample mean, which was based on the remaining raw values. Due to glitch removal, the number of samples used for the mean varied slightly, leading to an increase in uncertainty for the reference probe. The typical uncertainty for the free surface profiles was $\sigma = 5$ mm based on a minimum of 20 seconds of data. The longitudinal locations of the ultrasonic sensors was known to within ± 5 mm.

The free surface profile at the tunnel wall ($y/B_c = 2$) was estimated visually, aided by

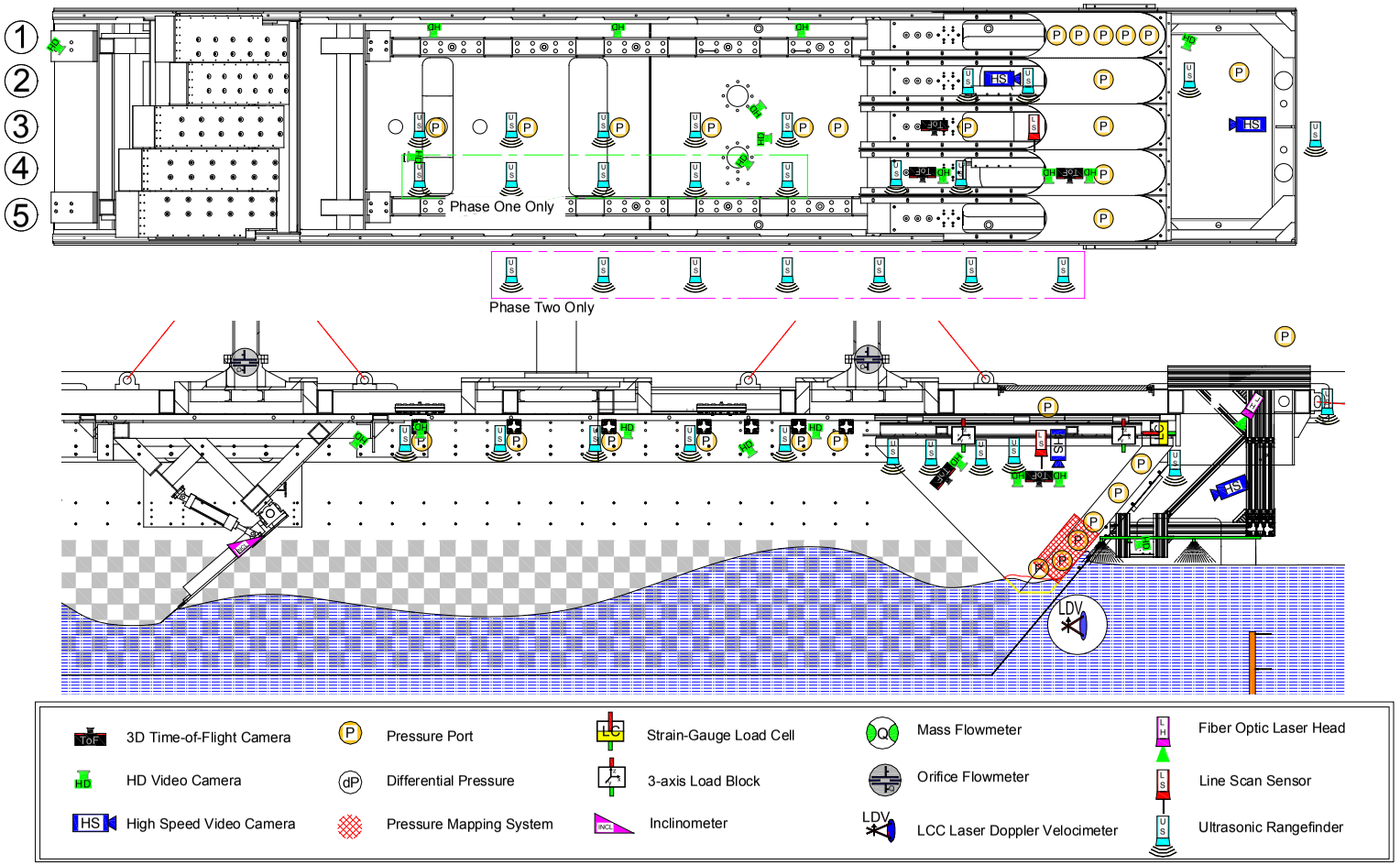

Figure 3.10 Instrumentation suite.

a series of transparent scales attached to the tunnel viewports. Tunnel wall measurements were typically taken during steady state conditions. The estimated uncertainty in the water level measurement is $\pm$12.5 mm due to unsteadiness and presence of run-up near the tunnel wall. Water level measurement is also susceptible to systematic errors estimated to be $\sim \pm 5$ mm due to uncertainty in the scale placement relative to the global (X_G, Y_G, Z_G) coordinate system. The longitudinal location of the tunnel wall measurements are prone to similar errors, $\pm$25 mm, as well as estimation differences among test team members.

3.4.2 Seal deformation

3-dimensional ToF measurements

Seal deformation is estimated using the 3-dimensional ToF system described in Section 3.2. Raw phase image information from the ToF camera was acquired at rates between 15 and 110 fps, dependent on integration time(s) and the desired region of interest.

A unique feature of the PMD cameras is their ability to return a simultaneous amplitude image along with the distance image. The amplitude image is related to the strength of the infrared return and the quality of the distance measurement. Even if the sensor is unable to receive a satisfactory return for all 200 x 200 pixels, the amplitude image data can be used to threshold the distance data to select measurements from only those pixels that provide reliable distance estimates. The same thresholding technique can also be applied to identify the seal/water interface as the free-surface generally possesses much poorer infrared reflectance properties than the white seal. In the presence of white caps, or other disturbances that changed the reflectance properties of the free-surface, quality returns were often observed in individual frames and did not persist for the duration of the run. An example of a distance image is shown in Figure 3.11 along with a contiguous region of seal that has a satisfactory return. As expected the return off the free-surface is poor.

A number of processing stages were required to derive smooth seal profiles and register

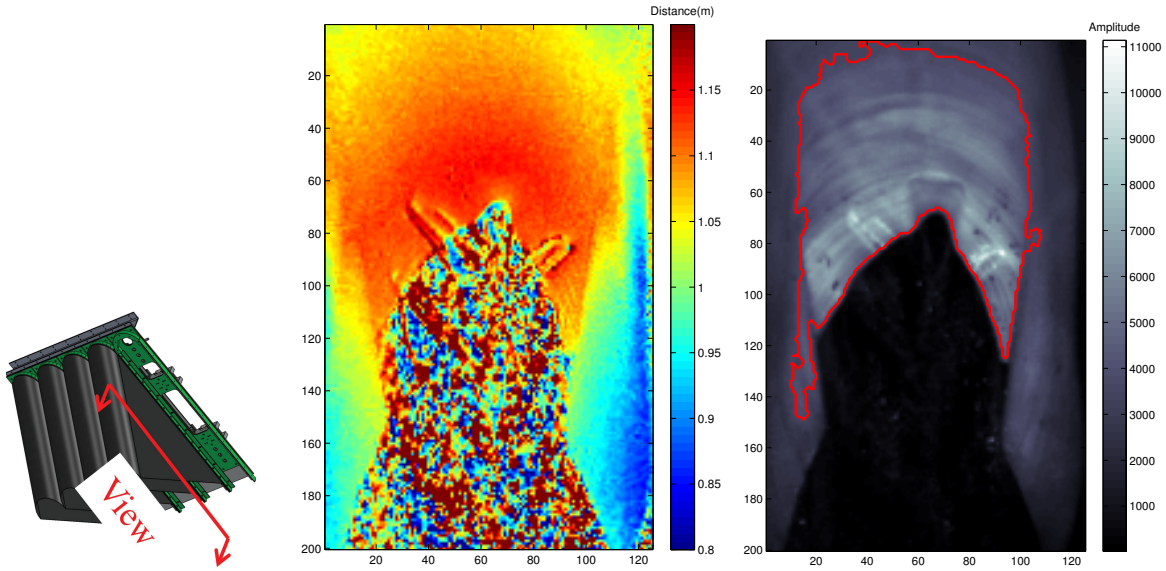

(a) View Shown **(b)** Distance Image. **(c)** Amplitude Image (outline after amplitude thresholding shown).

Figure 3.11 Amplitude and distance image pair as acquired by time-of-flight camera. Seal Type-0 (NN), $\delta_s = 77$ mm, $p_c = 330$ Pa , $U = 5.5$ m/s.

them in the global test platform coordinate system. The Matlab® image processing toolbox and OpenCV library were utilized for the image analysis.

ToF pre-processing stream

1. Using the software development kit provided by PMDtec, the camera manufacturer, raw phase images are converted into distance and amplitude images. A typical set of distance and amplitude images are shown in Figure 3.11. The amplitude image in Figure 3.11c, is related to the return signal strength and the distance measurement uncertainty (Foix et al., 2011). As expected, the return signal amplitude drops sharply at the seal tip-water interface due the poor infrared reflectance of water.

2. The distance and amplitude images are corrected for lens distortion using the OpenCV library, and camera and distortion matrices estimated from an offline calibration. The camera matrix, which contains information such as the lens focal length and principal points was estimated using the OpenCV toolbox and a series of amplitude image taken

of a chessboard grid at various orientations.

3. The corrected amplitude image is aggressively thresholded to identify pixels that might yield reliable distance measurements. Using the binary image produced by the thresholding, the boundaries of the seal are identified using a region analysis. The red contour shown in Figure 3.11c, traces a typical seal boundary from the region analysis. Pixels outside the seal boundary possessing quality return amplitudes are collected for further analysis.

4. The corrected distance images are then time-averaged, excluding any pixels that did not meet the amplitude criteria. Because the lower boundary of the seal may have moved between images, a compound seal boundary has to be identified. The compound seal boundary was arbitrarily defined as the boundary of the region where greater than 50% of the frames used in the time average met the amplitude threshold.

   Similarly, pixels outside the seal boundary possessing quality signal amplitude are time-averaged. The free surface is defined as locations not including the seal region where greater than 1% of the frames used in the time average meet the amplitude threshold. Free surface location are also required to be downstream of the seal edge.

5. The distance image is projected from the image plane into 3-dimensional space using a pinhole camera model and pixel vectors derived from the camera calibration.

6. The image is registered in the global coordinate system, using the camera location and rotation vectors derived from calibration images.

7. The seal surface is resampled in the global coordinate system and smoothed. The results after smoothing are shown in Figure 3.12.

After pre-processing, a number of quantities are derived from the 3-dimensional distance maps. These are described in more detail in later chapters and include quantities such as:

1. Sectional cuts including waterlines and seal shape at centerline.

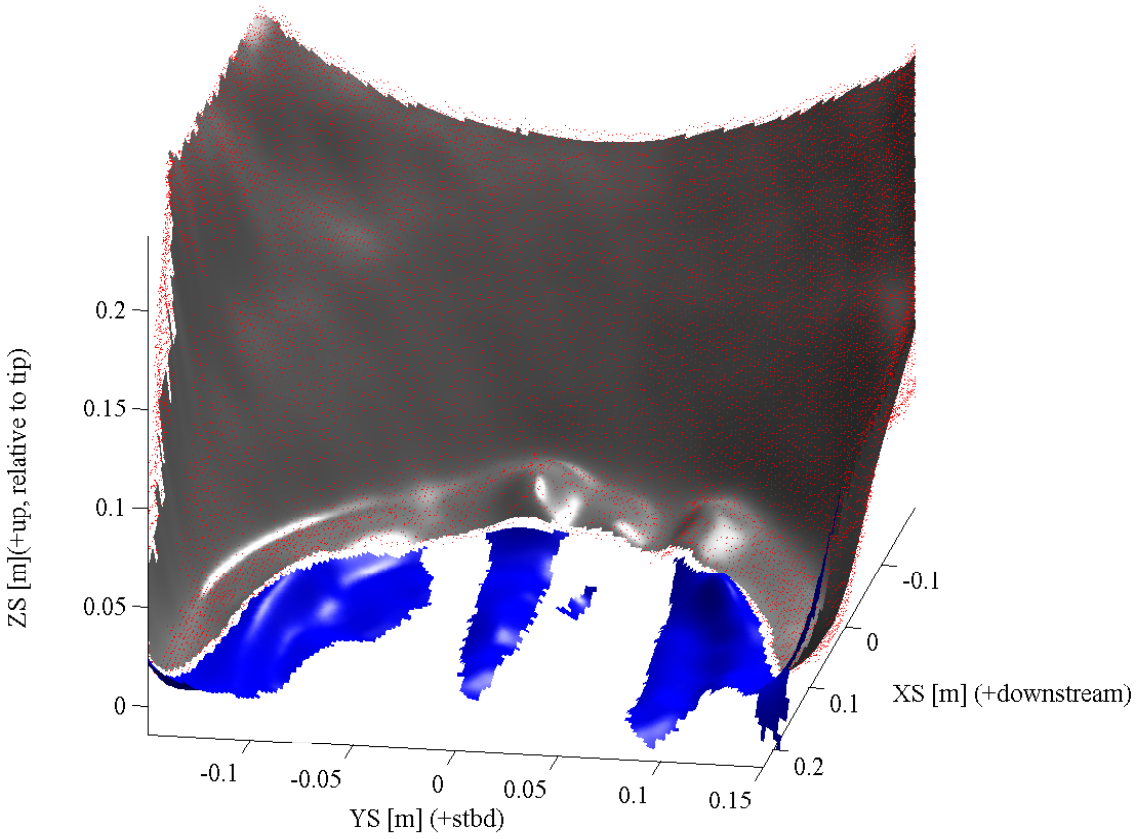

Figure 3.12 Time-of-flight distance map after post-processing, seal Type-0 (NN), $\delta_s = 12.7$ mm, $p_c = 640$ Pa, $U = 5.97$ m/s.

2. Statistics derived from the centerline profile including curvatures, wetted lengths and other geometric descriptors. In particular, the descriptor β, the angle of the wetted part of the seal with respect to the horizontal (similar to an angle of attack) is found to be an important variable in the conformation of bow seals.

3. Principal curvatures (and Gaussian curvature)

Uncertainty of 3-dimensional ToF Measurements

Quantifying the uncertainty of the distance measurements made by ToF cameras is an area of ongoing research (Rapp and Frank, 2008), and is affected nonlinearly by a number of factors. The principal factors relevant to uncertainty in the present work are the sensitivity of the distance measurement to: object reflectivity, location of the object relative to the center

of the image, and object inter-frame motion.

In order to minimize the measurement uncertainty, steps were taken with the experimental design. To maximize the signal return amplitude, the seal interior was painted a uniform flat white, and the cameras were positioned normal to the measurement surface, with the center of the image axis near the expected mean position of the knuckle. To minimize artifacts from inter-frame motion, short exposure times were used (typical less than 250 µs). However, as multiple exposures (two or four depending on phase estimation mode) are required for the distance calculation, motion artifacts could not be removed entirely. Reduction in the exposure times also has the undesired side-effect of reducing the signal amplitude and increasing the image noisiness. Regardless of these measures, significant noise in the resulting distance images remained, even for areas where there was no movement.

Figure 3.13b shows the standard deviation of the seal position along a seal centerline derived from the distance image in Figure 3.11. The standard deviation was calculated at each pixel location from 100 sequential frames. The typical uncertainty of the seal near the seal knuckle is estimated to be ± 5 mm. The camera was positioned such that the undeflected seal tip was roughly at the center of the image plane. As expected, due to movement, the uncertainty is largest near the seal tip. The standard deviation at the tip is confounded with the actual seal motion and motion artifacts. The uncertainty is lowest near the intersection of the free-surface and the seal. In the region, located near center of the image plane, the shape was found to be relatively stable. Because the free-surface was generally near the edge of the field-of-view, signal quality for the free-surface was adversely affected a number of factors including lower light intensity, and optical distortion.

Time averaging is also used to reduce the measurement uncertainty, typically between 10 and 3000 frames are used in the averaging process, corresponding to 1/10 and 30 seconds of data depending on the acquisition parameters. Shorter duration time averages were used to discern details on fabric folds, information that may be lost in longer averaging periods. Longer time averages were used to accumulate information on free-surface position. Longer

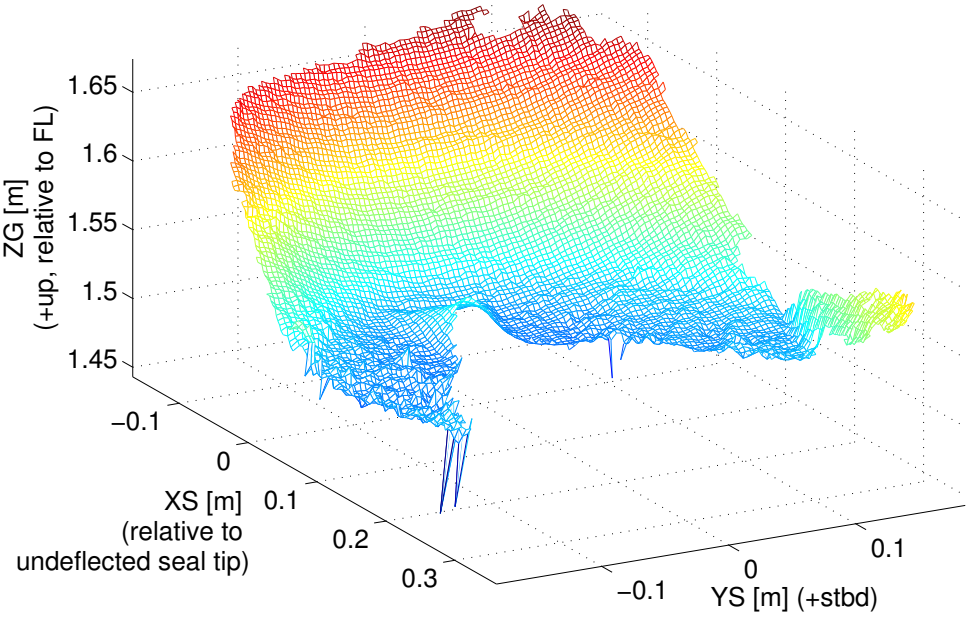

(a) Time averaged seal shape, prior to smoothing.

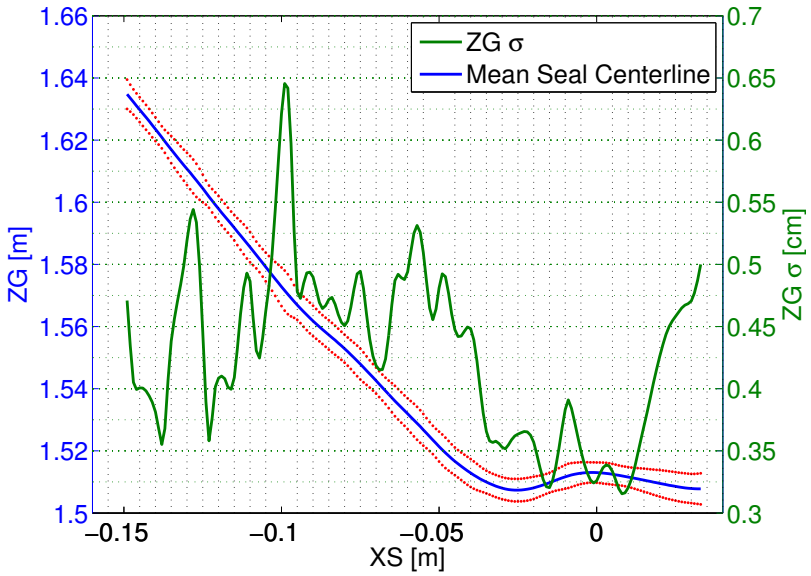

(b) Standard deviation σ along seal centerline profile.

Figure 3.13 Uncertainty along the seal centerline profile derived from ToF measurement.

time averages utilized running statistics to reduce the memory load.

The seal position is also susceptible to systematic errors from the camera calibration, which leads to biases in the 3-dimensional coordinates derived from the distance mea-

surement. Reprojection of the calibration images after correcting for distortion revealed systematic errors on the order of 3 mm. Additional systematic errors are present in the camera orientation estimation which is based on calibration images, and/or scale readings; orientation estimation errors manifest themselves in incorrect centerline cut positions, as well as suspect inflated seal positions relative to the free surface. Due to this, the systematic error in the derived vertical position of the seals could be as much as 25 mm. During the 2012 tests, a system of ground control points and a reference channel were added to reduce these errors.

Due to these limitations, the ToF technology is best suited for capturing stable features. Consequently, the ToF camera has difficulty resolving the unsteady and/or small-amplitude features typical of seals constructed of the compliant Type-1 (HN) material.

3.4.3 Processing of linescan profiles

Given the limitations of the 3-dimensional measurement technique described in Section 3.4.2, the Sick IVC-3D linescan camera, which provides high-resolution information on seal cross-flow response, serves as a valuable reference channel. Statistics derived from cross-flow profiles acquired by the linescan camera are used extensively in each of the three studies of the dissertation. Linescan data is also used in Appendix A to estimate the bending rigidity (D) of the seal materials. This section briefly describes the processing methods employed in deriving statistics such as the confinement ratio and bending energy that feature prominently in later sections.

Preprocessing

Linescan measurements are triggered at a rate of 500 Hz and are synchronized with the analog data acquisition system via a Transistor-Transistor Logic (TTL) trigger. Prior to processing, linescan profiles are converted from raw counts to physical units and corrected

for roll based on a calibration image. Due to the buffer arrangement in the linescan camera, a known lag existed between the linescan system and other measurement systems. In the preprocessing stream, this lag is calculated and all measurements are aligned to the common time base. Other preprocessing steps may include windowing the data. Often spray on the camera resulted in drop-outs. During the experiments this was minimized by application of compressed air and a hydrophobic coating to the lens (Rain-X®). In pre-processing, these drop-outs are identified. If a continuous profile is required for a downstream process, dropouts are filled using an inpainting (interpolation) algorithm.

Confinement ratio

The confinement ratio Δ is found to be an important parameter in seal response, acting as a constraint on the fold amplitude A. The confinement ratio, shown in Figure 3.14, is the end-displacement $\mathcal{S}$ [1], non-dimensionalized by the total arc-length L_{arc}. Δ is a measure of the packing of the seal, and in later chapters found to be set by the local draft and free-surface hydrodynamics. $\Delta = 0$ corresponds to the material in an uncompressed state. $\Delta = 1$ corresponds to the material compressed to the point that the ends contact (self-contact).

$$\Delta = \frac{\mathcal{S}}{L_{arc}} = 1 - \frac{X_{end} - X_{start}}{L_{arc}} \tag{3.4}$$

To calculate Δ from a raw linescan profile (shown in gray in Figure 3.14) requires extracting the segment of the profile of interest, after which the arc-length (L_{arc}) can be estimated. In most cases, the area of interest of the linescan profile is the center region (in black) which is in contact with the free-surface. The start ($x = x_{start}$) and end points ($x = x_{end}$) are located using an iterative algorithm that finds the location of local minima nearest the vertical sides of the seal.

Estimating the arc-length is straightforward. The approach involves first representing

[1] $\mathcal{S}$ is often referred to as the end-shortening or "shortening" in older literature (Singer et al., 1998).

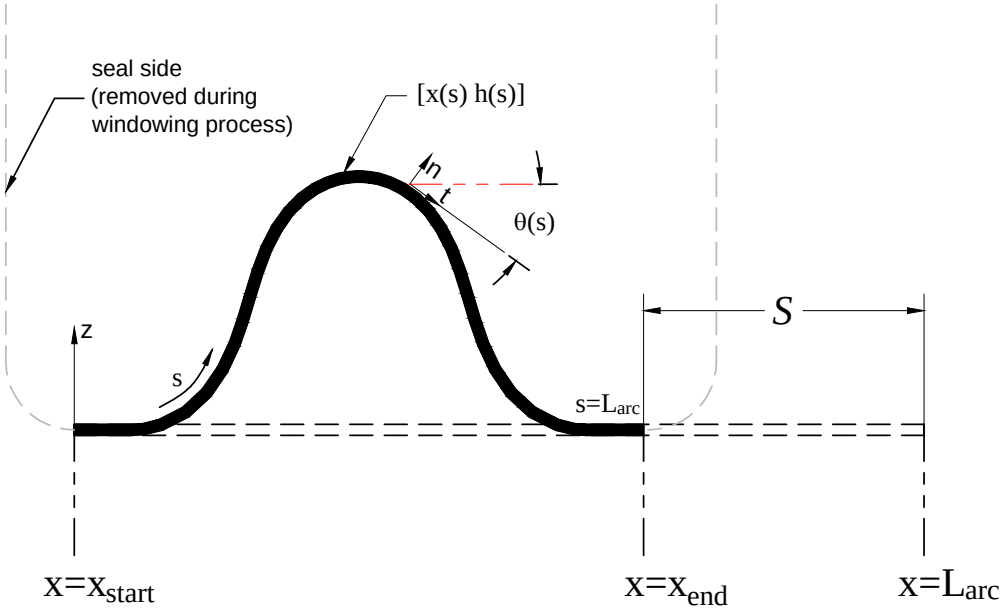

Figure 3.14 Definition of seal confinement ratio $\Delta = \frac{\mathcal{S}}{L_{arc}}$

the profile with a spline interpolant. Once in spline form, the arc-length is calculated via

$$L_{arc} = \int_{x_{start}}^{x_{end}} \sqrt{1 + \left(\frac{dh}{dx}\right)^2}\, dx, \tag{3.5}$$

where the derivative $\frac{dy}{dx}$ is calculated analytically from the spline coefficients. The arc-length of each ds segment is then found via numerical integration (Gaussian quadrature) and summed.

Curvature and bending energy

The curvature κ and bending energy Π_D of the cross-flow seal profile feature prominently in Chapters 5 and 6. Because of the large rotations θ typical of seal response, the exact expression for the curvature κ is used wherever possible,

$$\kappa = \frac{d\theta}{ds} = \frac{\frac{dh^2}{dx^2}}{[(1 + (\frac{dh}{dx})^2]^{3/2}}. \tag{3.6}$$

θ and s are the parametric representation of the profile (see Figure 3.14). Similar to the arc-length L_{arc} calculation previously described, the approach is to employ a spline representation of the windowed profile to calculate analytical derivatives. At the time the spline is estimated modifications to curve smoothness can be made. Smoothing may be required due to the $\frac{dh^2}{dx^2}$ term in the numerator of the expression for curvature.

With techniques developed for calculating both arc-length ds and κ, the bending energy Π_D can be calculated,

$$\Pi_D = \frac{1}{2}\int_0^L D\kappa(s)^2 ds, \tag{3.7}$$

where D is the bending rigidity of the seal material (see Appendix A). The integral for Π_D is evaluated numerically.

Turning point analysis

In order to examine fold amplitude (A), mode number (m) and wavelength (λ) more closely, turning point analysis (Brodtkorb et al., 2000) is conducted for each profile. Turning point analysis is a standard procedure for describing non-linear wave shape and is employed extensively in fatigue-life calculations. This type of analysis is useful in scenarios where the mean of a profile may shift, precluding use of a more standard level-crossing analysis. The nomenclature for the analysis is provided in Figure 3.15.

The turning point algorithm is straightforward. First, the local minima and maxima are extracted for each profile. Next, the geometry of the fold is described in terms of dimensions between these local extrema. For example, an estimate of a fold amplitude could be the difference in height between a local maximum $H_C[i]$ and an adjacent local minimum ($H_T[i+1]$), or $H_{C2T}[i] = H_C[i] - H_T[i+1]$, where i is the index to the crest or trough. Alternatively, H_{T2C} could be calculated, where $H_{T2C}[i] = H_C[i] - H_T[i]$. The corresponding half-wavelength is determined in a similar manner. The resulting amplitudes are

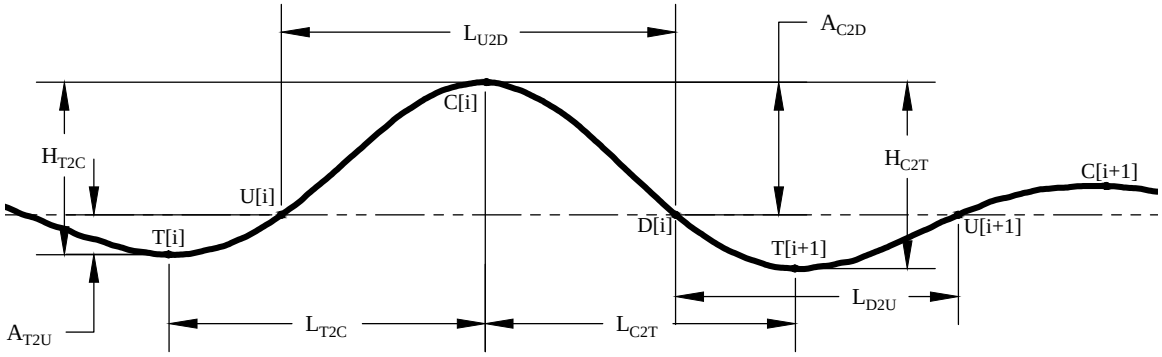

Figure 3.15 Turning point analysis nomenclature.

then sorted, with amplitudes smaller than a given threshold removed from the set. Typically only the wavelengths corresponding to the largest amplitudes are reported (indicated as $L_{C2T}|_{max(HC2T)}$ or often simply L_{C2T}). Because the computational cost of the turning point algorithm is low, all descriptors of the wave height and half-wave length are calculated for each profile and compiled, which may correspond to as many as 30000 individual profiles for a 60 s test.

Mode number

Statistics based on a turning point analysis are used extensively in later sections. In particular, the mode number is calculated from the number of half wavelengths,

$$m = \#(H_{T2C}) + \#(H_{C2T}) - 1. \tag{3.8}$$

When using crest-to-trough and trough-to-crest cycles to estimate mode number, care must taken in the classification of the profile start and end points. The above algorithm includes the end points as local extrema. Half-cycles that contain end points are excluded from sequence of wavelengths. Equivalently (in the case of zero-mean process), mode number can be estimated from the number of up/down level crossings or from the number of crest and troughs.

Chapter 4

Features of finger-seal hydroelastic response

Selected results from large-scale experiments conducted at the U.S. Navy's Large Cavitation Channel are presented. The experiments show the hydroelastic response of bow seals to be characterized by striking stable and unstable post-buckling behavior. This chapter identifies a number of key features in bow seal hydroelastic response, whereas Chapters 5 and 6 explore potential physical mechanisms responsible for these features.

Under the action of hydrodynamic forces and confinement seals reconfigure, changing cross-flow wavelength, fold amplitude, and stability. Mode number for the Type-0 material is observed to vary between $m = 1$ and $m = 7$, with a mode number of three typical for moderate immersions. Mode shapes for the stiff Type-0 material are generally symmetric and distribute across the full seal width, featuring amplitude modulation and raised central folds. Within the limited parameter space of the experiments, Type-0 seals are found to be stable for moderate immersions $\frac{\delta_s}{R_f} > 0.25$ and pressures $\frac{\delta_c}{\delta_s} > 0.6$, and are observed to lose stability at lower immersions and higher mode numbers through a convective mode-cycling type instability similar to that reported by Besch (1976).

In contrast, seals constructed of the more compliant Type-1 (HN) material exhibit a very different response than the Type-0 seals, suggesting the important role material properties such as bending rigidity and mass play in bow seal response. Mode number for the Type-1 seals is found to vary from $m = 3$ to $m = 11$, corresponding to significantly shorter wavelengths and smaller amplitudes than the Type-0 material. Unlike the Type-0 seals, mode

shapes for the Type-1 seals are generally localized rather than distributed in nature. Type-1 seals are unstable under almost all conditions. Instead of the mode-cycling found in the stiff Type-0 seals, where mode number is constant, the Type-1 seals are subject to high-frequency mode-switching.

A number of parameters driving seal conformation are identified. Of primary interest in this chapter is the seal confinement ratio, $\Delta = \frac{\mathcal{S}}{L_{arc}}$, where $\mathcal{S}$ is the effective cross-flow displacement and L_{arc} is the arc-length. Introduced in Section 3.4.3 and discussed in detail in Section 5.2, Δ is found to be set by free-surface conditions local to the bow seal. The confinement Δ is found to strongly influence buckling mode shape, acting as a constraint on mode amplitude. For the compliant Type-1 (HN) material, the large-scale measurements suggest that the slope of the mode shape $\frac{A}{\lambda} \sim \Delta^{0.5}$, where A is the amplitude, and λ is the wavelength. This scaling is found in Section 5.4 to follow from the inextensibility of the seal material. The buckling wavelength for the Type-1 (HN) material, λ is found to vary linearly with Δ approaching the hydrostatic buckling wavelength $\lambda_{\rho g} = 2\pi \left(\frac{D}{\rho_w g} \right)^{0.25}$ at higher confinements. This suggests that hydrodynamic components of the restoring force are relatively small at the velocities tested. The origins of this natural length scale are discussed Section 5.4. The work reveals the rich statics and dynamics of a buckled structure subject to fluid loading. It also identifies a number of distinct types of instabilities that may be responsible for seal vibration and wear.

4.1 Global response

4.1.1 Free surface elevation

Owing to their flexibility, bow seal behavior is closely tied to the free-surface environment set by the action of the pressurized air cushion on the free-surface. The placement of the seal system within the test environment at the LCC is shown in Figure 4.1. The centerline of a bow seal, derived from the ToF measurement is shown in red. The seal deflects sharply

near its intersection with the free-surface. Consistent with hydrostatic considerations, the average free surface elevation $\bar{\zeta}$, within the cushion is depressed relative to the external running level,

$$\bar{\zeta} = \frac{1}{L_C}\int_0^{L_C} \zeta(x_c)dx_c \approx \delta_c = -\frac{p_c}{\rho_w g}. \tag{4.1}$$

The wave elevation inside the cushion along centerline corresponds to $y/B_c = 0$, where B_c is the cushion beam and y is the transverse coordinate. The free-surface level external to the cushion was acquired via scale measurements at the windows of the water tunnel at $y/B_c = 1$.

The largest difference between the internal and external free-surface elevation occurs near the stern seal, with the inner wave profile ($y/B_c = 0$) describing a portion of a longer wave. This is consistent with the cushion-length based Froude number, $fn_c = 0.78$ of the test platform (Yun and Bliault, 2000).[1]

Downstream of the bow seal a local disturbance of the free-surface is present. Given the difficulties obtaining a quality return from the ultrasonic sensor at that location, it is not clear whether this rooster-tail-like disturbance is real or a measurement artifact.

[1]Linear wave theory can be applied to provide a rough check on the reasonableness of the wave profile. If in deep water, linear theory predicts that application of a semi-infinite pressure patch on a free-surface will generate a wave elevation ζ of wavelength λ_{fn} within the pressurized region (Lamb, 1932), where

$$\lambda_{fn} = 2\pi\frac{U^2}{g}. \tag{4.2}$$

The number of waves of length λ_{fn} occupied by the test platform is given by

$$k_{fn} = \frac{L_c}{\lambda_{fn}} = \frac{1}{2\pi fn_c^2} \tag{4.3}$$

where $fn_c = \frac{U}{gL_c}$ is the cushion based Froude number.

For the test platform, $fn_c \approx 0.78$, which corresponds to a $k_{fn} \approx 0.26$. Looking at Figure 4.1, it is seen that the internal free-surface may describe 26% of a wave with length λ_{fn}. A better estimate would employ λ_{fn} associated with finite depth. The simulations of Doctors (2012) approach this problem in a less adhoc manner.

4.1.2 3-dimensional seal shapes

Figure 3.12 shows a typical distance map for the stiff Type-0 material operating at a relatively shallow immersion δ_s of 12.7 mm. To isolate the free-surface, the thresholding process described in Section 3.4.2 has been applied. The post-buckled seal shape features a raised fold on centerline. The free-surface, as registered by the ToF camera, appears to detach cleanly, tangent to the trailing edge of the seal. The regions of quality return for the free surface appear coincident with raised folds on centerline. It is hypothesized that this is due to improved reflectance downstream of the folds. Underwater images, such as shown in Figure 4.2 indicate raised void fraction both downstream and upstream of the raised folds. It is suspected that the upstream influence is due to air leakage which appears greatest between adjacent seals. In general, the 3-dimensional distance maps indicate that buckling patterns for the stiff Type-0 material persist through the time-averaging process.

In contrast, the folds of the compliant Type-1 material are generally transient and do not survive the time-averaging process. In particular, folds at small immersions cannot be distinguished. Under these conditions fold amplitudes are of the same order as the noise floor of the ToF camera (see Figure 3.13b). A typical time-averaged distance map for the Type-1 material is shown in Figure 4.3. On average, the downstream section of the seal, often referred to as the "Tail", resembles a plane conforming closely with the free-surface. The vibrations captured by the linescan camera and presented in later sections occur about this mean plane.

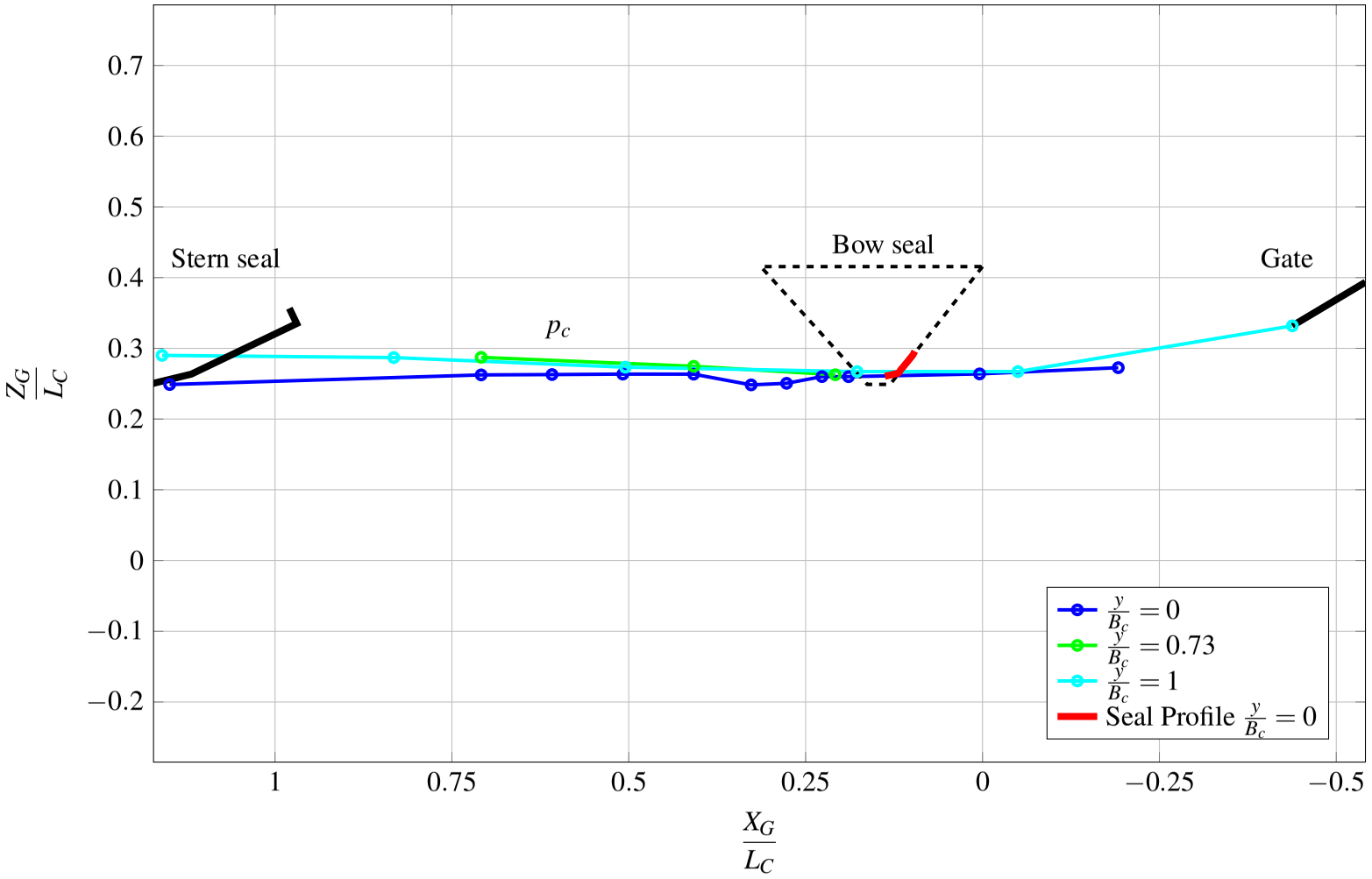

Figure 4.1 Typical free surface profile, Type-1 (HN), compliant material with $\delta_s = 152.4$ mm, $U = 5.93$ m/s, $fn_c = 0.75$, $fn_H = 1.45$. X_G is measured relative to forward perpendicular (FP). Z_G is measured relative to test section floor level (FL). See Figure 3.7 for more information on coordinate systems.

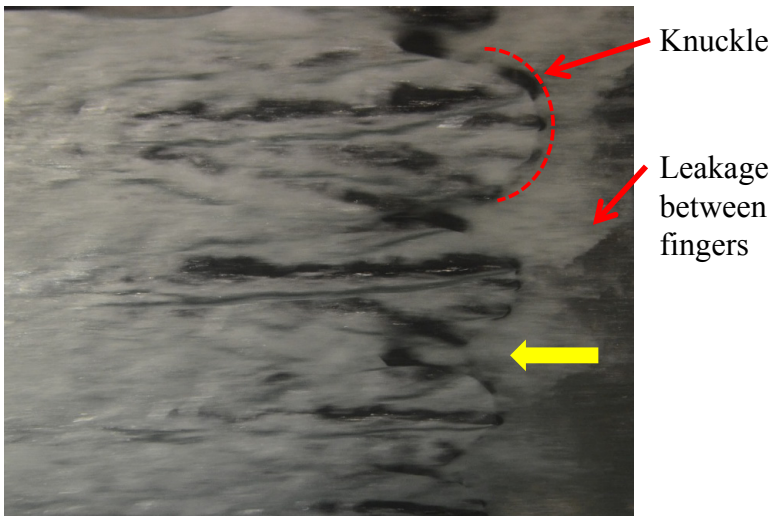

Figure 4.2 Underwater view of Type-0 (NN) seal, note raised void-fraction both and upstream and downstream of the raised folds in the seal. Arrow indicates direction of flow.

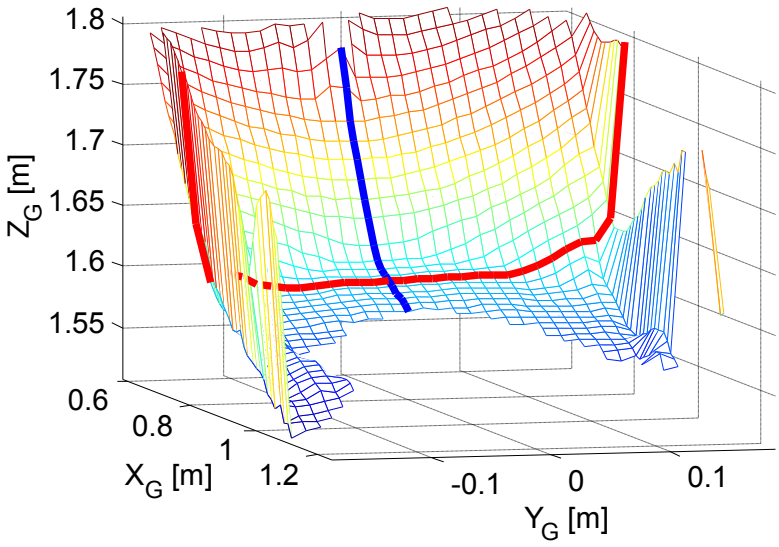

Figure 4.3 Type-1 (HN) seal shape as measured by ToF camera, $U = 6.5$ m/s, $\delta_s = 89$ mm, $p_c = 375$ Pa. ——, Seal centerline (streamwise) profile ($Y_G = 0$ m). ——, cross-flow profile ($X_G = 0.77$ m).

4.2 Streamwise response

To enable comparisons between seal shapes at different conditions, sectional cuts are extracted from the 3-dimensional distance maps. A typical centerline profile (y/B_c) for the stiff Type-0 seal at a fairly deep immersion of $\delta_s = 155$ mm is shown in Figure 4.4. In the centerline plane, it is observed that the seal buckles near the waterline and develops a radius between two segments of near zero curvature. Per Figure 4.4 the upper undisturbed part of the seal is denoted the Cylinder; the transitional region possessing non-zero curvature (κ_{Y_h} is referred to as the Knuckle and the segment appearing to lie parallel to the free-surface is the Tail. In Section 5.1, this arbitrary decomposition will be formalized using measures that examine the balance of stretching forces in each region. Figure 4.4 also presents an approximate pressure profile as measured by the Tekscan® pressure mapping system. A notable feature of the pressure profile is the absence of a pronounced stagnation point. It is hypothesized that seals cannot support the pressure differences associated with practical velocity and operate exclusively in a streamlined post-buckled state. In the next section, centerline profiles such as Figure 4.4 will be used to examine the influence of two independent variables, the local draft (immersion) δ_s and pressure p_c, on seal conformation. The first independent variable, the nominal local draft (immersion) δ_s is set by the angle of the free-surface forming gate. The second independent variable, the cushion pressure p_c is controlled via the pressure control system.

4.2.1 Influence of local immersion, δ

Figure 4.5 shows centerline profiles ($y/B_c = 0$) under the condition of fixed pressure p_c and increasing immersion δ_s. The local immersion δ_s was altered by changing the angle of the free-surface forming gate. An underwater view of a similar progression is shown in Figure 4.6a. It is observed that one effect of altering the local immersion δ_s is to change the vertical elevation at which the seal buckles. A similar trend is also observed for the stiff Type-0

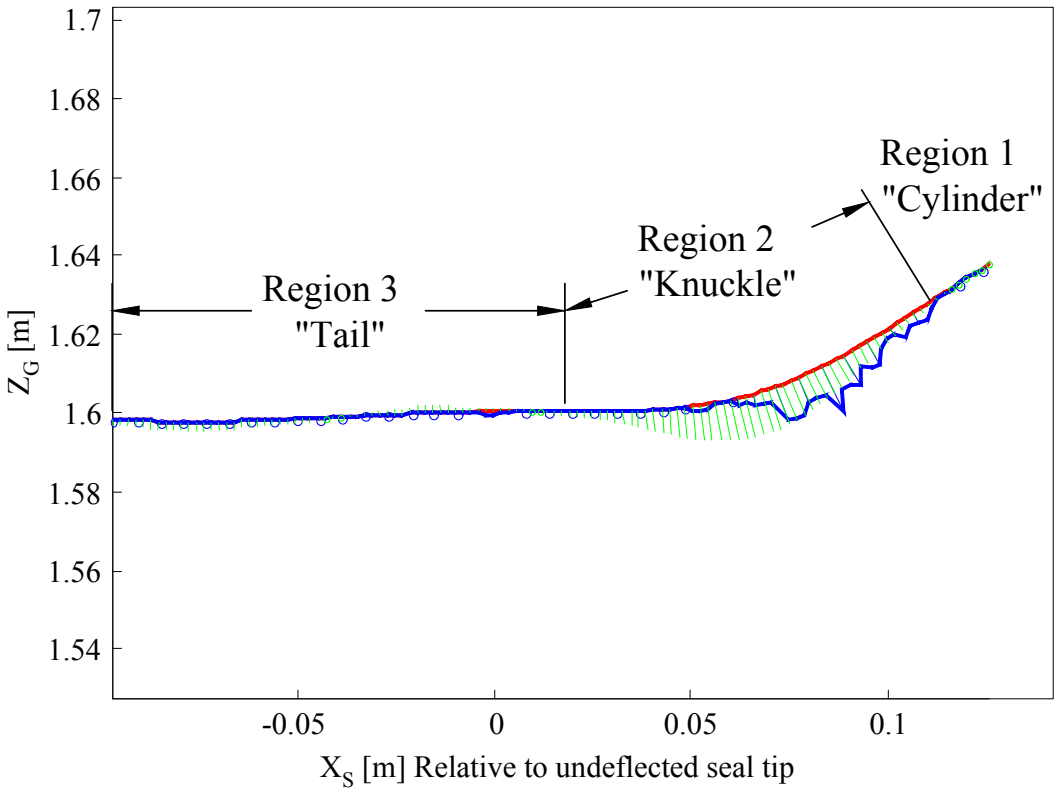

Figure 4.4 Type-0 (NN) material approximate pressure profile (blue) along centerline (red) via Tekscan® pressure mapping system (nominal units). Seal curvature (green) and approximate regions (Cylinder, Knuckle, Tail) of the seal based on curvature (κ_{Y_h}) are also shown. $\delta_s = 155$ mm, $p_c = 1150$ Pa, $U = 5.65$ m/s. Due to problems registering the seal tip, an offset between the pressure profile measurement location and centerline shape may exist.

material, however depending on the location of the centerline cut with respect to the stable folds in the Tail region the slope at trailing edge will vary. Looking closely at Figure 4.6a (a) another interesting feature can discerned. It is observed that cross-flow folds develop in the material which originate at points distributed along the curved Knuckle. Moving downstream of the Knuckle the folds spread. At some location upstream of the trailing edge adjacent folds appear to merge.

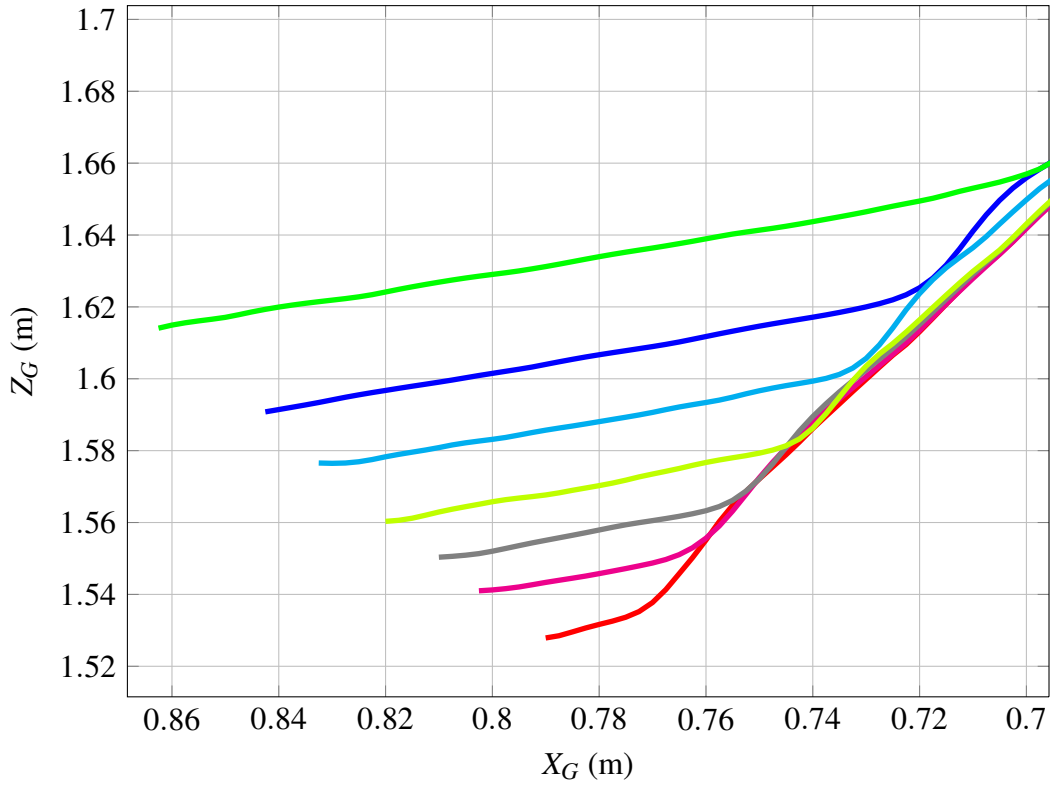

Figure 4.5 Effect of immersion (δ_s) on seal centerline profile, Type-1 (HN), compliant seal material, pressure is roughly the same for all profiles, $p_c = 740 - 820$ Pa, $U = 5.75 - 6.2$ m/s. δ_h is the immersion based on the estimated Hinge location (see Figure 3.9). $\delta_h = 10.8$mm, $\delta_s = 29.0$mm (—); $\delta_h = 25.8$mm, $\delta_s = 43.0$mm (—); $\delta_h = 40.5$mm, $\delta_s = 54.9$mm (—); $\delta_h = 56.7$mm, $\delta_s = 68.1$mm (—); $\delta_h = 76.3$mm, $\delta_s = 83.8$mm (—); $\delta_h = 98.1$mm, $\delta_s = 101.4$mm (—); $\delta_h = 131.0$mm, $\delta_s = 127.6$mm (—).

Influence of cushion pressure on wave rise

Figure 4.7 shows centerline profiles for varying cushion pressure p_c and fixed immersion δ_s. The effect of cushion pressure p_c on the seal elevation is counter-intuitive. It is observed that the Tail of the seal rises with cushion pressure, in opposition to the mean free-surface elevation in the cushion $\bar{\zeta}$, which as seen in Figure 4.1 is depressed relative to the external level.

The raising of the seal with cushion pressure may be partially explained by linear wave theory (Rayleigh, 1883; Lamb, 1932)[2] and the behavior of a free-surface subject to pressure applied to a patch of the free-surface extending from $x_c = 0$ to $x_c = L_c$. x_c is aligned with

[2]Lamb (1932), Chapter IX, Article 244

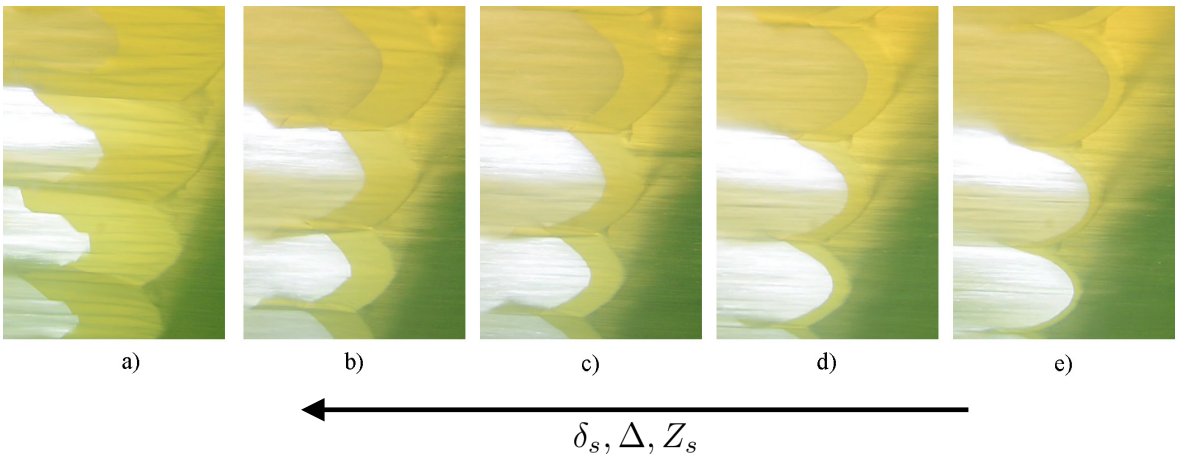

(a) Type-1 (HN) bow seal undergoing change in immersion (δ_s)

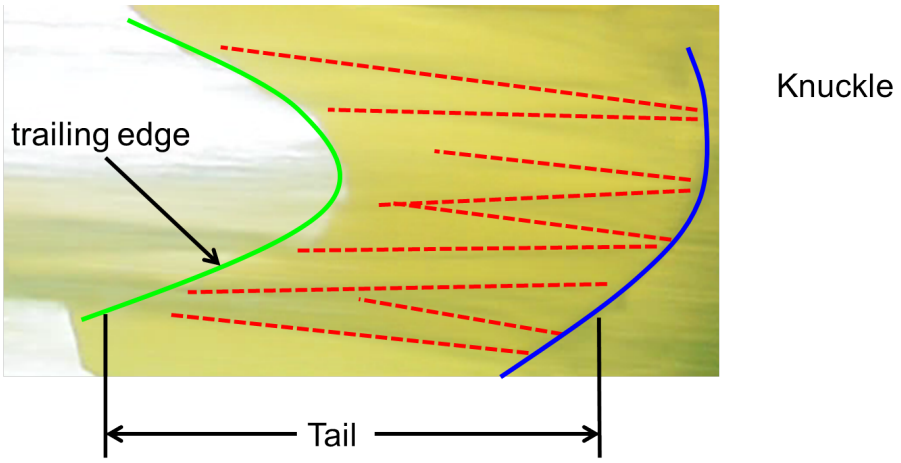

(b) Detailed view of a). Note almost linear spreading of the folds (red) from knuckle $x_h = 0$ to the trailing edge $x_h = L_{Tail}$.

Figure 4.6 Underwater view of Type-1 (HN) bow seal for a range of immersions (δ_s).

the global coordinate system (X_G, Y_G, Z_G), with the origin at the start of the pressurized air cushion. For simplicity, $x_c = 0$ is taken to be the intersection of undisturbed free-surface and the undisturbed seal face. In practice, due to wave rise, the region where the cushion begins to act on the free-surface ($x_c = 0$) is located a short distance forward of this point.

Figure 4.8 compares measured free-surface elevations inside the cushion to results from a simulation conducted by Doctors (2012) based on linear wave theory. To better represent the free-surface environment of the LCC, both finite-width and finite-depth effects are accounted for in the simulation. The simulation applies a smoothed distribution of pressure

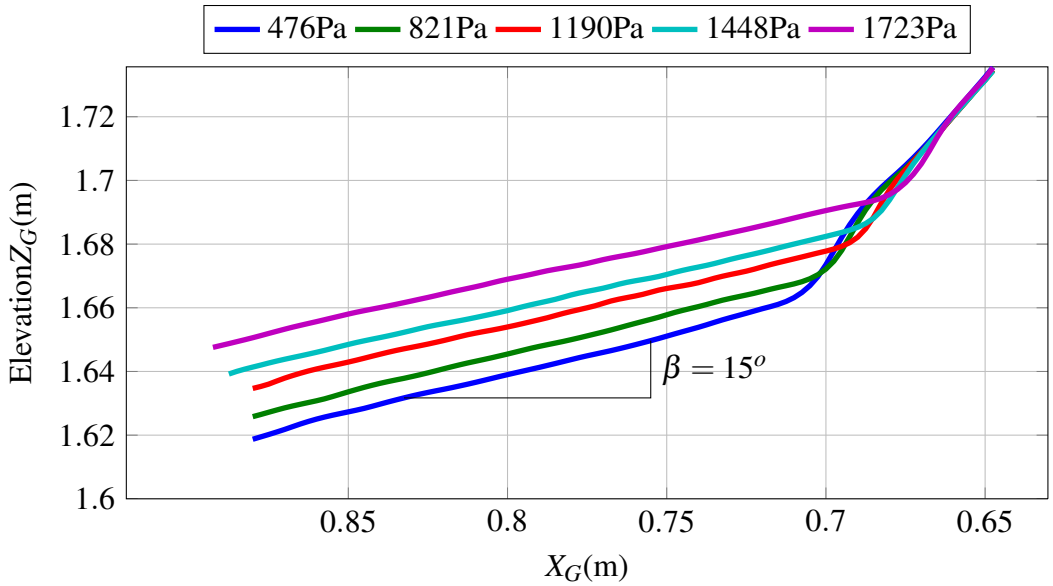

Figure 4.7 Effect of cushion pressure (p_c) on centerline profile, Type-1 (HN) compliant material, $\delta_s = 152.4$ mm, $U = 5.93$ m/s, $fn_c = 0.75$, $fn_H = 1.45$.

$p(x_c, y_c)$ in order to reduce "ringing" associated with the solution method:

$$p(x_c,y_c) = \frac{p_c}{4}(tanh(\alpha_x(x_c)) - tanh(\alpha_x(x_c - L_C)) \\ tanh(\alpha_y(y_c + B_c/2)) - tanh(\alpha_y(y_c - B_c/2)). \quad (4.4)$$

Four sets of free-surface elevations from the experiments are plotted in Figure 4.8, each at roughly the same cushion-length (L_C) based Froude number ($fn_c \approx 0.78$) and different pressures, denoted by $\frac{\delta_c}{L_C}$, where $\delta_c \sim p_c$.

At the bow seal location ($x_c/L_c \approx 0$), the simulation predicts a rise in the free-surface elevation. A wave rise is also present in the 2-dimensional classical results for the limiting case of a semi-infinite pressure patch (p_c extending from $x_c/L_c = 0$ to $x_c/L_c \to \infty$) acting on water of infinite depth ($d \to \infty$), where d is the water depth (Lamb, 1932). In this case, the wave rise at the origin $\zeta_\infty(0)$ is

$$\frac{\zeta_\infty(0)}{\delta_c} = 0.5. \quad (4.5)$$

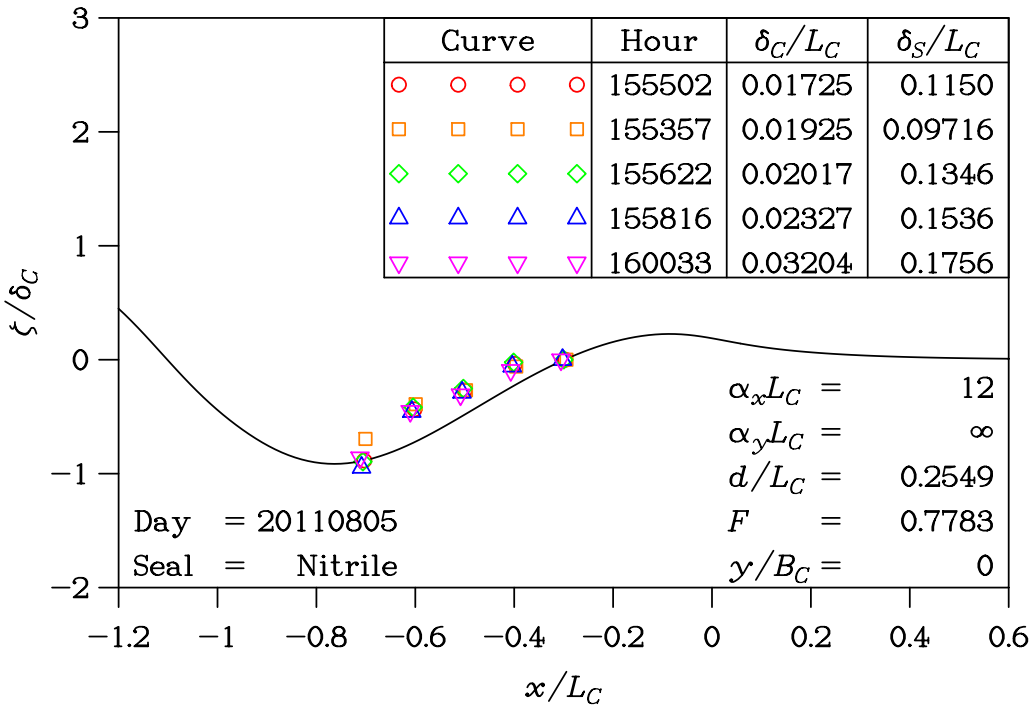

Figure 4.8 Effect of cushion pressure (p_c) on centerline profile, Type-1 (HN), compliant material, $\delta_s = 152.4$ mm, $U = 5.93$ m/s, $fn_c = 0.75$, $fn_H = 1.45$ Pressurized air cushion extends from $x/L_C = 0$ to $x/L_C = 1$. Note wave rise from $x/L_C = 0$ to 0.2. Per Doctor's nomenclature, d is the water depth, α_x and α_y are smoothing parameters for the cushion pressure distribution (see Equation 4.4). $F = fn_c$ is the cushion-length based Froude number.

δ_c is the cushion depression (see Figure 3.9),

$$\delta_c = \frac{p_c}{\rho_w g}. \tag{4.6}$$

The scaling of ζ reveals a potential source of the rise in seal elevation with pressure (Rayleigh, 1883; Lamb, 1932; Yeung et al., 2011).

$$\zeta \sim \frac{p_c}{\rho_w U^2} \tag{4.7}$$

The results of Lamb (1932) appear to hold for both shallow (subcritical and supercritical) and deep-water cases. Because $\zeta \sim p_c$, when expressed in dimensional terms, the wave rise observed at ($x_c/L_c \approx 0$) in Figure 4.8 is expected to increase with pressure. The linearity of this wave rise with respect to pressure is confirmed in Figure 4.9 which plots the seal

elevation at a fixed global location (X_G=0.75m) as the pressure is changed. The linearity is also confirmed by the collapse of the measured wave elevations in Figure 4.8. At lower velocities, the linearity with respect to pressure is expected to break down as the slope of the free-surface increases and non-linearities including wave breaking become significant (Kramer et al., 2013). Due to the relatively high Froude number of the experiments this non-linearity was not observed.

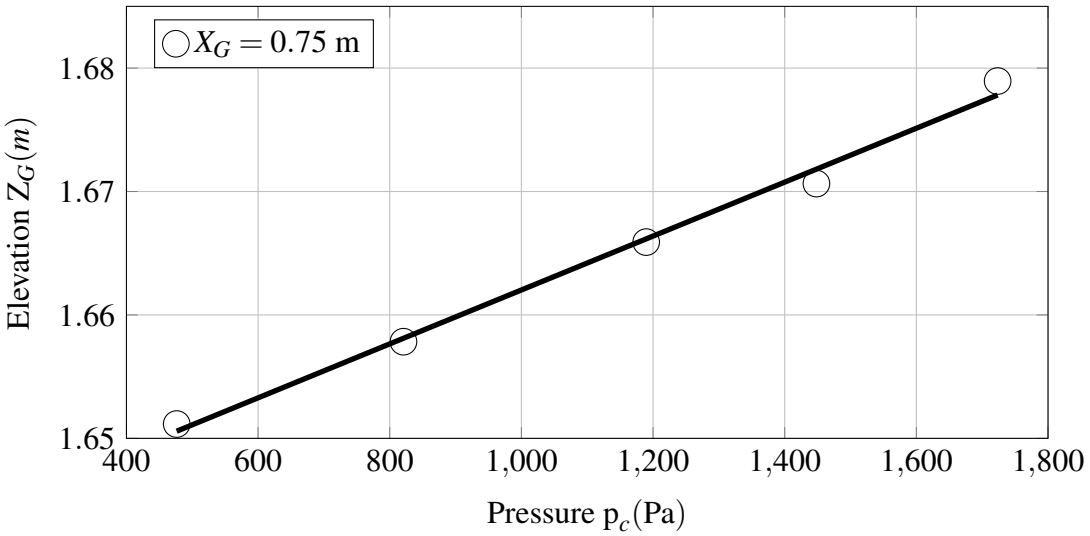

Figure 4.9 Vertical wave rise, ${}^{s}X_{IVC} = 0.75$ m , Type-1 (HN) seal material. Data has not been corrected for the streamwise shift in the hinge location concomitant with the wave rise.

As will be seen in Section 5.2, the relative rise of the seal from its undisturbed state, sets the confinement Δ of the seal fabric and the fold amplitude A. The wave rise associated with the cushion pressure represents one mechanism through which the cushion pressure p_c influences bow seal response.

4.2.2 Seal slope at centerline

The time-averaged centerline profiles shown in Figures 4.5 and 4.7 suggest a parametrization of the seal shape. This is shown in Figure 4.10, where the centerline profile is treated as two straight-line segments. The Tail, or lower segment (CD) is located at angle β from the horizontal. The angle between the inner seal face (Cylinder) and the Tail is given by $\pi - \alpha$.

The Knuckle or transition between the straight line segments, A-B-C, is treated as an arc with maximum curvature κ_{Y_h} (shortened to κ_h.

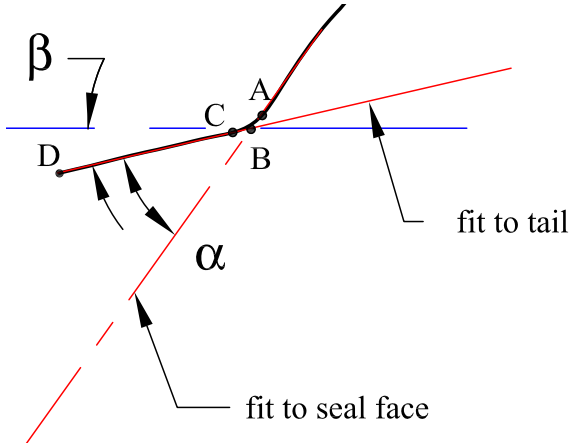

Figure 4.10 Parameters describing seal centerline shape.

To estimate the shape parameters in an automated fashion, a first-order spline with two segments is employed. A "free-knot" type spline is used to iteratively locate the best straightline fit for both the cylindrical face and Tail. The curvature κ_h of the Knuckle or the transition region between the straight line segment is estimated from a cubic spline fit to the data. Due to the large slopes, the nonlinear form of the curvature κ presented in Equation 3.6 is used.

An advantage of the spline fit in the Knuckle region is that the derivatives required for the curvature can be calculated analytically and are more tolerant to noise. The point within the hinge region with the maximum curvature is denoted by A. Point D corresponds to the trailing edge. The algorithm also estimates an effective wetted length, L_{AD}.

The variation in seal angle, β for the Type-1 material is shown in Figure 4.11. In Section 5.2 it will be seen that the local seal angle β has an influence on the confinement Δ. The results show that the seal angle $\beta \approx 13.5$ deg for the tests clustered around $fn_c = 0.77$. At the higher velocity $\beta \approx 15.0$ deg. As expected from linear wave theory, the pressure p_c has very little influence on the wave slope. Consistent with Equation 4.7, some dependence of the seal angle β on velocity is observed; however, due to the limited velocity range, the data did not support examining details of relationship between seal angle and velocity in detail.

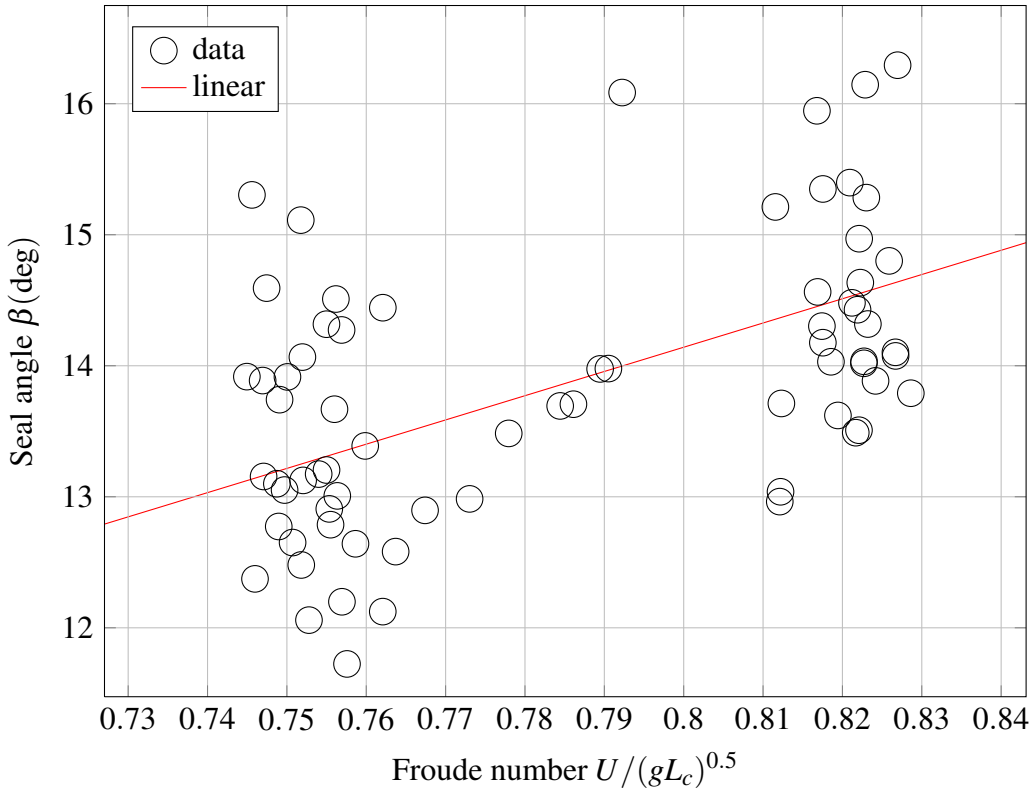

Figure 4.11 Seal angle β with respect to horizontal at centerline for Type-1 (HN), compliant material.

4.2.3 Curvature at centerline

The curvature at the hinge κ_h can be used to estimate the balance of bending and stretching forces in the hinge region. Due to the higher-order derivatives and sensitivity of the parameter to smoothing, there is considerable scatter in κ_h. As can be seen in Figure 4.12, κ_h varies from 10 to 150 m^{-1}, with the smaller curvatures occurring for the longer wetted lengths. This may suggest that the tension in the seal increases for the longer wetted lengths which is consistent with shear stress setting the tension in the Type-1 material. It will be shown in Section 5.1, that in the limiting case where bending rigidity can be ignored (membrane) tension at the leading edge $T(X_h = 0) \sim \frac{1}{\kappa_h} p_c$.

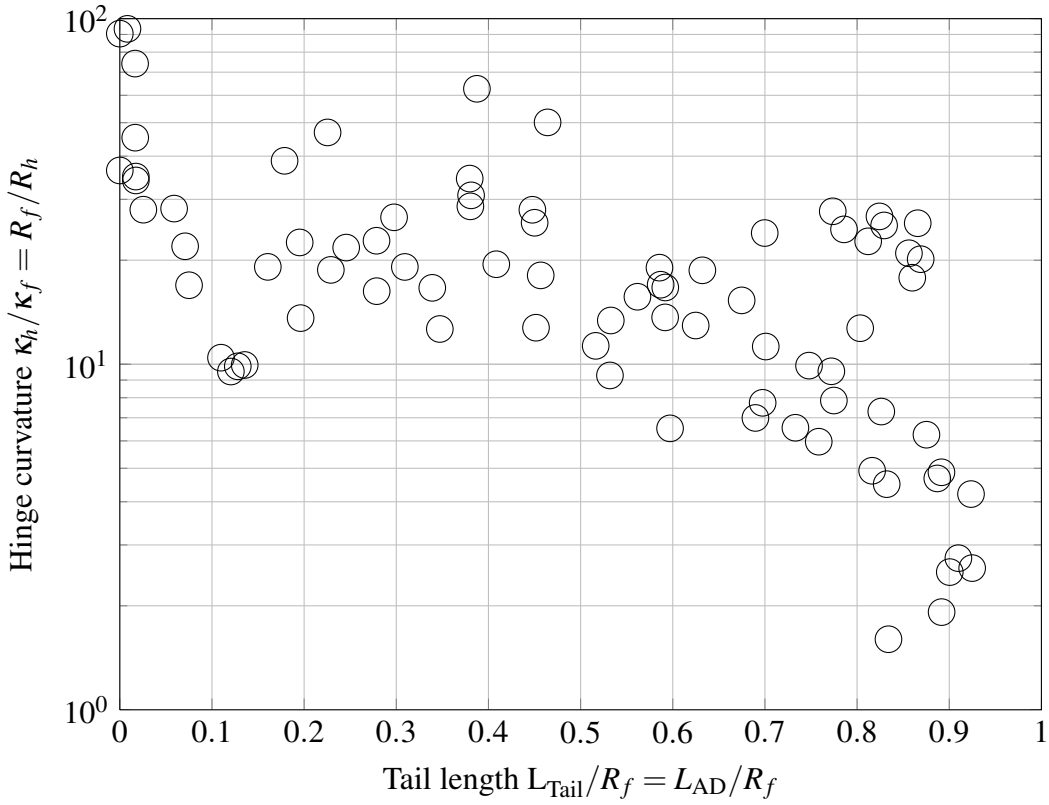

Figure 4.12 Curvature at hinge (κ_h) as function of Tail length (L_{Tail}), Type-1 (HN), compliant material.

4.3 Cross-flow response

In the previous section, it was observed in the streamwise profiles that the local draft δ_s, whether imposed through a change in gate angle or a change in pressure (via the wave rise), sets the vertical elevation at which the seal buckles. To study this behavior in more detail, the response in the cross-flow direction is examined. As shown in Figure 4.3, the cross-flow profiles are sectional cuts taken perpendicular to the streamwise profiles shown in the previous section. In practice, while the 3-d ToF imagery can be used to investigate the cross-flow behavior, due to the unsteady nature and relatively small amplitudes of the cross-flow folds, the high-resolution measurements from the linescan camera are preferred. Typical cross-flow profiles derived from the linescan camera for the stiff Type-0 material are shown in Figure 4.13, sorted by mean elevation Z_s. The letters a-g refer to particular

conditions and are used for cross-referencing. Likewise, cross-flow profiles for the compliant Type-1 material are shown in Figure 4.14.

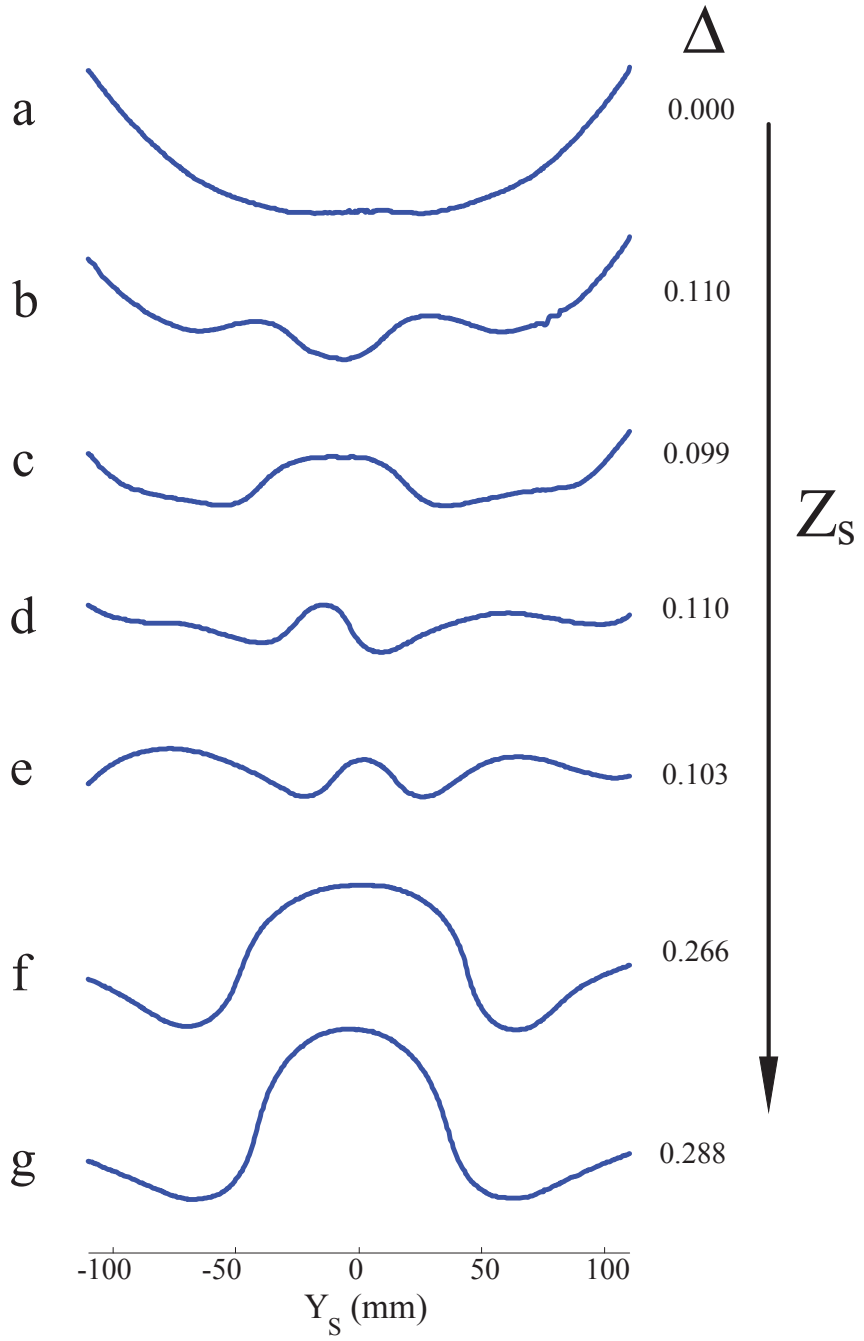

Figure 4.13 Representative *time-averaged* cross-flow profiles for stiff Type-0 (NN) material. Profiles (a-g) are presented in order of increasing confinement ratio ($\Delta = \mathcal{S}/L$) and average seal vertical position Z_S.

When seal response is viewed in the cross-flow plane, a salient effect of the immersion

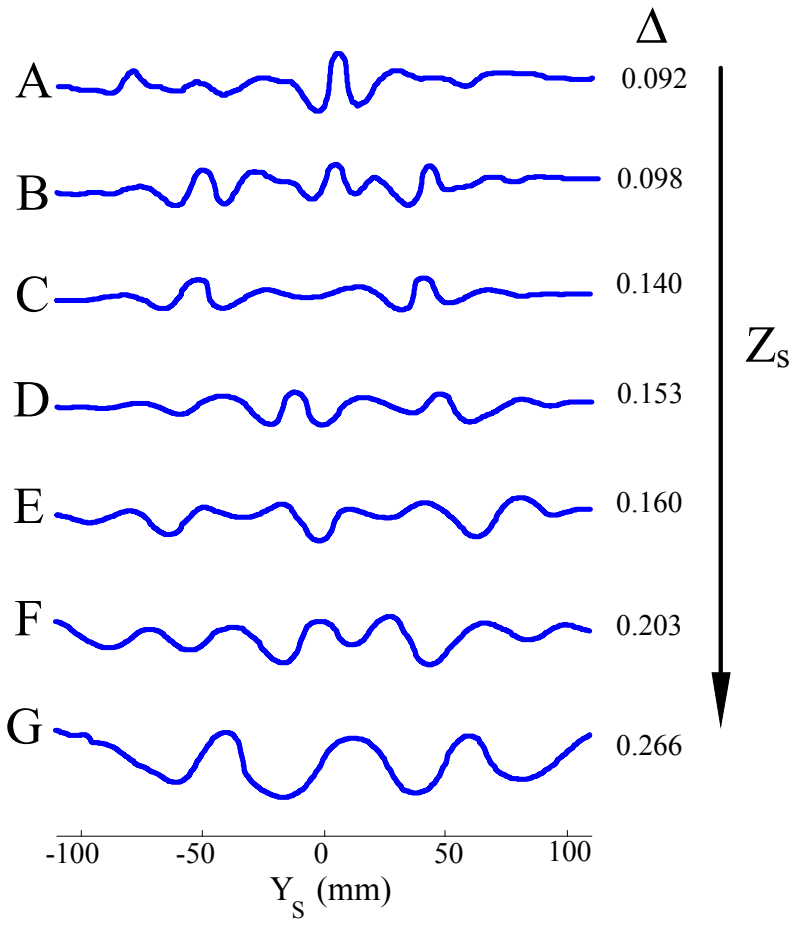

Figure 4.14 Representative *instantaneous* cross-flow profiles for compliant Type-1 (HN) material. Profiles (A-G) are presented in order of increasing confinement ratio ($\Delta = \mathcal{S}/L$) and average seal vertical position Z_s.

δ_s is observed. Due to the relative compliance of the seal material, all material previously below the waterline reconfigures to a new location at or above the free-surface. However, due to constraints imposed by neighboring seals and the sidewall, at this new position the seal must buckle. As seen in Figure 4.14, at this new position, the seal assumes a variety of mode shapes, characterized by different wavelengths (λ), amplitudes (A) and stability. These attributes are discussed in the following sections.

4.3.1 Seal confinement

A measure of the degree to which the seal material is packed within the available space is the confinement ratio Δ. First introduced in Section 3.4.3, Δ is the relative quantity of "excess" material previously below the waterline that must be accommodated. Δ is estimated using the high-resolution profiles acquired by the linescan camera (alternatively it could be calculated via the ToF imagery). The confinement ratio Δ is listed for each of the Type-0 (NN) profiles shown in Figure 4.13 and the Type-1 (HN) profiles in Figure 4.14. Confinement ratio (Δ) as a function of the mean vertical position of the seal (at the laser plane, Z_{IVC}) is shown in Figure 4.15. It is discovered that accompanying a change in local draft ($\delta_s \approx Z_{IVC} + {}^{s}X_{IVC} tan(\theta_{face})$), Δ increases almost linearly. Looking closer, it is observed that for a given Z_{IVC} the Type-0 seals are confined to a greater degree than the Type-1 seals and that there is additional scatter in the Type-0 confinement data. In Section 5.2, the relationship between mean seal elevation and confinement is studied in more detail. The results of the next chapter suggest that the seal effectively hinges at the local waterline and that the amplitude of the mode shape is closely related to Δ.

4.3.2 Type-0 (NN) stiff material

Mode shape

Time-averaged cross-flow profiles of the stiffer Type-0 material, covering the full range of elevations (Z_s) and pressures achieved during the large-scale experiments, are reproduced in Figure 4.13. These show, contrary to sea trial accounts, that folds for the stiffer material are stable and often persist for the length of a given test (typically 30 to 60s). The profiles are arranged in order of confinement ratio ($\Delta = \mathcal{S}/L$) (see Section 3.4.3). Per Figure 4.15, this arrangement also corresponds to sorting by vertical position Z_s (and by extension δ_s).

Among this sample of profiles, it is observed that Type-0 cross-flow mode shapes are amplitude-modulated with odd mode numbers ($\approx$ symmetric). Mode shapes are distributed

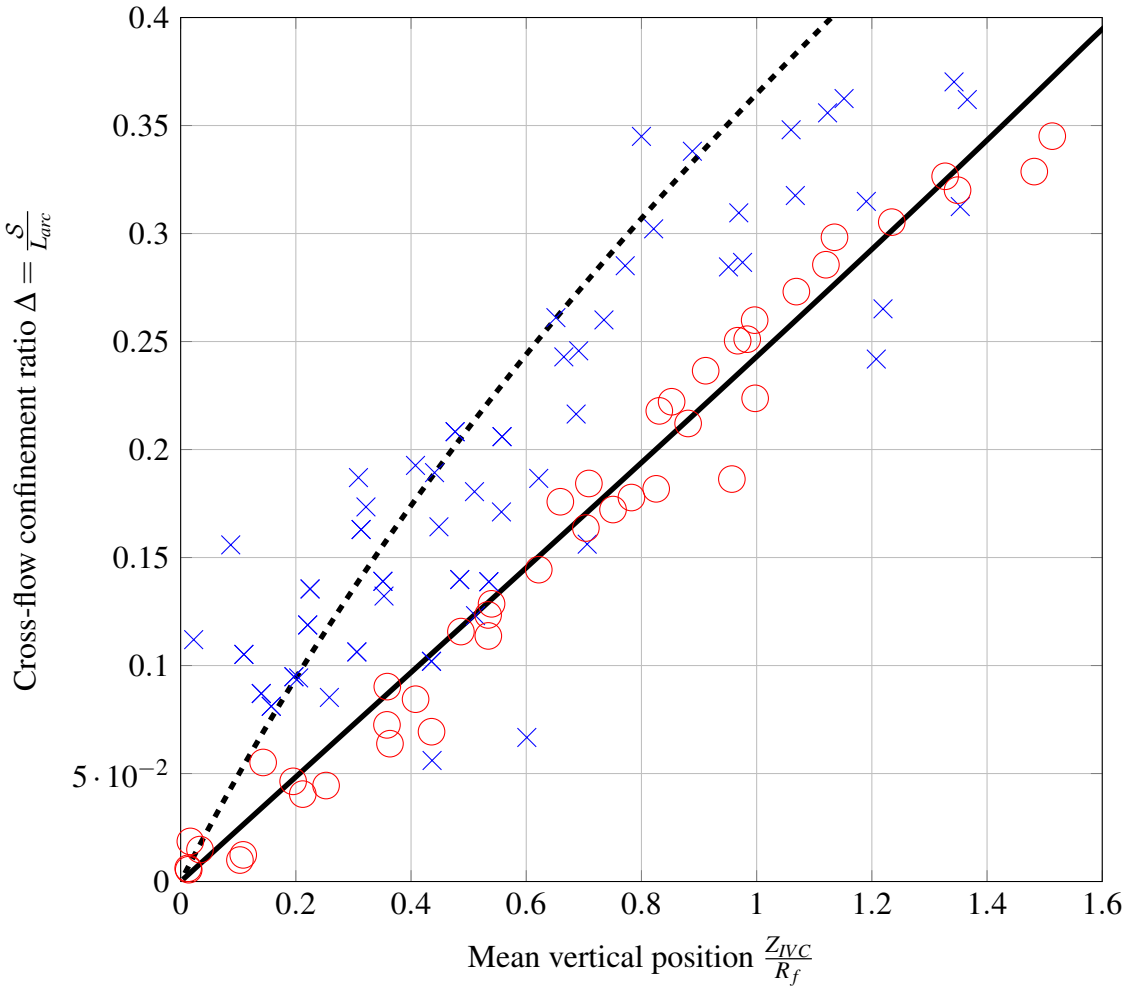

Figure 4.15 Change in confinement ratio $\Delta = S/L$ of Type-0 (NN) and Type-1 (HN) seals with vertical elevation (Z_{IVC}). Z_{IVC} is measured from the undeflected seal position (Figure 3.7). × Type-0 (NN) seal material; ○ Type-1 (HN) seal material. ━━ assumes that seal is hinged about a waterplane at angle, $\beta = 15$ deg to the horizontal; ▪▪▪ $\beta = 0$ deg. Comparison with the model suggest that the Type-1 (HN) material hinges about the local waterplane. See Section 5.2 for details of the hinge model.

across the full seal width and exhibit raised folds on centerline with the exception of (b). A pronounced central fold with a half-wavelength approaching the seal width is favored at the deeper immersions, while shorter wavelengths seem to be present in the profiles (b,d,e).

Mode number

Mode numbers for the Type-0 (NN) seal material are shown in Figure 4.16. While fairly scattered, the data presented does support some of the observations made in Figure 4.13.

First, the mode numbers are generally odd, with mode numbers $m = 1, 3, 5,$ and 7 dominating. Second, the variation in the mode number for a given test is smaller for lower mode numbers, suggesting that lower mode numbers may be stable to disturbances. This trend can be seen more clearly in Figure 4.17, where the standard deviation σ of m has been extracted and averaged. The $m = 1$ configuration is the most stable, while the standard deviation for $m = 7$ is nearly twice that for $m = 1$.

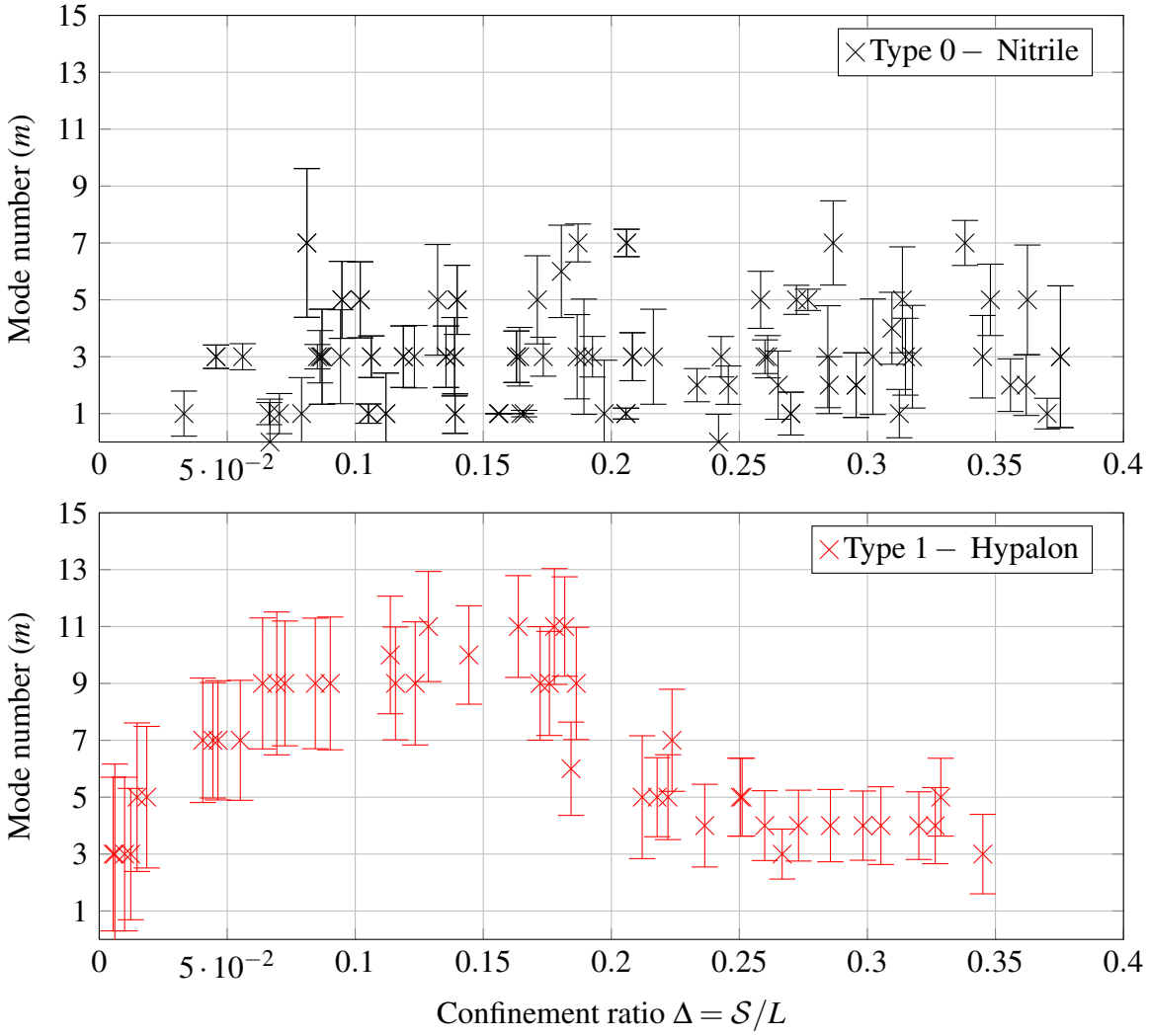

Figure 4.16 Mode number (m) as a function of confinement ratio ($\Delta = S/L$), Type-0 (NN) and Type-1 (HN) seal materials, based on turning point analysis of linescan data across all test conditions, fixed streamwise location ${}^{s}X_{IVC} = 0.75$ m.

The scatter in the data suggests that for seals constructed of the Type-0 material, mode

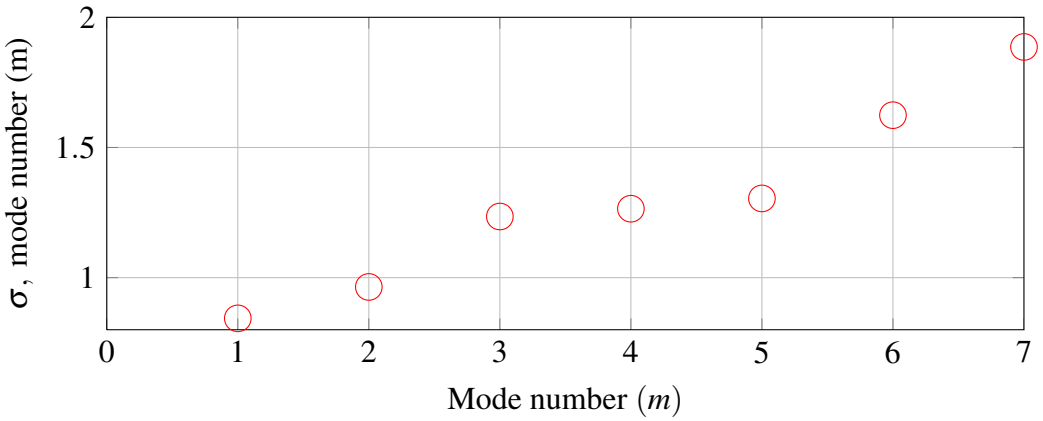

Figure 4.17 Mode-switching behavior as a function of mode number, Type-0 (NN) seal material, based on turning point analysis of linescan data across all test conditions. Note the increase in mode-switching at higher mode numbers.

number may not be strongly influenced by the seal confinement Δ. This is consistent with the results of Rivetti and Neukirch (2014). Alternatively, because Figure 4.16 contains data for a range of pressures and immersion, the effect of pressure may need to be parsed in order to isolate the physics. In addition, due to the fixed measurement location, the projected length (and arc-length) used for the confinement calculation (Equation 3.4) varies with Δ. As a result, mode number is biased toward lower mode numbers at smaller Δ. Due to this bias, the wavelength (λ), not the mode number may be a better descriptor of the seal shape.

Wavelength

Wavelength (λ) as a function of Δ for the Type-0 seal is shown in Figure 4.18. The wavelength is calculated using two methods. The first utilizes the turning point estimate,

$$\lambda_{C2T} = 2L_{C2T}|_{max(H_{C2T})} \tag{4.8}$$

The second is the effective buckling wavelength λ_e, which is a global estimate of the wavelength that balances bending and restoring energies. This descriptor is developed in Section 5.6.1. The wavelength is normalized by the hydrostatic buckling length $\lambda_{\rho g} = 2\pi(\frac{D}{\rho g})^{0.25}$ for the Type-0 (NN) material in the warp (X) direction. The basis for

this normalization is discussed at length in later sections. $\lambda_{\rho g} = 157$ mm for the warp (X) direction.

While considerable scatter exists in this figure, a few clear trends can be identified. The cross-flow wavelength increases with Δ until $\Delta = 0.25$. The measured wavelength is less than the $\lambda_{\rho g}$ for all conditions. At $\Delta = 0.25$ λ reaches a maximum of 70% of $\lambda_{\rho g}$. λ_e is proportional to λ_{C2T} above $\Delta = 0.2$, where an abrupt shift in the wavelength occurs in both measures.

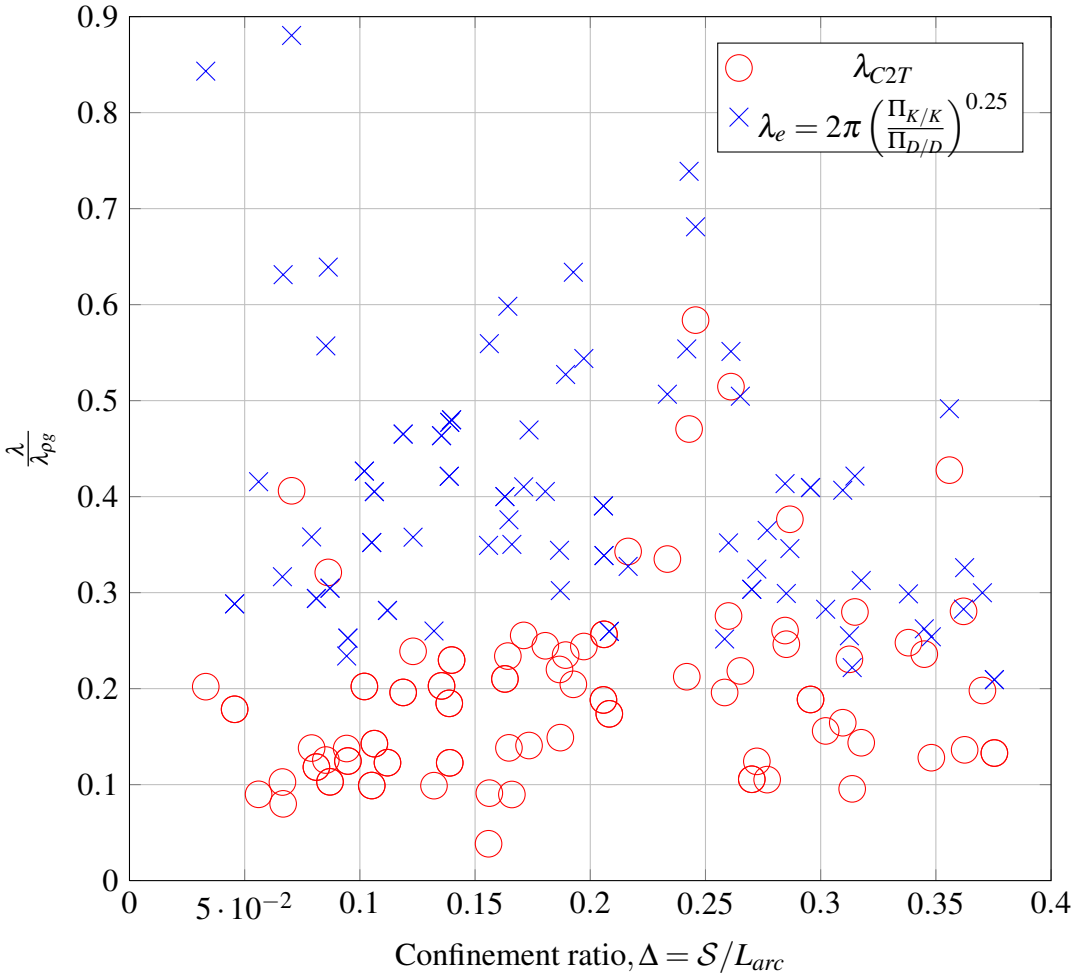

Figure 4.18 Change in buckling wavelength λ with seal confinement (Δ), Type-0 (HN), *stiff* seal material, ${}^{s}X_{IVC} = 0.75$ m. λ is estimated using the turning point analysis $\lambda_{C2T} \approx 2L_{C2T}$ as well as through the quotient of foundation and bending energies (λ_e). Wavelength is divided by $\lambda_{\rho g}$, the buckling wavelength at zero-speed. Unlike the Type-1 (HN) material, λ_e appears proportional to λ_{C2T} only above $\Delta = 0.2$. Hydrostatic wavelength $\lambda_{\rho g} = 157$ mm using average of warp/weft bending rigidities.

Amplitude

Fold slope A/λ as a function of confinement Δ for the stiff Type-0 material is shown in Figure 4.19. A/λ is estimated from the largest crest-to-trough cycle from the turning point analysis, where

$$\frac{A}{\lambda} \approx \frac{max(H_{C2T})}{4L_{C2T}|_{max(H_{C2T})}}. \tag{4.9}$$

It is observed that fold slope A/λ increases with confinement Δ, approximately obeying the power-law relationship $A/\lambda \sim \Delta^{0.5}$. There is considerable scatter in the A/λ data for the Type-0 material. Future work should examine the performance of the windowing and turning point algorithms used to generate Figure 4.19 and ensure that this a robust finding.

Stability

At lower immersions ($\frac{\delta_s}{R_f} < 0.25$) and pressure ratios ($\frac{\delta_c}{\delta_s} > 0.6$), a time history of a profile such as 4.13(c) would reveal that the seal response is marked by downstream travelling waves which are symmetric about the seal centerline, and outside the central fold. This type of instability is termed "mode-cycling" (Besch, 1976) as the mode number does not change. An example of this type of behavior can be seen in Figure 4.20, which shows that new crests of travelling waves reach the laser plane at a frequency of around 15 Hz. At the central fold on centerline, vibrations occur in phase with vibrations at the side lobes; however, the vibration at centerline occurs at a lower frequency, with one cycle occurring for every four full cycles of the side lobes. This corresponds to a vibration frequency at centerline of ≈ 3.75 Hz. Spatio-temporal analysis of these vibration patterns is outside the scope of the present work and is discussed in Chapter 8, Future Work. Instabilities are also observed at deeper immersions and lower pressures. However, under these conditions, the instability takes the form of low-frequency mode-switching as indicated by the variation in mode number in Figure 4.17. Unlike the mode-cycling instability, mode number changes during mode-switching.

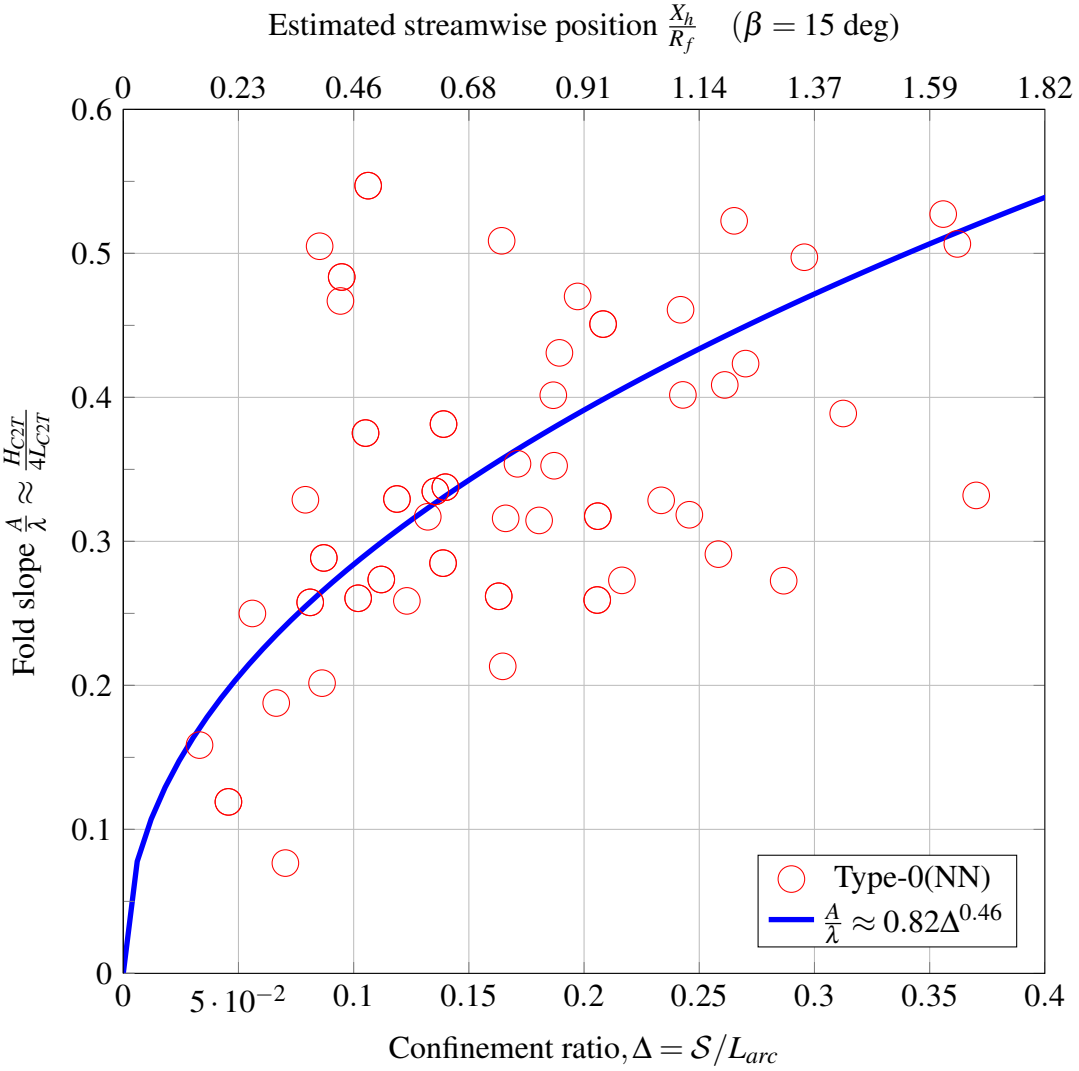

Figure 4.19 Influence of cross-flow confinement ratio ($\Delta = \mathcal{S}/L_{arc}$) on slope of buckled profile (A/λ), stiff Type-0 (NN) seal material. Slope is estimated from the turning point analysis, where $A/\lambda \approx \dfrac{H_{C2T}}{4L_{C2T}}$. Only the largest Crest-2-Trough (C2T) cycles are used in the slope estimate. Slope follows scaling $A/\lambda \sim \sqrt{\Delta}$ from small-angle approximation and inextensibility (Brau et al., 2010).

4.3.3 Type-1 (HN) compliant material

Mode shape

Cross-flow mode shapes for more compliant Type-1 (HN) material differ significantly from those observed for the Type-0 (NN) material, revealing the dramatic influence of material properties on cross-flow buckling behavior. Instantaneous cross-flow profiles for the more

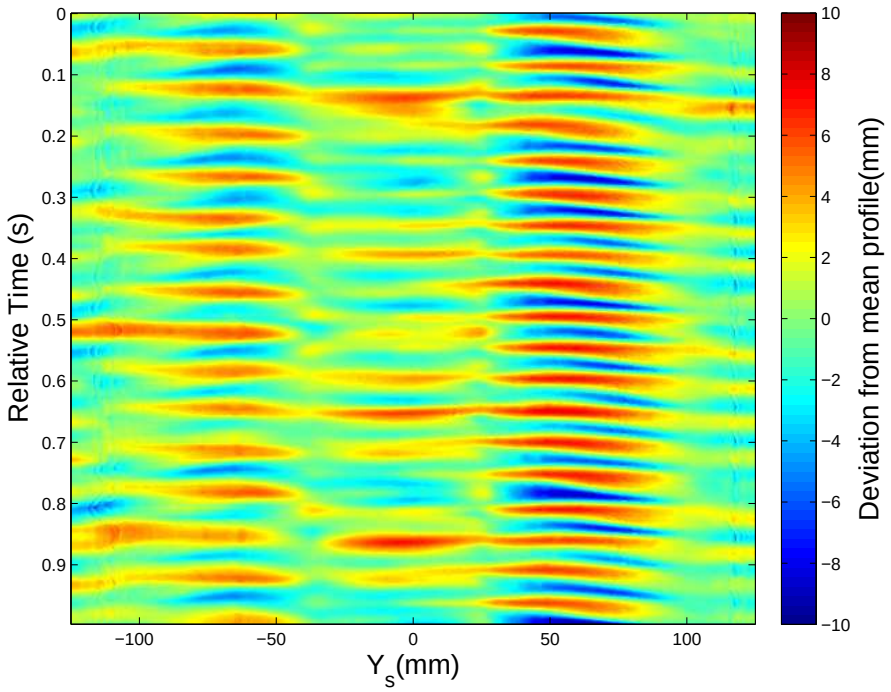

Figure 4.20 Traveling waves or "mode-cycling" (Besch, 1976) observed in Type-0 material. Central fold persists for the duration of the test. Waves are synchronized on both sides of the central fold ($U = 6.09$ m/s, $\delta_s = 50.8$ mm, $p_c = 1150$ Pa).

compliant Type-1 material are reproduced in Figure 4.14. Average cross-flow profiles for the Type-1 material are provided in Figure 4.21. Unlike folds in the Type-0 material, which where to found to persist for 30 seconds or more, folds for the more compliant Type-1 material are found to be transient – persisting for a very brief period if at all. The time-averaged profiles suggest that within the tail region cross-flow profiles for the compliant Type-1 material describe part of a plane (mode number $m = 0$).

In Figure 4.14, it is seen that in (A,B,C,D) the number of localized buckling packets may vary between 1 and 3, with the buckling profile (D) closely resembling profile (e) from the stiffer material (Figure 4.13). Mode shape for the Type-0 material at shallow immersion differ from the Type-0 response in that the response is localized rather than distributed across the seal width. Further increasing the immersion, other features are noted. Profile (E) contains buckling at two distinct wavelengths (period doubling). As the Z_s is further increased (G), buckling is no longer localized, and takes a regular almost sinusoidal form.

The wavelengths of the folds at (G) are significantly longer than at (A).

Mode number

Mode numbers for the Type-1 (HN) seal material are also shown in 4.16. Mode number reaches a maximum of $m = 11$ at $\Delta = 0.18$. Above $\Delta = 0.18$ mode number decreases sharply. This process be seen by comparing (F) and (G) in Figure 4.14. Similar to the Type-0 seal material, odd mode numbers are generally favored. A significant difference between the Type-0 and Type-1 response is that the Type-1 response features considerable variation in mode number for a given test condition (compare the standard deviation of mode number for a Type-0 $m = 1$ configuration to that a $m = 9$, Type-1 configuration). This may reflect the instability of configurations featuring high mode numbers and localized buckling as compared to the low mode-number configurations typical of the stiff Type-0 (NN) material. Given the steady state flow condition, this mode-switching behavior may also suggest that high mode configurations may be nearly energetically equivalent and may be highly sensitive to imperfections and perturbations. This hypothesis will be investigated in Section 5.5. Like the Type-0 material, mode numbers for the Type-1 material also suffer a bias due to the

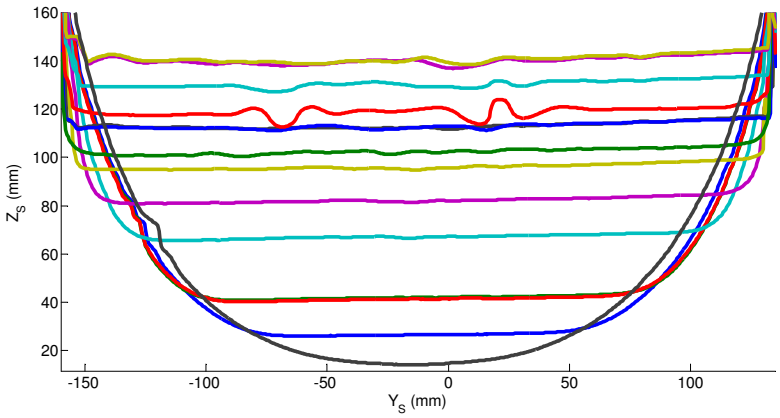

Figure 4.21 *Time-averaged* profiles for compliant Type-1 (HN) material at different local immersions. Time averaging period of 2 s. On average, folds such as shown in Figure 4.14 do not persist through the time-averaging process. At the lowest immersion, the seal shape at the laser plane describes a conic section. At deeper immersions the seal in the Tail is found to describe a plane ($m = 0$).

change in projected length with shortening. As such, the wavelength from the turning point analysis may be a more useful descriptor of the buckling mode shape.

Wavelength

The wavelength for the Type-1 material is shown in Figure 4.22. This tells a surprisingly clean story considering the variation in mode number with Δ. The wavelength is calculated using two methods; the first is the turning point analysis as described previously, where $\lambda_{C2T} \approx 2L_{C2T}$; the second, which is further described in Section 5.6.1, defines λ_e as the wavelength that balances bending and foundation (potential) energies. As will be described in Section 5.6.1, the wavelength reported by the turning point analysis is expected to be shorter than λ_e. As the confinement approaches $\Delta = 0.35$, $\lambda_e \approx \lambda_{\rho g}$. This may indicate that hydrostatic restoring forces dominate at the laser plane near $\Delta = 0.35$. As will be discussed in Section 5.2, because of the fixed location of the linescan camera and the method in which the immersion was altered, a change in seal confinement at a fixed ${}^{s}X_{IVC}$ may be equivalent to a shift downstream of the Knuckle. An estimate of this shift is shown in the upper axes of Figure 4.22.

Fold amplitude and slope

Fold slope A/λ as a function of confinement Δ for the Type-1 (HN) material is shown in Figure 4.19. The slope is estimated from the largest crest-to-trough cycles in same method as was applied to Type-0 profiles. Similar to the Type-0 material, it is observed that fold slope A/λ rises with confinement Δ. The compliant Type-1 seal appears to follow the power-law relationship $A/\lambda \sim \Delta^{0.5}$ closely, with considerably less scatter than the Type-0 results. In later sections, the potential origins of the $\Delta^{0.5}$ behavior will be studied in detail.

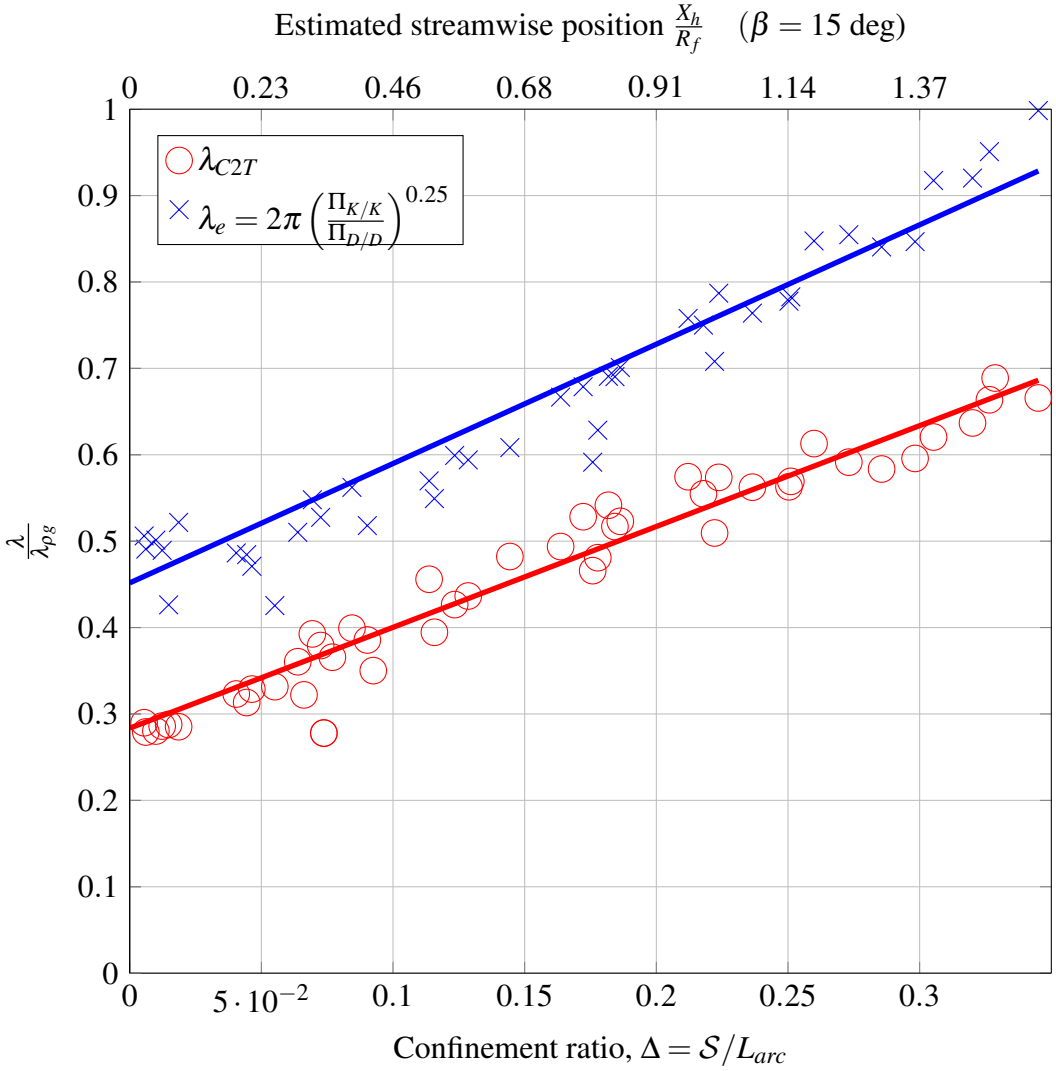

Figure 4.22 Change in buckling wavelength λ with seal confinement (Δ), Type-1 (HN), *compliant* seal material, ${}^{s}X_{IVC} = 0.75$ m. λ is estimated using the turning point analysis $\lambda_{C2T} \approx 2L_{C2T}$ as well as through the quotient of foundation and bending energies (λ_e). Wavelength is divided by the hydrostatic wavelength $\lambda_{pg} = 52$ mm using average of warp/weft bending rigidities.

Stability

Figure 4.21 shows time-averaged cross-flow profiles for seals constructed of the compliant Type-1 material. The same averaging period as the stiff Type-0 profiles shown in Figure 4.13 is applied. Figure 4.21 indicates, that on average, cross-flow folds for the Type-1 material are transient. This can also be seen in the large variation in mode number for the Type-1 configuration. As mode number varies considerably within a given run for this material, the

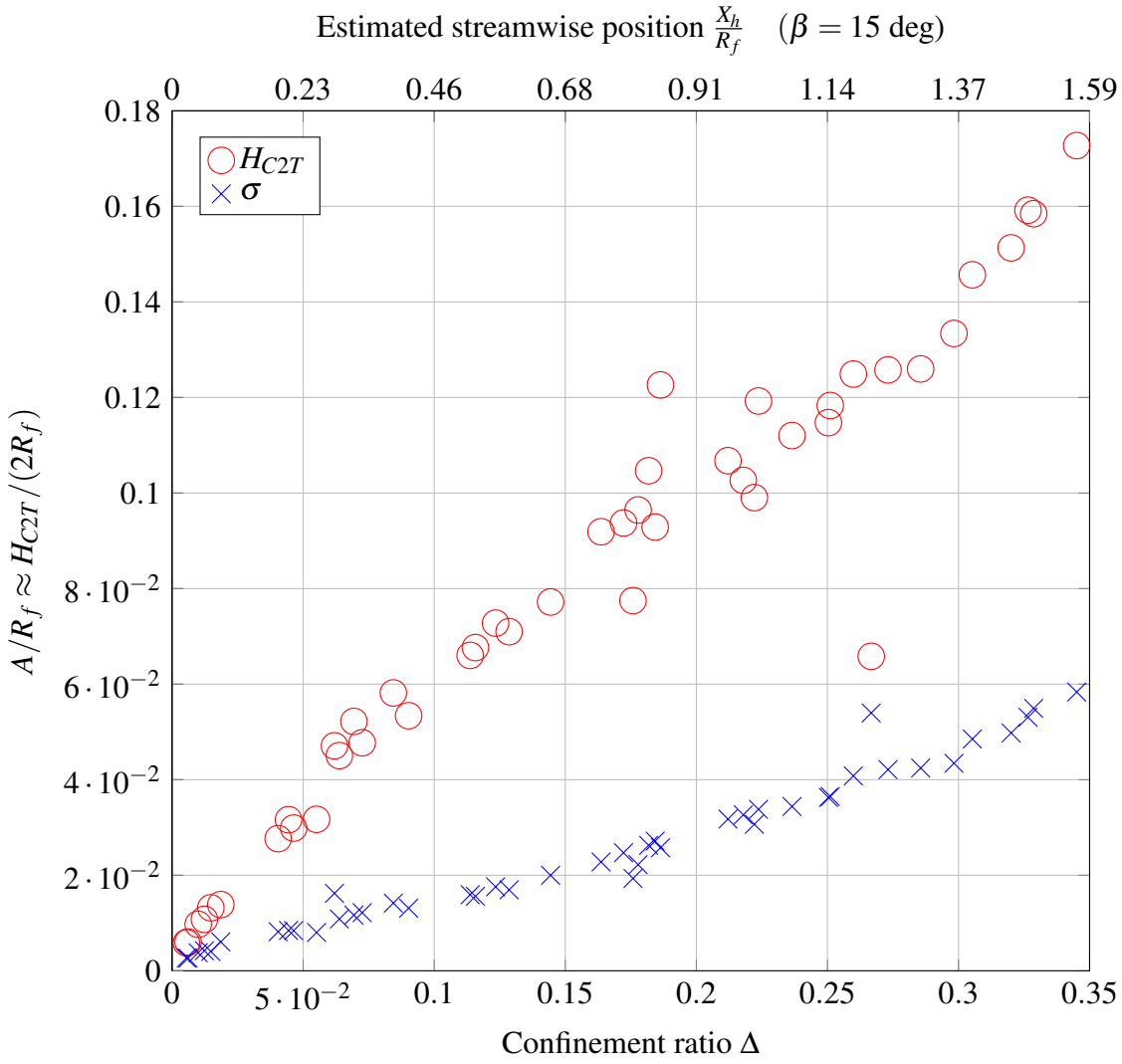

Figure 4.23 Change in fold amplitude $A \approx H_{C2T}/2$ (◯) and standard deviation σ (×) with seal confinement (Δ), Type-1 (HN), compliant seal material, ${}^{s}X_{IVC} = 0.75$ m. Both A and σ increase linearly with confinement Δ. This is consistent with a shift in the streamwise position of measurement plane (X_h) relative to the knuckle.

vibration does not take the form of a standing wave.

Clues as to the physical mechanism responsible for vibration of the Type-1 material are found by examining the seal behavior during a condition in Figure 4.21 where folds appear to persist for 0.2 s. A single profile from this run is shown in (C) of Figure 4.14 which is characterized by two localized buckling packets. The resilience of this configuration is rather surprising as the free surface disturbances emanating from the free-surface forming gate are estimated to be nearly 1/4 the fold amplitude.

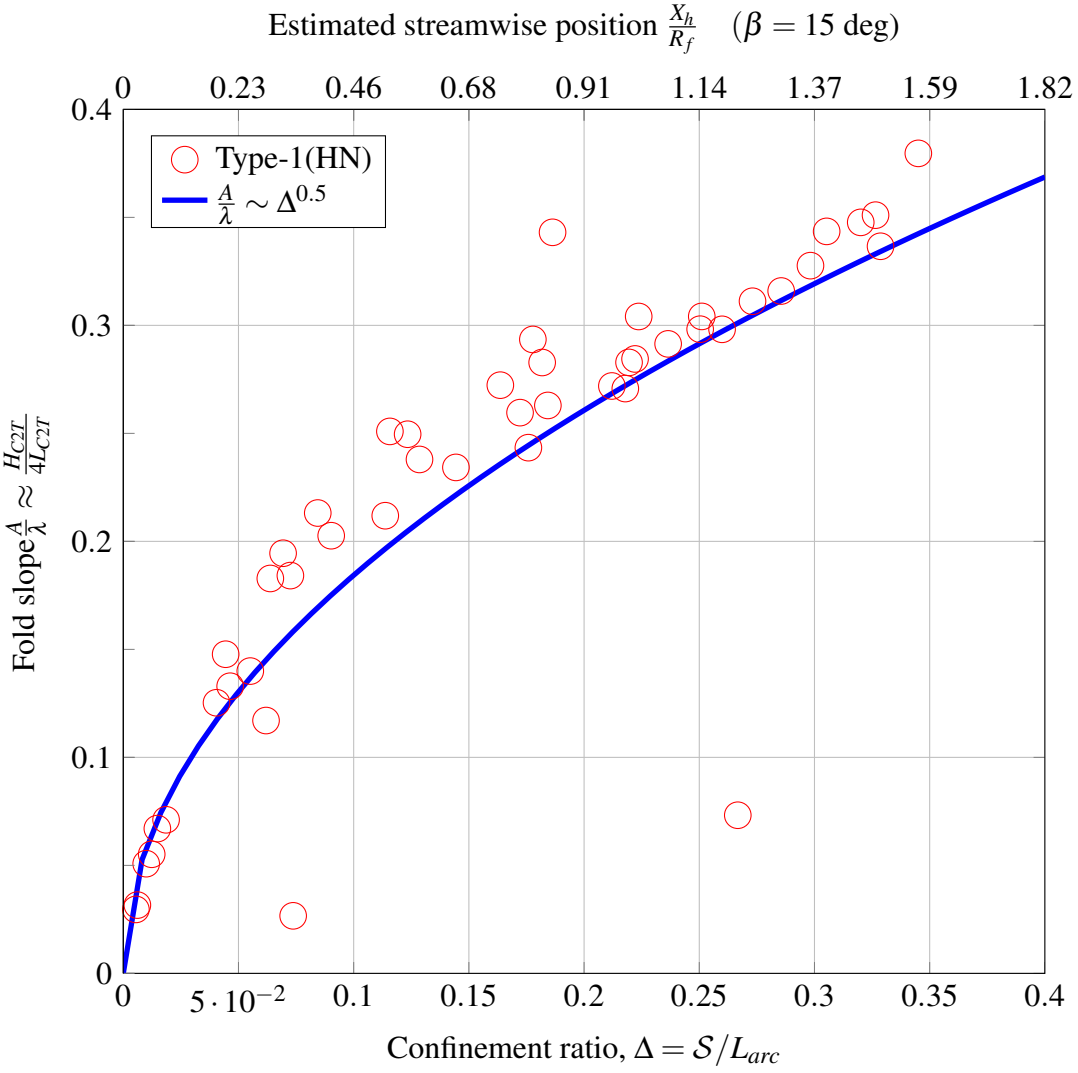

Figure 4.24 Influence of cross-flow confinement ratio ($\Delta = \mathcal{S}/L_{arc}$) on slope of buckled profile (A/λ), compliant Type-1 (HN) seal material. Slope is estimated from the turning point analysis, where $A/\lambda \approx \dfrac{H_{C2T}}{4L_{C2T}}$. Only the largest Crest-2-Trough (C2T) cycles are used in the slope estimate. Slope follows scaling $A/\lambda \sim \sqrt{\Delta}$ from small-angle approximation and inextensibility (Brau et al., 2010).

Figure 4.25 looks at the evolution of mode shape within this particular run. It is observed that in response to a disturbance (presumably), the localized buckling packet momentarily splits (B), expands to a higher mode number (C), breaking symmetry (A) before returning to a stable symmetric state (D) that is the up-down mirror of A). The profile in (C), has a higher bending energy than (A) or (D), which was triggered by the energy input due to the disturbance (Hunt et al., 1993). The beginning (A) and end (D) configurations are likely

equivalent in terms of total system energy. This suggests that vibrations of the Type-1 seal may be the result of a type of mode-switching; where in response to disturbances, localized buckling packets expand, contract and possibly merge. This is a distinct type of instability from the mode-cycling behavior observed for the stiff Type-0 (NN) material. That this mode switching behavior occurs during controlled steady-state conditions at the LCC suggests that very small changes in fluid work are required to change seal configuration. At sea, where the buckled seal system may be triggered continuously by disturbances such as waves and vessel motions, this type of vibration is likely exacerbated. Future work should investigate whether this type of instability may be responsible for the wear seen observed during sea trials.

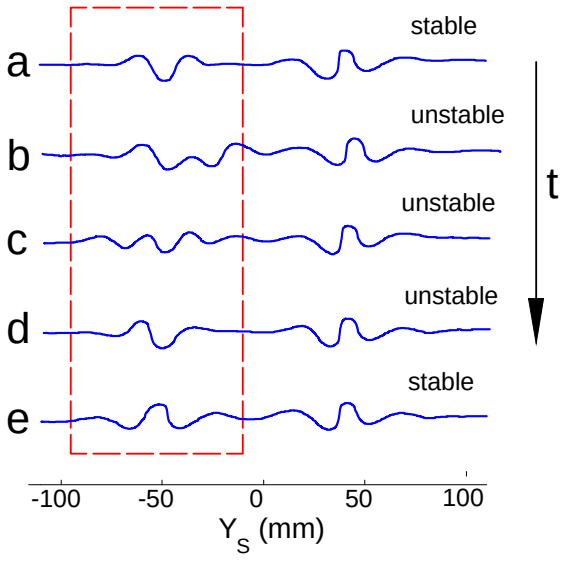

(a) Profiles

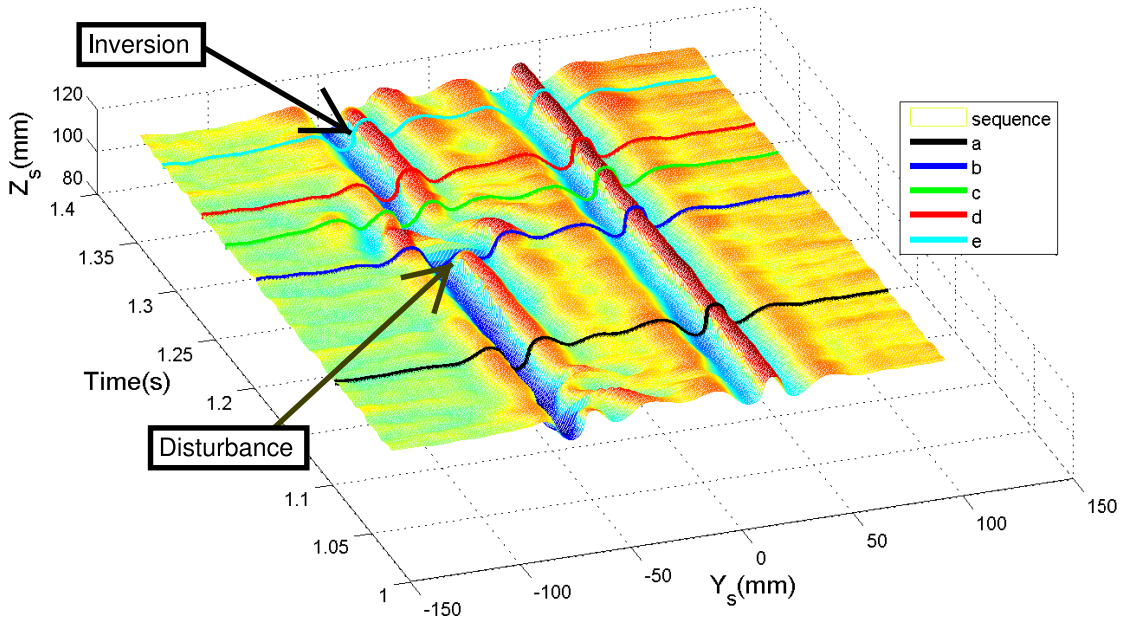

(b) Spatio-temporal plot

Figure 4.25 Evolution of localized buckling profile within a single test condition (same as Figure 4.14(c)), Type-1 (HN) material. Features seen within this test include (b) splitting, (c) expanding where the profile is becoming less localized, (d) symmetry breaking, (e) inversion. The term "stable" is used loosely here. Within the 2s file that was examined $\approx 90\%$ of the duration had the left fold in configuration (c). $Z_s = 124.8$ mm, $p_c = 443$ Pa, $U = 5.74$ m/s, confinement ratio for $L_{bb'} = 100$ mm is estimated as $\Delta = 0.140$ (a,c,d),$\Delta = 0.142$ (b,d).

4.4 Type-0 response regimes

A basic classification of the primary seal response regimes (Figure 4.26) for the Type-0 material is developed. As Figure 4.26 was created prior to the availability of high-quality seal shape measurements (Summer 2012), the classification is based solely on still images from the 2011 test campaign. The images are coded in terms of centerline symmetry (yes/no), mode number (m) and whether or not the folds were stable. The images are correlated with the test condition using the time stamp, such that they can be presented with respect to immersion ($\frac{\delta_s}{R_f}$) and pressure ratio ($\frac{p_c}{\rho g \delta_s} = \frac{\delta_c}{\delta_s}$). Here R_f is the radius of an individual finger seal, ρ is the water density, g the acceleration due to gravity and δ_s is the nominal immersion of the seal referenced to the undisturbed waterline. The variety of seal behavior presented in Figure 4.26, a stability regime map, was acquired over a fairly narrow speed range of $5.6\,\mathrm{m\,s^{-1}}$ to $6.3\,\mathrm{m\,s^{-1}}$ and at pressure ratios generally less than 1.25. The platform experienced difficulties achieving pressure ratios above 1.25 due to air leakage.

Despite being extremely subjective, Figure 4.26 reveals some interesting trends. Stable fold configurations were observed between pressure ratios of 0.6 to 1.1 and immersion ratios from 0.25 to 1.1. This regime is exemplified by the 3-dimensional seal shape ($m = 3$) in Figure 3.12. In this relatively small region of the experimental space, an equilibrium existed between the myriad forces acting on the seal material. The number of stable folds across the seal width varied from a single central fold ($m = 1$) at high immersion ratios to three folds ($m = 5$) at the lower wetted lengths, with the heavier material favoring the symmetric $m = 1$ and $m = 3$ configurations. Both of these mode shapes feature a well-defined fold, directed upward, near the centerline. The mode number tended to decrease with wetted length. At very deep immersions, the slack material took two different forms. Under some conditions, the seal sides gathered and doubled-over symmetrically. In other conditions, the central fold made self-contact and folded-over asymmetrically.

Besch (1976) utilizing the high-speed carriage at the David Taylor Model Basin examined the behavior of slightly larger ($R_f = 0.178\,\mathrm{m}$) and stiffer finger seals modeled after

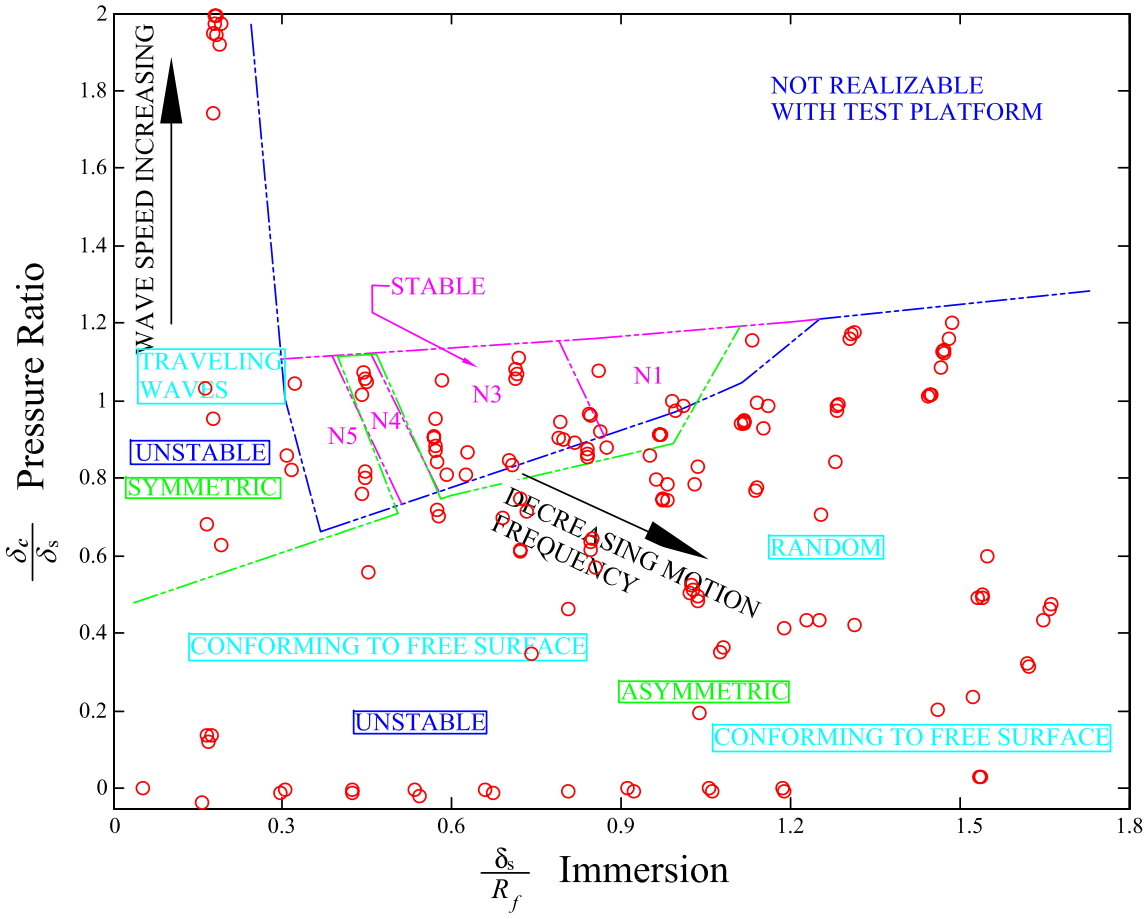

Figure 4.26 Qualitative finger seal response regimes, Type-0 (NN) material. ∘ indicates test cases where steady-state images were examined. All images are taken within the velocity range, $U = 5.6 - 6.3$ m/s.

those on the U.S. Navy's SES-100B testcraft. Like Figure 4.26, Besch also observed that the number of folds increased with decreasing immersion, in his case resulting in as many as 10 raised folds recorded at an immersion ratio $\frac{\delta_s}{R_f} = 0.08$. The velocities and pressures at which Besch's observations were made are unknown making detailed comparisons difficult. It is known that the majority of his experiments were performed at significantly higher speeds than those tested at the LCC, between 12.9 and 24.9 m/s. At immersion ratios $\frac{\delta_s}{R_f} < 0.25$ Besch observed outward travelling waves, a phenomenon he termed "mode cycling" as the mode number remained constant during the event. The "mode cycling" phenomenon observed by Besch likely corresponds to the travelling wave regime indicated

in Figure 4.26, that were also observed to occur for $\frac{\delta_s}{R_f} < 0.25$. Outside of the stable, and mode-cycling regimes, the seal was unsteady as well. In this case the instability took the form of relatively low-frequency travelling waves and mode-switching. The frequency of this behavior increased with cushion pressure.

4.5 Conclusions

In this chapter results from large-scale experiments conducted at the U.S. Navy's Large Cavitation Channel were presented. The hydroelastic response of two sets of seals constructed of materials with significantly different bending rigidities was compared. It is observed that mode shapes for the stiff Type-0 material are generally symmetric and distribute across the full seal width, featuring amplitude modulation and raised central folds. Within the limited parameter space of the experiments, Type-0 seals were found to be stable for moderate immersions and are observed to lose stability at lower immersions through a convective travelling-wave type instability. In contrast, mode shapes for the Type-1 seals generally feature localized buckling patterns. Type-1 seals are found to be unstable under almost all test conditions. Instead of the convective mode-cycling instability observed in the stiff Type-0 seals, Type-1 are subject to high-frequency mode-switching, where localized buckling packets appear to expand to higher mode configurations when subjected to disturbances. The mode-cycling and mode-switching type instabilities observed during the experiments, are distinct from the flutter-type instabilities that previous researchers (Ryken, 1978; Yamakita and Itoh, 1998) have attempted to link to seal vibration and are likely important in understanding the persistent problem of seal wear. The physical mechanisms behind the significant changes in configuration observed during the large scale experiment are unclear and warrant further study.

Both seals constructed of the Type-0 and those from the Type-1 material exhibit similar responses to confinement Δ. Cross-flow slope A/λ is found to increase with confinement Δ

as $A/\lambda \sim \Delta^{0.5}$. The agreement for this power law is particularly promising for the compliant Type-1 material, which in general seems to exhibit less scatter than the Type-0 material. Confinement Δ is found to be set by the mean elevation of the seal which is set by the local draft. As a result, the wave rise due to the cushion pressure that was reported has the effect of increasing the confinement. The linear rise in seal elevation with cushion pressure appears to follow from linear wave theory. This suggest that there is a tight coupling between seal behavior and local free-surface hydrodynamics.

Chapter 5
Cross-flow response model

This chapter uses qualitative modeling to investigate potential mechanisms responsible for the changes in seal configuration observed in the previous chapter; particular attention is paid to the wavelength, amplitude and stability of the post-buckled configurations. The role of boundary conditions in setting the symmetry of the post-buckled shapes is also elucidated. The analysis suggests that many of the hydroelastic features observed in the large-scale data are consequences of the fact that, unlike the majority of civil structures, bow seals operate in a post-buckled state.

First, in Section 5.1 measures are developed to estimate the balance of bending and stretching forces from 3-dimensional seal shapes such as acquired at the LCC. These measures are then used to subdivide the seal into three regions. Within each region the relative importance of material properties such as the bending rigidity, 3-dimensionality and type of fluid forcing is qualitatively different with a balance of forces determining the extent of each region. As such, the geometry and fidelity of models required to describe each region are significantly different. In the Cylindrical region, stretching forces dominate and the seal can be adequately described as a membrane. Near the intersection of the seal with the free-surface, the seal hinges and forms a "knuckle." Analysis of Gaussian curvature from 3-dimensional seal shapes indicates that in the Knuckle region of the seal large pressure gradients and material confinement combine to create localized areas of strain. Both bending rigidity and 3-dimensionality are needed to adequately describe the shape in this region. The remainder of the chapter focuses on the "tail" region, where the seal material lies parallel

to the free-surface. In this region, the seal possesses near-zero Gaussian curvature and is more amenable to simplified modeling. Analysis of this region is motivated by post-mortem photographs which show that seal damage is most prevalent in the Tail region.

Due to their flexibility, bow seals cannot support significant external pressures operate in a post-buckled state for all practical flow velocities. Section 5.2 looks at how the cross-flow displacement of the seal is a result of confinement due to the free-surface and neighboring seals. The large-scale data suggest, based on an analysis of the kinematics, that *compliant* Type-1 (HN) seals deflect as if hinged about the local waterplane. Scaling arguments are used to show that the confinement ratio Δ (a non-dimensional measure of the cross-flow displacement) acts as a constraint on the seal configuration, limiting the amplitude of the mode shape. The analysis indicates that the cross-flow fold slope $\frac{A}{\lambda}$, where A is the fold amplitude and λ is the buckled wavelength, follows the scaling $\frac{A}{\lambda} \sim \Delta^{0.5}$. This scaling is closely matches the large-scale data for the Type-1 material presented in Chapter 4.

Because of the large confinement ratios Δ typical of finger seals, seal response is characterized by large rotations and geometric nonlinearities. When the seal undergos large rotations (θ), the approximation for the curvature used in classical Euler-Bernoulli beam theory breaks down. The nonlinear approach taken is to model the material as an elastica (Timoshenko, 1961), where beam shape is described parametrically as a function of arc length s, and rotation θ. The model treats the Tail region of a finger seal as a 2-dimensional beam on an elastic foundation (BoF), a canonical problem of elastic stability (Hetényi, 1979).

In Section 5.4, the more tractable linearized version of the model is explored. The linear analysis identifies a number of dimensionless parameters driving the cross-flow response of finger seals. Of particular importance is $\eta = L/L_n = L(K_f/D)^{0.25}$, the system size (L) as non-dimensionalized by the natural buckling length L_n. L_n is the natural length-scale at which bending (strain) and external restoring energies are balanced and is given by $L_n = (D/K_f)^{0.25}$, where D is the bending rigidity and K_f is a foundation stiffness. Within

the BoF framework, the behavior of the stiff Type-0 (NN) and compliant Type-1 (HN) materials are contrasted. The behavior of the stiff Type-0 (NN) material, including features such as the stability at mode $m = 1$ and the presence of amplitude modulation, is found consistent with small η. In contrast, the behavior of the compliant Type-1 (HN) material is symptomatic of large η. A stability analysis demonstrates that, due to their buckled state, bow seals are susceptible to a mode switching instability, which may be a potential mechanism responsible for the damaging vibrations.

It is found that for both materials, at deep immersions, the buckling wavelength (λ) at the laser measurement plane approaches the hydrostatic ($K_f = \rho g$) wavelength. This suggests, under these conditions, that hydrodynamic components of the restoring force are relatively small. However, at shallower immersions, the buckling wavelength is considerably shorter than the hydrostatic wavelength. Within the BoF framework, the observed change in wavelength may be explained by an apparent increase in foundation stiffness. In Section 5.6.1, energy measures are developed in order to estimate the effective foundation stiffness K_{f_e} as reported by the measured seal shape.

The mechanisms responsible for the apparent increase in foundation stiffness are not fully understood. In Section 5.6.4, scaling arguments are employed to identify potential hydrodynamic mechanisms for the stiffness increase. In particular, viscous flow-induced tension may contribute significantly to the restoring force. The contribution of the tension K_τ to the effective stiffness is found to scale as $K_{f_\tau} \sim \dfrac{T(X_h)}{L_w^2}$, where $T(X_h)$ is the local streamwise tension and L_w is the wetted length. It is also found that an inviscid destabilizing force K_d may also be present due to local curvature. It is argued, that because curvature vanishes at the free trailing edge, both K_τ and K_d must vanish as well. This may begin to explain why hydrostatic effects were observed to dominate downstream of the Knuckle.

Refinements to these models are proposed in the Future Work, Chapter 8.

5.1 Seal regions

When discussing seal geometry, it is convenient to subdivide the seal into three regions based on curvature κ as shown in Figure 4.4. Within each region the relative importance of material properties, 3-dimensionality and fluid forcing is qualitatively different, with a balance of forces determining the extent of each region.

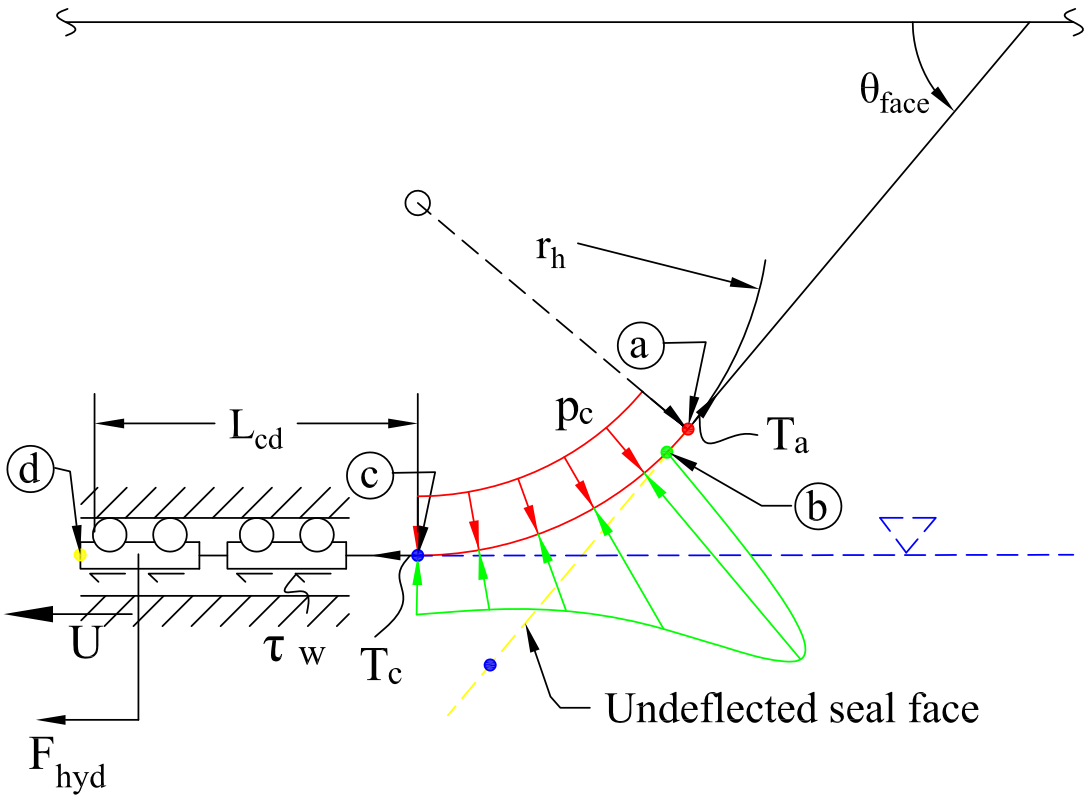

Figure 5.1 2-dimensional membrane model of bow seal at centerline.

To understand the load path for a highly compliant structure such as a bow seal, and whether the seal problem is amenable to analysis as a membrane such as seen in Figure 5.1, stresses due to stretching σ_s and bending σ_b of the structure are estimated. The separation of stretching and bending effects is a commonly adopted analogy employed when studying the behavior of elastic shells (Calladine, 1983).

The idea, taken from Calladine (1983) is to compare maximum stresses due to bending (σ_b) to those due to stretching (σ_s). The stretching stress σ_s is estimated via Equation 5.1,

where T is the uniaxial tension per unit width[1].

$$\sigma_s = \frac{T}{t_t}. \tag{5.1}$$

The bending stress (σ_b) is found from Equation 5.2, where ε is the strain.

$$\sigma_b \approx \frac{E}{1-\nu^2}\varepsilon \approx 12\frac{D\varepsilon}{t_t^3} \tag{5.2}$$

The maximum strain occurs at the outermost fibers ($y = t_t/2$) in the direction of the maximum curvature ($\kappa_1 = \frac{1}{R_1}$) and is estimated by Equation 5.3,

$$|\varepsilon| \leq \frac{t_t}{2}(\frac{1}{R_1} + \frac{\nu}{R_2}), \tag{5.3}$$

the strain for a thin isotropic plate in pure bending (Timoshenko et al., 1959). Per convention, the subscripts $()_{1,2}$ denote the principal directions associated with the maximum (1) and minimum (2) curvatures. R_1 and R_2 are the principal radii of curvature, ν is Poisson's ratio and y is the distance from neutral axis (Figure 2.11). Expression 5.2 is put in terms of the bending rigidity D which has been measured for each material. Note that, because the seal material is a composite, the measured rigidity D is more representative of the bending behavior than a bending rigidity derived from E, the tensile modulus of elasticity (see Appendix A).

In order for bending effects to be significant, $\frac{\sigma_b}{\sigma_s} \gg 1$. The balance, $\sigma_b \approx \sigma_s$ of bending and stretching stresses occurs at a weighted curvature $\kappa_{b=s}$,

$$\underbrace{\frac{1}{R_1} + \frac{\nu}{R_2}}_{\kappa_{b=s}} \sim \frac{Tt_t}{6D}. \tag{5.4}$$

When $\kappa_{b=s} > \frac{Tt_t}{6D}$ bending effects become significant. Lower bending rigidities and/or higher tensions are associated with larger curvatures.

[1]Twist and biaxial tension are not included in this qualitative analysis

In some cases, Equation 5.4 can also be recast in terms of cushion pressure. An upper bound for the seal tension can be estimated from Equation 5.5. When $T_1 = T_2$, Equation 5.5 is equivalent to the Young-Laplace equation for surface tension and is consistent with the membrane interpretation for σ_s. T_1 and T_2 are the (biaxial) tensions in the principal directions. The pressure drop across the surface is given by $\Delta p = p_c - p_{hyd}$, where p_{hyd} is the (spatially varying) hydrodynamic pressure on the surface. p_{hyd} can assume a positive or negative sign depending on the seal shape with $p_{hyd} \leq 0.5\rho U^2$, the stagnation pressure.

$$\Delta p \approx \frac{T_1}{R_1} + \frac{T_2}{R_2} \tag{5.5}$$

In the case of curvature only in R_1 (single curvature), $\frac{T_2}{R_2} \approx 0$, the tension T in Equation 5.4 can be estimated as $T_1 \approx \Delta p \cdot R_1$. For this simplified case,

$$\kappa_{b=s} \sim \frac{\Delta p \cdot R_1}{6D}. \tag{5.6}$$

In conjunction with the information on seal shapes such as shown in Chapter 4, Equation 5.3 can be used to infer how hydrodynamic loads are supported by the seal fabric. If the measured curvature $\kappa_{meas} \geq \kappa_{b=s}$ then the membrane hypothesis does not apply and equations such as 5.5 need to be modified to include interactions between stretching and bending, increasing the complexity of the structural modeling required.

Another useful quantity for determining the complexity of bow seal structural response from the detailed measurements presented in Chapter 4 is the Gaussian curvature, K_G,

$$K_G = \kappa_1 \kappa_2. \tag{5.7}$$

A change in Gaussian curvature indicates that the material has undergone strain at the middle plane[2] to maintain compatibility and reach the present configuration (Calladine,

[2] K_G is not an indicator for all types of strain. In particular, the measure is not sensitive to uniform strains such as due to the hoop stress in a cylinder. In this case, the corner angles of an element of the surface are left unchanged under the action of the hoop stress.

1983) from a base state. $K_G = 0$ indicates that the surface is "developable," that is, it can be unrolled to a flat state (Hilbert and Cohn-Vossen, 1952). The base state of a finger seal, see Figure 2.7, is characterized by $K_G = 0$. Therefore, changes from $K_G = 0$ are indicative of strain. Conversely, in the case of distortions that preserve lengths, such as isometric bending where lines of curvature remain straight, K_G is unchanged. Because of this, $K_G = 0$ is a necessary but insufficient condition for applying the assumption of inextensibility. In a similar application, geologists apply Gaussian curvature analysis (GCA) to 3-dimensional survey data to identify regions of strain (Lisle, 1994).

Applying these measures to centerline profiles and three-dimensional distance maps such as shown in Figure 4.1 three regions of the seal are identified based on their balance of bending and stretching stresses and whether assumptions such as inextensibility are justified. These regions are shown in the centerline profile for the Type-0 (NN) material in Figure 4.4.

Region 1 - Cylinder

The shape of cylindrical region of the seal remains largely unchanged with fluid forcing[3]. In terms of curvature, there is a single principal curvature direction where $\kappa_1 = \dfrac{1}{R_f}$ the seal radius, and $\kappa_2 = 0$. The Gaussian curvature $K_G = 0$, meaning that the surface is developable and can be unfolded.

$$K_G = \kappa_1 \kappa_2 = 0 \tag{5.8}$$

In the cylindrical region, a hoop stress of magnitude $T_1 = p_c R_f$ is present when the seal is inflated. The face of the seal may also support a tangential force when there is contact with the free surface; however because the lower end is free, the tangential force is not otherwise present. Substituting T_1 and material properties into Equation 5.4 and non-dimensionalizing by the curvature of the finger $\kappa_f = \frac{1}{R_f}$, it is found for a typical cushion pressure, $p_c \approx 2000$

[3] An exception to this is found at deep immersions where there is evidence (see Figure 4.5) that the angle of the seal face may change slightly under the action of hydrodynamic forces.

Pa,

$$\begin{aligned}\frac{\kappa_{b=s}}{\kappa_f} &= \frac{p_c R_f^2 t_t}{6D}, \\ &\approx 1 \cdot 10(\text{NN}) > 1, \\ &\approx 1 \cdot 10^2(\text{HN}) \gg 1.\end{aligned} \tag{5.9}$$

For both materials, in the cylindrical region due to the relatively large radius/hoop stress the seal can be modeled as a membrane. As expected, for the same curvature κ_f, the more compliant Type-1 (HN) material is better approximated as a membrane than the Type-0 (NN).

Region 2 - Knuckle or Hinge

Near the intersection of the free surface and the seal, the seal is subject to significant external pressures. Due to their flexibility, bow seals cannot support pressure differences, Δp associated with practical flow velocities, and operate in a post-buckled state[4].

The bending stiffness of the material has a significant effect in the Knuckle region. As seen in Figure 4.4 the knuckle region features significant curvature and is dominated by pressure drag. Once the seal has buckled, the hoop stress of the Cylindrical region is no longer present. A significant downstream tangential force due to shear stress may develop as the downstream wetted length is at a maximum in the knuckle region.

[4]For example, the pressure difference across the seal prior to initial buckling is $\Delta p \approx p_s - p_c \approx p_s$ as the stagnation pressure $p_s = 0.5\rho U^2 \gg p_c$, the cushion pressure. In addition, Δp is larger than the critical buckling pressure p_{crit} by 8 orders of magnitude. To see this, as a reference, consider the critical buckling pressure for a long cylindrical shell (or ring) subject to external pressure. In this case:

$$p_{crit} \approx \frac{E t_t^3}{4(1-\nu^2)R_f^3} \sim \frac{D}{R_f^3}$$

for the n = 2 (critical) circumferential mode (Tovstik and Andrei, 2001). Substituting $\Delta p = 0.5\rho U^2$ for the bow seal at $6m/s$ one finds that $\frac{\Delta p}{p_{crit}} \sim 10^8$(NN) and 10^{10} (HN).

To understand the balance of bending and stretching forces and whether the material may be viewed as inextensible, the magnitude of the curvatures in the Knuckle region are estimated. The maximum curvature is in the streamwise direction,

$$\kappa_1 = \kappa_h = \frac{1}{R_h}, \tag{5.10}$$

where κ_h and the associated R_h are the maximum curvature and radii of the Knuckle fabric along the centerline plane ($Y_h = 0$). R_h can be estimated from seal shapes such as shown in Figures 4.4 and 4.7. κ_2 is the curvature normal to κ_1, which is the curvature of the hinge-line itself. This can be measured or estimated from the geometry. Because of the higher order derivatives required to calculate κ_2 an estimate based on the geometry is employed. Borrowing an approach from Section 5.2, the free surface is treated as a plane acting at an angle β from the horizontal (see Figure 5.2). Assuming that the hinges at this waterplane, the hinge traces a segment of an ellipse with minor-axis ($B_e = R_f$) and major axis length $A_e = \dfrac{R_f}{sin(\theta_{face} - \beta)}$, where θ_{face} is the seal face angle. The curvature of the ellipse is κ_2 and is estimated at centerline ($Y_h = 0$) as,

$$|\kappa_2| \approx \frac{A_e}{B_e^2} \approx \frac{1}{R_f sin(\theta_{face} - \beta)}. \tag{5.11}$$

The maximum Gaussian curvature in the Knuckle region is therefore estimated as

$$K_G = \kappa_1 \kappa_2 \approx \frac{1}{R_h R_f sin(\theta_{face} - \beta)}. \tag{5.12}$$

A similar expression is derived by Das et al. (2007) looking at the post-buckling of a cylinder subject to a point load. Das et al. (2007) found that K_G decays rapidly away from the application of the external force.

The non-zero Gaussian curvature of the Knuckle region suggests that formation of the hinge from the fully inflated seal ($K_G = 0$) creates a small region of double curvature resulting in strains in the Knuckle region. The Gaussian curvature as estimated for a Type-1

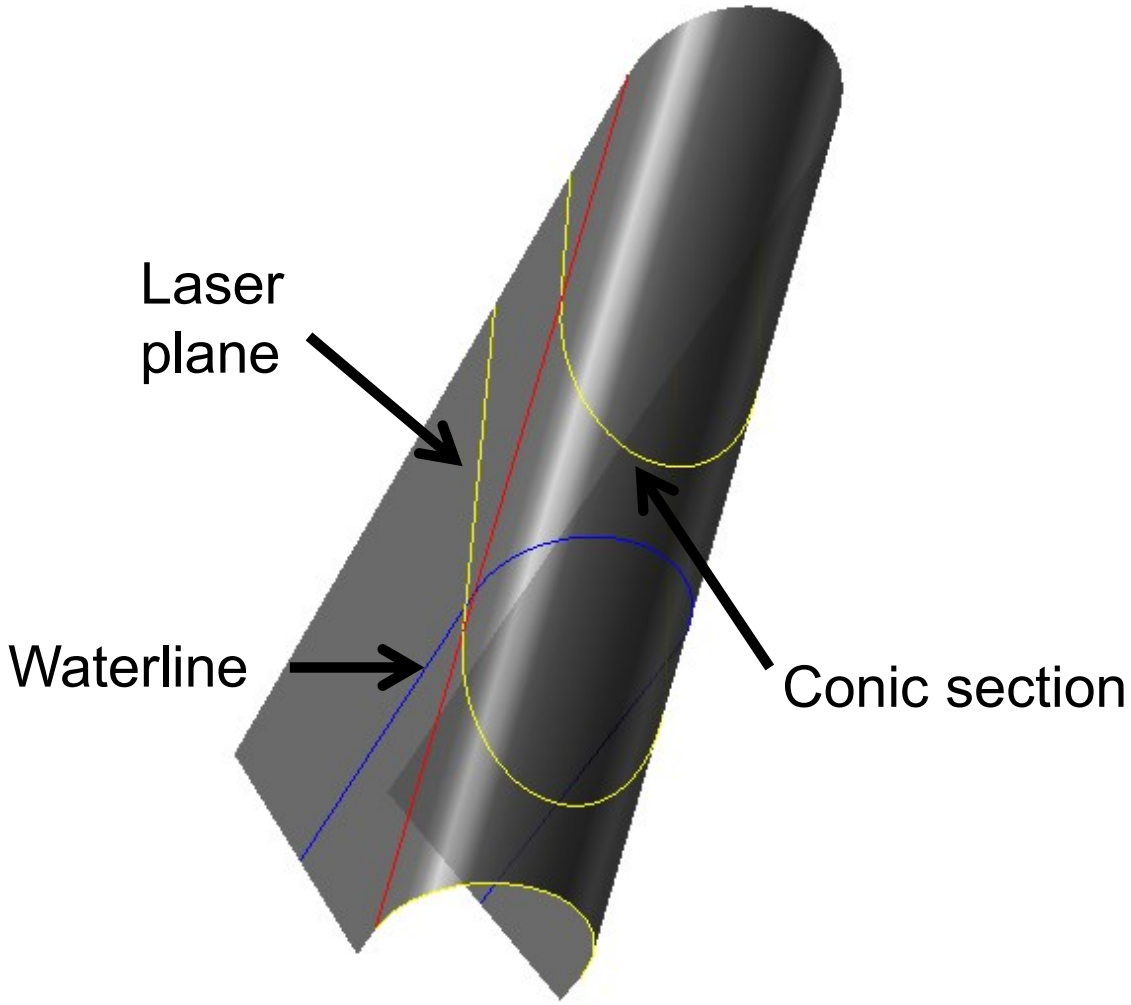

Figure 5.2 Conical sections cut by linescan camera (yellow) and waterplane (blue). Hinge model, shown in Figure 5.5 assumes seal rotates about intersection of waterplane (blue) and seal.

(HN) seal is shown in Figure 4.3, where a region of large K_G can be seen along a nearly elliptical hinge-line. Also note that on average $K_G \approx 0$ in both the Cylindrical and Tail regions. A peculiar feature of the Gaussian curvature estimate is that alternating regions of positive and negative K_G are present along the hinge-line, this may be an example of "twinning" (Das et al., 2007). Das et al. defines "twinning" as the tendency of a cylindrical shell to develop two local maxima in K_G in response to a single point load. More likely it is an artifact of the measurement resolution and would be removed with additional smoothing.

The importance of bending effects in the Knuckle region is confirmed by evaluating

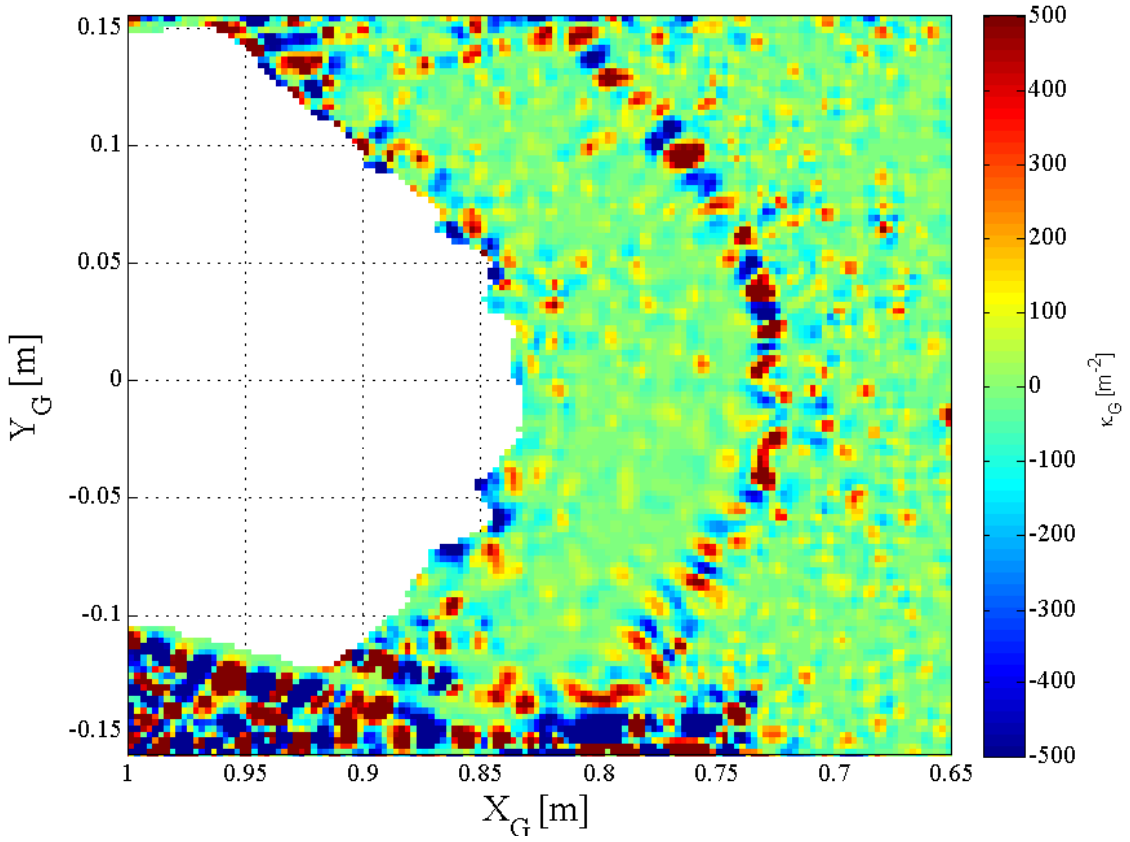

Figure 5.3 Gaussian curvature, $\kappa_G = \kappa_1 \kappa_2$, Type 1 (HN) seal, $U = 6.5$ m/s, $\delta_s = 89$ mm, $p_c = 375$ Pa.

the balance of bending to stretching stresses via Equation 5.6. To apply this equation, the pressure difference, Δp across the seal must be estimated. To do this it is assumed that there exists a point such as ⓐ in Figure 5.1 where $\Delta p \approx p_c$. Substituting typical values of the cushion pressure $p_c = 2000$ Pa and radii of curvature $R_h = 50$ mm for the NN material and $R_h = 15$ mm for the HN (see Figure 4.11), it is found that for both materials $\kappa_{b=s}$ is the same order as $\kappa_h = 1/R_h$, where

$$\begin{aligned} \frac{\kappa_{b=s}}{\kappa_f} &\approx \frac{p_c R_f R_h t_t}{6D}, \\ &\approx 2(\text{NN}) \not\gg \frac{\kappa_h}{\kappa_f}, \\ &\approx 8(\text{HN}) \not\gg \frac{\kappa_h}{\kappa_f}. \end{aligned} \tag{5.13}$$

This indicates that bending rigidity must be included in the Hinge region for both materials. As expected, the size of the region where bending effects dominate is smaller for the HN material than the NN material. It also suggests that under the action of hydrodynamic pressure and shear stress, the equilibrium configuration seeks to balance bending and stretching effects.

Region 3 - Tail

For deep immersions $\frac{\delta_s}{R_f} > 0.2$ a region develops downstream of the knuckle where, on average, the seal shape conforms to the free surface and is characterized by cross-flow buckling and single-curvature. κ_1, where the line of curvature is straight and directed on average in the streamwise direction. The curvature can be estimated from cross-flow profiles such as shown in Figure 4.7, where $\kappa_1 \sim \frac{A}{\lambda^2}$, where A is the fold amplitude and λ is the fold wavelength from the zero-crossing analysis.

Fluid forcing in this region is believed to be dominated by shear stress and hydrostatic/hydrodynamic restoring forces. Flow-induced tension, which decreases with distance from the knuckle or hinge, is lower in the Tail than elsewhere in the seal. This may explain why flagellation is more likely to occur near the trailing edge of the Tail than elsewhere (Morris-Thomas and Steen, 2009).

It is observed from Figure 4.4 that there is little or no pressure drop across the material in the Tail. The balance of bending and membrane forces depends on the streamwise location in the Tail region. At the trailing edge, ⓓ in Figure 5.1 ($X_h = L_w$), similar to the Kutta condition, there is no pressure drop across the material. Flow-induced tension also vanishes at the trailing edge. As a result, when looking at the cross-flow direction (Y_H) bending stresses, σ_b, and compressive forces dominate at the trailing edge and the seal cannot be treated as a membrane.

At the leading edge of Knuckle region, ⓒ in Figure 5.1 ($X_h = 0$), again there is very little pressure drop across the material. However, flow-induced tensions are significant and

enter the cross-flow force balance via Poisson's effect. Because of this, interactions between the streamwise and cross-flow directions should be included.

The Gaussian curvature in the Tail region is very small. This is confirmed in Figure 5.3. Because of this, the surface is developable and the assumption of inextensibility may hold in the Tail region. This assumption is commonly adopted in post-buckling studies[5]. On average the principal direction of curvature is downstream.

Application to modeling

In the Cylindrical region, is was seen that stretching forces dominate and the seal can be adequately described as a membrane. Near the intersection of the seal with the free-surface, the seal hinges and forms a "knuckle." In this small region, which decreases in size with the bending rigidity, the seal features localized areas of double curvature and both bending rigidity and 3-dimensionality are needed to adequately describe the shape. In the Tail region, the material lies parallel to the free-surface and features single curvature and buckling in the cross-flow direction. Analysis of the Tail region is somewhat simplified compared to the

[5]To better understand the suitability of the inextensibility assumption, the stress-strain state in the Tail region is estimated. The compressive stresses at zero-speed are expected to be of order $\sigma_{Y_h} = \frac{F_c}{t_t} \approx \frac{2\sqrt{\rho g D}}{t_t} \sim 10^4$ Pa for both materials, acting in the cross-flow or Y_h direction. This stress corresponds to the critical buckling load, F_c for a "long" beam of bending rigidity, D supported by a foundation of stiffness ρg (further discussed in Section 5.4). Stresses in the X_h direction are expected to be set by the flow-induced tension in the material (see Figure 5.23 for the coordinate system). Past experiments (Ryken, 1978) suggest that a conservative estimate of the viscous shear stress is roughly six times flat plate frictional drag. At the deepest immersions (wetted length $L_w = 0.3048$ m) and velocities tested ($U = 6$ m/s), the flow-induced stress near the leading edge, where it is highest, is estimated as $\sigma_{X_h} \approx \frac{\tau L_w}{t_t} \approx \frac{0.5 c_f(Re)\rho U^2 L_w}{t_t}$, where τ is the shear stress, estimated by a friction line approach with frictional drag coefficient c_f. For a 1/7 power-law turbulent boundary layer ($Re_{Lw} = \frac{U L_w}{\nu_{visc}} \approx 2 \cdot 10^6$), $c_f \approx 0.0039 \cdot 6$, where the 6 is a correction factor, it is found that $\sigma_{X_h} \approx 10^5$(NN) and 10^6(HN). This biaxial stress state corresponds to a maximum strain $\varepsilon_{X_h} = \frac{1}{E_t}(\sigma_{X_h} - \nu\sigma_{Y_h})$. E_t is the tensile modulus (see Appendix A), and ν is the Poisson's ratio, taken to be 0.5 since the coating is nearly incompressible. This results in a ε_{X_h} of order 10^{-3} for the Type-1 (HN) fabric and 10^{-4} for the Type-0 (NN) material supporting the assumption of inextensibility. At higher speeds the assumption of inextensibility, particularly for the HN material may not be warranted. For instance, it was observed that sides of the seals constructed of the HN material developed wrinkles while inflated (Cerda and Mahadevan, 2003) which is an indicator of stretching. The stress state for the sides of the seal is largely uniaxial with the stress magnitude close to the hoop stress $\varepsilon_{hoop} \approx \frac{\sigma_{hoop}}{E_t} = \frac{p_c R_f}{t_t E_t}$ or a strain of order 10^{-2}, which may approached by the HN material at higher velocities.

Knuckle, particularly near the trailing edge, where flow-induced tensions are the lowest and isometric (inextensible) deformations dominate. A simplified analysis of the Tail region is conducted in Section 5.3.

5.2 Seal kinematics

It is hypothesized that a primary effect of hydrodynamic forces acting on the seal fabric is to force all material below the free-surface at zero-speed, to a new location on or above the free-surface (Figure 5.4). In Chapter 4 it was shown that when confined between adjacent fingers and the free-surface, this "excess" material assumes a variety of configurations depending on the test condition. The final post-buckled configuration is expected to be set by a number of factors. Sections 5.3 and 5.4 explore the interplay of hydrodynamic, aerostatic and structural forces on the post-buckled configuration. This section examines the role of seal geometry and local free-surface hydrodynamics in setting the relative quantity of "excess" material due to buckling that must be accommodated. The relative quantity of "excess" material in the system is an important parameter in the post-buckling of finger seals.

Referring to Figure 5.4 the "excess" material is of length $\mathcal{S}$,

$$\mathcal{S} = L_{arc} - L_{bb'}, \tag{5.14}$$

where L_{arc} is the arc length of material below the waterline at zero-speed and $L_{bb'}$ is the projected width of the seal at the local waterline. S can be visualized as a compressive end displacement applied to a segment of material with uncompressed length L_{arc} (see Figure 3.14 for definition). The displacement $\mathcal{S}$ is non-dimensionalized by the arc-length L_{arc} to

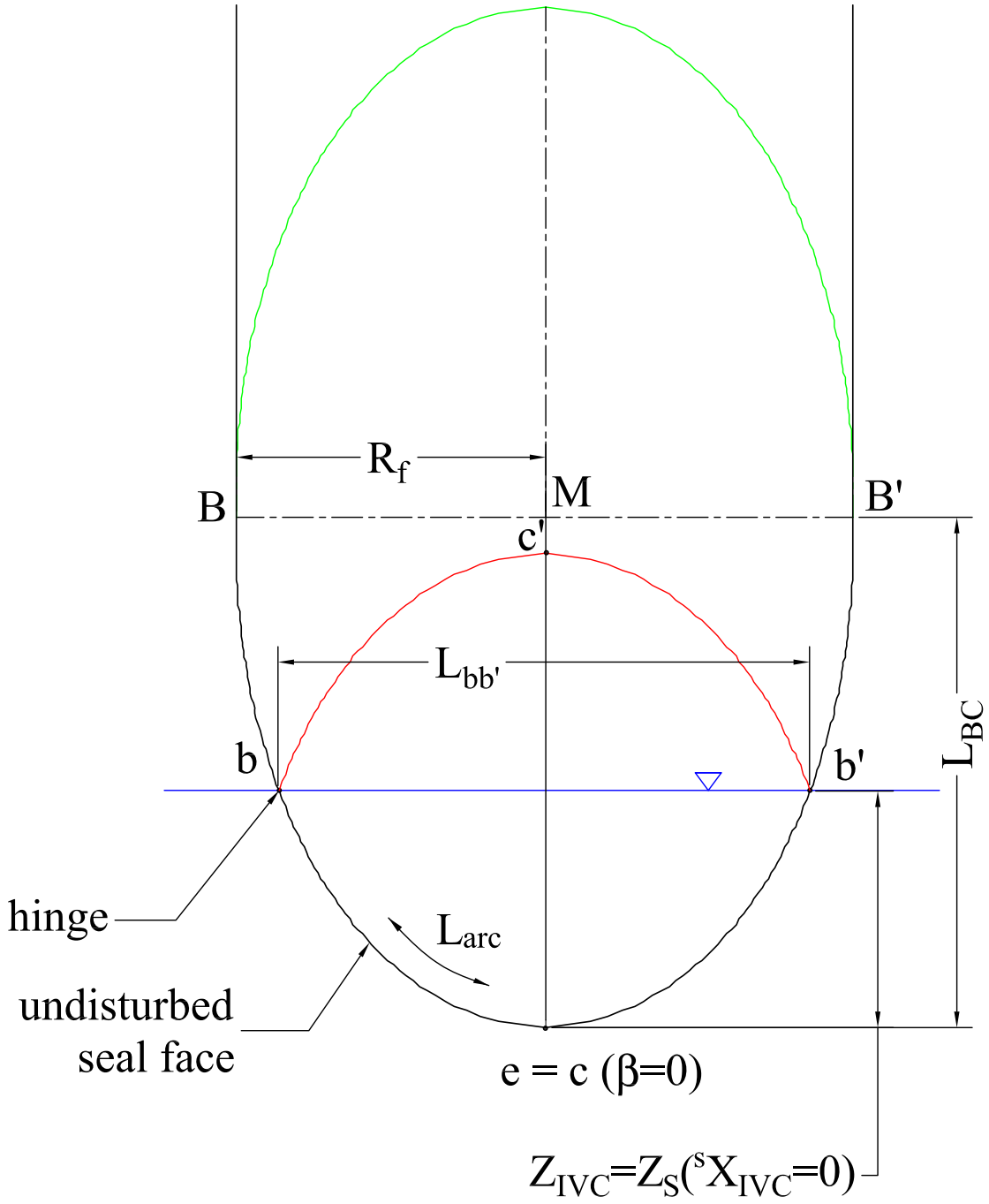

Figure 5.4 Hinge model in laser measurement plane. Model assumes all material below bb' is repositioned on of above the waterline.

form Δ.

$$\Delta = \frac{S}{L_{arc}} = 1 - \frac{L_{bb'}}{L_{arc}}. \tag{5.15}$$

As described in Section 3.4.3 Δ is a relative measure of the material confinement, or "confinement ratio". $\Delta = 0$ corresponds to the seal lying flat against the free-surface in an uncompressed state. Recalling Figure 4.15, $\Delta \to 0$ at the shallowest immersions. $\Delta = 1$ corresponds to the seal making self-contact, a phenomenon observed at deepest immersions tested at the LCC. In Section 5.2.3 it is shown that Δ acts as a constraint on the seal configuration, limiting the amplitude of the mode shape. Details on the calculation of Δ are provided in Section 3.4.3.

The kinematic analysis in this section is inspired by time-averaged centerline profiles of the Type-1 seal material such as shown in Figure 4.7 which suggest that the compliant seal hinges about the local waterplane. In the following analysis the seal material is assumed to be inextensible, such that lengths are preserved. In reality, significant strains would be present during buckling and at very high speeds, however due to stress-focusing (Witten, 2007) strains are likely to be localized a very small region near the "hinge", where there is a non-zero Gaussian curvature and the highest tension. Due to the stiff fabric core (large modulus of elasticity E_r) and the inability of flexible seal fabrics to sustain significant cross-flow compressive loads, the assumption of inextensibility is not unreasonable.

5.2.1 Hinge model

Figures 5.5 and 5.4 show the principal features of the model. The free surface is treated as a plane (AB) intersecting the cylindrical face of the seal at an angle,

$$\alpha = \theta_{face} - \beta, \tag{5.16}$$

with respect to the axis of the cylinder, where θ_{face} is the seal face angle (Figure 2.6) and β is the wave angle with respect to the horizontal, undisturbed free surface. The waterplane passes through point (A) on the inclined face of the seal and through point (B) at the tangent of the seal, describing a length L_{AB} when projected to the center of the seal. Due to the

narrow range of speeds during the large-scale experiments, $\beta = 12 - 16$ deg for the majority of test cases (see Figure 4.7). Consistent with linear theory, β was found independent of cushion pressure. The elevation of the waterplane at point (A) above the seal tip ($Z_S = 0$) is δ_h, which corresponds to the local draft or immersion of the seal. During the large-scale experiments δ_h was set by the test condition, primarily influenced by the angle of the free-surface forming gate and the cushion pressure. Consistent with linear theory, δ_h was found to be linearly dependent on the cushion pressure (see Figure 4.9).

To facilitate comparisons with seals of other sizes, all physical lengths are non-dimensionalized by the seal radius R_f. Lowercase letters generally denote dimensionless quantities. The geometry of the idealized waterplane and seal is described by a series of non-dimensional reference lengths, which are given in Equation 5.17,

$$\begin{aligned} l_{AB} &= csc(\alpha) & l_{AD} &= l_{AB}cos(\beta) \\ l_{BC} &= l_{AD}(tan(\alpha-\beta)+tan(\beta)) & l_{BE} &= l_{AD}(tan(\alpha+\beta)-tan(\beta)). \end{aligned} \tag{5.17}$$

The analysis seeks to understand the relationship between the vertical position of the seal (Z_{IVC}) in the laser measurement plane (bc') and the confinement ratio Δ. As seen in Figure 5.5, the laser measurement (bc') plane cuts the seal vertically, parallel with the action of gravity and normal to the undisturbed free-surface (see Figure 5.4). The laser measurement plane traces a conic section on the undeflected seal face, passing through the point (e) on the seal centerline (see Figure 5.4). Measurements of the seal elevation such as presented in Figure 4.15 are relative to the undeflected state. In Figure 5.5, seal elevation in the measurement plane (Z_{IVC}) is depicted as Z_{be}. As indicated Equation 5.18, Z_{be} and the other reference lengths non-dimensionalized the seal radius R_f.

$$
\begin{aligned}
z_{be} &= \frac{Z_{be}}{R_f} = \frac{Z_{IVC}}{R_f} \\
x_{Ab} &= \frac{X_{Ab}}{R_f} = \frac{X_h}{R_f} \\
x_{Ad} &= \frac{X_{Ad}}{R_f} \\
x_{bc} &= \frac{X_{bc}}{R_f}
\end{aligned}
\tag{5.18}
$$

By design, the laser measurement plane intersects the seal nearly perpendicular to the principal direction of curvature in the Tail region, therefore information on κ_1 and maximum seal slope is captured in the cross-flow profile data[6]. During the experiment, the seal measurement plane (and local coordinate system) was positioned at a fixed distance ${}^sX_{IVC}$ and orientation relative to the coordinate system (X_s, Y_s, Z_s) based at the seal tip (Figure 3.7). As a result, concomitant with a change in the free surface elevation (and immersion δ_h) is a shift in the position of measurement plane relative to the forward pivot A. The horizontal distance between the pivot and the measurement plane is given as x_{Ad}. The measurement plane (BC) intersects the tangent, point B on the hinge line at position, x_{Ad}= l_{AD}.

Both the water plane (AB) and the measurement planes (BC) trace conical sections on the seal face (see Figure 5.2). The minor axis length B_e of the sections for both planes is the seal radius R_f or 1 in dimensionless terms. The major axis length depends on the β, the angle of the waterplane. For the waterplane (AB), the major axis length is l_{AB}, while for the measurement plane it is of length l_{BC}.

[6]On average, for up-down symmetric profiles such as typified by the Type-1 material, the line of curvature for κ_1 is angled $\phi_1 = \beta$ with respect to the horizontal and directed parallel to the seal centerline. However, for stable mode shapes with raised folds, such as seen in Figure 4.13 (d), the principal direction of κ_1 deviates from β. In this case, an upper bound of the principal direction (ϕ_1) is given by $\phi_1 = \alpha - \beta = \theta_{face} - 2\beta$. Therefore, for large wave slopes β or large-amplitude stable folds, the laser as oriented during the large-scale experiment may not capture κ_1 nor the maximum fold slopes A/λ, where A is the fold amplitude and λ. As discussed in Chapter 8, future experiments can remedy this limitation by repositioning the laser or utilizing the full-field measurements provided by the ToF cameras.

The half-width (y_{bc}) of the measurement plane (BC) is given by,

$$y_{bc} = \sqrt{1 - (\frac{x_{bc}}{l_{BC}})^2}. \tag{5.19}$$

Therefore, the total arc length in the measurement plane, l_{arc} is,

$$l_{arc} = 2\int_{l_{BC}-x_{bc}}^{l_{BC}} \sqrt{1 + \left(\frac{dy_{bc}}{dx_{bc}}\right)^2}\, dx_{bc}. \tag{5.20}$$

Depending on the position of the measurement plane relative to the tangent line, x_{bc} may be less than or greater than the major axis length (l_{BC}). If $x_{bc} > l_{BC}$, the straight sides of the seal need to be included in the arc length estimate; hence

$$l_{arc}(x_{bc}) = \begin{cases} 2\int_{l_{BC}-x_{bc}}^{l_{BC}} \sqrt{1 + \frac{(\frac{x_{bc}}{l_{BC}})^2}{l_{BC}^2 + x_{bc}^2}}\, dx_{bc} & x_{bc} \leq l_{BC} \\ 2\int_{l_{BC}-x_{bc}}^{l_{BC}} \sqrt{1 + \frac{(\frac{x_{bc}}{l_{BC}})^2}{l_{BC}^2 + x_{bc}^2}}\, dx_{bc} + 2(x_{bc} - l_{BC}) & x_{bc} > l_{BC}. \end{cases} \tag{5.21}$$

Equation 5.21 can be evaluated analytically via incomplete elliptical integrals or integrated numerically, as is done in the present analysis. In Section 5.2.2 an explicit approximation for l_{arc} is developed.

Similarly, the projected length, $l_{bb'}$ varies depending on the position of the measurement plane with respect to the pivot A. If $x_{Ab} < l_{AB}$, $l_{bb'}$ is the width of an ellipse with major axis length l_{AB} at location $l_{AB} - x_{Ab}$. If $x_{Ab} > l_{AB}$ the projected length is simply the seal diameter $2R_f$ or $l_{bb'} = 2$ (Equation 5.22); hence

$$l_{bb'}(x_{Ab}) = \begin{cases} 2(1 - \sqrt{1 - (1 - \frac{x_{Ab}}{l_{AB}})^2}) & x_{Ab} \leq l_{AB} \\ 2 & x_{Ab} > l_{AB}. \end{cases} \tag{5.22}$$

Finally, the effective transverse displacement $\mathcal{S}$ is given by the difference between the arc-length l_{arc} and the projected distance $l_{bb'}$. The displacement $\mathcal{S}$ is non-dimensionalized

by the uncompressed length l_{arc} to form the confinement ratio Δ (Equation 5.23).

Influence of seal elevation (Z_{IVC}) on confinement ratio Δ To evaluate the influence of seal elevation $Z_{IVC} = z_{be}R_f$, on the confinement ratio Δ,

$$\Delta(z_{be}) = 1 - \frac{l_{bb'}(z_{be})}{l_{arc}(z_{be})}, \tag{5.23}$$

Equations 5.21 for the arc-length l_{arc} and Equation 5.22 for the projected width are recast in terms of z_{be}. This is accomplished via the relations in Equation 5.24,

$$\begin{aligned} c_h &= \frac{l_{BC}}{l_{AD}} \quad d_h = \frac{l_{AB}}{l_{AD}}, \\ c_z &= \frac{l_{BC}}{l_{BE}} \quad d_z = \frac{l_{AB}}{l_{BE}}. \end{aligned} \tag{5.24}$$

Making the change of variable,

$$x_{bc} = c_z z_{be} \tag{5.25}$$

$$x_{Ab} = d_z z_{be}, \tag{5.26}$$

the projected length $l_{bb'}(z_{be})$ is

$$l_{bb'}(z_{be}) = \begin{cases} 2(1 - \sqrt{1 - (1 - d_z z_{be})^2}) & z_{be} \leq \frac{l_{AB}}{d_z} \\ 2 & z_{be} > \frac{l_{AB}}{d_z}. \end{cases}$$

The integral for the arc-length becomes:

$$l_{arc}(z_{be}) = \begin{cases} 2\int_{l_{BC}/c_z - z_{be}}^{l_{BC}/c_z} c_z \sqrt{1 + \frac{(\frac{c_z z_{be}}{l_{BC}})^2}{l_{BC}^2 + c_z z_{be}^2}} dz_{be} & z_{be} \leq l_{BC}/c_z \\ 2\int_{l_{BC}/c_z - z_{be}}^{l_{BC}/c_z} c_z \sqrt{1 + \frac{(\frac{c_z z_{be}}{l_{BC}})^2}{l_{BC}^2 + c_z z_{be}^2}} dz_{be} + 2(c_z z_{be} - l_{BC}) & z_{be} > l_{BC}/c_z. \end{cases} \tag{5.27}$$

From $Z_{be} = z_{be}R_f = Z_{IVC}$ it is straightforward to calculate profile coordinates in global coordinates $Z_S = Z_{IVC} +^s X_{IVC} \cdot tan(\theta_{face})$ and $X_S = -^s X_{IVC}$ (see Figure 5.5). The superscript ^{s} refers to the destination reference frame for the transformation, while the subscript refers to the source reference system.

Influence of streamwise position (x_{Ad}) on confinement ratio Δ Using the same procedure as for the vertical position Z_{IVC}, it is straightforward to the estimate the influence of streamwise x_{Ad} position on Δ. To do this, the following substitutions are made into Equations 5.21 for the arc-length l_{arc} and Equation 5.22 for the projected width.

$$x_{bc} = c_h x_{Ad} \tag{5.28}$$

$$x_{Ab} = d_h x_{Ad} \tag{5.29}$$

Likewise, the confinement as a function of inclined distance from the hinge can be estimated. This distance is referred to $X_h = x_{Ab}R_f$ in Figure 3.9. x_{Ab} only needs to be put in terms x_{bc} for use in the terms arc-length integral (Equation 5.21) and can be used directly in Equation 5.22

$$x_{bc} = c_h cos(\beta) x_{Ab}. \tag{5.30}$$

5.2.2 Simplifications to hinge model

Given that Equation 5.21 requires numerical integration or evaluation of an elliptical integral, it is advantageous to find an approximate expression for the confinement ratio (Δ) as a function of mean seal height (Z_{IVC}). Two explicit approximations to Equation 5.21 are presented. The first maps a segment of the conical section (such as shown Figure 5.6) to part of a circular arc (Figure 5.13).

Once equivalent radius (R_e) and parametric angles (ϕ_e) of the circular arc are estimated

from the geometry, the arc-length is then given by

$$l_{arc}(x_{bc}) \approx R_e(x_{bc})\phi_e(x_{bc}). \tag{5.31}$$

The parametric angle ϕ_e is found from Equation 5.32.

$$\phi_e(x_{bc}) = cos^{-1}(1 - x_{bc}) \tag{5.32}$$

The effective radius R_e, Equation 5.35, is estimated from the parametric angle ϕ_e and chord length (C_r) which is found from the geometry as

$$\begin{aligned} C_r &= \sqrt{(x_{bc})^2 + l_{BC}^2 sin^2(\phi(x_{bc}))} \\ &= \sqrt{{x_{bc}}^2 + l_{BC}^2(1 - (1 - x_{bc})^2)}. \end{aligned} \tag{5.33}$$

Further simplification of the radius R_e can be made by the substitution,

$$sin(\phi_e/2) = \sqrt{\frac{x_{bc}}{2}}. \tag{5.34}$$

$$R_e(x_{bc}) = \frac{C_r}{sin(\phi_e/2)} \tag{5.35}$$

The resulting expression for the arc-length l_{arc} is

$$l_{arc}(x_{bc}) = \sqrt{2x_{bc} + 2\frac{l_{BC}^2}{x_{bc}}(1 - (1 - x_{bc})^2)}[cos^{-1}(1 - l_{BC})]. \tag{5.36}$$

With an approximation for the arc-length, an explicit equation for the confinement $\Delta(x_{bc})$

can be assembled:

$$\Delta(x_{bc}) = \begin{cases} 1 - \frac{\sqrt{2}(1-\sqrt{1-(1-\frac{l_{AB}}{l_{BC}}x_{bc})^2})[cos^{-1}(1-x_{BC})]}{\sqrt{x_{bc}+\frac{l_{BC}^2}{x_{bc}}(1-(1-x_{bc})^2)}} & x_{bc} \leq l_{BC} \\ 1 - \frac{\sqrt{2}[cos^{-1}(1-l_{BC})]}{\sqrt{l_{BC}+l_{BC}(1-(1-l_{BC})^2)+2(x_{bc}-l_{BC})}}. & x_{bc} > l_{BC} \end{cases} \tag{5.37}$$

Expressions for the confinement in terms of measurement plane coordinates X_{Ad}, $X_h = x_{Ab}R_f$ or $Z_{IVC} = z_{be}R_f$, can be created through a change of variables for x_{bc} and x_{Ab}. The coefficients required for the conversions are contained in Equation 5.24. For example, to find Δ in terms of streamwise position x_{Ad}, the substitutions $x_{bc} = c_h x_{Ad}$ and $x_{Ab} = d_h x_{Ad}$ are made, yielding:

$$\Delta(x_{Ad}) = \begin{cases} 1 - \frac{\sqrt{2}(1-\sqrt{1-(1-\frac{l_{AB}}{l_{BC}}c_h x_{Ad})^2})[cos^{-1}(1-c_h x_{Ad})]}{\sqrt{c_h x_{Ad}+\frac{l_{BC}^2}{c_h x_{Ad}}(1-(1-c_h x_{Ad})^2)}} & x_{Ad} \leq \frac{l_{BC}}{c_h}, \\ 1 - \frac{\sqrt{2}cos^{-1}(1-l_{BC})}{\sqrt{l_{BC}+l_{BC}(1-(1-l_{BC})^2)+2(c_h x_{Ad}-l_{BC})}} & x_{Ad} > \frac{l_{BC}}{c_h}. \end{cases} \tag{5.38}$$

A comparison of the exact Δ and the arc-length approximation is provided in Figure 5.6. The location of the seal tangent is also indicated. A linear approximation, based on a first-order approximation for the perimeter of an ellipse at the tangent $l_{arc}(l_{bc}) \approx \frac{\pi}{2}(1+l_{bc})$ is also shown.

$$\Delta(x_{Ad}) \approx \frac{c_h}{l_{BC}} \left(\frac{l_{BC}+1-\frac{4}{\pi}}{l_{BC}+1} \right) x_{Ad} \tag{5.39}$$

$$\Delta(z_{be}) \approx \frac{c_z}{l_{BC}} \left(\frac{l_{BC}+1-\frac{4}{\pi}}{l_{BC}+1} \right) z_{be} \tag{5.40}$$

$$\Delta(x_{Ab}) \approx \frac{c_h}{l_{BC}} \left(\frac{l_{BC}+1-\frac{4}{\pi}}{l_{BC}+1} \right) cos(\beta) x_{Ab} \tag{5.41}$$

For wave angles (β) greater than 15 deg, the error of the linear approximation is less than 10%. The error of the arc-length approximation (Equation 5.37) is less than 1%. Evaluated

at $\beta = 15$ degrees, the linear approximation yields,

$$\Delta \approx 0.2463 \cdot \frac{Z_{IVC}}{R_f} \tag{5.42}$$

$$\approx 0.2198 \cdot \frac{X_h}{R_f} \tag{5.43}$$

$$\approx 0.2275 \cdot x_{Ad}. \tag{5.44}$$

These relationships will be used extensively in later sections. For wave angles such as observed during the large-scale experiments, where $\beta \approx 15$ deg it is observed that $\Delta \sim x_{Ad} \sim z_{be}$. Ignoring wave rise,

$$x_{Ad} \approx \frac{\delta_s}{tan(\theta_{face})} - {}^{s}X_{IVC}, \tag{5.45}$$

where δ_s is the seal immersion (see Figure 3.9). Therefore changes in immersion δ_s can be interpreted as shift a downstream x_{Ad} of the hinge.

5.2.3 Upper bound for fold amplitude

The fit also suggests an upper bound for the amplitude of the fold. An inextensible strip of length l_{arc} fixed at $\pm l_{bb'}/2$ is limited to a maximum amplitude A, where

$$A^2 \leq (\frac{l_{arc}}{2})^2 - (\frac{l_{bb'}}{2})^2 \tag{5.46}$$

$$\frac{l_{bb'}}{l_{arc}} = 1 - \Delta \tag{5.47}$$

leading to Equation 5.48 and equivalently Equation 5.49 in terms of the confinement ratio Δ.

$$\left| \frac{A}{l_{arc}} \right| \leq \frac{1}{2} \sqrt{1 - (\frac{l_{bb'}}{l_{arc}})^2} \tag{5.48}$$

$$\left|\frac{A}{l_{arc}}\right| \leq \sqrt{\frac{\Delta}{2} - (\frac{\Delta}{2})^2} \tag{5.49}$$

At very small confinements $\frac{A}{l_{arc}} \sim \sqrt{\Delta}$. At $\Delta = 1$, the fabric contacts itself and reaches a maximum amplitude of 0.5. Equation 5.49 can also be used to estimate bounds on the fold amplitude as a function of position relative to the forward hinge. In Section 6.1 a slightly different confinement-amplitude relationship will be derived. Nonetheless, Equation 5.49 provides a good check on the feasibility of a given seal configuration.

5.2.4 Results and discussion of hinge model

Confinement ratio

The confinement ratio Δ based on the nonlinear Equation 5.23 for $\beta = 0$ and $\beta = 15$ deg is plotted along with the measured Δ in Figure 4.15. The agreement between the Type-1 material and the hinge model is quite promising for $\beta = 15$ deg, a typical wave angle from the experiments (see Figure 4.11). This suggests that the Type-1 fabric hinges about the local waterplane. Similar hinge regions have been reported by other researchers studying large deformations of shells (Das et al., 2007). This suggests that outside the small hinge region the seal undergos largely isometric bending. For the Type-0 material, there is some disagreement between the hinge model and the data. However, a similar trend of confinement increasing with immersion is observed. The seals constructed of the stiff appear to behave at a lower wave angle β than the Type-1 seals. There are a number potential sources of this discrepancy that require further investigation, as follows.

Potential sources of error, Type-0 material confinement ratio

1. Bias in the mean seal elevation as calculated by the zero-crossing analysis (see Figure 3.15) may be responsible for some of the differences. To see the source of this bias,

consider the mean of an idealized sinusoidal buckling profile, $h(Y_h) = Asin(\frac{n\pi Y_S}{L_{Y_h}})$, where n is the mode number and A is an amplitude. The effective hinge is assumed to be at $Z_{h_{hinge}} = 0$, however the mean derived from the buckling profile may contain a vertical shift for odd mode number n. This shift is estimated in Equation 5.50.

$$|Z_{h_{hinge}}|_{bias} \approx \int_0^{L_{Ys}} Asin(\frac{n\pi y}{L_{h_s}})dy \approx A\frac{1-(-1)^n}{n\pi} \tag{5.50}$$

$|Z_{h_{hinge}}|_{bias} > 0$ for $n = 2m-1$ and $|Z_{S_{hinge}}|_{bias} = 0$ otherwise, where m is an integer. Odd mode numbers are favored for both seal types (see Figure 4.16), leading to a nonzero bias; due to higher mode numbers($n \gg 1$) and smaller amplitudes, the bias is expected to be less significant for the Type-1 (HN) material. Because of the low mode numbers and large amplitudes typical of the Type-0 (NN) response, the bias may be significant.

2. Slack seal sides. The model assumes that all excess seal material is confined to the measurement plane. In reality, because the NN material can support a compressive load through buckling, some of the excess material is taken up by bowing (buckling) of the seal sides. This effect would tend to decrease the Δ for a given seal elevation, shifting the NN data further above the $\beta = 15$ deg hinge model.

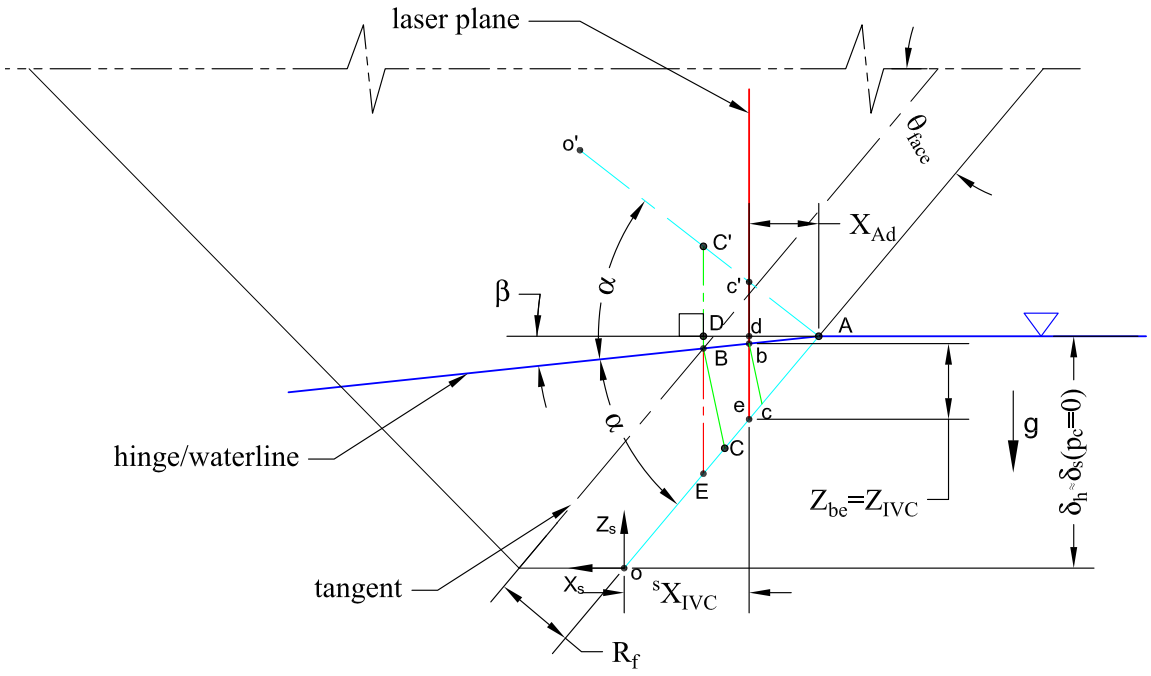

(a) Profile

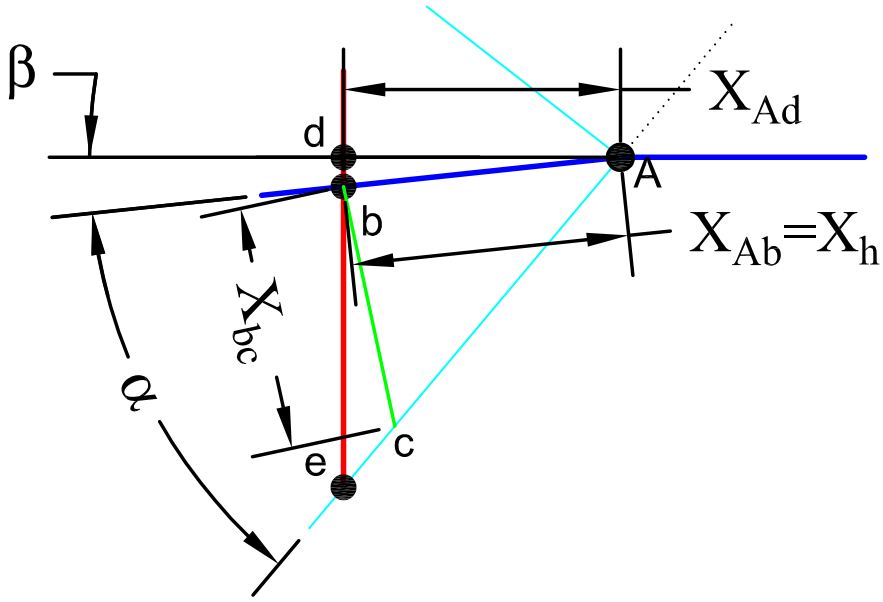

(b) Detail

Figure 5.5 Profile of Hinge model, β is the angle of the local waterplane with respect to the horizontal. See Figure 5.23 for additional details on δ_h and the hinge-based (X_h, Y_h, Z_h) reference frame. Other coordinate system information is provided in Figure 3.7.

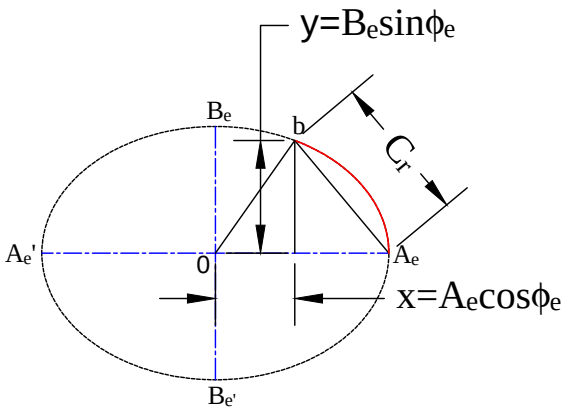

Figure 5.6 Circular-arc method for approximating incomplete elliptical integral.

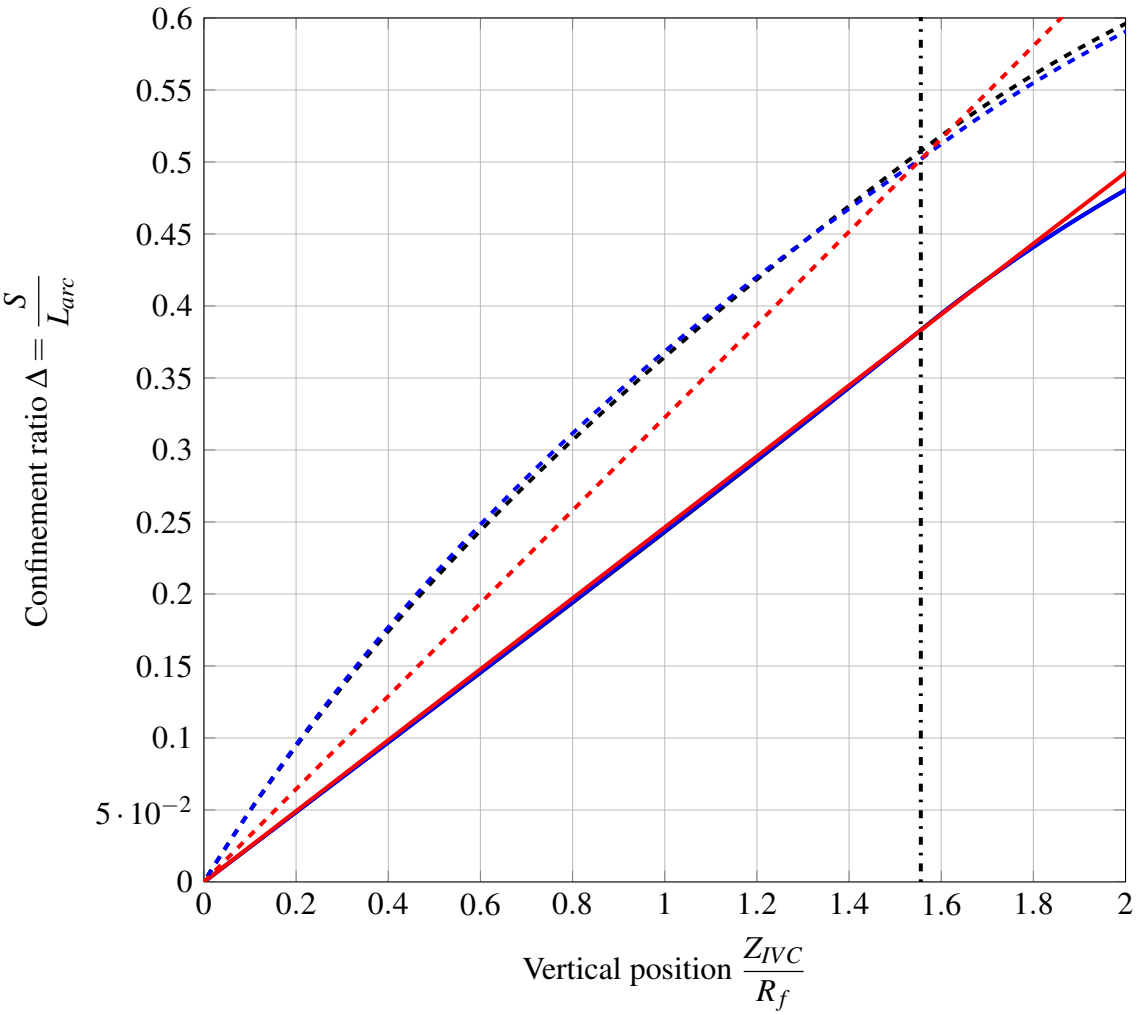

Figure 5.7 Change in seal compression (Δ) with immersion (Z_s) as estimated by hinge model. Linear and arc-length approximations to the exact elliptical integrals are shown. ——, exact $\beta = 15$ deg; ——, arc-length approximation $\beta = 15$ deg; ——, linear approximation $\beta = 15$ deg. - - -, exact $\beta = 0$ deg; - - -, arc-length approximation $\beta = 0$ deg; - - -, linear approximation $\beta = 0$ deg. Integral simplifies for $Z_s/R_f > L_{BE}/R_f$ (·- - -·).

5.3 Geometrically-nonlinear buckling on a foundation

The large-scale experimental data presented in Figure 4.24 indicates that as seal confinement Δ increases, material slope $dh/dx \sim A/\lambda$ increases as well, appearing to following the scaling relationship $A/\lambda \sim \Delta^{0.5}$. Due to the relatively large confinement ratios (Δ) at deep immersions, seal cross-flow response is characterized by large rotations ($\theta \sim \Delta^{0.5} - ..$), where θ is the tangent angle. Because of this, the approximation for the curvature $d\theta/ds \approx dh^2/dx^2$, adopted in classical Euler-Bernoulli beam theory breaks down and an approach which accounts for geometric nonlinearities must be adopted.

The nonlinear approach taken is to model the material as an elastica (see Timoshenko (1961) and Frisch-Fay (1962)), where, as shown in Figure 5.8a beam shape is described parametrically as a function of arc length s, and rotation θ. The model, depicted in Figure 5.8a, treats cross-flow dX_h strips of the Tail region as 2-dimensional beams on an elastic foundation (BoF), a canonical problem of elastic stability (Hetényi, 1979), which retains many of the essential features of the problem in the Tail region. The model is most suited to deep immersions of the compliant Type-1 (HN) material, where the ToF data indicates that cross-flow curvature $\kappa_{Y_h} \approx 0$. In this regime, the mean surface of the seal appears to describe a plane which conforms to the free-surface (see Figure 4.7). About this plane, cross-flow profiles indicate that the Type-1 material assumes a variety of post-buckled configurations. The model may have some applicability to shallower immersions, however for shallow immersions it is suspected (based on video) that there may be upstream influence due to the curved Knuckle. Extensions of the model to 3-dimensions and other modifications to more realistically capture seal behavior are discussed in the Future Work (Chapter 8).

A full derivation and solution of the nonlinear equations governing the buckling of a nonlinear beam on a foundation is outside the scope of this effort. The goal is to develop a framework within which to view seal conformation. The reader is referred to Diamant and Witten (2011) for the nonlinear problem and Hetényi (1979) or Timoshenko (1961) for the linear problem.

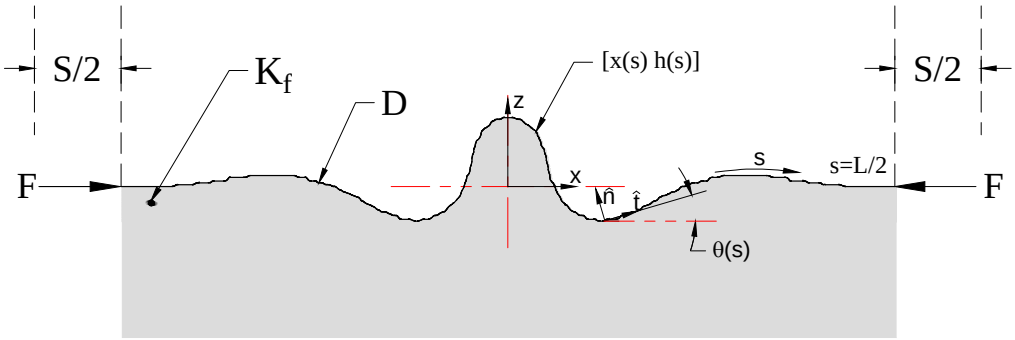

(a) Nonlinear floating elastica model.

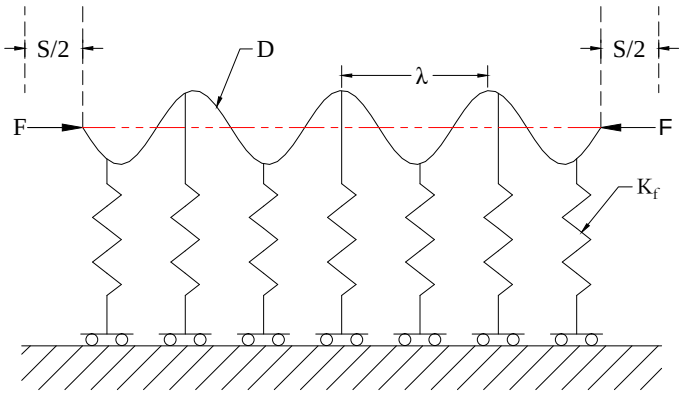

(b) Linearized model, beam on an elastic foundation.

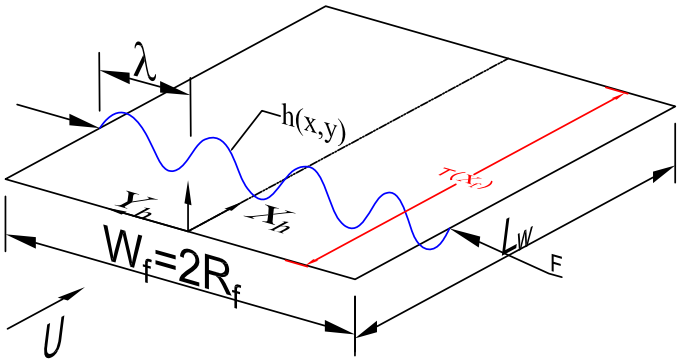

(c) 3-dimensional coordinate system in Tail region (flow is in the $+X_h$ direction).

Figure 5.8 Linear and geometrically-nonlinear seal buckling models in the Tail region.

For reference, the relationship between the cartesian and parametric representations of beam shape is given in Figure 5.9. Following the convention of Diamant and Witten (2011)

the origin is located mid-span: x extending from $-L/2$ to $L/2$. x corresponds to the global cross-flow direction Y_h (see Figure 3.9 and Figure 5.8a for the coordinate system)[7]. The cartesian displacement of the beam is related to the elastica description by the differential equations,

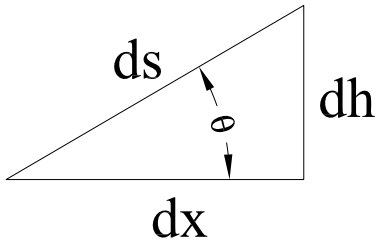

Figure 5.9 Conversion between parametric/elastica (s,θ) and cartesian (x,h) representation

$$\dot{x}(s) = cos(\theta), \tag{5.51}$$

$$\dot{h}(s) = sin(\theta), \tag{5.52}$$

where the dot refers to a derivative with respect to arc-length s, and h is the vertical displacement from the mean seal position. The curvature of the beam κ is given by

$$\kappa(s) = \dot{\theta}(s). \tag{5.53}$$

Per Euler-Bernoulli beam theory $\dot{\theta}(s)$ is related to bending moment by $M = D\dot{\theta}(s)$. To derive the governing equations, a functional representing the total work on the system is formed. The functional is shown in Equation 5.56, where Π_D is the bending or strain energy, given by,

$$\Pi_D = \frac{1}{2} D \int_L \dot{\theta}(s)^2 ds. \tag{5.54}$$

Π_K is the foundation energy. For the case of a hydrostatic foundation $K_f = \rho g$, where

[7] In later sections, the origin is placed at one end of the profiles, with x varying from 0 to L

the pressure varies with height h, Π_K represents the change in potential energy and is given by,

$$\Pi_K = \frac{1}{2} K_f \int_L h(s)^2 cos(\theta) ds. \tag{5.55}$$

W_c is the work performed by the compressive force F in displacing the ends of the beam a total distance $\mathcal{S}$, i.e. $W_c = F\mathcal{S}$, where $S = L - \int_L (cos(\theta) ds) = \int_L (1 - cos(\theta)) ds$.

$$\begin{aligned} \Pi_T(\theta, \dot{\theta}, h, \dot{h}) &= \Pi_D + \Pi_K - W_c - Q(s)(\dot{h}(s) - sin(\theta(s)) \\ &= \int_L \Big[\underbrace{\frac{1}{2} D \dot{\theta}(s)^2}_{\Pi_D} + \underbrace{\frac{1}{2} K_f h(s)^2 cos(\theta(s))}_{\Pi_K} \\ &\quad - \underbrace{F(1 - cos(\theta(s)))}_{W_c} - \underbrace{Q(s)(\dot{h}(s) - sin(\theta(s)))}_{\text{Constraint } \dot{h}(s) = sin(\theta)} \Big] ds \end{aligned} \tag{5.56}$$

$Q(s)$ is a Lagrange multiplier used to impose the local constraint $\dot{h}(s) = sin(\theta)$. After substituting each of these terms into $\Pi_T(\theta, \dot{\theta}, h, \dot{h})$, all lengths are non-dimensionalized by the natural buckling length L_n, where

$$L_n = (\frac{D}{K})^{0.25}. \tag{5.57}$$

The non-dimensional system size η is given by

$$\eta = \frac{L}{L_n}. \tag{5.58}$$

The compressive force F is non-dimensionalized by $(DK_f)^{0.5}$ to form

$$f^* = \frac{F}{(DK_f)^{0.5}}. \tag{5.59}$$

The natural buckling length L_n and the associated system size η feature prominently in later

sections.

The term within the integral is considered a Lagrangian (Equation 5.61), where h^* and s^*, and f^* are now non-dimensional.

$$\begin{aligned}\Pi_T(\theta,\dot{\theta^*},h^*,\dot{h^*}) &= \int_\eta \frac{1}{2}\dot{\theta}^*(s^*)^2+\frac{1}{2}h^*(s^*)^2 cos(\theta(s))-f^*(1-cos(\theta(s^*)) \\ &\quad -Q(s^*)(\dot{h}(s^*)-sin(\theta(s^*)))ds^*\end{aligned} \tag{5.60}$$

(5.61)

To minimize Π_T, Diamant and Witten (2011) employ Hamilton's Principle to transform the Lagrangian Π_T into a Hamiltonian and to ultimately derive a system of equations for the momenta. From these, after eliminating $Q(s)$ from the system of equations and differentiating to replace h with $\dot{h}(s)$, such that $\dot{h}(s) = sin(\theta)$ can be substituted, a single nonlinear differential equation describing the BoF is found

$$\dddot{\theta} + (3/2)\dot{\theta}^2 + f\ddot{\theta} + sin(\theta) = 0. \tag{5.62}$$

where the stars * have been dropped. In the case where $K_f = 0$, a simpler expression (Wang, 1984) (Equation 5.63) is obtained which closely resembles the governing equation for a pendulum without the small angle approximation. In Equation 5.63, lengths are non-dimensionalized by the geometric length L, and the load F by D/L^2.

$$\ddot{\theta} + \frac{FL^2}{D}sin(\theta) = 0 \tag{5.63}$$

Equation 5.63 represents the limiting case where the $\eta \to 0$, and may be used to estimate the shape of a fold that has completely detached from the free surface.

5.3.1 Solving the nonlinear equation

A number of numerical and analytical approaches have been applied to understand the behavior of nonlinear differential equations similar to Equation 5.62. In general, for realistic boundary conditions, the approach is to use standard techniques for solving boundary value problems such as implemented in Matlab® with the collocation solver bvp5c (or to use a shooting method with a Runge-Kutta integrator such as ODE45). Various perturbation (Hunt et al., 1989) and analytic continuation (Rivetti and Neukirch, 2014) methods have also been applied to understand the behavior near the critical buckling load. In the present study, the non-linear foundation-less model (Equation 5.63) is solved using numerical techniques. The non-linear model in the presence of a linear foundation (Equation 5.62) is examined in light of a recent analytical solution proposed by Diamant and Witten (2011) for an infinite beam. The more general problem of a finite-width elastica supported by a foundation is studied in a linearized form in Section 5.4.

Non-linear model without a foundation

Images of the stiff Type-0 (NN) seals operating at deep immersions, such as shown in Figure 4.14 (g), suggest that in many cases the free-surface has partially separated from the trailing edge of the seal. Accompanying this "blistering" (Wagner and Vella, 2011) is significant air leakage through the raised central fold. In this blistered condition, the foundation stiffness is estimated as $K_f \approx 0$.

To model the post-buckled seal shape for $K_f = 0$, the nonlinear differential equation given in Equation 5.63 is solved subject to clamped boundary conditions. $\theta(0) = \theta(L) = \frac{d\theta}{ds}(L) = 0$. Justification for this choice of boundary conditions is provided in Section 5.4.1, which shows that due to the tight radius of curvature near the vertical sides of the seals, profiles such as shown in Figure 4.13 are effectively clamped.

Similar to Wang (1984), symmetry is used to model only half the elastica. To solve these equations, they are written as a system of first-order differential equations for $H = [\theta, \dot{\theta}, x, h]$

and numerically integrated in Matlab® using the ODE45 solver. Because the ODE45 solver is meant for initial value problems, a shooting method is used to iteratively satisfy the boundary conditions. The shooting parameter used is $\frac{d\theta}{ds}(0)$ or the moment at center of the beam.

Results and comparison A comparison of the clamped elastica model without a foundation and the central fold of Figure 4.14 (g) is shown in Figure 5.10. The experimental data is windowed to contain only the central fold. The effective end-displacement ($\mathcal{S}$) is calculated based on this window. Despite considerable uncertainty owing to selection of appropriate boundary conditions, window size and an unknown pressures acting on the lower face, there is favorable agreement between the predicted and measured shape. The amplitude of the central fold is captured well and is set by the confinement Δ. The measured profile seems to have lower curvature than the prediction. Consistent with Wang (1984), the load f that the beam can support post-buckling is found to increase with end-displacement $\mathcal{S}$. The relevant length scale for this finite-width problem is the geometric length L.

Non-linear model with linear foundation, infinite plate solution

Images of the Type-1 (HN) material such as shown in Figure 4.6a indicate that the free-surface remains attached to the compliant HN seal under most conditions. In order to begin to understand the behavior of the geometrically-nonlinear BoF a recently proposed solution to Equation 5.62 proposed by Diamant and Witten (2011) that satisfies $h \to 0$ as $x \to \pm\infty$ is examined. It is hypothesized, that the infinite plate ($\eta \to \infty$) solution may support comparisons to large but finite system sizes η. The infinite plate solution, given in Equation 5.64, takes a form similar to a solitary wave, where $k = \frac{(2+f)^{1/2}}{2}$, $c = \frac{(2-f)^{1/2}}{2}$ and ϕ is an arbitrary phase.

$$\theta(s) = -4tan^{-1}(\frac{csin(k(s+\phi)}{kcosh(cs)}) \tag{5.64}$$

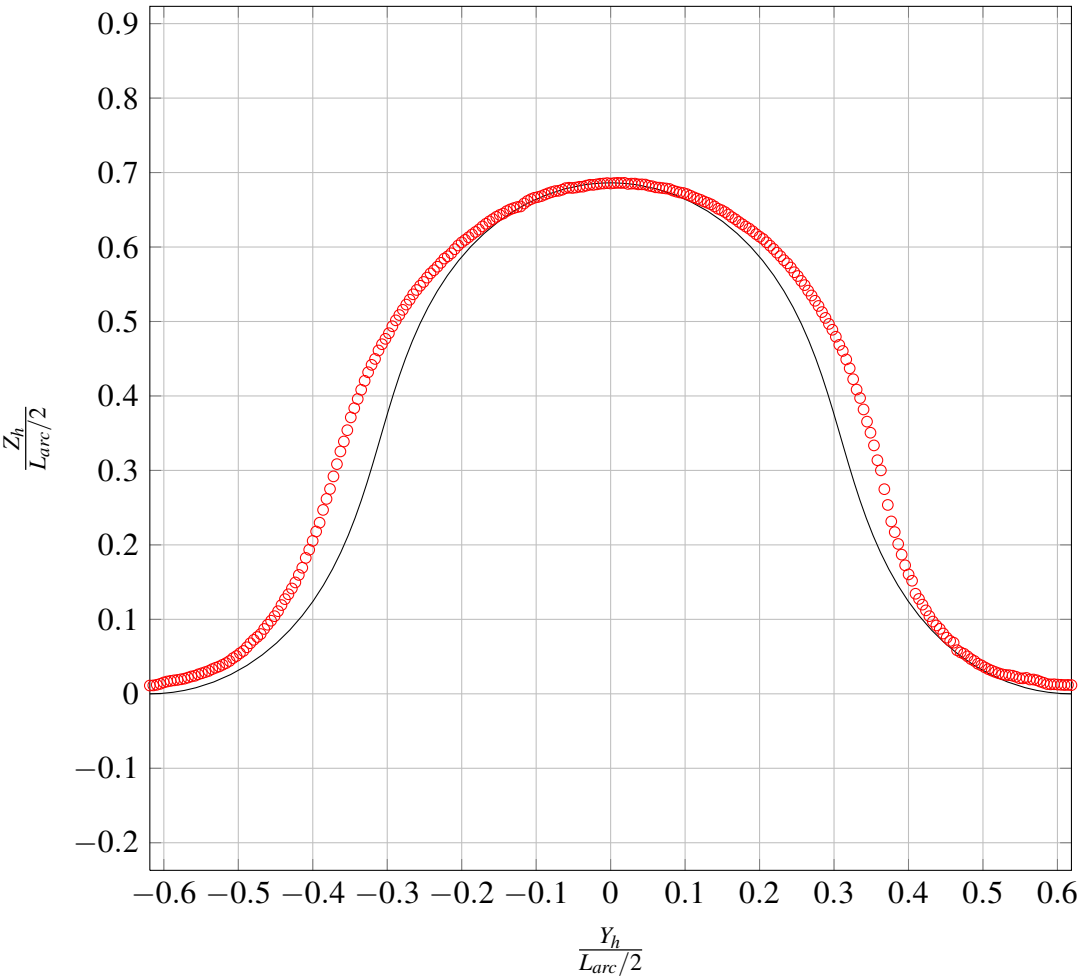

Figure 5.10 Comparison of foundation-less elastica model (——) with measured seal profile (○), $\Delta = 0.38$, Type-0 (NN). Measured profile is the same as shown in Figure 4.14 (g). Fabric mass is not included. Note that applied $\Delta = 0.38$ differs from that listed in Figure 4.14; this is due to the use of a narrower width for comparisons with the foundation-less model.

In contrast to the elastica without a foundation discussed in the previous section, the compressive load f that the beam can support *decreases* with end-displacement,

$$f = 2 - \frac{\Delta_n^2}{16}, \tag{5.65}$$

where Δ_n is the end-displacement $\mathcal{S}$ non-dimensionalized by the natural buckling length L_n. As a result, under dead loading of magnitude $\approx f$ the end-displacement will continue to increase until self-contact.

Results and discussion Examples of sample solutions per Equation 5.64 are shown in Figure 5.11. As f approaches the critical buckling load $f_c = 2$ the solution becomes periodic taking the wavelength of the linear buckling solution $\lambda = 2\pi L_n$. Qualitatively, the family of solutions represented by Equation 5.64 and depicted in Figure 5.11 for an infinite plate resemble measured buckling profiles of the Type-1 material (see Figure 4.25). To see whether this comparison holds more closely, a method for estimating the natural buckling length $L_n = (\frac{D}{K_f})^{0.25}$ needs to be developed. In particular, it is not clear how the stiffness K_f is set.

Figure 5.12 shows a comparison between the infinite plate solution and the measured profile using the hydrostatic stiffness $K_f = \rho g$ and the bending rigidity D for Type-1 material (see Appendix A). $K_f = \rho g$ corresponds to the stiffness experienced by the system at zero-speed or a regime where buoyancy effects dominate. While the form of the buckling profile is captured by the model reasonably well, it is observed that an increase in the foundation stiffness K_f above ρg is required to reproduce the measured buckling mode shape. It is hypothesized that this effect is real and that membrane/hydrodynamic restoring forces act in parallel with hydrostatic pressure to set the foundation stiffness. Section 5.6 explores potential physical mechanisms responsible for this apparent increase in foundation stiffness.

Due to finite-width effects, the applicability of the infinite plate solution to the stiff Type-0 material supported by a hydrostatic foundation is limited. In particular, the hydrostatic buckling wavelength,

$$\lambda_{\rho g} = 2\pi(\frac{D}{\rho g})^{0.25} \tag{5.66}$$

is the same order as the seal width $L = 2R_f$. The ratio of these lengths is related to non-dimensional system size $\eta_{\rho g}$, where

$$\eta_{\rho g} = \frac{2\pi L}{\lambda_{\rho g}} = L(\frac{\rho g}{D})^{0.25}. \tag{5.67}$$

For the Type-0 (NN) material, the hydrostatic system size $\eta_{\rho g} = 8.56$ using the seal width

($L = 2R_f$) for the characteristic length L. The infinite beam solution may be more applicable to the compliant Type-1 (HN) material, where $\eta_{\rho g} = 30.33$. In addition, the analytical result per Diamant and Witten cannot reproduce complex waveforms such as seen in Figure 4.14 which contain a number of localized packets.[8] A critical difference between the infinite plate solution for the BoF and the non-linear system without a foundation discussed earlier is that the relevant length scale is not the geometric length scale L, but the natural buckling length, L_n. Later sections explore the implications of the natural length scale L_n for the bow seal problem.

[8]Because the system is nonlinear, a simple superposition of modes is not possible.

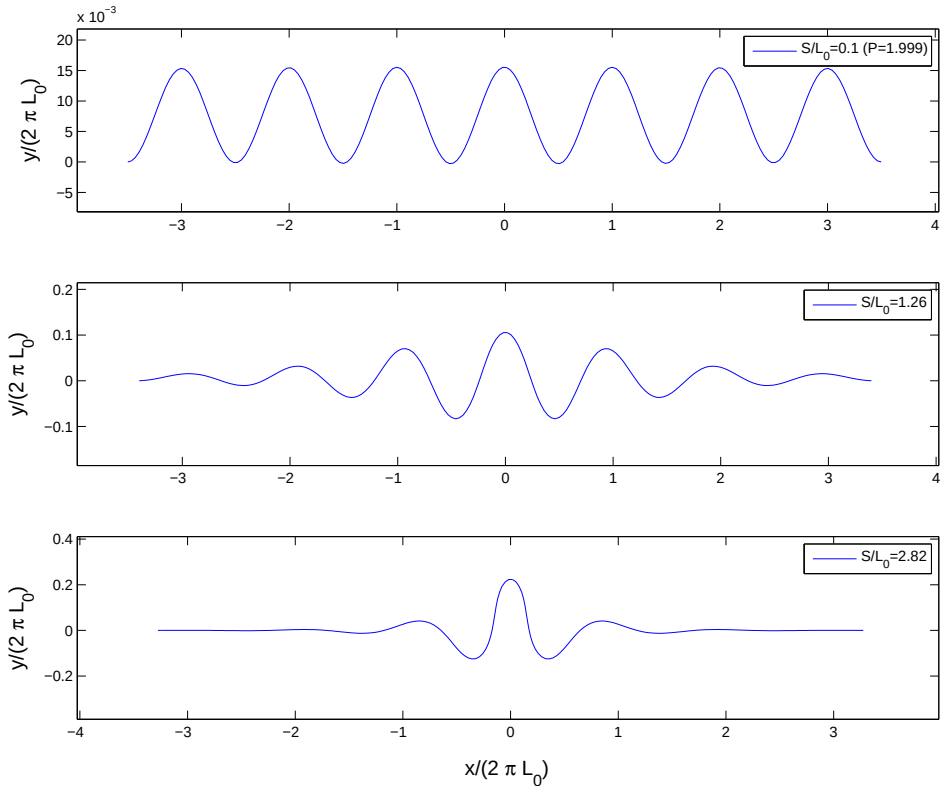

(a) Varying confinement $\Delta = \frac{S}{L_n}$

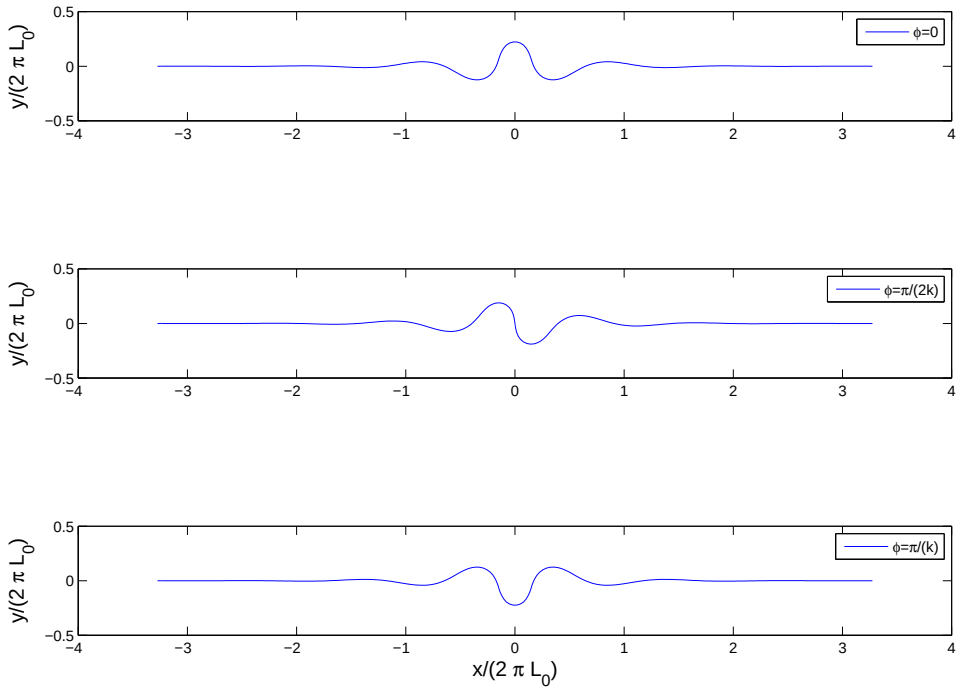

(b) Varying phase ϕ

Figure 5.11 Effect of phase (Φ) and confinement (Δ) on infinite-plate solution (Equation 5.64) per Diamant and Witten (2011). L_0 is the buckling length at the inception of buckling, $L_0 = (D/K_f)^{0.25}$. Each of the configurations in (b) are energetically equivalent.

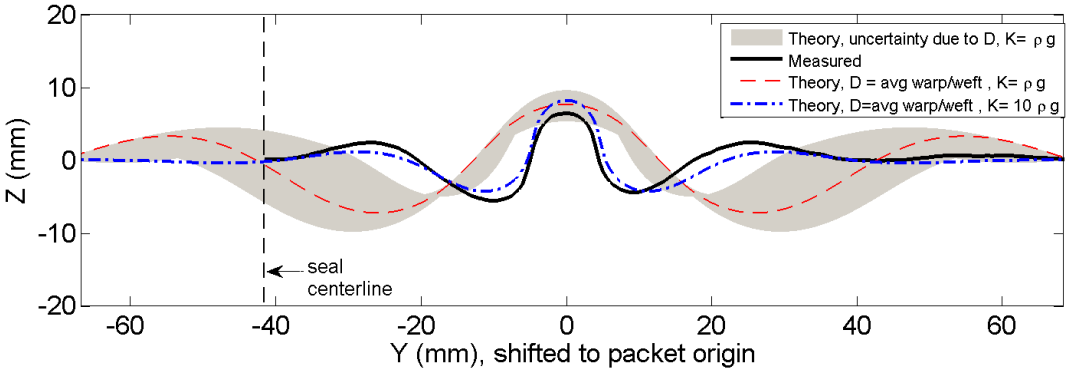

Figure 5.12 Comparison of Type-1 measured localized buckling profile with infinite-plate ($\eta \to \infty$) analytical solution per Diamant and Witten (2011), corresponds to rightmost packet of Figure 4.14(c), $\Delta = \mathcal{S}/L_{arc} \approx 0.107$ for the isolated packet, $\mathcal{S}/L_{\rho g} \approx 0.689$ based on $K_f = \rho g$ and average of warp/weft bending rigidities $D_{\overline{XY}}$, where $L_{\rho g} = \left(\frac{D_{\overline{XY}}}{\rho g}\right)^{0.25}$. $Z_s = 124.8$ mm,$p_c = 443$ Pa, $U_0 = 5.74$ m/s Uncertainty due to estimate of bending rigidity D shown in gray. Note that a significant increase in foundation stiffness is required to match the measured buckling wavelength.

5.4 Linear buckling on a foundation

To interpret properties such as the natural length scale,

$$L_n = (\frac{D}{K_f})^{\frac{1}{4}}, \tag{5.68}$$

which feature prominently in the geometrically-nonlinear problem, as well as to study the effects of finite width which is comparatively difficult to incorporate into the geometrically-nonlinear model, the behavior of a BoF is examined under the restriction of small slopes, $\frac{dh}{dx} \ll 1$. The ordinary differential equation resulting from this linearization has been treated extensively in the classical literature, first by Winkler (1868) who formalized the idea of a linearly elastic distributed foundation, and later by Ratzersdorfer (1936) and Hetényi (1979). Recent work has extended this work to the post-buckling regime (for example Potier-Ferry (1987), Champneys et al. (1999)). This work has been driven by experimental observations which show that the response of a BoF departs significantly from linear theory as confinement Δ is increased. Rather than a global, distributed type buckling response, experiments indicate that the mode number may switch (Stein, 1959; Boucif et al., 1991) with the response becoming increasingly localized (Pocivavsek et al., 2008) at large confinements. There has also been a resurgence of interest in geometrically non-linear "elastica" (Timoshenko, 1961) models which demonstrate localization without the introduction of nonlinear terms in the foundation stiffness or initial imperfections (Antman, 2005; Diamant and Witten, 2011).

The beam-on-elastic foundation (BoF) problem arises in a wide variety of engineering problems. Originally developed to model foundation and soil interaction on structures such as railroad rails (Hetényi, 1979), it has found application in the modeling of river and sea ice (Ashton, 1986; Bažant and Cedolin, 2010; Wagner and Vella, 2011), biological membranes (Cerda and Mahadevan, 2003) and nanoparticle monolayers (Pocivavsek et al., 2008). The BoF problem also serves as a useful analogy for interpreting solutions to Donnell's equations

governing the behavior of shell structures (Calladine, 1983).

To derive the linearized differential equation governing buckling of the beam, the geometrically-nonlinear functional Π_T presented in Section 5.3 is approximated to leading order. Referring to Figure (5.9), when linearized, the differential ds for the arc-length becomes dx:

$$\begin{aligned} ds &= dx\sqrt{1+(\frac{dh}{dx})^2}, && (5.69)\\ &\approx dx(1+\frac{1}{2}(\frac{dh}{dx})^2-\frac{1}{8}(\frac{dh}{dx})^4+...), && (5.70)\\ &\approx \underbrace{dx}_{|\frac{dh}{dx}|\ll 1}. && (5.71) \end{aligned}$$

Likewise, the tangent angle, θ when linearized becomes $\frac{dh}{dx}$:

$$\begin{aligned} \theta &= tan^{-1}(\frac{dh}{dx}), && (5.72)\\ &\approx \frac{dh}{dx}-\frac{1}{3}(\frac{dh}{dx})^3+\frac{1}{5}(\frac{dh}{dx})^5-... && (5.73)\\ &\approx \underbrace{\frac{dh}{dx}}_{|\frac{dh}{dx}|\ll 1}. && (5.74) \end{aligned}$$

Evaluating the exact curvature $\kappa = \frac{d\theta}{ds}$ in cartesian coordinates (Equation 5.75) and expanding the denominator in a Taylor series about $(\frac{dh}{dx})^2|_0$ it is found that $\kappa \approx \frac{d^2h}{dx^2}$ for small slopes with an error of 10% at a slope of 1/4.

$$\begin{aligned} \frac{d\theta}{ds} &= \frac{\frac{d^2h}{dx^2}}{(1+(\frac{dh}{dx})^2)^{3/2}}\\ &\approx \frac{d^2h}{dx^2}(1-\frac{3}{2}(\frac{dh}{dx})^2+\frac{15}{8}(\frac{dh}{dx})^4-..) && (5.75)\\ &\approx \underbrace{\frac{d^2h}{dx^2}}_{|\frac{dh}{dx}|\ll\frac{\sqrt{6}}{3}} \end{aligned}$$

Using these relations for ds, θ and κ, the linearized bending and foundation energies can now be written, where

$$\Pi_D = \frac{1}{2}\int_L D(\frac{d^2h}{dx^2})^2 dx \tag{5.76}$$

and,

$$\Pi_K = \frac{1}{2}\int_L K_f h^2 dx. \tag{5.77}$$

One term, which necessarily retains a second-order term at leading order is the work due to the compressive force, W_c:

$$\begin{aligned} W_c &= F\int_L (1-cos(\theta))ds = P(\int_L ds - \int_L dx) \\ &= F(\int_L (\sqrt{1+(\frac{dh}{dx})^2}-1)dx) \\ &\approx F\int_L (\frac{1}{2}(\frac{dh}{dx})^2 - \frac{1}{8}(\frac{dh}{dx})^4 + ...)dx \\ W_c &\approx \frac{1}{2}F\int_L (\frac{dh}{dx})^2 dx. \end{aligned} \tag{5.78}$$

Combining these terms, the following dimensional (Equation 5.79) and non-dimensional functional (Equation 5.80), is generated;

$$\Pi_T(x,h,\frac{dh}{dx},\frac{d^2h}{dx^2}) = \frac{1}{2}\int_L \underbrace{[D(\frac{d^2h}{dx^2})^2}_{\Pi_D} - \underbrace{F(\frac{dh}{dx})^2}_{W_c} + \underbrace{Kh^2]}_{\Pi_K} dx \tag{5.79}$$

$$\Pi^*_T(x^*,h^*,\frac{dh^*}{dx^*},\frac{d^2h^*}{dx^{*2}}) = \frac{1}{2}\int_L [(\frac{d^2h^*}{dx^{*2}})^2 - f^*(\frac{dh^*}{dx^*})^2 + h^{*2}]dx \tag{5.80}$$

where the same non-dimensionalization as the non-linear problem is adopted. That is

$x^* = \frac{x}{L_n}$ $h^* = \frac{h}{L_n}$ $f^* = \frac{F}{(K_f D)^{0.5}}$, where $L_n = (\frac{D}{K_f})^{0.25}$ and the system size is given by $\eta = \frac{L}{L_n}$. From this point forward, the stars denoting non-dimensionalization are dropped. Notice that there are no prefactors on Π_D or Π_K. The total energy Π_T is non-dimensionalized by $K_f^{0.25} D^{0.75}$.

Methods from variational calculus are employed to find configurations for which the first variation $\delta\Pi$ is extremized with respect to the the generalized coordinate $h(x)$. Applying the Euler-Lagrange equation,

$$\frac{\partial \Pi}{\partial h} - \frac{d}{dx}\frac{\partial \Pi}{\partial \dot{h}} + \frac{d}{dx^2}\frac{\partial \Pi}{\partial \ddot{h}} = 0 \tag{5.81}$$

to the functional, the fourth-order ordinary differential equation governing the BoF problem for small slopes, Equation 5.82 is found.

$$\frac{d^4 h}{dx^4} + f\frac{d^2 h}{dx^2} + h = 0. \tag{5.82}$$

Assumptions of model

In order to apply the Euler-Lagrange equation, a number of significant approximations are implied:

1. The system is assumed to be in static equilibrium and the variation in kinetic energy can be ignored.

2. The system is acted upon solely by conservative forces.

3. The boundary conditions are of the standard kinematic (Dirichlet) type.

For additional caveats on the application of Equation 5.81 as applied to solid mechanics see Langhaar (1962) and Bažant and Cedolin (2010) .

As seen in Figure 4.26, the assumption of static equilibrium is strictly valid for only a small portion of the experimental space. Equation 5.82 therefore constitutes a quasi-static

model, whereby kinetic energy is either assumed small or independent of the configuration. In addition, it is suspected that non-conservative forces such as viscous damping and path-dependent forces play a role in the response of the fabric, particularly if the model were to be extended to include dynamics.

A potentially significant path dependent force in the bow seal system is the tendency of the Type-0 seals at large fold amplitudes to separate from the free-surface (or "blister"). One way to incorporate this "blistering" effect into the model is to introduce a nonlinear term to the spring stiffness (Wagner and Vella, 2011), turning the spring "off" ($K_f(h > A_c) = 0$) above a certain critical amplitude (A_c). Experience with the benchtop buckling experiments (see Section 6.1) indicates that this detachment/reattachment process may not be reversible. The cut-off amplitude is dependent on whether Δ is increasing or decreasing ($A_{c+} \neq A_{c-}$). This hysteretic "blistering" behavior is a non-conservative force. Therefore, the model is best suited to small excursions from a configuration where the flow is fully attached, where the hydrodynamic foundation can be represented by a spring and the buckling profile is stable.

A differential equation equivalent to Equation 5.82 can be also derived from a balance of forces and moments on an infinitesimal segment of the beam (Hetényi, 1979). The weak form of the equation of motion is used in this discussion; a variant of Equation 5.80 will be used later to infer bounds on work performed by the fluid.

Solutions to the ODE

The linear differential Equation 5.82 is solved using standard methods. Assuming a solution of the form $h(x) \sim e^{\Lambda x}$, where Λ is a complex wave number, the following characteristic equation is generated:

$$\Lambda^4 + f\Lambda^2 + 1 = 0. \tag{5.83}$$

The characteristic equation yields four eigenvalues:

$$\Lambda^2 = -\frac{f}{2} \pm \sqrt{(\frac{f}{2})^2 - 1}. \tag{5.84}$$

For the finite length case, the boundary conditions of interest (simply-supported and clamped-clamped) can only be satisfied for the trivial case or if there is an oscillatory response (Hetényi, 1979), i.e. $f > 2$, where $f = 2$ represents the critical buckling load for the infinite length beam. When $f > 2$ there are two pairs of purely imaginary eigenvalues

$$\Lambda_{\pm(k_1,k_2)} = \pm i \underbrace{\sqrt{\frac{f}{2} + \sqrt{(\frac{f}{2})^2 - 1}}}_{k_1}, \pm i \underbrace{\sqrt{\frac{f}{2} - \sqrt{(\frac{f}{2})^2 - 1}}}_{k_2}. \tag{5.85}$$

The buckling wavenumbers k_1 and k_2 are related to the buckling load via Equation 5.86 (see Everall and Hunt (1999)). Note that as the system size increases, or $\eta \to \infty$, the critical buckling load approaches $f = 2$. In this case $\frac{k_2}{k_1} \to 1$ or a repeated eigenvalue.

$$\frac{k_2}{k_1} = \frac{f}{2} - \sqrt{(\frac{f}{2})^2 - 1}. \tag{5.86}$$

The general solution of Equation 5.82 for $f > 2$ is given by equation 5.87 where the amplitudes are determined by the boundary conditions:

$$h(x) = A sin(k_1 x) + B cos(k_1 x) + C sin(k_2 x) + D cos(k_2 x). \tag{5.87}$$

5.4.1 Effective boundary conditions

A challenge in applying a model such as described in Section 5.3.1 is the selection and application of appropriate boundary conditions. This is especially important in the case of smaller system sizes (η) such as near the trailing edge of the Type-0 (NN) sample. Boundary conditions play an important role in mode number selection (Potier-Ferry, 1987);

for example, Everall and Hunt (1999) found that m+1 type bifurcations are favored for pinned-pinned boundary conditions while m+2 bifurcations, which maintain symmetry, are energetically favorable for the clamped-clamped boundary condition. This mechanism may begin to explain why odd mode numbers are primarily observed during the experiment.

To understand the approximate boundary conditions imposed during the experiments, a qualitative model based on the curvatures observed during the experiments is developed. The model treats the cross-flow folds created at the intersection of the vertical seal face and the free-surface as a hinge with torsional spring of stiffness K_ϕ (see Figure 5.13). The stiffness of this spring is estimated by relating rotations (ϕ_0) at the support (point 0) to the restoring moment (M) caused by the change in curvature κ (Equations 5.88 and 5.90). The transition between the vertical face is approximated as a circular arc whose radius is estimated from the chord length (C_r) measured during the large-scale experiments.

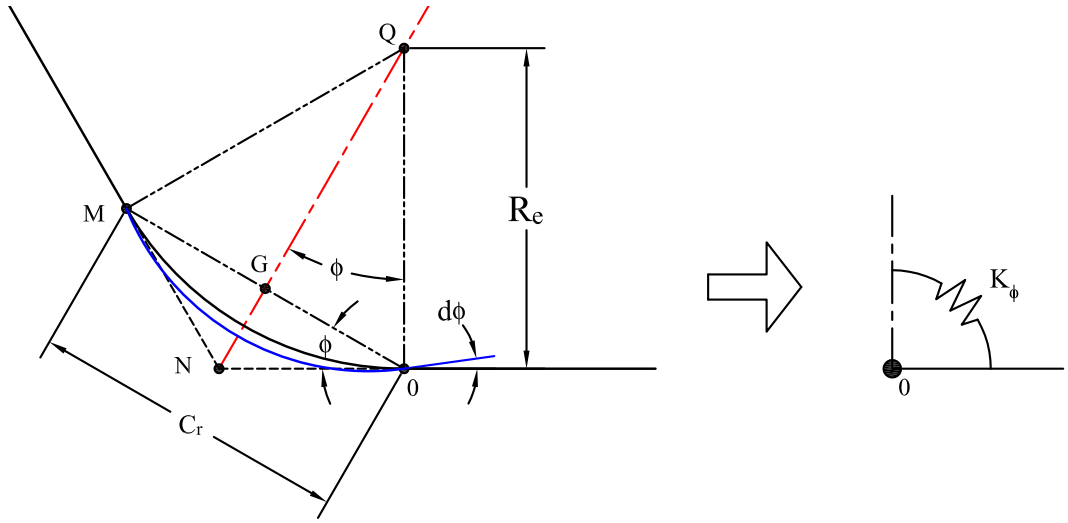

Figure 5.13 Cross-flow profile effective boundary conditions, construction used to estimate K_ϕ, torsional spring stiffness. C_r is the chord length.

$$\kappa(\phi) = \frac{2sin(\phi)}{C_r(\phi)} \tag{5.88}$$

$$\frac{d\kappa}{d\phi} = \frac{2cos(\phi)}{C_r} - \underbrace{2\frac{sin(\phi)}{C_r^2}\frac{dC_r}{d\phi}}_{\frac{dC_r}{d\phi}\approx 0} \tag{5.89}$$

$$\begin{aligned} K_\phi\big|_0 &\approx \tfrac{dM}{d\phi} \\ &\approx D\,\tfrac{d\kappa}{d\phi}\Big|_0 \\ &\approx \tfrac{2Dcos(\phi_0)}{C_r} \end{aligned} \tag{5.90}$$

Figure 5.14 shows typical corner fold and their chord-lengths as measured during the large-scale experiments. Due to the constraint from the neighboring seal and the free-surface is it assumed $dC_r/d\phi \approx 0$.

The stiffness of K_ϕ is compared with the restoring forces associated with the foundation (K_f) and material rigidity (D), via the non-dimensionalization shown in Equation 5.91 (Everall and Hunt, 1999). $K_\phi^* = 0$ is equivalent to a pinned-pinned connection, while $K_\phi^* = 1$ corresponds to a clamped-clamped connection.

$$K_\phi^* = \frac{K_\phi}{K_\phi + (K_f D^3)^{0.25}} \tag{5.91}$$

In practice, the chord length (C_r) is dependent on many factors, including material properties, pressure and immersion. As shown in Figure 5.4, at zero immersion, the cross-flow profile is a conical section with minor axis,

$$B_e = R_f, \tag{5.92}$$

and major axis,

$$A_e = \frac{R_f}{sin(\theta_{face})}. \tag{5.93}$$

R_f is the width of the finger and θ_{face} is the seal face angle (50 deg) (see Figure 2.6). This

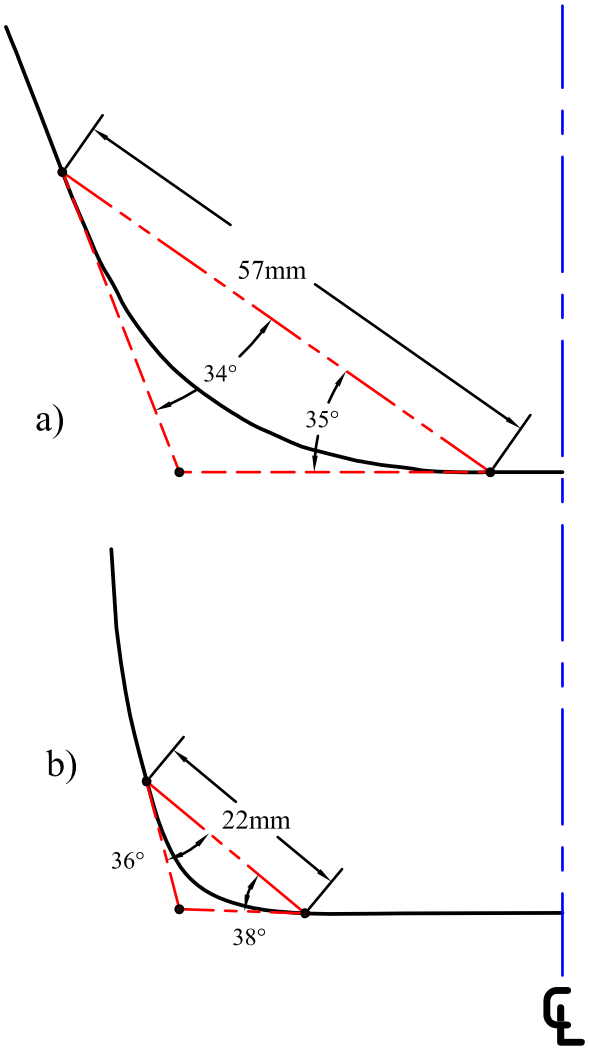

Figure 5.14 Typical cross-flow corner folds as measured for a) Type-0 (NN) and b) Type-1 (HN) material.

results in a curvature in the laser plane of $\kappa_0 = \frac{A_e}{B^2} = \frac{1}{R_f sin(\theta_{face})}$ and a principal curvature ($\kappa_1 = \frac{1}{R_f}$) aligned with the seal face. Dimensionally, this equates to a chord length of $C_r = 251$ mm and $\phi = 52.5$ deg.

Using $K_f = \rho g$ and the respective bending rigidities of NN and HN in Equations 5.90 and 5.91, which inscribe a circle of radius $1/\kappa_0$, it is seen that $K_\theta^* \approx 0.1$ for the stiff Type-0 (NN) material and 0.04 for the more compliant Type-1 (HN) material. Therefore, due to a large radius of curvature at small immersions, there is minimal resistance due to bending

and a pinned-pinned boundary condition might be suitable for a local analysis.

In contrast, at the deep immersions, particularly when the elevation of the seal Z_s exceeds L_{BE}, the height of the tangent line (see Figure 5.5) , κ_0 increases significantly and the system behaves more like it is clamped. At $Z_s = 100$ mm, $C_r \approx 56$ mm the Type-0 (NN) material and $C_r \approx 22$mm for the Type-1 (HN), resulting in a K_θ^* of around 0.6 for both materials. Therefore, to understand the range of boundary conditions experienced by the seals, both pinned-pinned and clamped-clamped boundary conditions should be examined. Section 5.4.2 investigates the pinned-pinned case. The clamped-clamped case is treated in Section 5.4.3.

5.4.2 Pinned-pinned boundary condition

Typical of lower immersions, pinned-pinned boundary conditions are imposed. The pinned-pinned case is important as an explicit relation between mode shape m and buckling load f can be developed. For other boundary conditions such as the clamped-clamped case which is discussed in Section 5.4.3 a transcendental equation must be solved to find the critical buckling load.

For the pinned-pinned case, the deflection h and bending moment, M vanish at the supports, that is:

$$h(0) = h(\eta) = 0, \tag{5.94}$$

$$\frac{d^2h}{dx^2}(0) = \frac{d^2h}{dx^2}(\eta) = 0, \tag{5.95}$$

from the Euler-Bernoulli equation, $M = D\kappa \approx D\frac{d^2h}{dx^2}$. Applying these four boundary conditions it is found that $B = -D = 0$ and that only the $sin(k\eta)$ terms persist. The boundary condition $h(\eta) = 0 = Asin(k_1\eta) + Bsin(k_2\eta)$, leads to a condition for the existence of non-trivial $(A, C \neq 0)$ solutions. This condition requires that the wavenumber k be integer

multiples of $\frac{\pi}{\eta}$:

$$sin(k_1\eta) = 0, \quad sin(k_2\eta) = 0, \tag{5.96}$$

$$k_1 = \frac{m\pi}{\eta}, \quad k_2 = \frac{n\pi}{\eta}. \tag{5.97}$$

At equilibrium, the total potential energy, $\Pi_{PE} = \Pi_D + \Pi_K$ of the system is balanced by the external work, W_c performed by the compressive load f. Recasting the characteristic equation, Equation 5.98 in terms of f, an explicit relationship between the buckling load f and the buckling eigenvalues can be formed.

$$f = \left(\frac{\pi m}{\eta}\right)^2 + \left(\frac{\eta}{\pi m}\right)^2 \tag{5.98}$$

Equation 5.98 is shown in Figure 5.15, in which the buckling load f is plotted for mode numbers spanning the hydrostatic system sizes $\eta_{\rho g}$ for the two materials used during the experiments. For the Type-0 (NN) seals, $\eta_{\rho g} \approx 8.56$, using $L = 2R_f$. Similarly, for the Type-1 (HN) seals, $\eta_{\rho g} \approx 30.33$. In Section 5.6, more detailed estimates of η based on the measured geometry are developed.

Each point on Figure 5.15 represents a different viable configuration. Of these configurations, for a given η, the mode m that minimizes f:

$$\frac{df}{dm}(m) = 0, \tag{5.99}$$

is also associated with the lowest potential energy state of the system, as $W_c = \Pi_D + \Pi_K \sim f$. This load, f is known as the critical buckling load, f_c. The minimum critical buckling load $f_c = 2$ occurs when the mode (m) divides a system of dimensional length L into half-waves

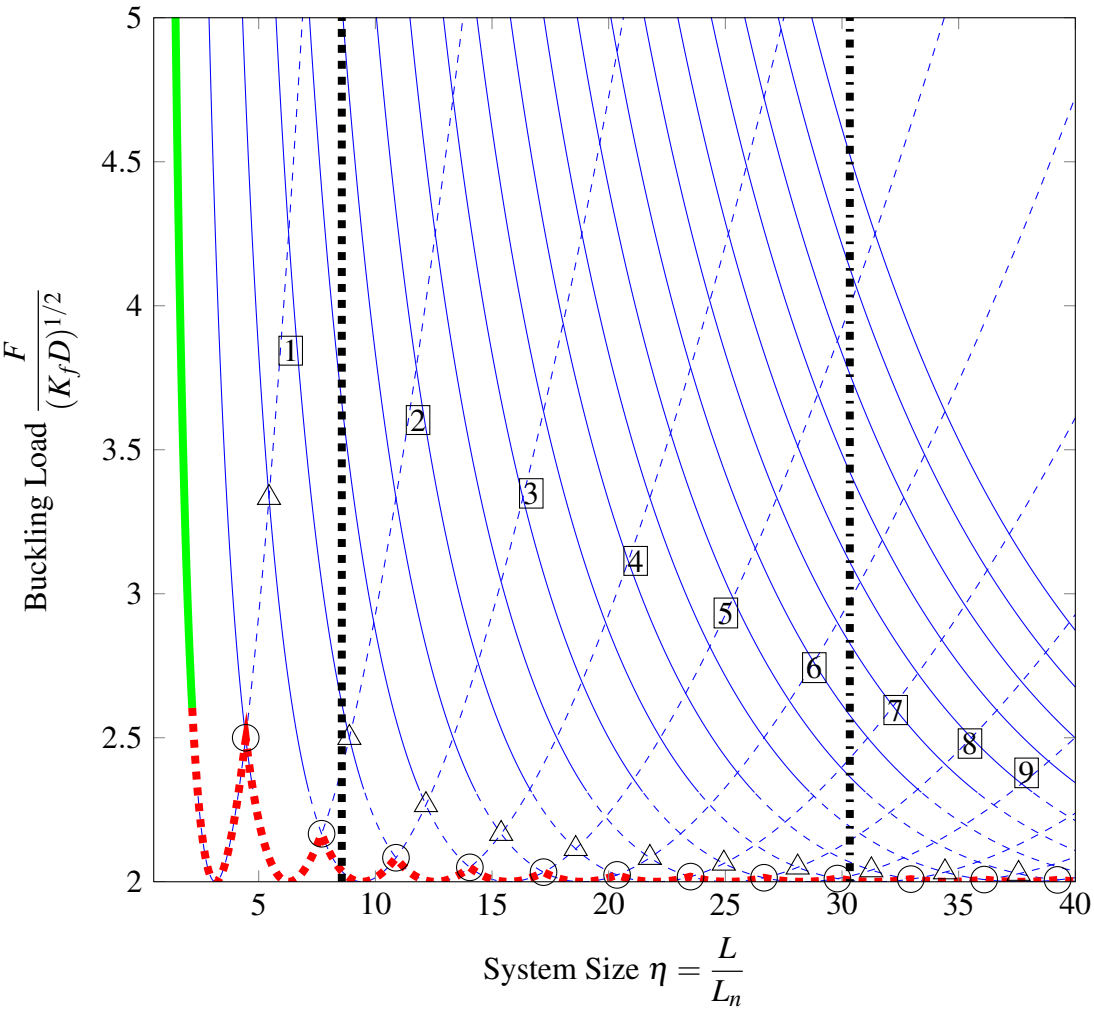

Figure 5.15 Influence of system size (η) on buckling load (F) and mode number (m), linear beam-on-foundation (BoF) model, *pinned-pinned* (p/p) boundary condition; ▬, critical buckling load, F_c, *stable* per (Koiter and van der Heijden, 2009). ▪▪▪, critical buckling load, F_c, *unstable*. Unstable (- - -) and stable (——) configurations for each mode number are also shown. System size at zero-speed ($\eta_{\rho g}$) is shown for the Type-0 (NN) (▪▪▪) and Type-1 (HN) (▪▪▪) materials. Potential branch points are also indicated; ◯, $m+1$; △, $m+2$.

of length πL_n; equivalently, in terms of the non-dimensional system size η,

$$m|_{min(f)} = \frac{\eta}{\pi} = m = \frac{L}{\pi}\left(\frac{K_f}{D}\right)^{0.25}. \tag{5.100}$$

Thus, the minimum buckling load $f_c = 2$ only occurs at specific system sizes η. However, f approaches $f_c = 2$ as $\eta \to \infty$. Substituting the mode shape associate with $m|_{min(f)}$ into the functional (Equation 5.80), it is also seen that the natural buckling wavelength,

$L_n = (\frac{K_f}{D})^{0.25}$ is that which partitions the potential energy into equal parts bending and foundation energies. This balance of bending and foundation energies at equilibrium will be used in Section 5.6.1 to infer bounds on the work performed by the fluid.

Figure 5.15 shows another interesting and relevant feature of the the BoF problem, for certain configurations (η) the total potential energy $(\Pi_D + \Pi_K) \sim f$, is the same for mode m and another mode n (Rivetti and Neukirch, 2014). These branch points are located at system sizes $\eta_{mn} = \pi(m^2 n^2)^{0.25}$.

For case of a pinned-pinned boundary condition branch points of type $n = m+1$ occur along the f_c path (Everall and Hunt, 1999). Other branch points, such as $n = m+2$, are observed, however these occur at higher energies. Because of this, if the system were compressed from an initial flat condition in a load (f)or confinement (Δ) controlled manner, these higher branch points might never be reached as the system would buckle near f_c and follow a post-buckling path associated with that bifurcation, never reaching the higher energy state. In dynamic buckling, however, these higher energy states may be experienced (Lindberg and Florence, 1987) as it may be possible for the structure to sustain impulse-type loads greater than f_c.

5.4.3 Clamped-clamped boundary conditions

The case of a clamped-clamped boundary is also considered. This represents the effective boundary condition of the system at deeper immersion. The general solution, Equation 5.87 is solved subject to the boundary conditions that the deflection and slope vanish at the support:

$$h(0) = h(\eta) = 0 \tag{5.101}$$

$$\frac{dh}{dx}(0) = \frac{dh}{dx}(\eta) = 0. \tag{5.102}$$

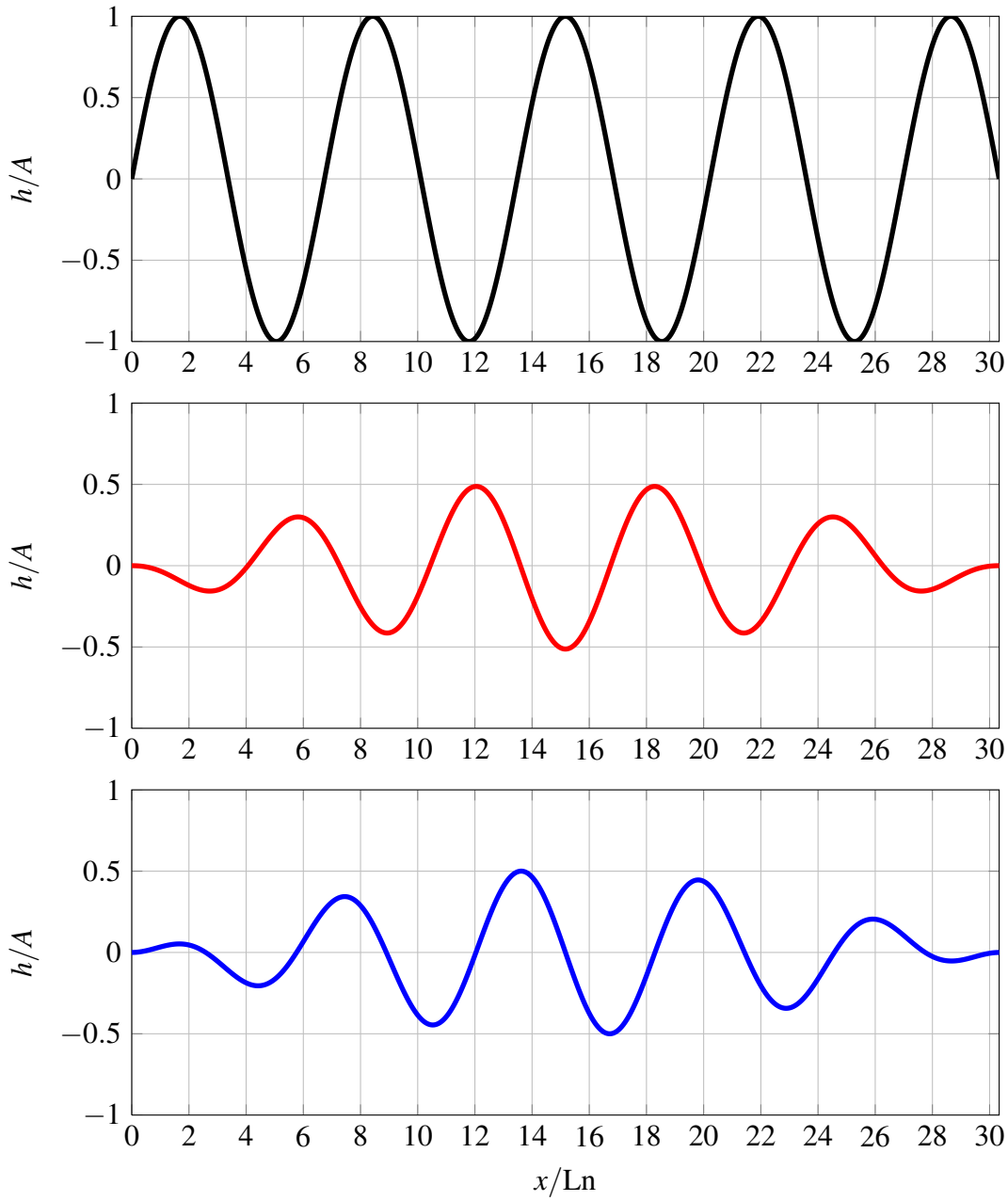

Figure 5.16 Mode shapes for linear beam-on-foundation (BoF), system size $\eta = 2R_f(\frac{\rho g}{D_X})^{0.25} = 30.33$ corresponds to Type-1 (HN) *compliant* material at zero-speed; ——, pinned-pinned boundary condition ($m = 9, f_c = 2.020$); ——, clamped-clamped boundary symmetric ($m = 9, f_c = 2.041$); ——, clamped-clamped asymmetric.

Solving now for the coefficients, the condition $h(0) = 0$ leads to:

$$B = -D.$$

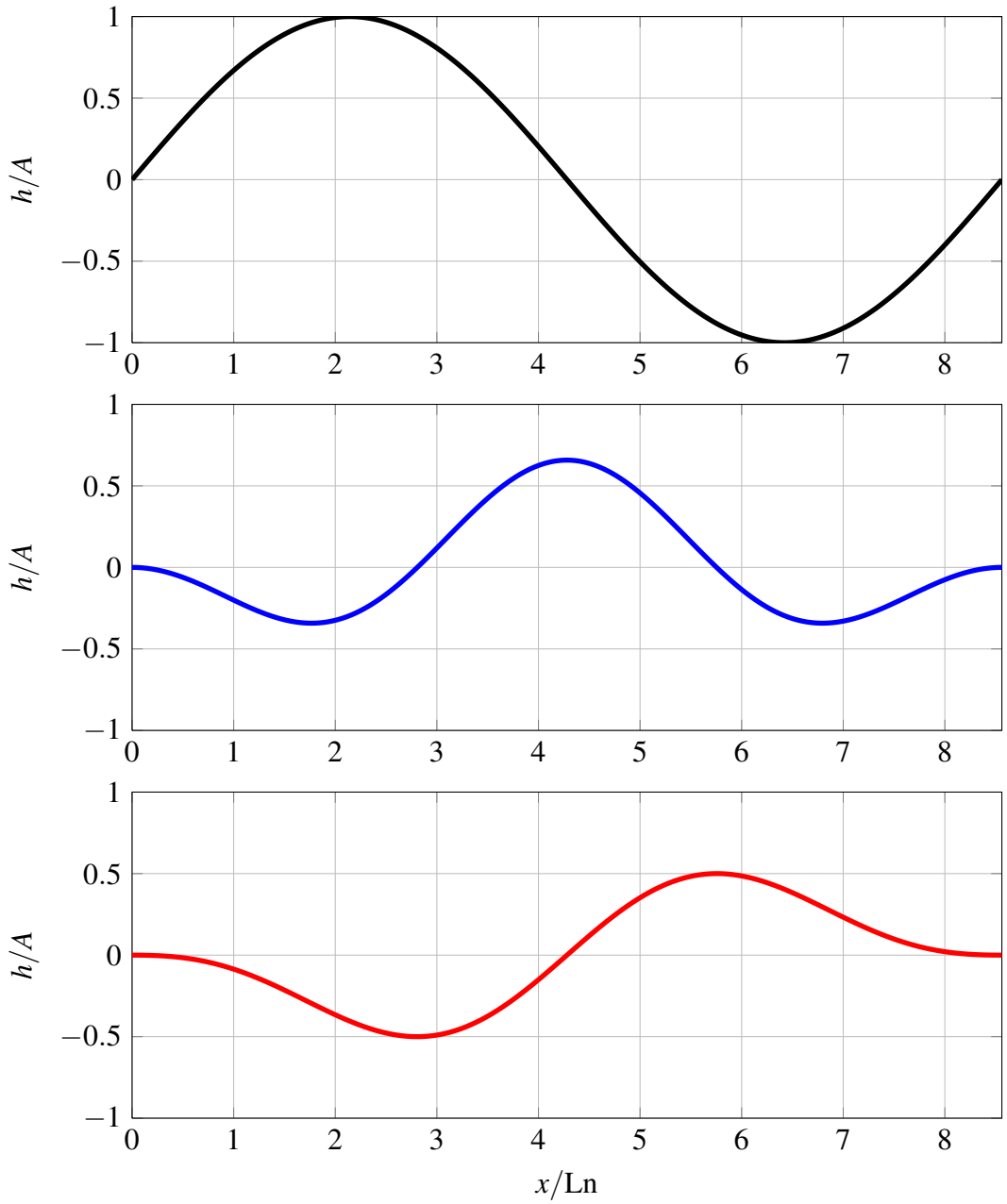

Figure 5.17 Mode shapes for linear beam-on-foundation (BoF), system size $\eta = 2R_f(\frac{\rho g}{D_X})^{0.25} = 8.56$, corresponds to Type-0 (HN) *stiff* material at zero-speed; ——, pinned-pinned boundary condition ($m = 9, f_c = 2.020$); ——, clamped-clamped boundary symmetric ($m = 9, f_c = 2.041$); ——, clamped-clamped asymmetric.

Taking the derivative $\frac{dh}{dx}(0)$ and setting it to zero, the number of unknown coefficients is further reduced:

$$C = -A\frac{k_1}{k_2}.$$

Applying the two remaining boundary conditions at $x = \eta$, a system of equations for the two remaining coefficients is assembled (Equation 5.103). In order for non-trivial solutions to exist one must have $Det(M) = 0$.

$$\underbrace{\begin{bmatrix} sin(k_1\eta) - \frac{k_1}{k_2}sin(k_2\eta) & cos(k_1\eta) - cos(k_2\eta) \\ k_1(cos(k_1\eta) - cos(k_2\eta)) & -k_1 sin(k_1\eta) + k_2 sin(k_2\eta) \end{bmatrix}}_{Det(M)=0} \begin{bmatrix} A \\ B \end{bmatrix} = \begin{bmatrix} 0 \\ 0 \end{bmatrix} \tag{5.103}$$

This leads to the condition shown in Equation 5.104. k_1 and k_2 are related via f. To solve for f, the roots of Equation 5.104 are found using Matlab®. The critical buckling load f_c is taken as the lowest of the roots.

$$cos(k_1\eta)cos(k_2\eta) + \frac{f}{2}sin(k_1\eta)sin(k_2\eta) - 1 = 0 \tag{5.104}$$

Depending on whether $sin(k_1\eta) + C_1 cos(k_1\eta) = +C_1$ or $-C_1$, symmetric or asymmetric solutions are formed. C_1 is a constant based on the boundary conditions (Equation 5.105):

$$C_1 = \frac{sin(k_1\eta) - k_1/k_2 sin(k_2\eta)}{cos(k_1\eta) - cos(k_2\eta)}. \tag{5.105}$$

Finally, the mode shape associated with the clamped-clamped boundary condition is given by

$$\frac{h(x)}{A} = sin(k_1 x) + C_1 cos(k_1 x) + (\frac{k_1}{k_2}sin(k_2 x) + C_1 cos(k_2 x)). \tag{5.106}$$

Results and Discussion

Solutions to Equation 5.104 for the clamped-clamped boundary condition are plotted in Figure 5.18. Comparing this to the pinned-pinned results in Figure 5.15, it is seen that boundary conditions have a significant impact on wavelength selection.

Symmetric solutions in Figure 5.18 are shown in the red (•), the asymmetric solutions in blue •). Unlike the simply supported case, branch points along the f_c path take the form of $n = m + 2$ bifurcations. These preserve symmetry and may begin to explain why odd mode numbers are dominant and observed for both materials, across a range of test conditions (see Figure 4.16).

Using a hydrostatic foundation stiffness ($K_f = \rho g$), mode shapes for the clamped-clamped case (Equation 5.106) are shown in Figures 5.17 and 5.16. Mode numbers for both the Type-0 (NN) material ($m = 3$) and Type-1 (HN) ($m = 9$) are in the same range as observed for deeper immersions (see Figure 4.16). This may suggest that buoyancy is an important restoring force in the Tail region. However, to enable more detailed comparisons improved estimates of the system size η and foundation stiffness are required. As expected, the clamped-clamped mode shapes exhibit amplitude modulation, reflecting the influence of the boundary. This is consistent with observed cross-flow profiles such as seen in Figure 4.13(b) which demonstrate amplitude modulation.

5.4.4 Fold amplitude

The mode shapes for the linearized BoF problem provided in Section 5.4 do not provide information on fold amplitude. To estimate the amplitude, a scaling argument based on the condition of inextensibility is applied. Similar approaches are taken by Cerda and Mahadevan (2003) and Brau et al. (2010).

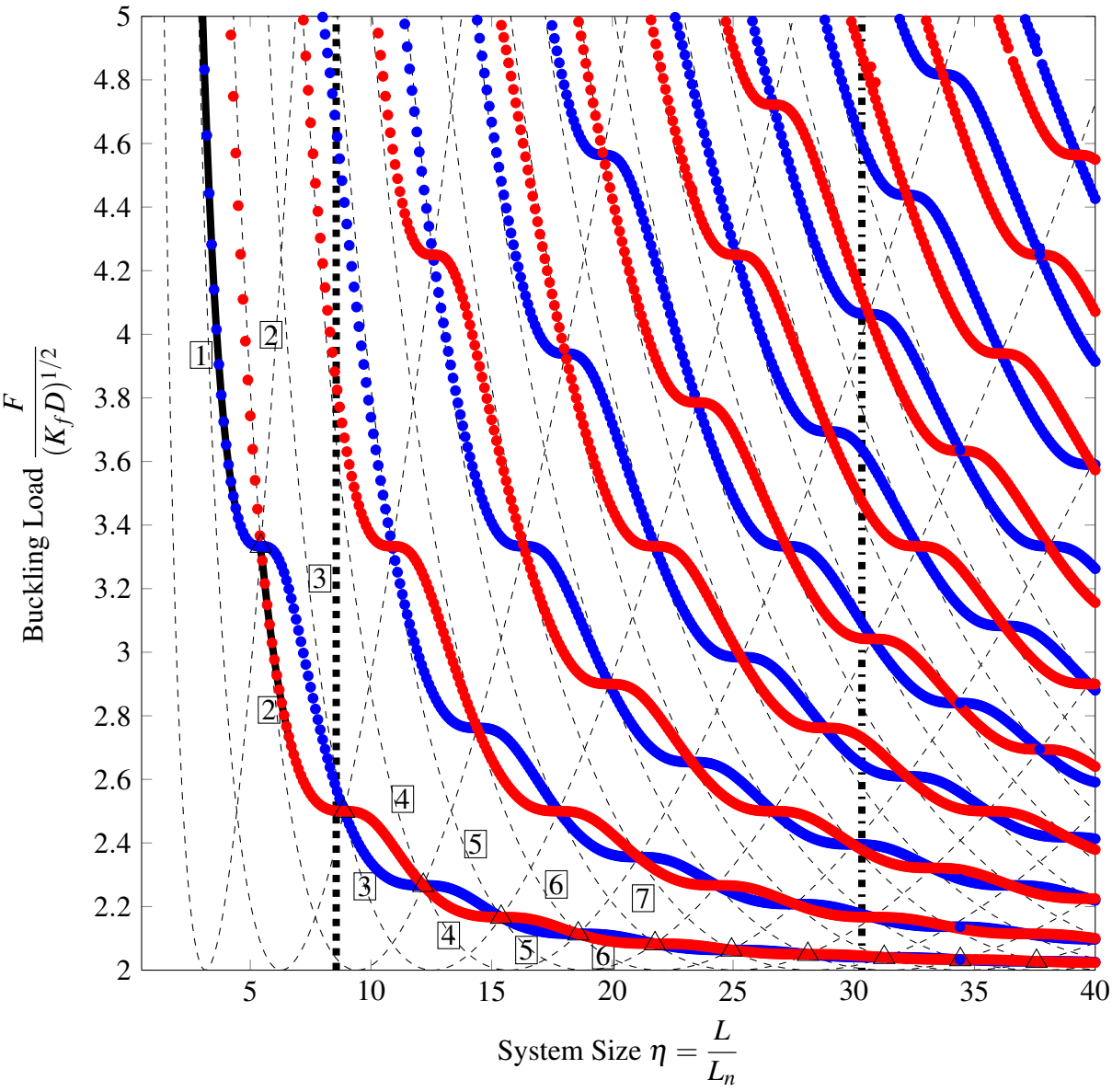

Figure 5.18 Influence of system size (η) on buckling load (F) and mode number (m), linear beam-on-foundation (BoF) model, *clamped-clamped* (c/c) boundary condition. ▬, critical buckling load; •, symmetric configurations; • asymmetric configurations. System size at zero-speed ($L_n = L_{\rho g}$) is shown for the Type-0 (NN) (▪▪▪), $\eta_{\rho g} \approx 8.6$ and Type-1 (HN) (▪·▪·▪), $\eta_{\rho g} \approx 30.3$, materials. Symmetry preserving $m+2$ branch points (△) are also indicated. For reference, pinned-pinned buckling loads (- - -) are also shown. Notice the limits on wavelength selection for the clamped-clamped system as compared to the pinned-pinned.

In non-linear form, the end-displacement, $\mathcal{S}$ is given by:

$$S = \int_L (1 - cos(\theta(s))ds, \tag{5.107}$$

which when expanded into powers of $\frac{dh}{dx}$, yields

$$S = \int_L (\frac{1}{2}(\frac{dh}{dx})^2 - \frac{1}{8}(\frac{dh}{dx})^4 + ...)dx. \tag{5.108}$$

The analysis conducted in Section 5.4 shows that the pinned-pinned BoF admits mode shapes of the form, $y = Asin(\frac{2\pi}{\lambda})$. In this case the scaling of $\frac{dh}{dx}$ can be estimated as

$$\left|\frac{dh}{dx}\right| \approx 2\pi\frac{A}{\lambda} \tag{5.109}$$

Substituting $\left|\frac{dh}{dx}\right|$ into the integral for the end-displacement (Equation 5.108), the material slope A/λ can be solved for

$$\frac{A}{\lambda} \approx \frac{\sqrt{2}}{\pi}(\frac{\mathcal{S}}{L})^{0.5} = (\frac{\mathcal{S}}{L})^{0.5}. \tag{5.110}$$

A similar expression was derived in Section 5.2.3. At large confinements ($\Delta > 0.3$), the amplitudes are expected to diverge from the $\Delta^{0.5}$ behavior, which assumes small rotations. Higher order approximations are provided by Brau et al. (2010).

Seal slope during the large-scale experiments reproduced in Figure 4.24 is found to agree closely with the power law $(A/\lambda) \sim \Delta^{0.5}$ across all test velocities. The agreement to the power-law fit is better for the compliant compliant Type-1 (HN) than the stiff Type-0 (NN) material.

5.5 Stability of equilibrium configurations

Large-scale experimental data indicate that for a small region of the experimental space, configurations of the stiff Type-0 (NN) seals are stable. In contrast, configurations of the compliant Type-1 (HN) seals are unstable under all conditions. One potential clue as to the source of this behavior is shown in Figure 4.17; a marked increase in mode-switching behavior is observed above mode number $m = 3$. Understanding this transition, and whether

it may be viewed as a loss of static stability, may provide insight as to the physical mechanisms responsible for seal vibration. Based on experimental evidence, it is hypothesized that mode number (and by extension, η) impacts the stability of seal configurations. In this section, the beam-on-elastic foundation analogy is extended to study the stability of equilibrium configurations to perturbations. A nonlinear stability analysis for realistic boundary conditions is outside the scope of the present study, the reader is referred to Future Work, Chapter 8 for a discussion of potential refinements to this approach. This approximate analysis identifies general trends in the stability of a pinned-pinned beam on an elastic foundation. The stability criterion is then applied to the interpretation of the large scale data.

5.5.1 Pinned-pinned BoF

The stability analysis closely follows Koiter and van der Heijden (2009) and Audoly (2010). The approach applies the energy criteria for elastic stability developed by Trefftz and Koiter and van der Heijden (2009). The stability of a conservative system requires that the functional representing the potential energy Π_T must be positive-definite in the neighborhood of the equilibrium solution (z). That is,

$$\Pi_T|_z| > 0. \tag{5.111}$$

In order to apply this criteria to the study of equilibrium solutions such as found in Section 5.4.3, the nonlinear functional given in Equation 5.56 is required. The linearized version of the functional does not provide information on the sign of $\Pi_T|_z$ post-buckling. Rewriting the functional 5.56 in cartesian coordinates and retaining derivatives with respect to the arc-length s, gives

$$\Pi_T = \int_0^L \frac{1}{2} D \frac{\frac{d^2h}{ds^2}^2}{1-(\frac{dh}{ds})^2} - \frac{1}{2} K_f h^2 \sqrt{1-(\frac{dh}{ds})^2} + F(\sqrt{1-(\frac{dh}{ds})^2} ds. \tag{5.112}$$

The functional is expanded to fourth order and terms are collected by order,

$$\Pi_T = \int_0^L \underbrace{\frac{1}{2}D(\frac{d^2h}{ds^2})^2 + \frac{1}{2}K_f h^2 - \frac{1}{2}F(\frac{dh}{ds})^2}_{\Pi_{[2]}} + \underbrace{\frac{1}{2}D(\frac{d^2h}{ds^2})^2(\frac{dh}{ds})^2 - \frac{1}{4}K_f h^2(\frac{dh}{ds})^2 - \frac{1}{8}F(\frac{dh}{ds})^4}_{\Pi_{[4]}} ds + ... \tag{5.113}$$

As expected, $\Pi_{[2]}$ is equivalent to the functional from the linearized BoF problem (Equation 5.79). The fourth-order terms, $\Pi_{[4]}$ are due to geometric non-linearities. In Section 5.4, it was found that in the case of pinned-pinned boundary conditions,

$$h(0) = h(L) = 0, \tag{5.114}$$

$$\frac{d^2h}{ds^2}(0) = \frac{d^2h}{ds^2}(L) = 0, \tag{5.115}$$

$\Pi_{[2]}$ is minimized by solutions of the form:

$$z(s) = Asin(\frac{m\pi s}{L}). \tag{5.116}$$

For non-trivial solutions to exist, the following relationship between mode number, m and compressive force, F must be maintained (previously given in Equation 5.98):

$$F = D\frac{m^2\pi^2}{L^2} + K_f\frac{L^2}{m^2\pi^2}. \tag{5.117}$$

The stability of π_T determined by the higher order terms of $\Pi_{[4]}$. To see this, consider the stability criterion:

$$\Pi_T|_{(z)} = \Pi_{[2]}|_{(z)} + \Pi_{[4]}|_{(z)} > 0 \tag{5.118}$$

However, because z (Equation 5.116) represents the equilibrium solution to $\Pi_{[2]}$,

$$\Pi_{[2]}|_{(z)} = 0. \tag{5.119}$$

Therefore, the sign of Π_T is set by $\Pi_{[4]}|_{(z)}$ and higher-order terms.

$$\Pi_{[4]}|_{(z)} = \int_0^L \frac{1}{2} D(\frac{d^2h}{ds^2})^2(\frac{dh}{ds})^2 - \frac{1}{4}K_f h^2(\frac{dh}{ds})^2 - \frac{1}{8}F(\frac{dh}{ds})^4 ds > 0 \tag{5.120}$$

Substituting the admissible mode shape, z into $\Pi_{[4]}$ (Equation 5.120) and integrating:

$$\begin{aligned}\Pi_4|_{(z)} =& \int_0^L \frac{1}{2} D(-\frac{m^2\pi^2}{L^2} Asin(\frac{m\pi s}{L}))^2(\frac{m\pi}{L} Acos(\frac{m\pi s}{L}))^2 \\ & - \frac{1}{4}K_f(Asin(\frac{m\pi s}{L}))^2(\frac{m\pi}{L} Acos(\frac{m\pi s}{L}))^2 - \frac{1}{8}F(\frac{m\pi}{L} Acos(\frac{m\pi s}{L}))^4 ds \\ =& \frac{A^4 m^4 \pi^4}{64L^3}(\frac{4Dm^2\pi^2}{L^2} - \frac{2K_f L^2}{m^2\pi^2} - \frac{3F}{L}).\end{aligned} \tag{5.121}$$

Finally, substituting Equation 5.117 for F into $P_{[4]}$ a stability criterion for the mode number is found:

$$P_{[4]} = \frac{A^4 m^4 \pi^4}{64L^3}(\frac{4Dm^2\pi^2}{L^2} - \frac{2K_f L^2}{m^2\pi^2} - \frac{3(D\frac{m^2\pi^2}{L^2} + K_f \frac{L^2}{m^2\pi^2})}{L}), \tag{5.122}$$

or,

$$P_{[4]} = \frac{A^4 m^2 \pi^2}{64L^5}(\frac{Dm^4\pi^4}{L^4} - 5K_f). \tag{5.123}$$

The stability criteria, $\Pi_{[4]} > 0$, reads:

$$(\frac{Dm^4\pi^4}{L^4} - 5K_f) > 0. \tag{5.124}$$

The criterion can be recast in dimensionless terms,

$$\eta < \frac{\pi m}{5^{0.25}}, \tag{5.125}$$

where $\eta = L\left(\frac{K_f}{D}\right)^{0.25}$.

5.5.2 Discussion of stability criteria

The stability criteria is depicted for each of the mode numbers in Figure 5.15, where dashed lines (- - -)indicate unstable configurations for a given mode number m. ▪▪▪ are unstable regions along the critical f_c path.

Tracing the stability of equilibrium solutions, $\eta|_{f_c}$ along the f_c path (minimum total potential energy), it is found that the system is stable only for a small segment of the $m = 1$ mode region. This is expected, as $\eta = 0$ is equivalent to the canonical unsupported Euler beam which is known to be stable about the critical point. In general, for mode numbers $m > 1$ the BoF is found to be *unstable* to disturbances. Equation 5.181 indicates the stability boundaries along f_c:

$$\eta|_{f_c} < \frac{\pi}{5^{0.25}} \text{ stable} \tag{5.126}$$

$$\eta|_{f_c} > \frac{\pi}{5^{0.25}} \text{ unstable} \tag{5.127}$$

This is qualitatively consistent with the large-scale observations. The $m = 1$ mode was the most stable mode shape for the Type-0 material. It may begin to explain why high mode numbers such as those typified by the Type-1 material are generally unstable. The hypothesized influence of clamped-clamped boundary condition is to increase the extent of the stable region. This may improve the agreement between the theory and experiment.

More importantly, due to their buckled state, seals are found to be highly susceptible to this mode switching instability, which is distinct from flutter a common instability type in fluid-structure-interaction problems that has previously been associated with the bow seal problem (Ryken, 1978). The stability criteria also suggests, that nonlinearities in the foundation stiffness K_f could dramatically influence the stability map, potentially leading to discontinuous regions along the f_c path. This suggests a possible mechanism behind some of the rich dynamics observed during the experiments.

The qualitative post-buckling analysis presented in this section suggests that an approach similar to this may have utility in determining analytical stability boundaries for the seal problem. As is discussed in Future Work, Chapter 8, the stability of post-buckled configurations should be investigated more rigorously. Refinements such as foundation non-linearities and realistic boundary conditions should be introduced. Numerical approaches may be required as explicit relations such as Equation 5.117 do not exist for more general boundary conditions.

5.6 Estimating BoF model parameters

Configurations of seals constructed of the stiff Type-0 (NN) material were found to differ dramatically from those constructed of the compliant Type-1 (HN) material. Fluid-loaded configurations of the stiff Type-0 material are characterized by relatively long wavelengths and large amplitude folds. Type-0 configurations are often stable with respect to perturbations. In contrast, configurations of the compliant Type-1 seals are characterized by short wavelengths and are unstable to perturbations. Section 5.3 identifies the natural buckling length $L_n = (\frac{D}{K_f})^{0.25}$ and associated non-dimensional system size $\eta = \frac{L}{L_n}$ as key post-buckling parameters. L_n is the natural length-scale at which bending (strain) and external restoring energies are balanced.

The analytical work presented in the previous sections show that L_n and η are closely linked to both the buckling wavelength and the stability of buckled configurations. Through the inextensibility of the material, fold amplitude is also linked to L_n; the work in Section 5.4.4 indicated that $A \sim L_n\sqrt{\Delta}$. Qualitatively, within the context of the BoF problem, the response of the Type-0 material appears representative of small η, while the Type-1 material is representative of large system size η. In Section 5.5, preliminary guidance on what constitutes "large" and "small" η is provided. However, to understand whether the BoF analogy supports more detailed comparisons additional information is required.

The goal of this section is to estimate parameters of the BoF model. In the process, the section identifies a number of potential physical mechanisms responsible for seal conformation. The approach is two-fold; first, in Section 5.6.1, energy measures are developed to infer the effective system size η_e and foundation stiffness K_{f_e} from the measured seal shape. These estimates are then compared to the known hydrostatic stiffness ($K_f = \rho g$) to gauge the relative importance of the hydrodynamic restoring forces. This analysis shows that for the Type-1 (HN) material, hydrostatic restoring forces dominate at large confinements $\Delta > 0.2$, corresponding to immersions $\delta_s/R_f \approx Z_{IVC}/R_f > 0.8$. However, at shallower immersions, a marked increase in the effective foundation stiffness K_{f_e} is reported.

Second, in Section 5.6.4, potential hydrodynamic mechanisms responsible for this apparent increase in K_{f_e} are investigated using scaling arguments. Particular attention is paid to the contribution of flow-induced tension (K_τ) to the total effective foundation stiffness. To estimate K_τ, an analogy between a tensioned sheet under the influence of gravity (Cerda et al. (2004)) and the Tail region of the seal under the action of viscous shear stress is developed. Flow-induced tension is found to contribute $K_\tau(X_h) \sim \frac{T(X_h)}{L_w^2}$ to the effective foundation stiffness, where $T(X_h)$ is the velocity and position-dependent tension, and L_w is the wetted length. Because the restoring force due to flow-induced tension is dependent on curvature ($\frac{d^2h}{dx^2}$), it is hypothesized that this contribution will tend to vanish at the free trailing edge where both $T(L_w) \to 0$ and $\frac{d^2h}{dx^2} \to 0$. The section shows that the mechanisms responsible for the apparent increase in foundation stiffness are poorly understood and require further study. The section also highlights the significant limitations of the static, 2-dimensional approach adopted in the present study.

5.6.1 Effective system size and buckling wavelength

This section develops a series of global energy measures to infer the effective system size η_e and the foundation stiffness K_{f_e} from the measured seal shape. Recall η is the physical system size L non-dimensionalized by L_n, the natural length-scale that balances bending

and foundation energies,

$$\eta = \frac{L}{L_n}. \tag{5.128}$$

Thus, to estimate η for a given profile requires the physical system size L and the natural buckling length L_n. The physical system size L can be estimated from the arc-length of the profile, $L = L_{arc}$ per the methods outlined in Section 3.4.3.

Estimation of the natural buckling L_n is less straightforward. One potential approach for estimating L_n is to use the results of the turning-point analysis described in Section 3.4.3. With this method, the natural buckling wavelength may be described by the extrema of the profile. For instance, for crest-to-trough cycles, $L_n \approx \frac{\lambda_{C2T}}{2\pi}$. Alternatively, other descriptors such as up-crossing or down-crossing periods can be used to estimate L_n (see Figure 3.15 for alternatives).

The turning point approach suffers from a number of limitations. First, it is a local measure. In the form adopted in the present study, the method discards all information from the profile except for two-points. Turning point analysis yields a sequence of wavelengths, $\lambda_{C2T}[i]$, where i is the index of the half-wavelengths. For aperiodic or localized profiles such as observed in Figure 4.13 (a)-(d), considerable variation exists within the wavelength sequence. The approach taken in Figures 4.22 and 4.18 is to winnow the $\lambda_{C2T}[i]$ by extracting only the largest amplitude Crest-to-Trough cycle $\lambda_{C2T}|_{max(H_{C2T})}$ from each profile. The largest Crest-to-Trough cycles for each profile are then collected and time-averaged for the duration of a test condition. Maximum amplitude cycles are chosen because they are relatively insensitive to high-frequency noise and are associated with the largest material slope $|\frac{dh}{dx}|$. It is shown in Section 5.4.4 that $|\frac{dh}{dx}|$ is closely tied to scaling relationships for seal confinement Δ[9]. A histogram of λ_{C2T} (downsampled by a factor of 20) for a single condition is shown in Figure 5.19. Considerable information pertaining to the energy of a

[9] Alternatively, an average of the $\lambda_{C2T}[i]$ sequence could be employed, however a simple arithmetic mean of $\lambda_{C2T}[i]$ for a localized waveform would significantly bias the bending energy. A physical basis for a weighted-average scheme is proposed in Section 5.6.2.

given configuration is lost in the turning point analysis. In addition, both turning point and level-crossing analysis suffer from coordinate frame dependence which introduces additional subjectivity to the measure. Implied in all parameter estimation approaches in this section is the assumption that the observed buckling profile reflects a static minimum total energy state and that the seal is acted on solely by conservative forces. Implications of these assumptions were previously discussed in Section 5.4. Chapter 8, Future Work proposes methods for loosening these restrictions.

The goal is to develop a global measure of the buckling length L_n from which the effective system size η_e can be estimated. To do this, the weak definition of the natural buckling length is exploited. That is, at equilibrium, the effective natural wavelength $L_n \approx L_e$ is that which partitions the potential energy, $\Pi_{PE} = \Pi_D + \Pi_K$ into equal parts bending Π_D and foundation energy Π_K. While strictly true for the pinned-pinned case at system sizes $\frac{\eta}{\pi} = m$, where m is an integer, the approximation improves at larger system sizes where eigenvalues of the system become spaced closer together. Experimentally, the approximate equipartition of energy is verified in Chapter 6 for a simplified case of seal material supported by a foundation of known hydrostatic stiffness ($K_f = \rho g$). Analytically, $\Pi_D \approx \Pi_K$ follows from minimization of the potential energy and can be verified by substituting mode shapes such as found in Sections 5.4.2 and 5.4.3 into suitable expressions for Π_D and Π_K.

The scaling of the bending (Π_D) and foundation energies (Π_K) with wavelength λ is examined to show that $\Pi_D(L_n) = \Pi_K(L_n)$. A mode shape of the form,

$$h(x) = Asin(\frac{2\pi x}{\lambda}), \tag{5.129}$$

is adopted. Provided $\lambda = 2L/n$, the mode shape is kinematically admissible for pinned-pinned boundary conditions ($h(0) = h(L)$). Recalling the linearized bending energy Π_D,

$$\Pi_D = \frac{1}{2}\int_0^L D\kappa^2 ds \approx \frac{1}{2}\int_0^L D\left(\frac{d^2h}{dx^2}\right)^2 dx, \tag{5.130}$$

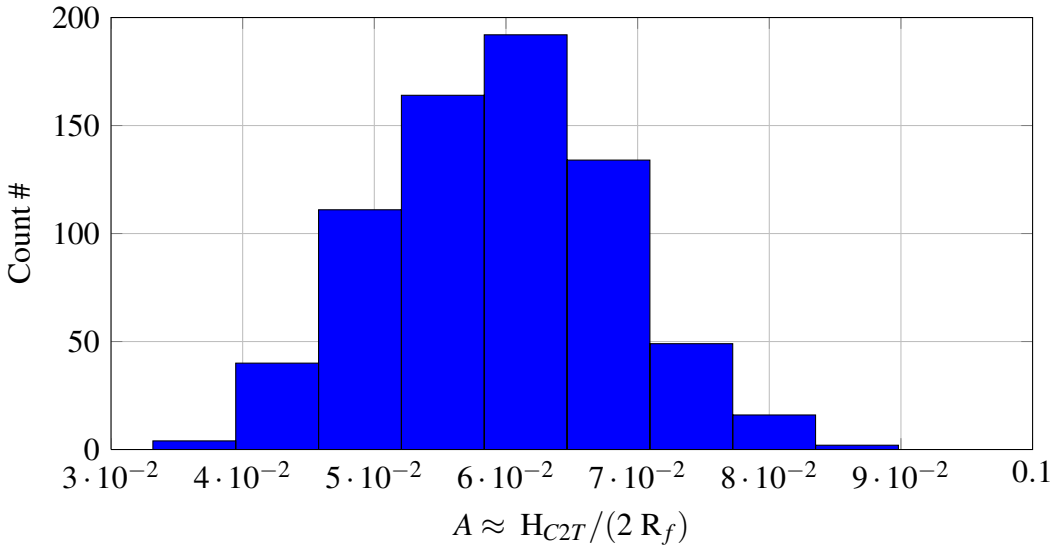

(a) Crest-to-trough amplitude

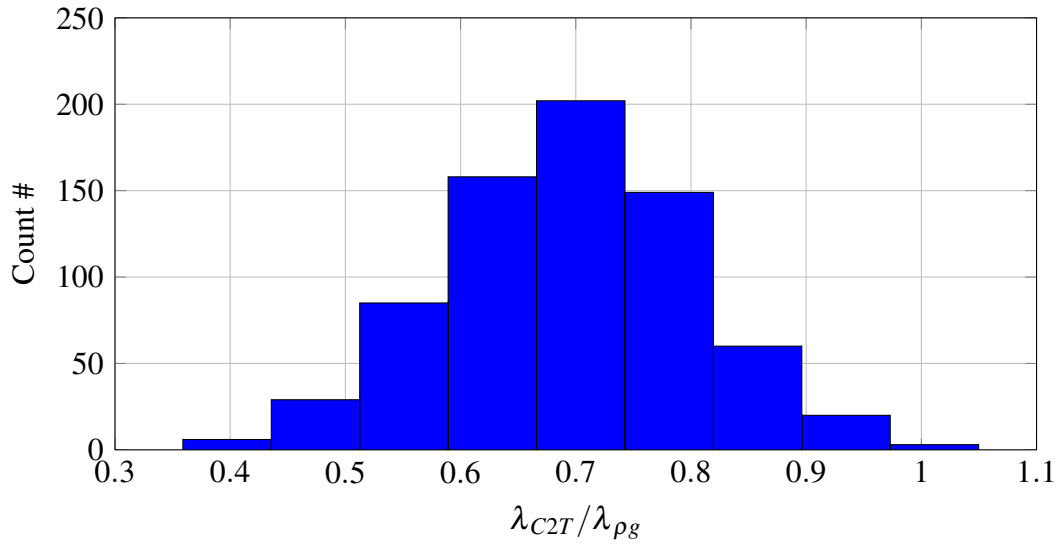

(b) Wavelength

Figure 5.19 (a) Histogram of largest crest-to-trough amplitudes ($H_{C2T}/(2R_f)$); (b) buckling wavelength ($2L_{C2T}/\lambda_{\rho g}$). Type-1 (HN) seal material, confinement ratio $\Delta = 0.236$, immersion $\delta_s/R_f = 1.0$, pressure $\delta_c/R_f = 0.97$.

the bending energy is found to scale as:

$$\Pi_D(\lambda) \approx \frac{8\pi^4 D A^2 L}{\lambda^4}, \tag{5.131}$$

which indicates that the bending energy is set by the shortest wavelengths λ in the system.

Similarly, the foundation energy Π_K is found to scale as:

$$\Pi_K = \frac{1}{2}\int_0^L K_f h^2 cos(\theta) ds \approx \frac{1}{2}\int_0^L K_f \left(\frac{d^2h}{dx^2}\right)^2 dx, \tag{5.132}$$

or

$$\Pi_K \approx \frac{KA^2L}{2}. \tag{5.133}$$

This indicates that the foundation energy Π_K is independent of wavelength.

As all forces are conservative, the work-energy theorem requires that the potential energy of the BoF (Π_{PE}) be balanced by the external work W_c performed by the compressive force F acting over distance $\mathcal{S} = \Delta L$,

$$\Pi_T = \Pi_{PE} - W_c = 0, \tag{5.134}$$

where W_c is the work performed by the compressive force F, given by:

$$W_c = \frac{1}{2}F\int_0^L \left(\frac{dh}{dx}\right)^2 dx = F\Delta L. \tag{5.135}$$

W_c is found to scale with λ as

$$W_c = F\frac{A^2\pi^2}{2\lambda^2}L, \tag{5.136}$$

from which one recovers the fold amplitude-confinement relationship developed in Section 5.4.4, $\frac{A}{\lambda} = \frac{\sqrt{2}}{\pi}\Delta^{0.5}$.

Assembling the scalings for each of the terms in Π_T, it is seen that $\Delta \sim \Pi_{PE}$, a result which is confirmed experimentally in Chapter 6. $\Delta \sim \Pi_{PE}$ provides an energy-based interpretation for the changes in configuration observed with Δ.

$$F\Delta L = \underbrace{F\frac{A^2\pi^2}{2\lambda^2}L}_{W_c} = \underbrace{\frac{8\pi^4 DA^2L}{\lambda^4} + \frac{KA^2L}{2}}_{\Pi_{PE}}, \tag{5.137}$$

$\Pi_{PE} \sim F$ is minimized,

$$\frac{dF}{d\lambda}(\lambda) = 0, \tag{5.138}$$

by,

$$\lambda_n = 2\pi \left(\frac{D}{K_f} \right)^{0.25}. \tag{5.139}$$

D is the bending rigidity as estimated in Appendix A. Substituting $\lambda = \lambda_n$ into the scalings for Π_D and Π_K it is verified that $\Pi_D = \Pi_K$ at the natural buckling length.

The energy interpretation for the natural wavelength λ_n provides a powerful tool for estimating an effective natural wavelength λ_e from the seal shape. An advantage of this approach is that neither D nor K_f are required a priori. λ_e is given by,

$$\lambda_e = 2\pi \left(\frac{\Pi_{K/K}}{\Pi_{D/D}} \right)^{0.25} = 2\pi \left(\frac{\int_0^L h(s)^2 cos(\theta) ds}{\int_0^L (\frac{d\theta}{ds})^2 ds} \right)^{0.25}, \tag{5.140}$$

where $\Pi_{D/D}$ is the non-linear bending energy divided by the bending rigidity, D. $\Pi_{K/K}$ is the foundation energy without the stiffness coefficient K. Both $\Pi_{D/D}$ and $\Pi_{K/K}$ are quantities that can be estimated from the shape alone. The effective foundation stiffness K_{f_e} is assumed constant across the span. In practice, the seal may blister and detach from the free-surface leading to a discontinuous K_f. The effective wavelength λ_e estimated in this method is analogous to a natural frequency estimated using Rayleigh's method (Strutt, 1877; Den Hartog, 1956). In that case ω_n is the frequency that balances potential and kinetic energy and represents an upper bound for the natural frequency of vibration.

The effective buckling wavelength λ_e is non-dimensionalized by the hydrostatic wavelength $\lambda_{\rho g} = 2\pi(\frac{D}{\rho g})^{0.25}$.

$$\frac{\lambda_e}{\lambda_{\rho g}} = \left(\frac{\rho g \int_0^L h(s)^2 cos(\theta) ds}{D \int_0^L (\frac{d\theta}{ds})^2 ds} \right)^{0.25} \tag{5.141}$$

Equation 5.141 suggests that λ_e may be used as a reporter for the effective foundation stiffness K_{f_e}; rearranging Equation 5.141 gives

$$\frac{K_{f_e}}{\rho g} \approx \left(\frac{\lambda_{\rho g}}{\lambda_e}\right)^4. \tag{5.142}$$

(In Chapter 6, it is shown for a simplified system that Equation 5.142 is a sensitive measure capable of detecting whether the seal has detached from the free-surface (blistering)). Finally, taking the ratio of the physical system size L to the effective natural wavelength L_e the effective system size η_e can be estimated,

$$\eta_e = \frac{L}{L_e} = L\left(\frac{\int_0^L (\frac{d\theta}{ds})^2 ds}{\int_0^L h(s)^2 cos(\theta) ds}\right)^{0.25}. \tag{5.143}$$

For a pinned-pinned BoF, mode number $m \approx \eta/\pi$.

5.6.2 Interpretation of effective natural buckling length, λ_e

As can be seen in Figures 4.13 and 4.14 the measured cross-flow shape of the seal is more complex than the linear or even geometrically-nonlinear model suggests. The profile may be comprised of multiple frequency components (see Figure 4.14 (E)) or may be spatially localized see Figure (4.14 (A-C)). Amplitude modulation is also present in most profiles. The goal of this section is to better understand the behavior of the effective buckling length L_e descriptor prior to applying it to noisy real-world data in the next section.

Consider a mode shape $h(x)$ of the general form:

$$h(x) = \sum_{n=1}^{\infty} A_n sin(\frac{n\pi}{L}x), \tag{5.144}$$

which is comprised of modes for the linearized pinned-pinned system. As before, the effective wavelength $\lambda_e = 2\pi L_e$, where L_e is buckling length $L_e \sim \frac{L}{n\pi}$. In terms of the general

mode shape, $\Pi_{K/K}$ in the numerator of L_e becomes,

$$\begin{aligned}\Pi_{K/K} = \int_0^L |h(x)|^2 dx &= \int_0^L \sum_{n=1}^{\infty} |A_n sin(\frac{n\pi}{L}x)|^2 dx \\ &= \frac{L}{2}\sum_{n=1}^{\infty} |A_n|^2.\end{aligned} \tag{5.145}$$

Due to the orthogonality of the modes (n), $\Pi_{K/K}$ contains solely A_n^2 terms. Similarly $\Pi_{D/D}$ is expanded as

$$\Pi_{D/D} = \int_0^L |\frac{d^2h}{dx^2}|^2 dx = \frac{L}{2}\sum_{n=1}^{\infty} \frac{n^4\pi^4}{L^4}|A_n|^2. \tag{5.146}$$

Equations 5.145 and 5.146 are a consequence of Parseval's theorem.

Hence, the series representation of the buckling length L_e is,

$$L_e \approx (\frac{\Pi_{K/K}}{\Pi_{D/D}})^{0.25} = \left(\frac{\sum_{n=1}^{\infty}|A_n|^2}{\sum_{n=1}^{\infty}\frac{n^4\pi^4}{L^4}|A_n|^2}\right)^{0.25}. \tag{5.147}$$

Both the numerator and denominator of L_e contain averages of the profile power. In the denominator, the power A_n^2 of the each mode is weighted by mode number n^4. Due to the weighting by n^4, profiles require smoothing (or low pass filtering) to reduce the noise amplification inherent in the measure.

To illustrate the tendency of L_e to amplify noise, consider a mode shape of base frequency $\frac{1}{L_n} = \frac{n\pi}{L}$ that is contaminated by noise at a spatial frequency $\frac{n_\varepsilon\pi}{L}$:

$$h_{+\varepsilon}(x) = A_n sin(\frac{n\pi x}{L}) + A_\varepsilon sin(\frac{n_\varepsilon \pi x}{L}). \tag{5.148}$$

A_ε is the noise amplitude. For this simplified case, L_e represents an estimator of L_n where,

$$L_e = L_n\left(\frac{1+\frac{A_\varepsilon^2}{A_n^2}}{1+\frac{n_\varepsilon^4}{n^4}\frac{A_\varepsilon^2}{A_n^2}}\right)^{0.25}. \tag{5.149}$$

Depending on the frequency of the noise relative to the base frequency, the effect of the

noise on L_e can be disproportionate to amplitude. In a typical case where $\frac{n_\varepsilon^4}{n^4} > 1$, L_e is a lower bound for L_n. Once the effective buckling length L_e is calculated, the total bending energy is given by $\Pi_D = \frac{D_e \sigma^2 L}{2L_e^4}$, where σ^2 is the variance of the profile. The foundation energy is given by $\Pi_K = \frac{K_{f_e} \sigma^2 L}{2}$.

For the complex and unsteady buckling patterns typical of large system sizes η, interpretation of L_e as a ratio of spectral moments may be utilized,

$$L_e = \left(\frac{M_0}{M_4} \right)^{0.25}. \tag{5.150}$$

where M_0 and M_4 and refer to a k$^{\text{th}}$ moment of the form:

$$M_k = \sum_{n=1}^{\infty} \frac{n^k \pi^k}{L^k} |A_n|^2. \tag{5.151}$$

In terms of moments, the total work $\Pi_T = 0$ can be rewritten as,

$$\underbrace{\frac{1}{2} F_e M_2}_{W_c} = \underbrace{\frac{1}{2} D_e M_4}_{\Pi_D} + \underbrace{\frac{1}{2} K_{f_e} M_0}_{\Pi_K}. \tag{5.152}$$

At equilibrium, $\Pi_D \approx \Pi_K$ which leads to the previously derived expression for L_e (Equation 5.150).

If it can be shown that mode amplitudes A_n are Gaussian and the spatial frequencies narrow-banded, statistical methods for random waves can be applied. A histogram of the amplitude and wavelength for a Type-1 (HN) profile at an average confinement ratio $\Delta = 0.24$ was previously shown in Figure 5.19. It is observed, at the relatively deep immersion of Figure 5.19, that the data may support the narrow-banded approximation. However, at shallower immersions, the seal develops spatially localized folds such as seen in Figure 4.14 (A)-(D). In the limiting case where the localized folds approach self-contact, their frequency domain representation widens and the narrow-banded assumption can no longer be applied.

In particular, random wave theory can be applied to compare the effective buckling

length (L_e) to a statistical estimate of the turning point length ($L_{TP} \approx \frac{L_{C2T}}{\pi}$). To develop a statistical estimate of the turning point length L_{TP}, Rice's formula is employed (Rice, 1944; Longuet-Higgins, 1957). The average zero-crossing length L_{ZC} is estimated from the spectral moments of $h(x)$ as,

$$L_{ZC} \approx (\frac{M_0}{M_2})^{0.5} = \left(\frac{\int_0^L |h|^2 dx}{\int_0^L |\frac{dh}{dx}|^2 dx} \right)^{0.5}. \tag{5.153}$$

For a Gaussian process L_{ZC} is closely related to the half wavelength as estimated by the zero-crossing analysis

$$L_{U2D} \approx L_{D2U} \approx \pi L_{ZC}. \tag{5.154}$$

With a change of variable, Equation 5.153 can be used to estimate the average Crest-to-Trough wavelength $L_{TP} \approx \frac{L_{C2T}}{\pi}$. This is done by taking the derivative of h and estimating the mean distance between extrema, which are at the zero-crossings of $\frac{dh}{dx}$. Substituting $\frac{dh}{dx}$ for h and $\frac{d^2h}{dx^2}$ for $\frac{dh}{dx}$ into Equation 5.153, the average turning point length L_{TP} is estimated as

$$L_{TP} \approx (\frac{M_2}{M_4})^{0.5} = \left(\frac{\int_0^L |\frac{dh}{dx}|^2 dx}{\int_0^L |\frac{d^2h}{dx^2}|^2 dx} \right)^{0.5} = \left(\frac{\sum_{n=1}^{\infty} \frac{n^2\pi^2}{L^2} |A_n|^2}{\sum_{n=1}^{\infty} \frac{n^4\pi^4}{L^4} |A_n|^2} \right)^{0.5}. \tag{5.155}$$

The ratio of L_{TP} to the effective buckling length L_e is

$$\frac{L_{TP}}{L_e} \approx (\frac{M_2^2}{M_4 M_0})^{0.25}. \tag{5.156}$$

The Cauchy-Schwarz inequality is invoked to show that $\frac{L_{TP}}{L_e} \leq 1$

$$\left| \sum_{i=1}^{n} x_i \bar{y}_i \right|^2 \leq \sum_{j=1}^{n} |x_j|^2 \sum_{k=1}^{n} |y_k|^2, \tag{5.157}$$

where $x_j = A_j$, $y_k = \frac{A_k k^2 \pi^2}{L^2}$

$$\underbrace{\left| \sum_{i=1}^{n} \frac{A_i^2 k^2 \pi^2}{L^2} \right|^2}_{M_2^2} \leq \underbrace{\sum_{j=1}^{n} |A_j|^2}_{M_0} \cdot \underbrace{\sum_{k=1}^{n} |\frac{A_k k^2 \pi^2}{L^2}|^2}_{M_4}. \tag{5.158}$$

.

Because $L_{TP} \approx \frac{L_{C2T}}{\pi}$ is always less than or equal to the effective buckling length L_e, the turning point buckling length L_{TP} overestimates the bending energy ($\Pi_D \sim L_n^{-4}$).

5.6.3 Results and discussion

Using the energy measures developed in the previous section, the effective wavelength λ_e is calculated for cross-flow profiles acquired during the large-scale test program. Prior to calculating λ_e, profiles are smoothed and missing samples are replaced with interpolated values. The reported turning point wavelength $\lambda_{C2T} = 2L_{C2T}|_{max(HC2T)}$ is the time-average of the wavelength corresponding to the largest amplitude half-cycle for a given profile.

Effective buckling wavelength, λ_e

λ_e and λ_{C2T} for the compliant Type-1 material are shown as a function of confinement Δ in Figure 4.22. The upper axes shown in Figure 4.22 indicate the estimated non-dimensional streamwise position (x_h) of the measurement plane relative to the hinge. Per Equation 5.141, the wavelength is normalized by the hydrostatic buckling wavelength $\lambda_{\rho g} = 2\pi(\frac{D}{\rho g})^{0.25}$. Dimensionally, $\lambda_{\rho g} = 52$ mm for the Type-1 material using the average of the warp/weft bending rigidities. For the Type-0 material, $\lambda_{\rho g} = 157$ mm.

Despite the local nature of the turning point analysis, for the Type-1 material the effective wavelength λ_e is proportional to the turning point wavelength λ_{C2T} across the full range of confinement ratios Δ. The proportionality between methods is observed both for localized profiles typical of small Δ (see Figure 4.26 (A)-(D)) and distributed patterns typical of large

Δ (see Figure 4.26 (G)). The agreement between methods suggests that the large amplitude waves selected for $L_{C2T}|_{max(H_{C2T})}$ contribute significantly to the total bending energy. On average $\lambda_{C2T}/\lambda_e \approx 0.65$. This result is consistent with Section 5.6.2, where it was shown that λ_{C2T} is less than λ_e.

The buckling wavelength for the Type-1 material increases linearly with Δ (and x_h), with λ_e approaching the hydrostatic buckling wavelength $\lambda_{\rho g}$ above $\Delta = 0.35$. This suggests that restoring forces due to buoyancy are significant for large confinements Δ at the laser plane. As seen in Figure 4.15, $\Delta = 0.35$ corresponds to a mean non-dimensional seal elevation of $z_{IVC} \approx 4.0\Delta$ or 1.4. This places the measurement plane downstream of the tangent line and elliptical part of the waterline. Similar to the cropped material at zero immersion, the seal is unable to support hoop stress at this streamwise location and must support hydrodynamic loads through other mechanisms.

For a BoF, to first order, λ is independent of the confinement. That λ is observed to *increase* with confinement Δ runs contrary to the higher order analysis of Brau et al. (2010) who shows that λ *decreases* with Δ. It is hypothesized that the fixed streamwise position of the laser confounds effects of confinement Δ with changes in relative streamwise position x_h. In Chapter 6, an experimental approach is adopted which allows independent control of Δ. When the upper axes are considered, the change in wavelength is interpreted as spatial spreading with streamwise position. This interpretation is supported by the underwater videography (Figure 4.6b). Examination of the detail (Figure 4.6b) shows that the number of folds does not seem to change from knuckle to trailing edge and that for each fold, there seems to be a point near the knuckle from which it emanates. Moving downstream of the Knuckle the folds spread. At some location upstream of the trailing edge adjacent folds seem to merge. When the wavelength data are interpreted as a shift in streamwise position x_h, the wavelength of the resulting folds at the merging location may be the hydrostatic wavelength $\lambda_{\rho g}$. At this point, this line of reasoning is purely speculative. Future work should investigate the spatial evolution of the buckling wavelength within a single condition.

These results can then be compared with Vandeparre et al. (2011) who provides potential scaling laws for the spatial evolution of folds within a tensioned sheet.

Effective system size, η_e

The influence of buoyancy on seal configuration is clearly seen in Figure 5.20, which shows the change in effective system size η_e and hydrostatic system size $\eta_{\rho g}$ with confinement. When this non-dimensionalization is adopted, η_e appears to converge to the hydrostatic system size for $\Delta > 0.2$ ($x_h > 0.8$). L_e does not exceed $L_{\rho g}$ within the range of confinements tested. This suggests that the flow is fully attached. This finding is also consistent with the finding in Section 5.6.2 that L_e constitutes a lower-bound estimate of natural buckling length which appears to be the hydrostatic buckling length in this regime.

Variation in the hydrostatic system size $\eta_{\rho g}$ with Δ in Figure 5.20 is due entirely to changes in arc-length L_{arc} at the measurement plane. The trend in $\eta_{\rho g}$ indicates that the amount of "excess" material within the laser plane reaches a maximum near $\Delta = 0.18$ and remains constant with further confinement. The scatter in $\eta_{\rho g}$ suggests that there may be uncertainty in the algorithm used to identify the beginning and end points of the profile (Section 3.4.3). This is complicated by the inability of the laser to register the vertical sides of the seal and by occlusions caused by folds that have made self-contact. Future work should refine the algorithms used to window the profile or consider changing laser orientation.

Typical buckling profiles responsible for the trends in η_e are shown in Figure 4.26. Below $\Delta = 0.2$, the relatively small quantity of "excess" material in the system reconfigures into localized buckling packets. As Δ approaches 0.2, these buckling packets increase in scale (amplitude and wavelength) and eventually join to form distributed buckling patterns. Phenomena such as period-doubling are also observed (Figure 4.26 (E)). The physical mechanism responsible for the period-doubling is not clear. Similar phenomena are observed for BoFs supported by nonlinear foundations (Brau et al., 2010) and in transitional regions of

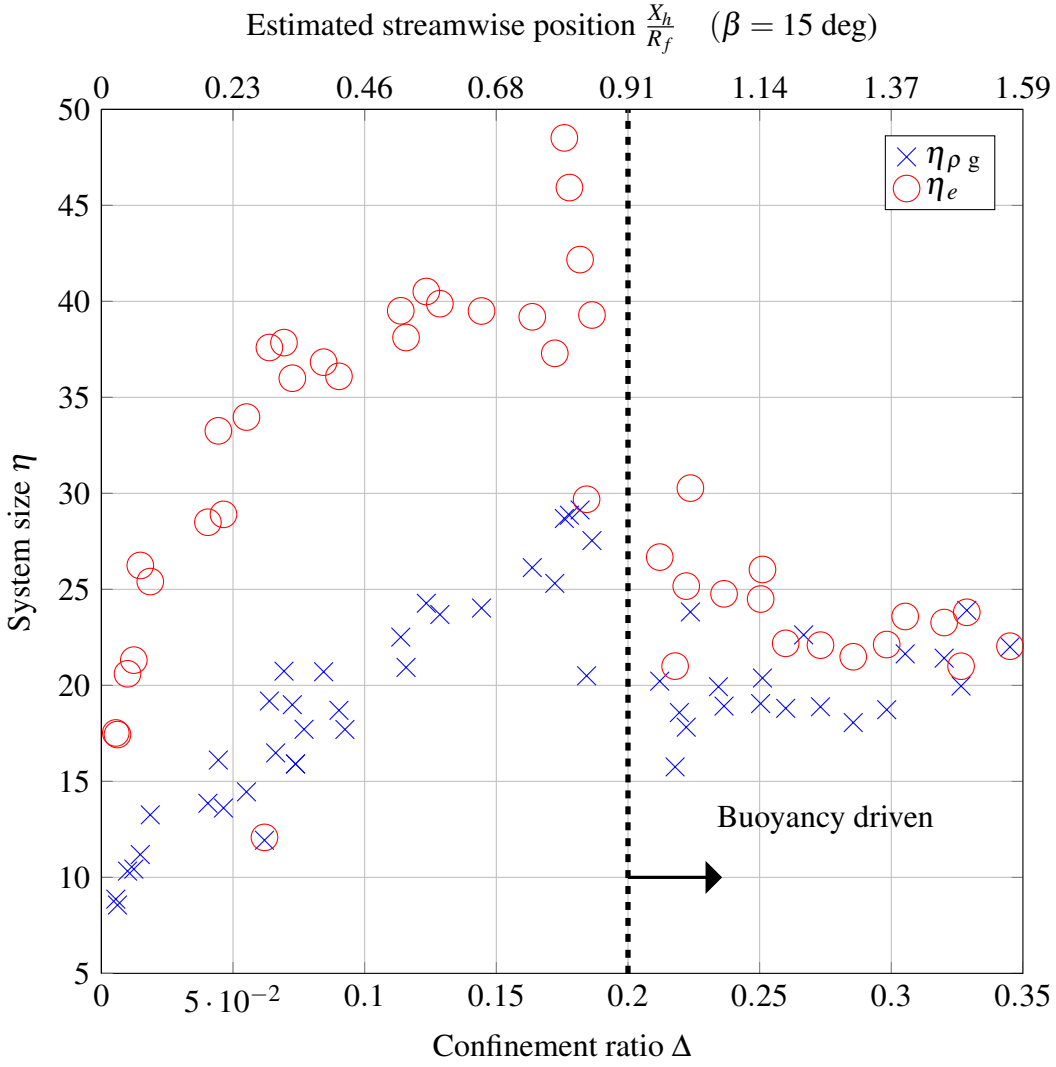

Figure 5.20 Change in effective system size η_e (◯) with seal confinement (Δ), Type-1 (HN), compliant seal material, ${}^{s}X_{IVC} = 0.75$ m. $\eta_e = L_{arc}/L_e$, L_{arc} is the finite-difference estimate of the arc-length. Beginning (b) and end points (b') of each profile are found iteratively. Effective natural buckling length L_e is based on quotient of foundation $\Pi_{K/K}$ and bending energies $\Pi_{D/D}$, $L_e \approx \left(\frac{\Pi_{K/K}}{\Pi_{D/D}}\right)$. The hydrostatic system size $\eta_{\rho g}$, based on the measured L_{arc} is also shown (×), $\eta_{\rho g}$. $\eta_e \geq \eta_{\rho g}$ for all test conditions. For configurations $\Delta > 0.2$, $\eta_e \approx \eta_{\rho g}$ indicating that buoyancy is the dominant restoring force.

sheets forced to buckle at prescribed wavelengths (Vandeparre et al., 2011).

Above $\Delta = 0.2$ profiles are spatially distributed across the seal width and are typified by buckling patterns such as Figure 4.26 (G). The profile in Figure 4.26 (G) corresponds to a confinement $\Delta = 0.266$ and effective system size $\eta_e \approx 26.5$. The observed mode number $m = 7$. Referring to Figure 5.18, for a clamped-clamped configuration, the symmetric

mode shape with the minimum potential energy at $\eta = 26.5$ is the $m = 7$ configuration (the asymmetric $m = 8$ mode shape has slightly lower energy). The profile as compared to the clamped-clamped mode shape is shown in Figure 5.21. Mode number can also be estimated via the results presented in Section 5.4.2 for a pinned-pinned beam. In the pinned-pinned case mode number $n_{p/p} \approx \eta/\pi \approx 8$, which is higher than observed. However, one expects the effective system size of a clamped/clamped system to be smaller than the pinned-pinned case. This analysis shows the effective buckling wavelength η_e to be a useful descriptor for complex patterns. Additional comparisons between a beam on a hydrostatic foundation and the theory developed in this chapter are presented in the next chapter.

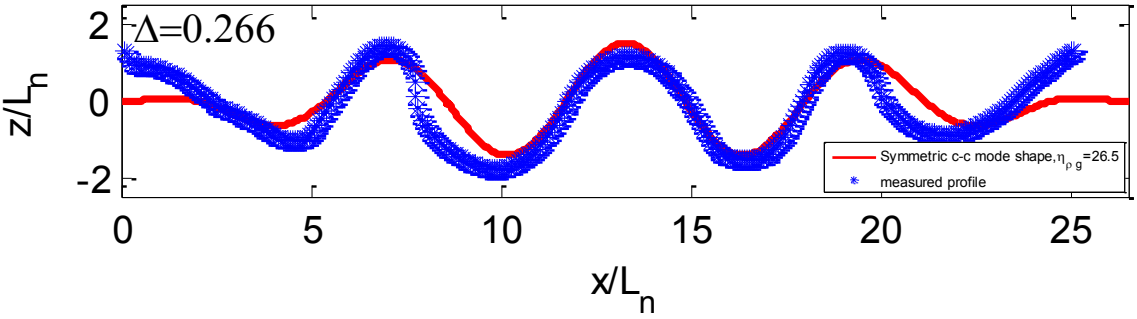

Figure 5.21 Comparison of clamped-clamped mode shape (red) with measured cross-flow profile (blue). Type-1 (HN) seal material at deep immersion, $\Delta = 0.266$, $\delta_s/R_f = 1.14$, $\delta_c/R_f = 1.06$.

Effective foundation stiffness

As indicated in Equation 5.142, buckling wavelength information can also be recast as an effective foundation stiffness K_{f_e}. K_{f_e} for the Type-1 material is shown in Figure 5.22, which confirms that the effective foundation stiffness is greater than or equal to the hydrostatic stiffness ($K_f = \rho g$) across the range of conditions. This effect was illustrated previously in Figure 5.12, which showed a significant disparity between measured and predicted mode shape unless the foundation stiffness was increased. It is not clear as to the physical mechanism responsible for the apparent increase in the foundation stiffness at small confinements. The next section will examine potential contributors to K_{f_e} such as flow-induced tension and

geometric stiffness.

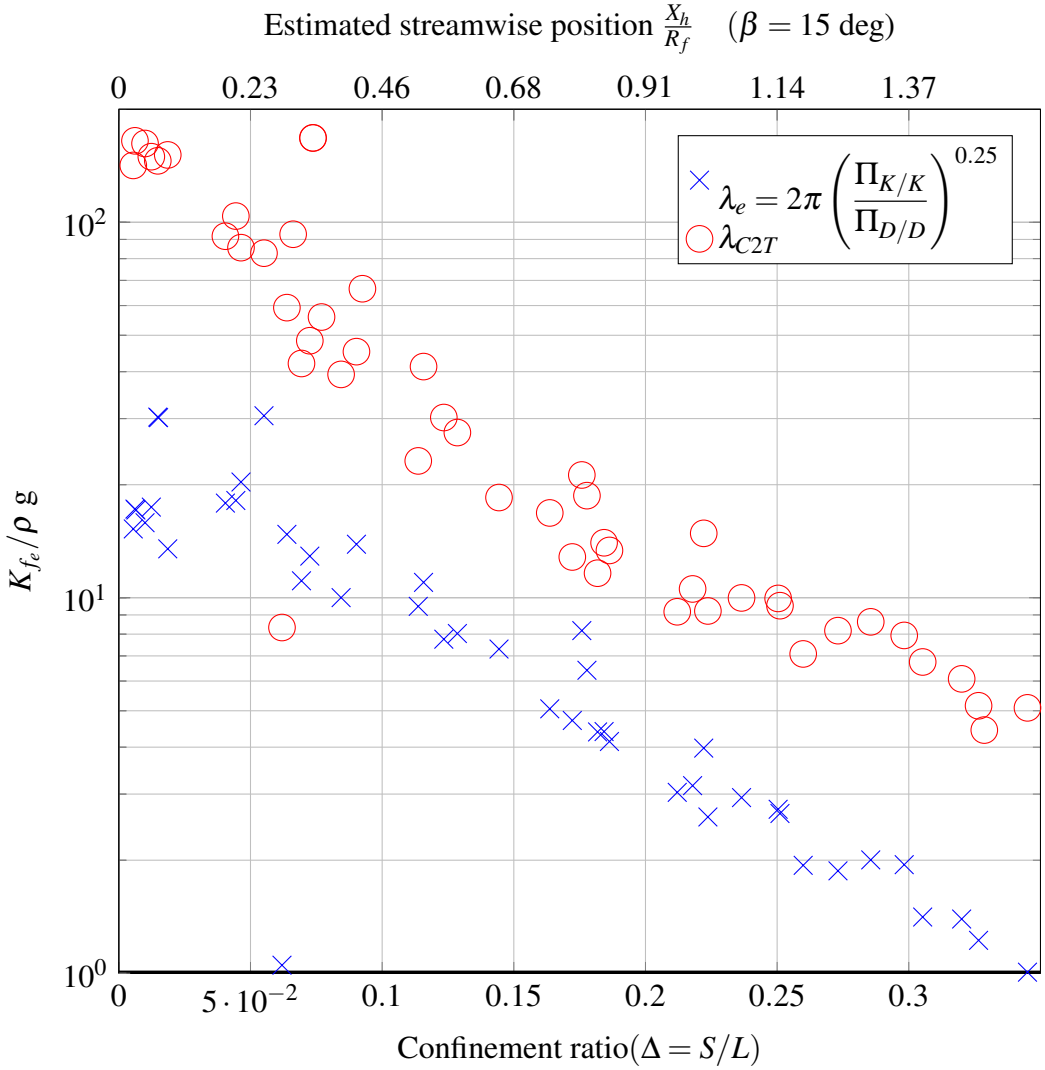

Figure 5.22 Effective foundation stiffness inferred from buckling wavelength ($\frac{K_{fe}}{\rho g} \sim \left(\frac{\lambda_{\rho g}}{\lambda}\right)^4$) with seal compression, Type-1 (HN), *compliant* seal material, fixed ${}^{s}X_{IVC} = 0.75$m, λ estimated using turning point analysis ($\lambda \approx 2L_{C2T}$) and quotient of foundation energy and bending energy

5.6.4 Looking forward: restoring forces and seal response

As seen in Figure 5.12, a significant increase in the local foundation stiffness K_f above ρg is required to match the observed buckling wavelength at small confinements Δ. It is hypothesized that this effect is real, and that to realistically model the small Δ regime additional stiffness components are required. A challenge with the 2-dimensional approach adopted in

the present study is that the response in the streamwise (X_h) and transverse (Y_h) directions are coupled, complicating efforts to reduce the streamwise interactions to a single effective stiffness $K_{f_e}(X_h)$. In particular, at small confinements Δ, the Tail region has not extended past the tangent of the seal and may be strongly influenced by confinement at the curved leading edge. Additionally, as will be shown, many of the hypothesized components in the effective stiffness $K_{f_e}(X_h)$ are velocity dependent. Due to speed limitations, hypotheses on the speed dependence of K_{f_e} cannot be confirmed with the available data.

The approach taken in this section is to study the scaling of the restoring forces in a qualitative model of the Tail region. This is done to uncover features of the effective foundation stiffness K_{f_e} and also to highlight the complex interplay between geometry and hydrodynamics in the Tail region. The scaling arguments developed in this section show that due to boundary conditions at the trailing edge of the seal ($\frac{d^2h}{dX_h} = 0$), and the energetically unfavorable nature of cross-flow curvature κ_{Y_h} in general (the subscript refers to the direction of curvature), consistent with the finding of Section 5.6.3, restoring forces due to buoyancy are expected to dominate near the free trailing edge.

Inspired by centerline profiles of the Type-1 material such as shown in Figure 4.5, the mean state $\bar{h}(X_h, Y_h)$ of the Tail region is taken to be a plane aligned with the mean flow. About this mean state, the instantaneous configuration of the seal is a corrugated sheet with sinusoidal folds whose axes run parallel to the free-stream (see Figure 5.8c). The qualitative analysis in this section studies the structural and hydrodynamic restoring forces that accompany a vertical perturbation from the mean state. The shape of the corrugations is similar to the pinned-pinned mode shape, that is:

$$h(X_h, Y_h) = A sin(\frac{2\pi}{\lambda} Y_h). \tag{5.159}$$

For simplicity the wavelength λ and amplitude A are held constant along the length of the Tail. The cushion pressure p_c is assumed independent of $h(X_h, Y_h)$, the fold elevation. Consistent with the 2-dimensional buckling model developed previously, the transverse or

cross-flow direction (Y_h) is separated from the streamwise direction (X_h). The directions are coupled via the effective foundation stiffness K_{f_e} and in this section via an effective bending rigidity D_I which is intended to capture the gross bending behavior of the corrugations. This separation simplifies the analysis. Because fold slopes $|\frac{A}{\lambda}|$ are finite in the cross-flow direction, as was shown in Section 5.3, a geometrically-nonlinear approach would be required. However, in the longitudinal direction, displacements are relatively small $\frac{\bar{h}}{L_w} \ll 1$ with respect to the wetted length L_w, which is defined loosely as the distance from the hinge ($X_h = 0$) to the trailing edge ($X_h = 0$). These assumptions are most applicable to the compliant Type-1 (HN) material at deep immersions where L_w is large (such as seen in Figure 4.6b).

The trailing edge of the Tail region is free and subject to the mean boundary conditions,

$$\frac{d^2\bar{h}}{d^2X_h}(L_w) = 0 \quad \frac{d^3\bar{h}}{d^3X_h}(L_w) = 0. \tag{5.160}$$

The instantaneous leading edge of the plate is clamped in a sinusoidal form $h(0,Y_h) = Asin(\frac{n\pi}{2R_f}Y_h)$, and $\frac{dh}{dX_h}(0,Y_h) = 0$, where A is the fold amplitude. In terms of mean displacement: $\bar{h}(0) = 0$, and $\frac{d\bar{h}}{dX_h}(0) = 0$. The clamped boundary condition at the leading edge is an approximation as there is evidence (Section 5.2) that rotation, or hinging about the leading edge ($X_h = 0$) is an important degree of freedom.

Equation 5.161 provides the general form of a linearized differential equation describing the mean streamwise response of the seal in the Tail region (Manela and Howe, 2009) per unit width. Equation 5.161 closely resembles the linearized equation for buckling in the cross-flow direction (Equation 5.82) with a number of key differences.

$$D_I\frac{d^4\bar{h}}{dX_h^4} - \frac{d}{dX_h}(T(X_h)\frac{d\bar{h}}{dX_h}) = \Delta p \tag{5.161}$$

$T(X_h)$ is the flow-induced tension which acts in the downstream $+X_h$ direction. The effective bending stiffness D_I is used rather than the measured bending rigidity D as the seal will

develop "geometric stiffness" if cross-flow folds grow sufficiently large in amplitude, A ($D_I \to D$ as $A \to 0$). Δp is the pressure drop across the material. Each of these terms will be described and their scaling discussed.

The effective foundation stiffness is decomposed into four components, which are identified based on the scaling of Equation 5.161. K_I is the geometric stiffness. K_τ is the membrane (viscous) component. The pressure drop Δp is further decomposed into a hydrostatic component, $K_b = \rho g$ (as before) and a hydrodynamic (inviscid) component K_d,

$$K_{fe} \approx \underbrace{K_I}_{\text{from } D_I \frac{d^4 \bar{h}}{dX_h^4}} + \underbrace{K_\tau}_{\text{from } \frac{d}{dX_h}(T(X_h)\frac{d\bar{h}}{dX_h})} + \underbrace{K_b + K_d}_{\text{from } \Delta p}. \tag{5.162}$$

Membrane stiffness component, K_τ

The scaling of the stiffness component K_τ is determined from the membrane term in Equation 5.161, $-\frac{d}{dX_h}(T(X_h)\frac{dh}{dX_h})$. The spatially varying flow-induced tension $T(X_h)$ acts in the downstream $+X_h$ direction. In contrast to the buckling problem (see Equation 5.82), in which F does compressive work, the sign of the tensile $T(X_h)$ of the term in Equation is negative. Because of this, flow induced-tension T is stabilizing, indicated by a positive K_τ.

It is hypothesized that tension $T(X_h)$ in the Tail region is mainly set by the frictional shear stress acting on the seal material. Flow-induced tension is assumed to vary in the streamwise direction, with the tension highest at the hinge ($X_h = 0$),

$$T(x) \approx \int_{x_h}^{L_w} \tau(X_h, Re) dX_h, \tag{5.163}$$

where τ is the shear stress. Because the K_τ stiffness component is primarily a viscous term, it is expected to be dependent on parameters influencing frictional drag such as Reynolds number (Re), velocity (U), surface roughness, and wetted length (L_w).

The manner in which a restoring force due to out-of plane tension enters a 2-dimensional

model can be visualized by considering the local stiffness at a point along a tensioned rope supported at $x = 0$, $x = L$. To second order the stiffness $K_{rope}(x)$ (not stiffness/length such as K_f) at any point can be approximated as $K_{rope}(s) = 0.5T(\frac{1}{x} + \frac{1}{L-x})$ (Biot, 1964). An alternative interpretation is that stiffness K_f is similar to the stiffness matrix that would be associated with a nodal (local) displacement of nonlinear beam element in the finite-element method.

The membrane term $\frac{d}{dX_h}(T(X_h)\frac{dh}{dX_h})$ is cast as a local foundation stiffness using scaling arguments, i.e. $\frac{dT}{dx} \sim T/L_w$ and $\frac{dh}{dx} \sim h/L_w$, where L_w is the wetted length. For examples of similar scaling arguments applied to estimate local restoring forces due to tension see Vandeparre et al. (2011). Cerda et al. considers the problem of a sheet hanging under the action of gravity. In their case, the spatially varying tension is set by gravity and the fabric density.

$$-\frac{d}{dX_h}(T(X_h)\frac{d\bar{h}}{dX_h}) \sim \frac{T(x)\bar{h}}{L_w^2} \tag{5.164}$$

$$K_\tau \sim \frac{T(x)}{L_w^2} \sim \frac{d\bar{h}^2}{dX_h^2} \tag{5.165}$$

To understand how K_τ scales with velocity, a friction-line approach is adopted. As the wetted-length (L_w) based Reynolds numbers range from $90,000 - 3,000,000$, a skin friction coefficient $C_f(Re)$ based on a $1/7$ power-law turbulent boundary layer profile is used, where

$$C_f = 0.0725Re^{-\frac{1}{5}}. \tag{5.166}$$

Based on Equation 5.163

$$T(X_h) \approx 0.5\rho C_f(L_w - X_h)U^2, \tag{5.167}$$

leading to

$$K_\tau \sim \frac{\rho(L_w - X_h)U^2}{L_w^2}. \tag{5.168}$$

The viscous stiffness component K_τ reaches a maximum at the knuckle ($X_h = 0$), where $K_\tau \sim \frac{U^{9/5}}{L_w}$. Evidence from the tablecloth problem (Cerda et al., 2004) suggests that mode number is set by the tension at the table edge, which is equivalent to the Knuckle location in the seal buckling problem. Underwater footage of the Type-1 seal (see Figure 4.6b) may support this interpretation. The images suggest that individual folds emanate from points distributed along the leading edge, where the tension is highest. The number of folds does not appear to change with streamwise position. The individual folds do appear to spread and merge near the trailing edge.

In Chapter 8, Future Work, data-driven approaches for estimating the tension in the seal are proposed. These procedures utilize the curvatures (κ_1, κ_2) derived from the 3-dimensional seal shapes and pressure profiles acquired during the large-scale experiments.

Geometric stiffness component, K_I

In Section 5.1, it was observed that the Tail possesses near-zero Gaussian curvature, with the lines of curvature directed on average in the streamwise direction. As a consequence, deformations which impart curvature in the cross-flow direction, perpendicular to the principal direction, such as $\frac{d^2\bar{h}}{dX_h^2}$ result in non-zero Gaussian curvature and are thus associated with strain (Cerda et al., 2005) at the mid-plane of the seal material. Due to the large tensile modulus of elasticity E_r of the fabric reinforcement, the seal material is highly resistant to cross-flow bending, particularly at large fold amplitudes. As a result, the material likely prefers softer isometric (inextensible) modes, such as hinging. Evidence was presented in Section 5.2 that suggested that the seal hinges at the waterline.

The 2-dimensional model described in this section is not suitable for describing general

isometric (inextensible) deformations that may occur in the Tail region. Instead, the resistance to bending is examined to understand how the material stiffens with fold amplitude. The seal is treated as a corrugated plate characterized by sinusoidal folds

$$h(X_h, Y_h) = Asin(\frac{2\pi}{\lambda}Y_h) \tag{5.169}$$

of amplitude A and wavelength λ in the cross-flow direction. Per Lee and Park (2004), the bending rigidity per unit width of the plate D_I is estimated as

$$D_I \approx \frac{E_t t_t}{1-\nu^2}\frac{1}{\lambda}\int_0^{\lambda/4} A^2 sin^2(\frac{2\pi Y_h}{\lambda})(1+\frac{A^2\pi^2}{\lambda^2}cos^2(\frac{2\pi Y_h}{\lambda}))^{-0.5}dY_h, \tag{5.170}$$

where E_t is the tensile modulus of elasticity of the composite and t_t is the material thickness. Looking at the scaling of the bending term,

$$D_I\frac{d^4\bar{h}}{dX_h^4} \sim \frac{E_t t_t A^3 \bar{h}}{L_w^4}, \tag{5.171}$$

the geometric stiffness coefficient K_I to cross-flow bending (κ_{Y_h}) is estimated to scale as

$$K_I \sim \frac{E_t t_t A^3}{L_w^4}. \tag{5.172}$$

This shows that as fold amplitude A increases, K_I rises dramatically. To visualize this, consider a sheet of paper that has been folded in an accordion fashion. Now apply a bending moment in a direction perpendicular to the folds. Note that the paper prefers to distort in modes other than bending. It is hypothesized that as fold amplitude increases, so does the resistance to bending.

Hydrodynamic stiffness component, K_d

The pressure drop across the seal is assumed to have two components,or

$$\Delta p \approx K_b \bar{h} + K_d \bar{h}. \tag{5.173}$$

The restoring force due to buoyancy is given by the K_b term,

$$K_b = \rho g. \tag{5.174}$$

The hydrodynamic pressure is taken to scale as

$$\Delta p_d \sim -\rho U^2 \frac{d^2 \bar{h}}{dX_h^2}. \tag{5.175}$$

This approximation is employed in fluid-structure problems such as subsonic panel flutter (Dowell, 1975) and flutter in travelling webs (Chang et al., 1991). It follows from Bernoulli's equation and is based on the pressure drop Δp associated with radial acceleration along a streamline with linearized curvature $\frac{d^2\bar{h}}{dX_h^2}$. This is depicted in Figure 5.23. Circulatory contributions to Δp and flow details near the leading and trailing edge are not considered in this crude hydrodynamic model. The sign of the hydrodynamic contribution is such that a downward pressure (-) is developed for a concave-up ($\frac{d^2\bar{h}}{dX_h^2} > 0$) profile. As a result, when brought to same side of the force balance as the membrane K_τ term and differentiated,

$$K_d \sim -\frac{\rho U^2}{L_w^2}, \tag{5.176}$$

K_d is found to have a destabilizing effect – unlike the other stiffness components previously discussed.

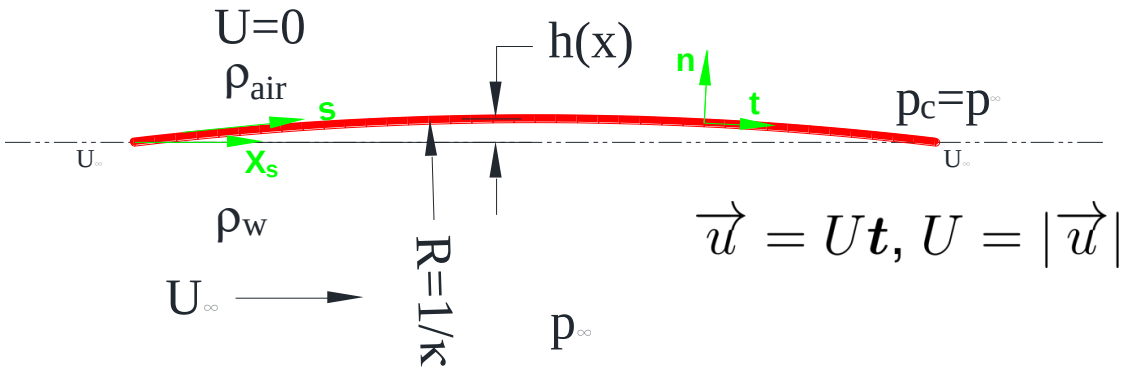

Figure 5.23 Streamline-based coordinate system

Discussion

Assembling the stiffness terms, the total effective foundation stiffness K_{fe} is found to comprise the following:

$$K_{fe}(X_h) \sim \underbrace{\frac{c_1 E_t A^3}{L_w^4}}_{K_I \sim \frac{d^4}{dX_h^4}} + \underbrace{c_2 \frac{\rho(L_w - x)U^{\frac{9}{5}}}{L_w^2}}_{K_\tau \sim \frac{d^2}{dX_h^2}} + \underbrace{\rho g}_{K_b} - \underbrace{c_3 \frac{\rho U^2}{L_{w^2}}}_{K_d \sim \frac{d^2}{dX_h^2}}, \tag{5.177}$$

where c_1, c_2 and c_3 are arbitrary constants. Qualitative at best, Equation 5.177 indicates a number of forces at work in the Tail region. Except for the destabilizing effect of the hydrodynamic term K_d, the other components of K_{f_e} act to increase stiffness above the hydrostatic stiffness $K_b = \rho g$. All restoring forces except buoyancy are dependent on the curvature $\frac{d\bar{h}^2}{dX_h^2}$ (K_I through the bending moment). This is significant for a number of reasons. First, at the free trailing edge ($x_h = L_w$), boundary conditions stipulate that $\frac{d^2\bar{h}}{dx^2}(L_w) = 0$. Because of the $\frac{d^2\bar{h}}{dX_h^2}$ dependence, the only local stiffness component to persist at the trailing edge is that due to buoyancy K_b. In addition, recalling Equation 5.163, $T(x)$, the flow-induced tension, is expected to vanish near the trailing edge as well; this also suggests that $K_\tau \to 0$ as $X_h \to 0$. The dominance of K_b near the trailing edge is consistent with the observations shown in Section 5.6.3 for the Type-1 (HN) material which show that for $x_h > 0.8(\Delta > 0.2)$, $K_f \to K_b$.

It also suggests that deformations which do not change $\frac{d^2\bar{h}}{dX_h^2}$ (Gaussian curvature $\kappa_G = 0$) may be energetically favorable. Configurations that satisfy this requirement are those whose lines of curvature remain straight. Examples of possible "isometric" (Cerda et al., 2005) deformations observed during the experiments include hinging about $x_h = 0$ and translation of buckling packets in the cross-flow direction.

The amplitude dependence of the geometric stiffness K_I suggests that the balance of forces changes significantly with condition. It was observed that in most cases folds persisted along straight lines of curvature from the hinge. However, at deep immersions, it was found that fabric pooled near the vertical sides of the seal. The remaining fabric, $A \approx 0$ seemed to conform and bend along with the free-surface. This type of behavior was not observed at large fold amplitudes. At small amplitudes, there is also the potential, depending on interactions between the restoring forces, for $K_{fe} \to 0$. This would represent a case of static divergence (Kornecki, 1976). It is not clear whether divergence occurs within the parameter range of the large-scale data, however due to A^3 in the K_I term, divergence may be self-limited to fairly small amplitudes.

Equation 5.177 indicates that under most conditions the effective foundation stiffness K_{fe} is set by a number of variables, including the geometry, material properties, velocity, fold amplitude and the wetted length. Because of this, it is very difficult to isolate particular physical mechanisms at work within K_{fe}. Equation 5.177 also suggests that dynamic similitude for the effective stiffness is difficult to maintain at small scale, as it would require similarity between Froude number ($\sim \frac{K_b}{K_d}$), Reynolds number (K_τ) and geometry (strain) (K_I). These speed dependent distortions further complicate the small-scale material selection process described in Section 2.5.1, where it was shown that at zero-speed (only K_b is present) the required bending rigidity for viable scale factors lies outside the range of commercially available fabrics. In Chapter 6, a benchtop experiment is presented which permits independent control of the confinement Δ and the foundation stiffness K_f.

5.7 Conclusions

This chapter develops a framework for interpreting the dramatic changes in seal configuration observed in the large-scale experiments.

First, in Section 5.1, curvature-based measures are developed to understand the balance of bending and stretching forces in the seal. These measures are then applied to the 3-dimensional seal shapes acquired as part of Study 1. Based on this analysis, the seal is decomposed into three regions, which are denoted the Cylinder, Knuckle and Tail regions (see Figure 4.4). Analysis of Gaussian curvature indicates that in the Knuckle region, large pressure gradients and material confinement combine to create localized areas of strain. In contrast, the Tail region, characterized by single curvature, undergos largely inextensible (isometric) deformations. The Tail region, which often comprises a significant portion of the seal in contact with free surface, is the focus of the chapter.

Next, in Section 5.2 the kinematics of the Tail region are studied. It is found that the seal behaves as if it were hinged about the local waterplane. Consistent with this analogy, the measured cross-flow confinement ratio Δ,

$$\Delta = \frac{\mathcal{S}}{L_{arc}}, \tag{5.178}$$

defined as the local transverse displacement of the material ($\mathcal{S}$), divided by the total arc-length (L_{arc}), is found to increase almost linearly with the local draft δ_s and with streamwise position relative to the forward hinge X_h. The parameter Δ is also influenced by the cushion pressure via the wave-rise, which consistent with linear theory was found to vary linearly with the pressure p_c.

Due to the inextensibility of the seal material, the confinement ratio is closely tied to the amplitude of the post-buckled mode shape. A power-law relationship is predicted, based on the assumption of small-slopes,

$$\frac{A}{\lambda} \sim \Delta^{0.5}, \tag{5.179}$$

where A is the amplitude and λ is the buckling wavelength. In both the Type-1 (HN) and Type-0 (NN) materials the $\frac{A}{\lambda} \sim \Delta^{0.5}$ scaling is observed. The agreement is better for the compliant Type-1 seals. The results for the Type-0 material exhibit considerable scatter. Similar $\frac{A}{\lambda} \sim \Delta^{0.5}$ power-law type behavior is observed in the benchtop experiments to be discussed in Chapter 6 and is also reported across a range of physical scales by other researchers, encompassing diverse systems such as sea ice, biological membranes, curtains and nano-structures (Brau et al., 2010).

To understand how the cross-flow buckling wavelength λ is set, a 2-dimensional model of the Tail region based on a beam-on-an-elastic foundation (BoF) is developed. The BoF, a classical problem of elastic stability, is used to identify potential dimensionless parameters driving the cross-flow response. Of particular importance is

$$\eta = \frac{L}{L_n} = L(\frac{K_f}{D})^{0.25}, \tag{5.180}$$

the system size L as non-dimensionalized by the natural buckling length L_n. L_n is the natural length-scale at which bending (strain) and foundation energies are balanced and is given by $L_n = (D/K_f)^{0.25}$, where D is the bending rigidity and K_f is a foundation stiffness. The natural wavelength is related to the buckling length as $\lambda = 2\pi L_n$. At zero-speed the foundation stiffness K_f is given by the hydrostatic stiffness $K_f = \rho g$.

In Section 5.4, the linearized form of the BoF model is examined. This analysis shows that the non-dimensional system size η is closely tied to mode number m and to the relative effect of boundary conditions. Small system sizes η are found to be strongly influenced by the boundaries, while large system sizes η are insensitive to boundary conditions and often prefer localized responses (Hunt et al., 1989). Corner folds with curvatures typical of deep immersions are found to impose a clamped-like boundary condition. This may explain why amplitude modulation is observed in the cross-flow profiles. There is also evidence that the clamped seal edges may influence the symmetry of fold configurations. Along the critical

buckling load path, the clamped-clamped BoF favors symmetry-preserving m+2 bifurcations. However, it is not clear why Type-0 finger seals prefer symmetric configurations over asymmetric configurations that may be energetically favorable.

In Section 5.5, the stability of pinned-pinned configurations to perturbations is examined. The Koiter stability criteria is applied to study variations in the total system energy in the neighborhood of the equilibrium configuration. Stability is found to be set by the mode number (m) relative to system size η,

$$\eta < \frac{\pi m}{5^{0.25}}. \tag{5.181}$$

The stability analysis indicates that along the critical buckling path, the pinned-pinned BoF is unstable for all mode numbers except $m = 1$. This is qualitatively similar to the observed behavior, which showed a significant increase in mode-switching behavior at mode numbers above $m = 1$. The stability analysis also suggest that due to their buckled nature, bow seals are susceptible to a loss of static stability that is distinct from stability types typically encountered in fluid-structure interaction problems. In Chapter 8, it is proposed that the stability analysis be extended to include more realistic boundary conditions. This analysis may help identify the physical mechanism responsible for the wear causing vibrations.

Within the BoF framework, many of the features of the Type-1 seal appear to exemplify large system size η ($\eta_{\rho g}|_{R_f} \approx 30.3$) behavior ($|_{R_f}$ refers to η as estimated from the seal diameter). Conversely, many features of the Type-0 seals appear to exemplify small η, ($\eta_{\rho g}|_{R_f} \approx 8.56$) behavior. In order to support further analysis, guidance is required in the selection of suitable model parameters such as η_e and the effective foundation stiffness K_{f_e}. To do this, a global energy method is developed to estimate the effective system size η_e from the cross-flow profile. L_e is defined as the length that balances bending $\Pi_{D/D}$ and

foundation energies $\Pi_{K/K}$. From this, the effective system size η_e is estimated as:

$$\eta_e = \frac{L}{L_e} = L\left(\frac{\int_0^L (\frac{d\theta}{ds})^2 ds}{\int_0^L h(s)^2 cos(\theta) ds}\right)^{0.25}, \tag{5.182}$$

where θ is the tangent angle and s is the arc-length in the parametric representation of the seal profile. When η_e is estimated for the Type-1 buckling profiles an interesting feature is observed; for $\Delta > 0.2$ ($x_h > 0.8$) the system responds at the hydrostatic buckling length $\lambda_{\rho g}$, suggesting that buoyancy is a significant restoring force in this regime. However, below $\Delta = 0.2$ there is a significant increase in the apparent stiffness K_{f_e} to around $20\rho g$. It not clear the reason for this transition and it requires further study.

Lastly, in Section 5.6.4 scaling arguments are employed to try to understand the physical mechanisms responsible for the apparent increase in stiffness at small confinement ratios Δ. This analysis shows that stiffness K_τ associated with the flow-induced tension $K_\tau \sim \frac{T}{L_w^2}$ acts to increase the total effective stiffness K_{f_e}. Conversely, the inviscid component $K_d \sim \frac{\rho U^2 {}^2}{L_w}$ acts to decrease the effective stiffness, creating the potential for static divergence. Both viscous (K_τ) and inviscid (K_d) contributions to K_{f_e} are found to scale with cross-flow curvature $\frac{dh^2}{dX_h^2}$. It is argued, that because curvature vanishes at the free trailing edge, both K_τ and K_d must vanish as well. This may begin to explain why hydrostatic effects were observed to dominate for $x_h > 0.8$. In addition, because cross-flow bending requires stretching, the analysis suggests that isometric (inextensible) deformations where lines of curvature remain straight are energetically favorable in terms of the restoring force, particularly as fold amplitude increases.

Due to the complex geometry and number of competing factors, it is difficult to isolate the physical mechanisms responsible for the apparent increase in foundation stiffness K_{f_e} observed at small Δ. In the next chapter, a benchtop experiment is described which offers explicit control of the system size, confinement and foundation stiffness. This will be used to verify some of the scalings developed in this chapter.

Chapter 6

Experimental evaluation of the cross-flow model

6.1 Benchtop experiment: buckling in presence of known stiffness

6.1.1 Experimental method

In order to verify the scalings for amplitude and wavelength introduced in Chapter 5 a series of benchtop buckling experiments were conducted. Buckling in the presence of a known foundation stiffness ($K_f \approx \rho g$) was induced using the experimental setup shown in Figure 6.1. A material sample of known size and bending rigidity is suspended on the free-surface and uniaxially compressed via a manual translation stage. The sample is clamped between a pair of knife edges to approximate a pinned-pinned boundary condition (Singer et al., 1998). As the ends are moved closer, the buckled profile away from the lateral boundary is measured with the linescan camera previously utilized in the large-scale experiments and described in Section 5. Photographs such as reproduced in Figures 6.2 (Type-1) and 6.3 (Type-0) are acquired and post-processed to the determine the buckling profile at the wall and to assess whether blistering has occurred. Blistering (Wagner and Vella, 2011) is the tendency of the system at large Δ to favor configurations separated from the free-surface. An example of a blistered profile can be seen in Figure 6.4. While the blistering phenomenon may be related to the physical mechanism responsible for air leakage in bow seals, the model

described in Section 5.3 would have be modified to include a discontinuous foundation in order to begin to capture this effect.

Blistering aside, the buckling profiles are then post-processed to identify local extrema which are used to track the evolution of buckling wavelength (λ) and fold amplitude (A) with compressive transverse displacement (Δ). To understand the influence of Δ on the balance of bending and foundation energies, estimates of these energies are made integrating along the profile length. As these quantities require higher-order derivatives which tend to amplify noise, non-linear curve fitting is employed to smooth the profiles.

In contrast to the large-scale experiments, where the effective transverse displacement ($\Delta = \mathcal{S}/L$) of the seal was found to be dependent on a large number of factors including streamwise location, cushion pressure (via the wave rise), immersion and free-surface slope, the benchtop experiment shown in Figure 6.1 affords independent control of the compression. Similarly, the foundation stiffness (K_f) and system size ($\eta = \dfrac{L}{L_n}$) can be controlled. Extending the beam on an elastic foundation analogy, the hypothesized effect of velocity on

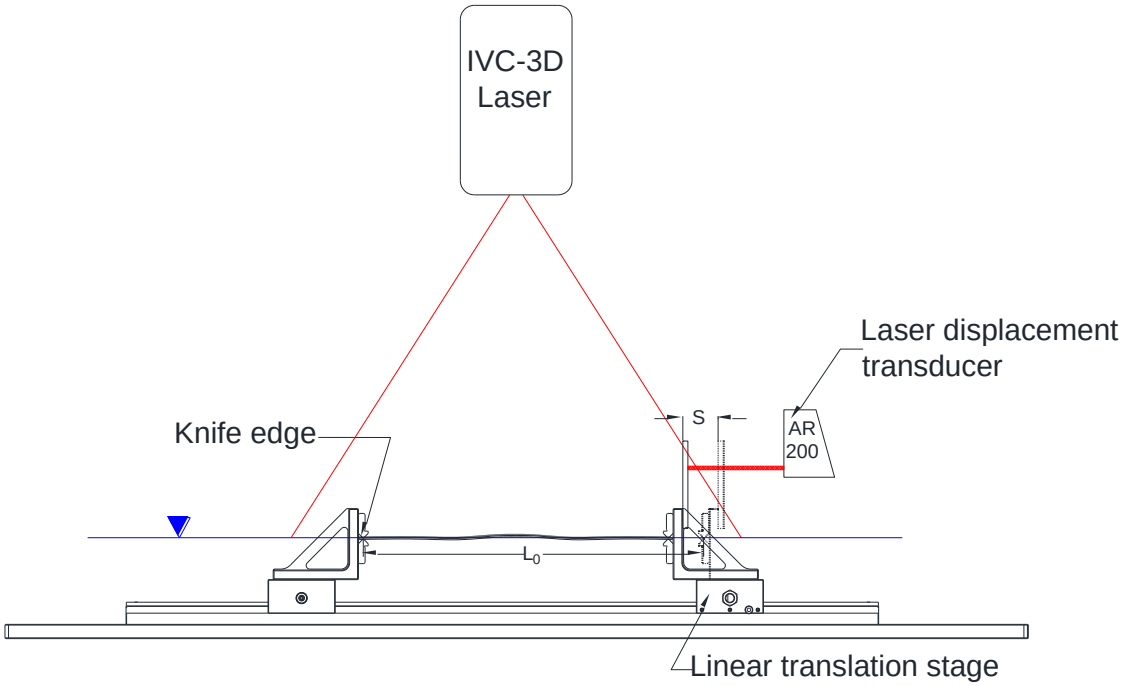

Figure 6.1 Schematic of benchtop experiment for measuring buckling length in presence of hydrostatic foundation $K_f = \rho g$

the foundation stiffness can be visualized as a change in system size (beam length) and/or a change in fluid density.

The buckling experiment was repeated across a range of bending rigidities ($D = 10^{-6} - 10^{-3}$ N m^2 /m). In addition to the orthotropic Type-0 (NN) and Type-1 (HN) materials from the large-scale experiments, isotropic samples were also tested. The isotropic samples (N0,N1,N2) were composed of nitrile or Buna-N rubber, the coating of the composite NN sample. A extremely flexible silicone sample, S0 ($D = 10^{-6}$) was also tested to verify the scaling for a very compliant material. Properties for the materials tested are shown in Table 6.1.

Detailed information on the bending moment versus curvature relationship for the materials was obtained through a specialized bending length test procedure developed as part of the effort (see Appendix A). The bending rigidities of all the samples except Type-0 (NN) and N2 overlap with the experimental work of Pocivavsek et al. (2008). These two materials are markedly stiffer and heavier than those used by Pocivavsek et al. (2008). Testing of these relatively heavy samples (NN, and N2) posed problems as they were susceptible to sinking and required a longer test bed to reduce the effect of boundary conditions. The study also differs from Pocivavsek et al. (2008) in that relatively small system sizes were also examined. Fluid density was held constant throughout the experiments.

It was found that the samples could be prevented from sinking by coating both sides of the material with a commercial hydrophobic coating (Rustoleum Neverwet®) employing surface-tension to help support the fabric. The coating on the top surface increases the ability of the material to shed water which enables a larger range of Δ before sinkage. Because the magnitude of the surface tension σ_T is significantly less than the compressive force needed to buckle the material $F \approx 2(\rho g D)^{0.5}$ for all samples except for the silicone(S0), the effect of surface tension is expected to be small and confined to a region of length $L_{cap} = \dfrac{\sigma_T}{\rho g}$ near the free edge (Huang et al., 2010). Also, because the buckling profiles are acquired at centerline well away from the boundary, edge effects are minimized. The hydrophobic

Abbreviation	Coating	Base Fabric	t_t (mm)	Direction	L (mm)	$D = \frac{dB_m}{d\kappa}$(Nm^2/m)	$L_{\rho g} = (\frac{D}{\rho g})^{0.25}$ (mm)	$\eta_{\rho g} = \frac{L}{L_{\rho g}}$ (avg warp/weft)
NN	Nitrile	Nylon	1.59	Warp(X)/Weft(Y)	305,508	$4.10 \cdot 10^{-3} (3.56 \cdot 10^{-3})$	25.4(24.6)	12,20
HN	Hypalon	Nylon	0.24	Warp(X)/Weft(Y)	305,508	$6.17 \cdot 10^{-5} (3.38 \cdot 10^{-5})$	8.91(7.66)	36,72
N0	Nitrile	None	0.79	N/A	102,203,305,406,508	$7.20 \cdot 10^{-4}$	16.5	6,12,18,24,30
N1	Nitrile	None	1.59	N/A	305,508	$2.76 \cdot 10^{-3}$	23.0	13,22
N2	Nitrile	None	2.38	N/A	305,508	$3.55 \cdot 10^{-3}$	24.5	12,20
S0	Silicone	None	0.25	N/A	305	$1.75 \cdot 10^{-6}$	3.68	20.8,41.7,62.5,83.3

Table 6.1 Benchtop experiment: test plan for buckling in the presence of a hydrostatic foundation.

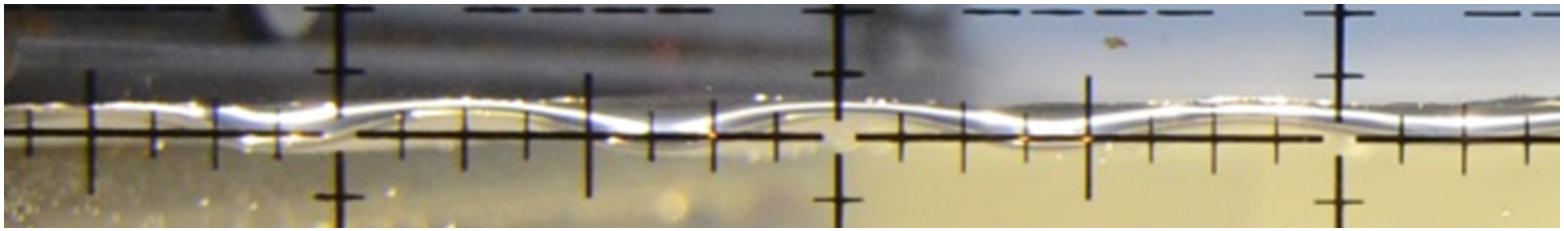

(a) Silicone (S0) sample, $\eta = 43$.

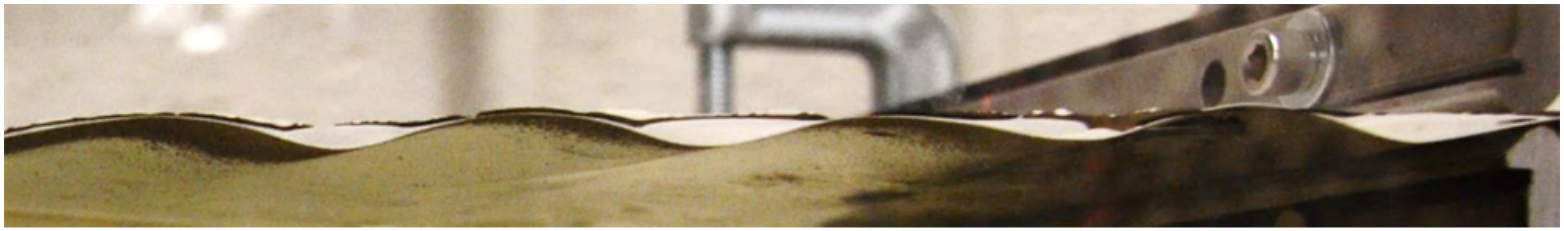

(b) Type-1 (HN) sample, $\eta = 57$.

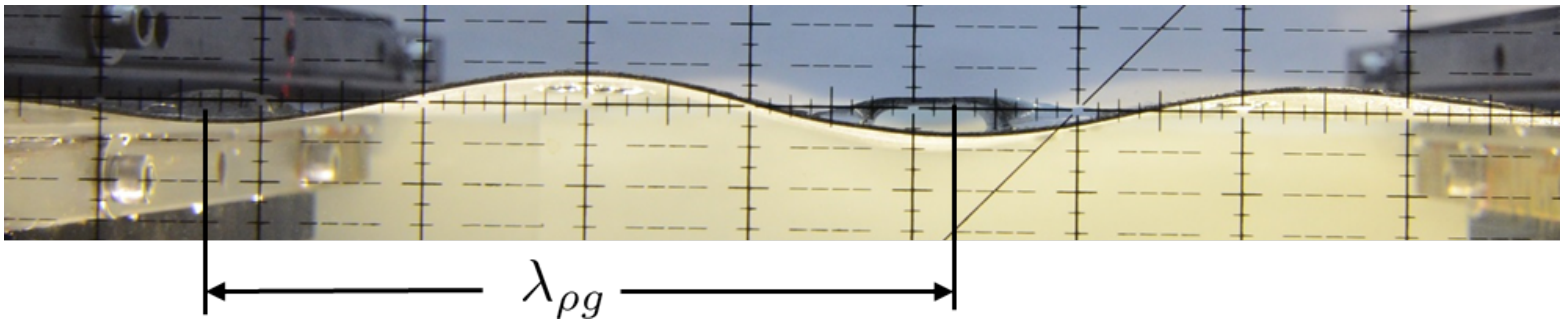

(c) Isotropic nitrile (N0) sample, $\eta = 19$.

Figure 6.2 Distributed buckling patterns for silicone (S0) (a), Type-1 (HN) (b) and isotropic nitrile (N0) (c) samples. Measured wavelength (λ) compares favorably to natural buckling wavelength $\lambda_{\rho g}$ as estimated based on a hydrostatic foundation of stiffness $K_f = \rho g$ and bending rigidity, D from the bending length experiment (see Figure 6.11).

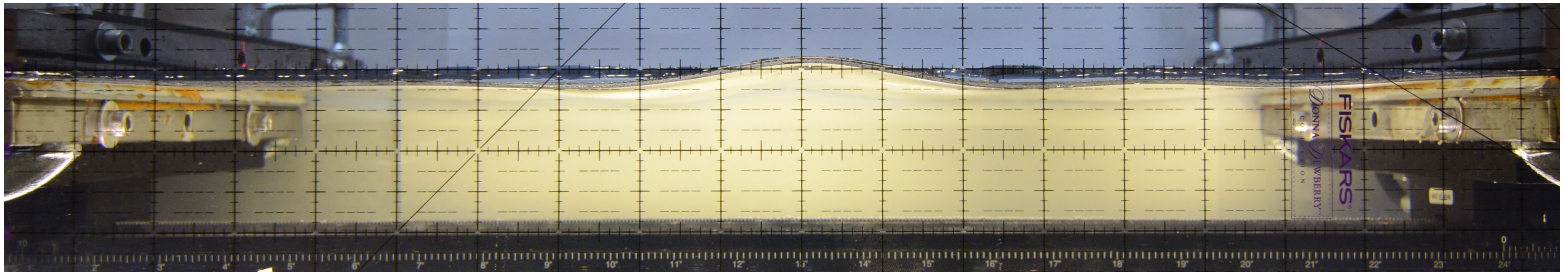

(a) Type-0 (NN) sample, compressed in weft(Y) direction, $L = 508$ mm, $\eta = L/L_{\rho g} = 20.6$.

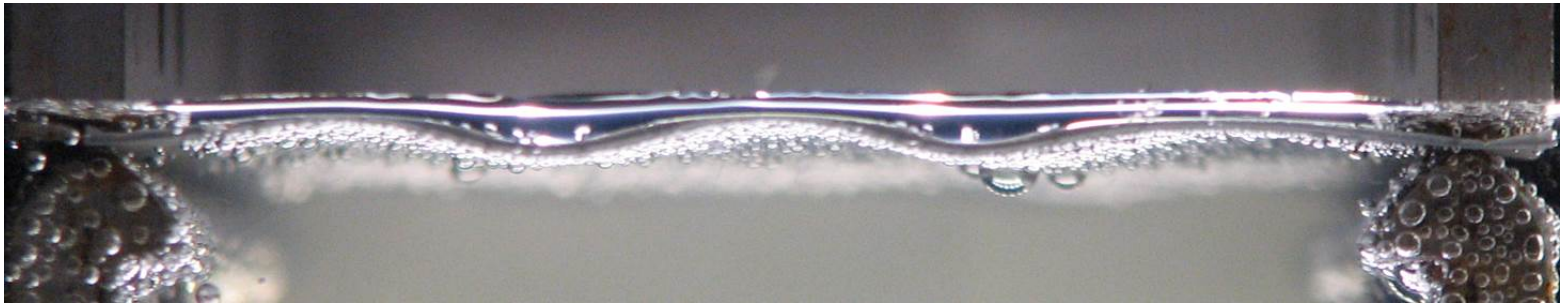

(b) Silicone (S0) sample, $L = 76.2$ mm, $\eta = L/L_{\rho g} = 20.8$.

Figure 6.3 Finite-width post-buckled shapes. Type-0 (NN) (a) and silicone (S0) (b) samples. Despite bending rigidities between (a) and (b) differing by $2 \cdot 10^3$, owing to both systems having roughly the same non-dimensional system size η, mode shapes are similar. Fold slope (A/λ) of S0 sample is higher than NN sample owing to larger relative confinement Δ.

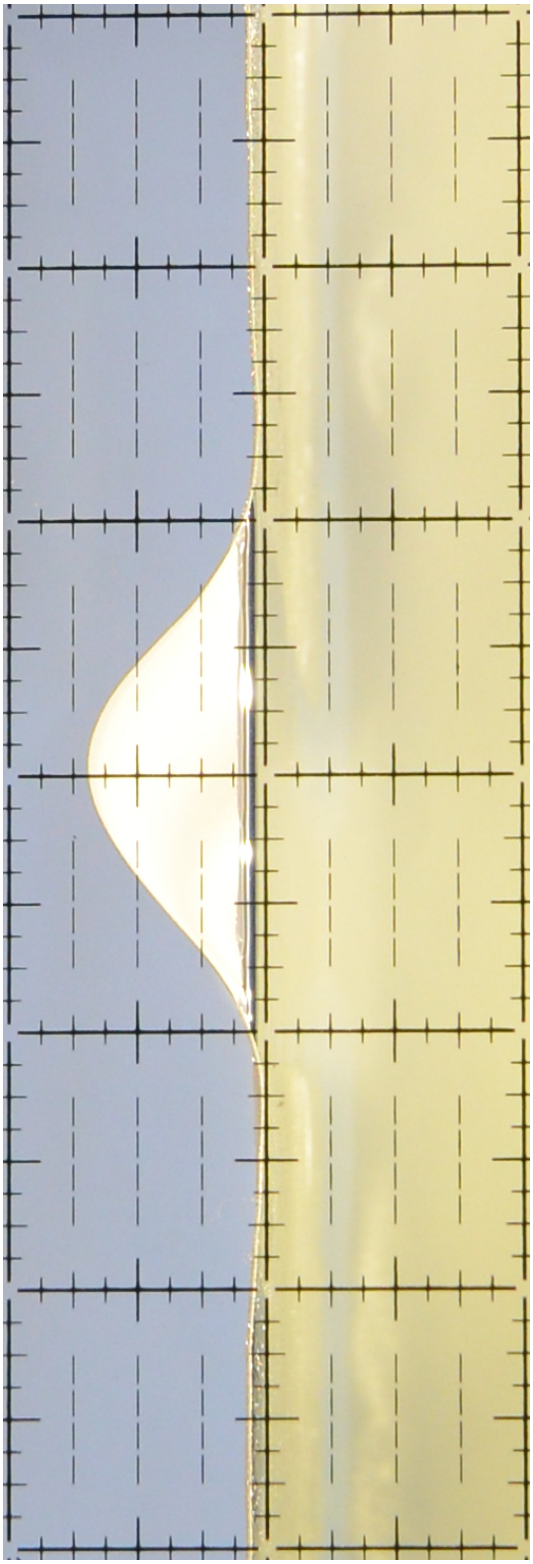

Figure 6.4 Blistered profile. Type-1 (HN) sample, $\eta = 57$, $\Delta = \mathcal{S}/L = 0.02$ (see Figure 6.8).

coating was not used on the more compliant Type-1(HN) and S0 samples as it tended to increase the likelihood of the material separating from the free-surface (blistering).

6.1.2 Test Plan

The test plan is provided in Table 6.1. To maximize the effective system size η[1] achievable with the test setup (L=508 mm), pinned-pinned boundary conditions were imposed for all tests. Realizing pinned-type boundary conditions experimentally is challenging; in practice the actual boundary conditions are between pinned-pinned and clamped (Boucif et al., 1991) which can significantly impact mode shape particularly for small system sizes (Everall and Hunt, 1999). Another artifact of the experimental set-up was that the fabric was restrained at the clamps from expanding laterally (due to Poisson's effect) introducing an out-of-plane stress. Due to the relatively large sample sizes evaluated, this effect is expected to be confined a small segment of the total sample width, localized to the immediate vicinity of the clamps.

Physical system size varied from 102 mm to 508 mm. The width of samples was 305 mm for all samples. The non-dimensional system size $\eta_{\rho g}$ ranged from 6 for the nitrile (N0) sample to 139 for silicone. This corresponds to linearized mode numbers ($m_{\rho g} = \frac{\eta_{\rho g}}{\pi}$) from 1 to 44. Despite the asymptotic behavior of the differential equations governing the beam on an elastic foundation, finite width effects were experienced for the longest samples of the Type-0 (NN) and N2 samples even at $\eta_{\rho g} = 20$. (This can be seen in Figure 5.18 which shows the critical buckling load as a function of system size.) The rate at which the critical buckling load approaches the infinite plate solution $F_c = 2(K_f D)^{0.5}$ is dependent on the boundary conditions (Everall and Hunt, 1999). In the simply supported case, at $\eta_{\rho g} = 20$ the critical load is almost exactly the solution for the infinite plate. In the clamped-clamped case, F_c decays much slower and remains 6% higher than the infinite plate solution at $\eta_{\rho g} = 20$.

[1]For instance, the "effective" length of a pinned-pinned Euler column in terms of load carrying capacity is twice that of clamped-clamped column (Jones, 2006).

The finite-width effect confounds interpretation of buckling profiles such as in Figure 6.3. In the finite width regime, the buckling profile is amplitude modulated with the shape of the envelope set by the physical length scale and the width of the boundary layer near the support (Audoly, 2010; Walton, 1999; Rivetti and Neukirch, 2014). In the case of an infinite floating beam that has degenerated into a localized response, the envelope shape is set by the natural buckling length (λ_n) rather than the physical length scale (Diamant and Witten (2011)).

6.1.3 Results

Mode shape

The test procedure consisted of imposing a known axial displacement ($\mathcal{S}$) to a sample of uncompressed length (L). At each displacement buckling profiles and still images were acquired. Due to rapid changes in material configuration near the critical buckling load, small increments in displacement had to be executed ($dS \approx 0.25$ mm). Figure 6.5 shows the evolution of a typical sample as the relative compression Δ is increased. The right edge of the sample is compressed in the -X direction. The sample installed in this case is N2, an isotropic nitrile sample with bending rigidity at small curvatures $D \approx 3.55 \cdot 10^{-3}$ Nm which is approximately the same bending rigidity as the Type-0 material ($D \approx 3.56 \cdot 10^{-}3$ Nm) in the weft (Y) direction used during the large-scale experiment. The N2 sample has an uncompressed length $\eta = \frac{L}{L_{\rho g}} = 20.6$. Under the end displacement the material buckles almost immediately. After the initial bifurcation the material assumes a nearly sinusoidal shape consistent with a pinned-pinned boundary condition (Equation 5.106). Because the inception of buckling occurs at very small confinement ratios (Δ), the amplitude (A) of the sinusoidal shape is very small ($A \sim \Delta^{0.5}$) and may only be observable with the linescan camera. However as transverse displacement is increased, a large central fold develops and the mode shape becomes amplitude modulated with the width of the envelope decreasing

near supports. It is hypothesized that this amplitude modulation is due to the knife edges restricting rotation, causing the system to behave as if it were clamped at larger slopes.

This hypothesis is further supported by Figure 6.6, which shows the buckled shape for the same N2 material at a smaller system size, $\eta = 12$ than Figure 6.5 ($\eta = 20.6$). Similar to Figure 6.5 the mode shape for $\eta = 12$ is amplitude modulated and symmetric. Commensurate with the change in system size, mode number decreases from $m = 5$ to $m = 3$. For comparison, the symmetric mode shape ($\eta = 12$) with the lowest total potential energy based on linear theory and clamped-clamped boundary conditions is also shown. Good agreement between the predicted mode shape and the experimental data suggests that pinned-pinned boundary conditions are not enforced by the knife edges.

The prevalence of symmetric solutions is somewhat surprising as linear theory predicts a slightly smaller (0.5%) critical buckling load F_c and thus total potential energy at $\eta = 12$ if the system were to assume an asymmetric "even" configuration[2]. It is also not clear as to the mechanism responsible for the material favoring configurations with the large central fold directed "up" and away from the free-surface; the "up" configurations are equivalent to "down" configurations in terms of total potential energy. Recalling large-scale experimental data such as presented in Figure 4.13, symmetric "up" configurations similar to Figure 6.6 were also favored during the large-scale experiments. Mode shapes at $\eta = 12$ are reminiscent to those observed for the Type-0 (NN) material during the large-scale experiments ($\eta_{\rho g} \approx 8.6$). This is consistent with the view that hydrostatics are a significant component of the restoring force at the large-scale test velocities. A potential difference between the large-scale experiments and the benchtop experiment is that bow seals operated at significantly larger confinements Δ than can be achieved with the benchtop experiment. However, this doesn't significantly limit the comparisons that can be made, as there is evidence presented in Figure 4.16 that mode number is largely independent of the shortening (Rivetti and Neukirch, 2014).

[2]One potential explanation is that the mass of the fabric, similar to a catenary, introduces symmetry in the initial undisturbed configuration which is preserved upon compression.

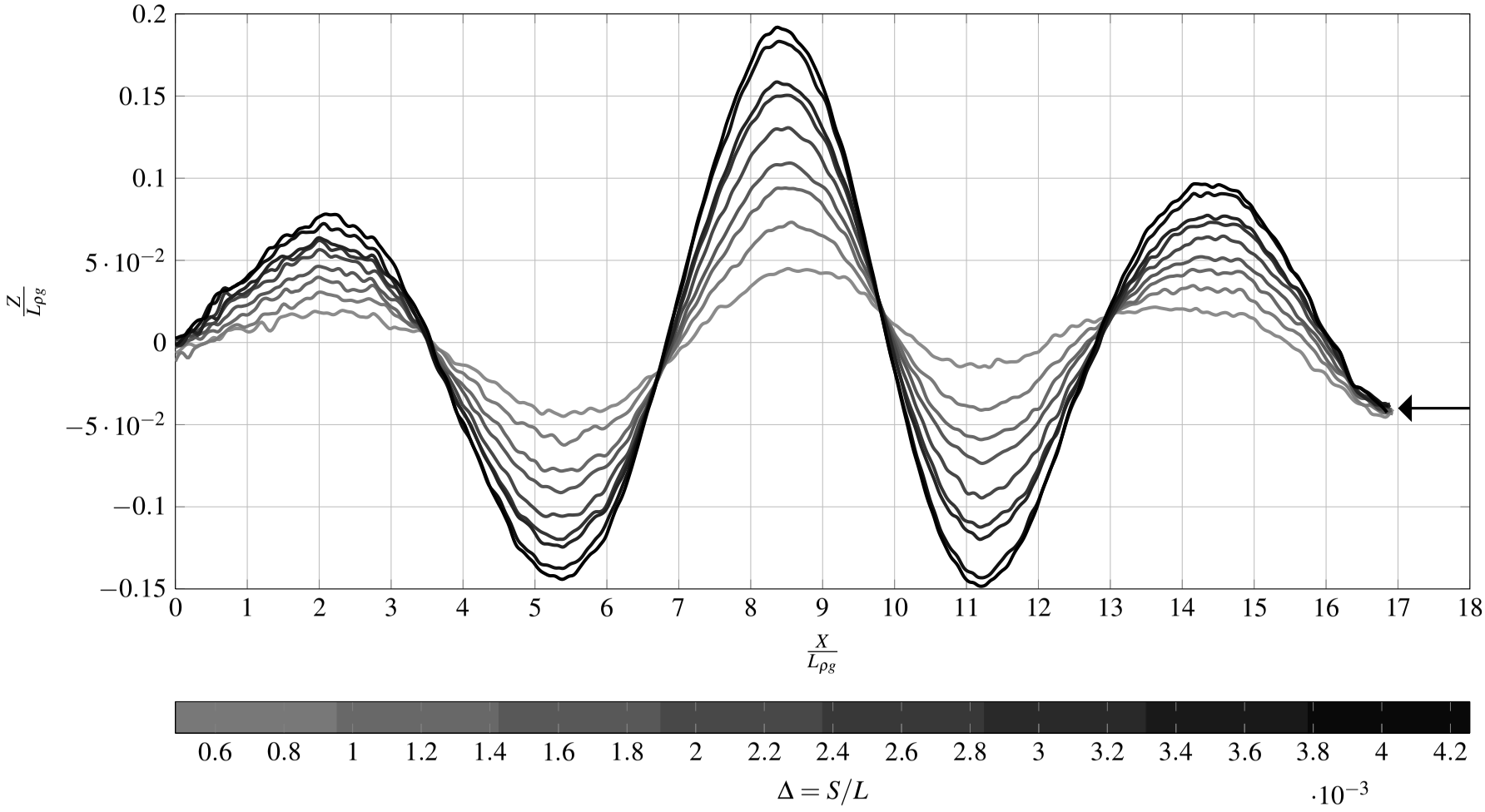

Figure 6.5 Sequence of post-buckled shapes acquired during benchtop experiment, isotropic nitrile (N2) material, system size (to knife edges) $\eta_{\rho g} = 20.6$, $\Delta = 0.5 \cdot 10^{-3} - 4.2 \cdot 10^{-3}$.

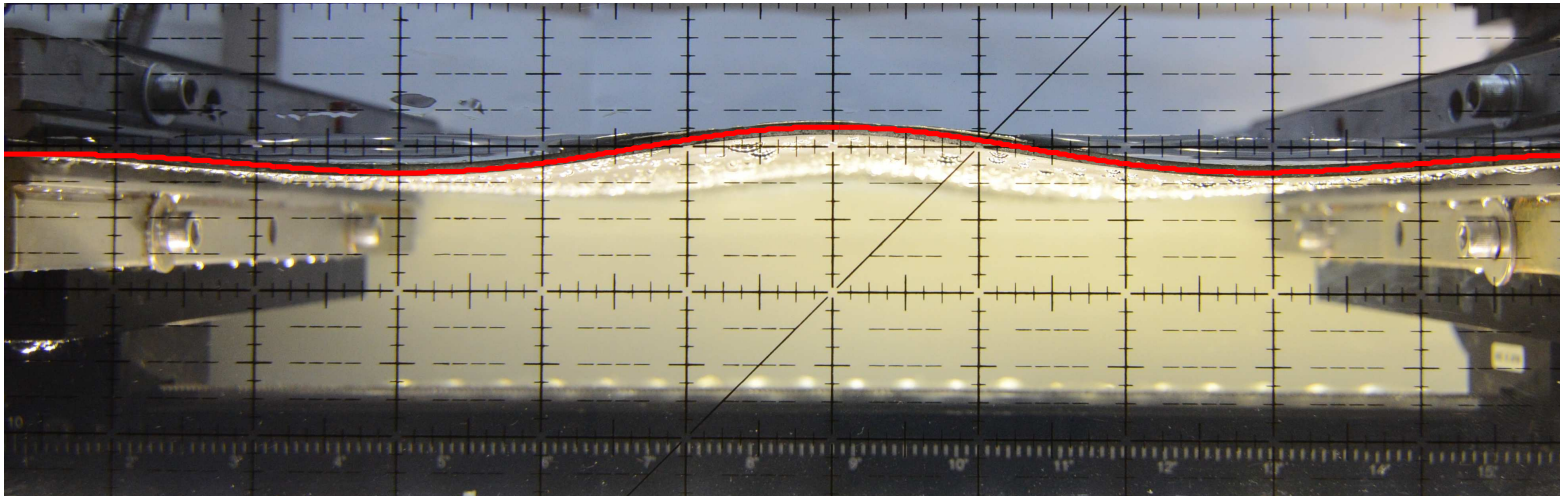

Figure 6.6 Post-buckled shape, isotropic nitrile (N2) material, system size $\eta = L/L_{\rho g} = 12$, $\Delta = 0.0043$. ——, is the symmetric linear solution for a clamped-clamped beam on a foundation of stiffness $K_f = \rho g$ (Equation 5.106). Amplitude modulation suggests that pinned-pinned boundary conditions are not achieved by the knife edges (restricting rotation) and the material behaves as if it were clamped. The measured buckling wavelength (λ) closely matches linear theory ($\lambda_{\rho g}$). Because the amplitude of the mode shape is indeterminate in linear theory, an arbitrary amplitude is applied. A rough estimate of mode amplitude (A) is given by $A \approx \frac{\sqrt{2}}{\pi}\lambda_{\rho g}\Delta^{0.5}$ (Cerda and Mahadevan, 2003).

Effect of confinement (Δ) on system energy

To better understand the balance of forces at work and the role of seal confinement Δ in setting the total energy of the static system, the potential (strain) energies due to bending (Π_D) and the foundation (Π_K) are computed. The geometrically nonlinear forms for (Π_D) and (Π_K), previously presented in Chapter 5 are employed. The foundation stiffness is taken to be $K_f = \rho_w g$. The dimensional bending rigidity, D is based on the bending length experiments (see Appendix A)

$$\Pi_D = \frac{1}{2} D \int_0^L (\frac{d\theta}{ds})^2 ds. \tag{6.1}$$

Before estimating the curvatures ($\kappa = d\theta/ds$) required for the bending energy Π_D calculation, the measured buckling profile must be post-processed. This entails removing dropouts and smoothing the profile such that higher-order derivatives can be calculated. In the case of relatively straightforward symmetric profiles such as seen in Figure 6.5, a non-linear curve fit based on mode shapes from Wadee et al. (1997) is applied. This mode shape, given in Equation 6.2, is based on a perturbation analysis of a BoF with nonlinear terms in the foundation stiffness.

$$h_{fit}(x) = A_0 + A_2 sech(\alpha x) cos(\omega x) + A_1 (sech(\alpha x))^2 + A_3 (sech(\alpha x))^2 cos(2\omega x) \tag{6.2}$$

The amplitudes (A1,A2,A3), spatial frequency ω and envelope parameter α are estimated through least-squares error minimization, as implemented in Matlab® via the lsqlincurvefit (Levenberg – Marquardt) solver. For non-blistered profiles the parameter ω can be taken as the buckled wavelength. The form of Equation 6.2 is attractive as the $A_1(sech(\alpha x))^2$ term allows the fit to approximate profiles such as Figure 6.2 as well as blistered profiles such as Figure 6.4, which feature up-down asymmetric folds. For symmetric shapes as observed in Figure 6.5, the quality of the fit is very good; however for asymmetric or 3-dimensional

profiles the parameter estimation may fail to converge. In these cases, a more-conventional cubic smoothing spline is applied. In both cases analytical derivatives of the basis functions are used to reduce error as compared to finite-difference derivative estimates.

Similarly, the potential energy of the foundation is estimated via the non-linear form of Π_K given in Equation 6.3,

$$\Pi_K = \frac{1}{2} K_f \int_0^L h(s)^2 cos(\theta) ds. \tag{6.3}$$

Using $K_f \approx \rho g$, the foundation energy at each shortening in Figure 6.5 is calculated. This is shown in Figure 6.7. Consistent with Section 5.4, energy is non-dimensionalized by $(\rho g)^{0.25} D^{0.75}$. Due to the large system size η, at equilibrium, linear theory predicts the contributions of bending and foundation energy to the total energy to be equal. In Figure 6.7, one observes that for the benchtop system at a given Δ, bending Π_D and foundation energies Π_K are relatively balanced. Π_D is greater than Π_K across the range of Δ tested. This may be due to the fact that Π_D is biased due to noise. As Δ is increased, the total potential energy $\Pi_{PE} = \Pi_D + \Pi_K \sim \Delta$, increases almost linearly as well. When applied to the large-scale data, as $\Delta \sim Z_s$, the total potential energy of the seal configuration (Π_T) increases with immersion.

As is discussed in Section 5.6 the finding that $\Pi_K \approx \Pi_D$ is significant and has application as a tool for interpreting buckled profiles such as those captured in the large-scale experiments. It may aid in the interpretation of buckled profiles without detailed knowledge of the forces at work. As an example, consider Figure 6.8, which is the bending and strain energy for the Type-1 (HN) material as a function of Δ. A challenge in the benchtop testing samples of the Type-1 (HN) material is that at a critical confinement, Δ_{crit}, the material detaches from the free surface and blisters (Figure 6.4). Information about the energetics associated with this event is useful. During the benchtop experiments, blistering could be verified visually through the clear glass sides. However, during the large-scale experiments, it was difficult to ascertain whether blistering has occurred as spray and a relatively high void fraction near

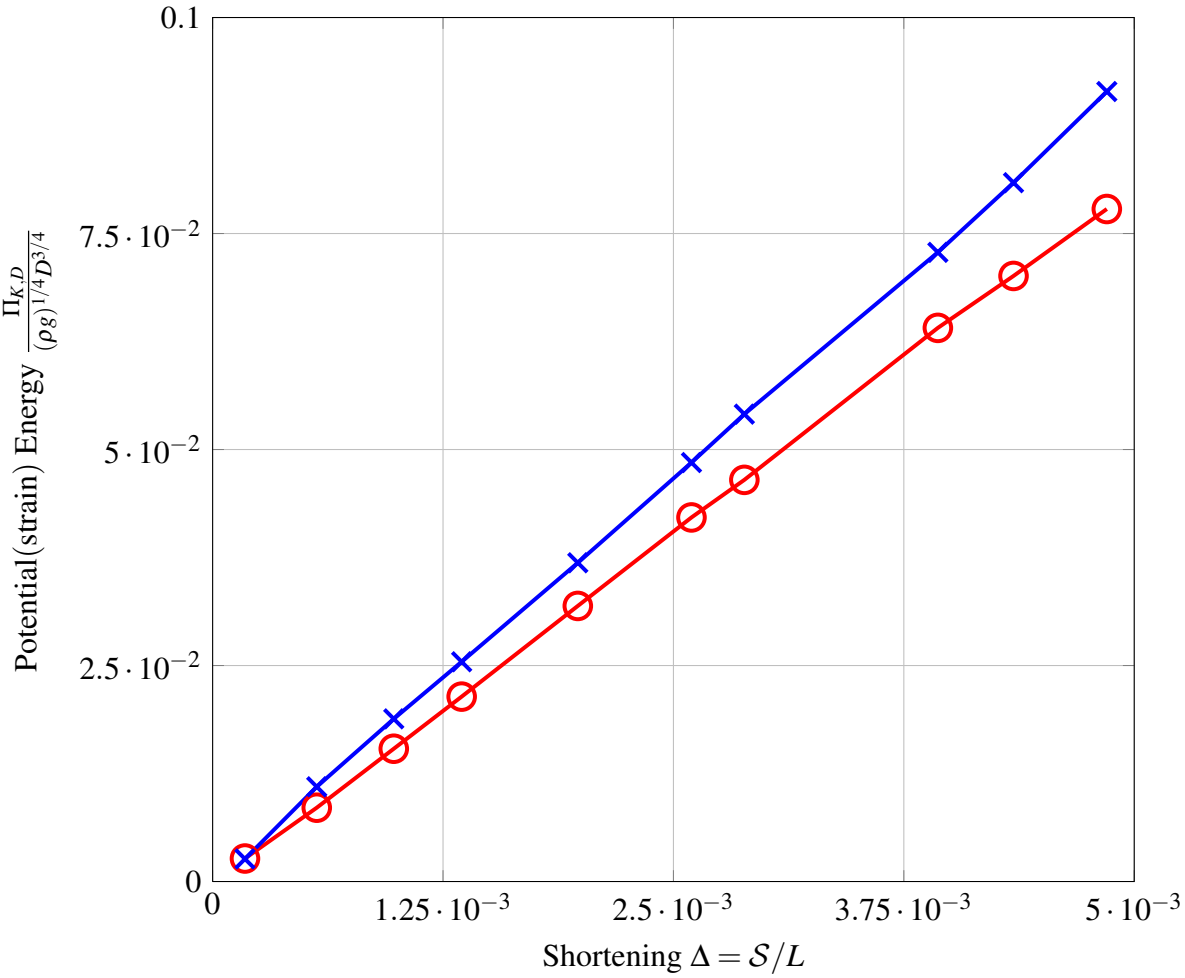

Figure 6.7 Effect of confinement ratio (Δ) on potential energy of post-buckled configuration, isotropic nitrile (N2) sample, system size $\eta_{\rho g} = 16$; ⟶×⟵, Π_B potential energy due to bending; ⟶○⟵, Π_K potential energy due to hydrostatic foundation. Note that bending and foundation terms contribute almost equally to the total energy. The free-surface is fully attached for the duration of the test.

the seal precluded straightforward observation. In place of visual confirmation, the ratio of the bending and foundation energies can be used track whether blistering had occurred. This can be seen in Figure 6.8; bending and foundation energies are balanced until a critical confinement $\Delta_{crit} = 0.11$ at which point the foundation energy, if allowed to remain attached would sharply diverge. At confinements above Δ_{crit}, $K_f = 0$ the seal configures itself to an equilibrium determined by the balance of bending, mass and aerodynamic forces. Above Δ_{crit}, the bending energy seems to be roughly constant suggesting that additional work is

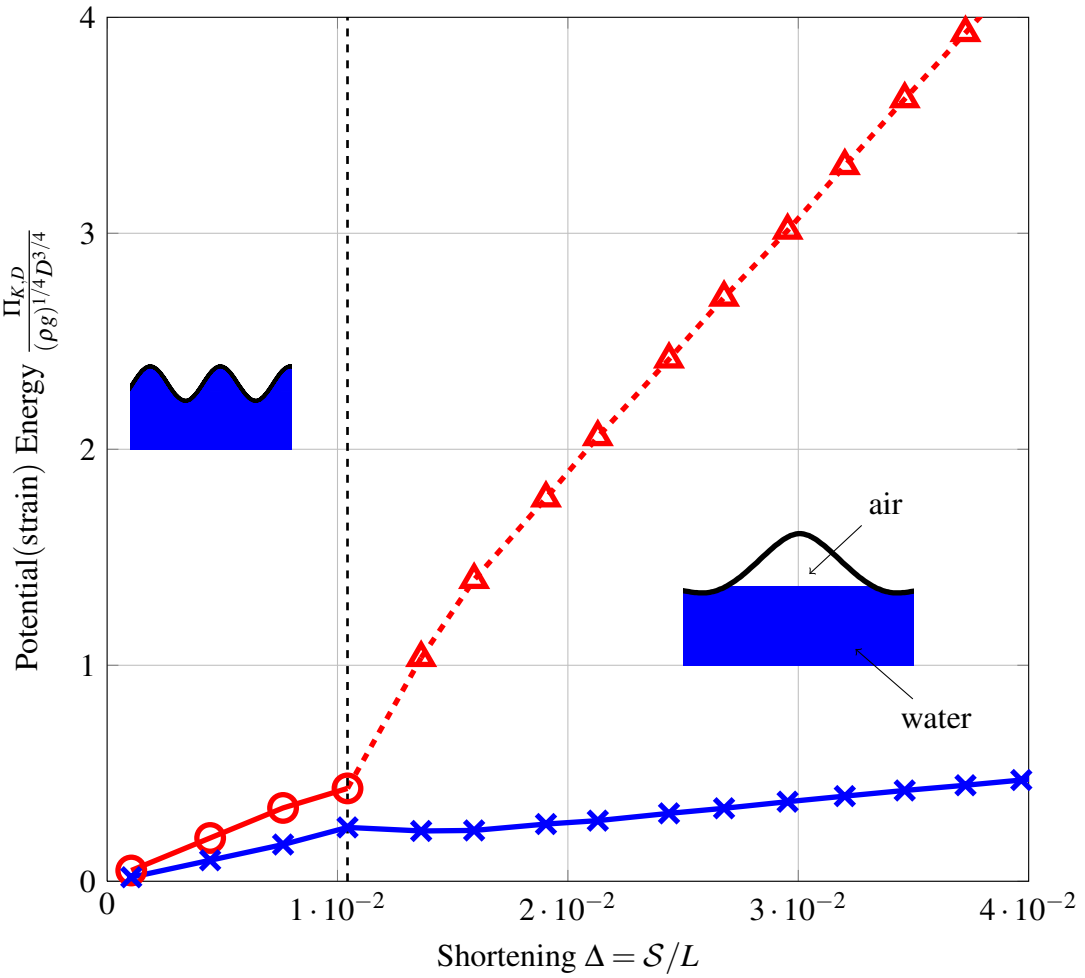

Figure 6.8 Effect of Δ on the potential energy of post-buckled configuration, Type-1 (HN) sample, system size $\eta_{\rho g} = 57$; -×-, Π_B potential energy due to bending; -○-,Π_K potential energy due to fully-attached hydrostatic foundation (prior to blistering); -△-,Π_K potential energy due to hydrostatic foundation if foundation were to stay attached. Prior to blistering ($\Delta = 0.011$), bending and foundation terms contribute almost equally to the total energy.

not required to compress the seal further.

Buckling wavelength and effective foundation stiffness

Another useful consequence of the balance of bending and foundation energies at equilibrium is that an estimate of the buckling wavelength λ_e can be found from energy measures. The interpretation of λ_e was previously discussed in Section 5.6.2. Setting $\Pi_K \approx \Pi_D$ and

assuming a constant effective foundation stiffness K_{f_e} and bending rigidity D,

$$\lambda_e = 2\pi \left(\frac{\Pi_{K/K}}{\Pi_{D/D}} \right)^{0.25} = 2\pi \left(\frac{\int_0^L h(s)^2 cos(\theta) ds}{\int_0^L (\frac{d\theta}{ds})^2 ds} \right)^{0.25} \tag{6.4}$$

$$\frac{\lambda_e}{\lambda_{\rho g}} = \left(\frac{\rho g \int_0^L h(s)^2 cos(\theta) ds}{D \int_0^L (\frac{d\theta}{ds})^2 ds} \right)^{0.25} \tag{6.5}$$

where λ_e is defined as the effective wavelength that balances the bending and foundation energies. $\Pi_{D/D}$ is the bending energy divided by the bending rigidity, D. $\Pi_{K/K}$ is the foundation energy without the foundation stiffness. Both $\Pi_{D/D}$ and $\Pi_{K/K}$ are quantities that can be estimated from the shape alone.

Figure 6.9 plots the buckling wavelength for the test shown in Figure 6.9 as computed by a number of methods. The bending wavelength derived from the bending energy λ_e is proportional to the wavelength computed by curve fitting and turning-point analysis ($2\,L_{C2T}$). λ_e is much closer to the wavelength from the curve fit λ_{fit} than the turning-point estimate λ_{C2T}. In Section 5.6.2, it is shown that for a random buckling pattern, λ_{C2T} should be less than or equal to λ_e. Specifically, the waveform in Figure 6.9 may be loosely approximated by an amplitude modulated sinusoid of the form,

$$h(x) = Asin(\frac{n\pi}{L}x)sin(\frac{\pi x}{L}). \tag{6.6}$$

where the wavelength of interest $\lambda_{fit} = \frac{2L}{n\pi}$. Using Equation 6.4, the effective buckling wavelength λ_e is estimated from the bending energy as

$$\lambda_e = \lambda_{fit} \frac{(1 + \frac{6}{n^2} + \frac{1}{n^4})^{0.25}}{(1 + \frac{1}{n^2})^{0.5}}. \tag{6.7}$$

Substituting mode $n = 5$ into Equation 6.7, is it found that $\lambda_e \approx 0.95\lambda_{fit}$ which is in line with the data. A more exact solution would work directly with the curve fit (Equation 6.2).

From linear theory, the measured buckling wavelength at small confinements, λ_0 should

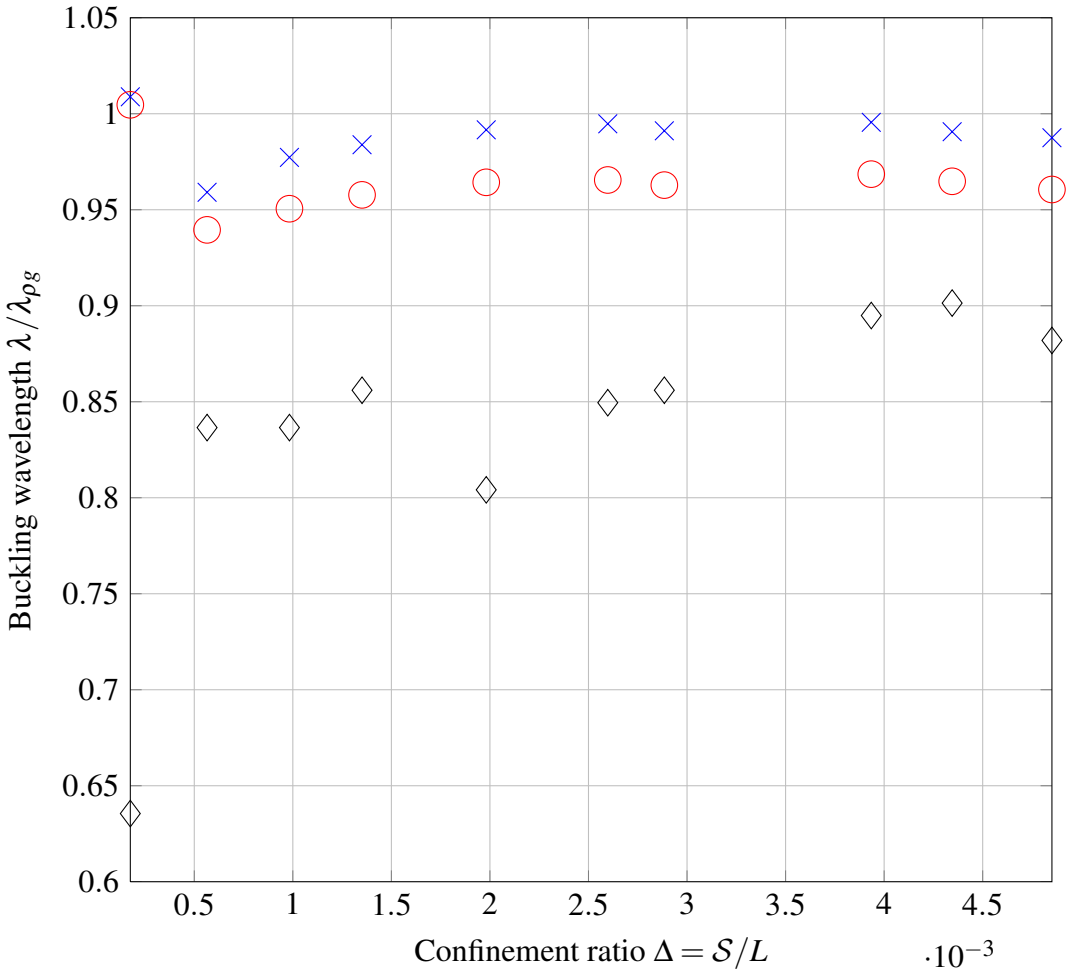

Figure 6.9 Effect of Δ on buckling wavelength (λ) as estimated using three methods, isotropic *nitrile* (N2) sample, $\eta = 16$. Wavelength (λ) is normalized by the natural buckling length $\lambda_{\rho g}$; $\times$, λ from non-linear curve fit (Equation 6.2); $\diamond$, turning-point analysis, $\lambda \approx 2 \cdot L_{C2T}$, $\bigcirc$, balance of bending and foundation energies $\lambda_e \approx 2\pi \left(\frac{\Pi_{K/K}}{\Pi_{D/D}} \right)^{0.25}$.

be equal to $\lambda_{\rho g} = 2\pi(\frac{D}{K})^{0.25}$. This is confirmed in Figure 6.11, which shows λ_0, as estimated using the curve-fit across a wide range of bending rigidities. Except for the N1 sample, λ_0 is within 20% of the prediction. This confirms both the model and the estimate of the bending rigidity, D, based on the test procedure described in Appendix A.

The balance of bending and foundation energies suggests another interpretation of the blistering event such as observed in Figure 6.4. Rearranging Equation 6.4, and non-dimensionalizing with respect to the zero-speed foundation stiffness $K_f = \rho g$, an estimate

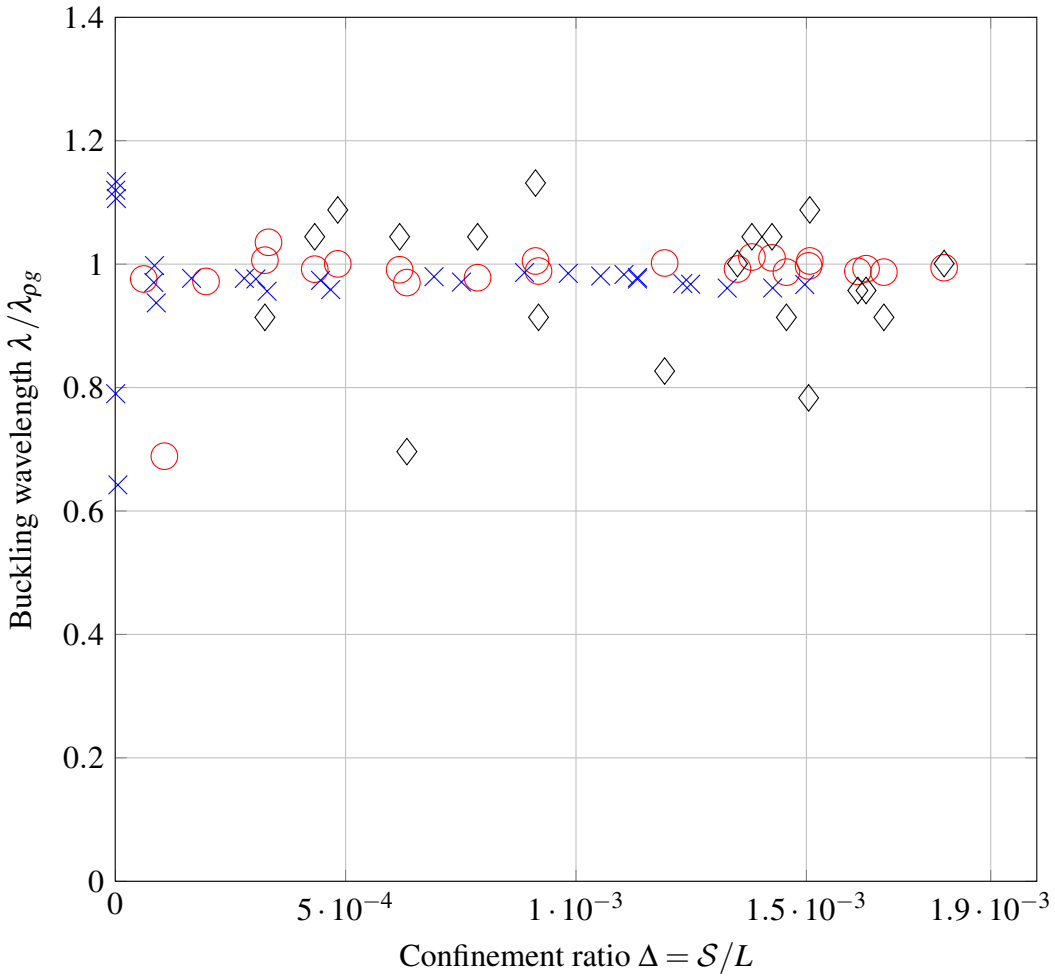

Figure 6.10 Effect of Δ on buckling wavelength (λ) as estimated using three methods, highly-compliant *silicone* (S0) sample, $\eta = 83$. Wavelength (λ) is normalized by the natural buckling length $\lambda_{\rho g}$; ×, λ from non-linear curve fit (Equation 6.2); ♢, turning-point analysis, $\lambda_{C2T} \approx 2 \cdot L_{C2T}$, ◯, balance of bending and foundation energies $\lambda_e \approx 2\pi \left(\frac{\Pi_{K/K}}{\Pi_{D/D}}\right)^{0.25}$.

of the effective foundation stiffness K_{f_e}:

$$\frac{K_{f_e}}{\rho g} \sim \left(\frac{\lambda_{\rho g}}{\lambda}\right)^4. \tag{6.8}$$

Figure 6.12 shows the effective stiffness $\frac{K_{f_e}}{\rho g}$, relative to hydrostatics, during the blistering event. As expected, the effective foundation stiffness K_{f_e} is close to $K_f = \rho g$ until Δ_{crit}. Above Δ_{crit}, the effective foundation stiffness decreases sharply. Should the seal detach entirely, one would expect $\frac{K_{f_e}}{\rho g}$ to go to zero.

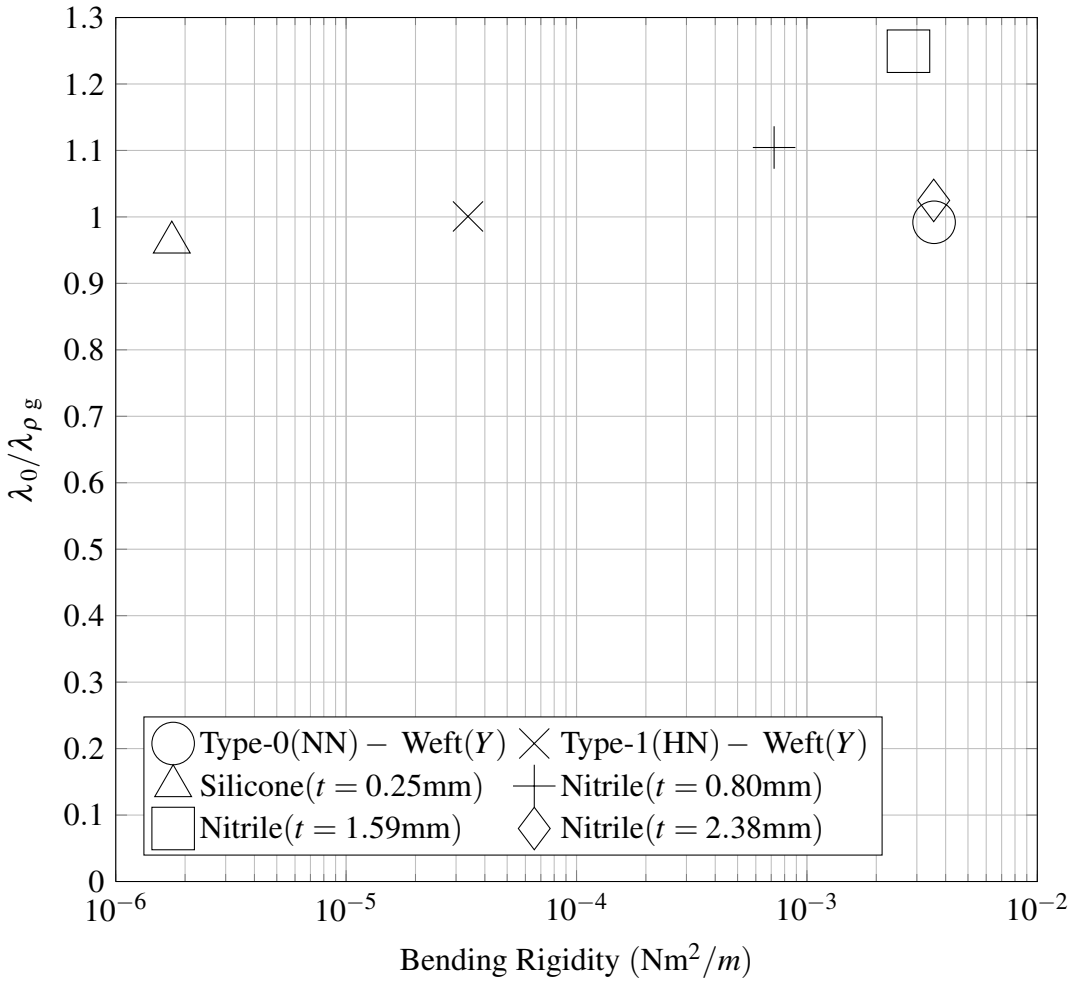

Figure 6.11 Benchtop experiment: measured initial buckling wavelength λ_0 compared to natural hydrostatic buckling wavelength $\lambda_{\rho g}$ across a range of bending rigidities. Non-linear method was used to estimate λ_0.

Buckling load

The total system work is

$$\Pi_T = \Pi_K + \Pi_D - W_c, \tag{6.9}$$

where Π_K is the foundation energy, Π_D is the bending (strain) energy and W_c is the work performed by compressive load F. Substituting $W_c = FS$ into Equation 6.9, and factoring

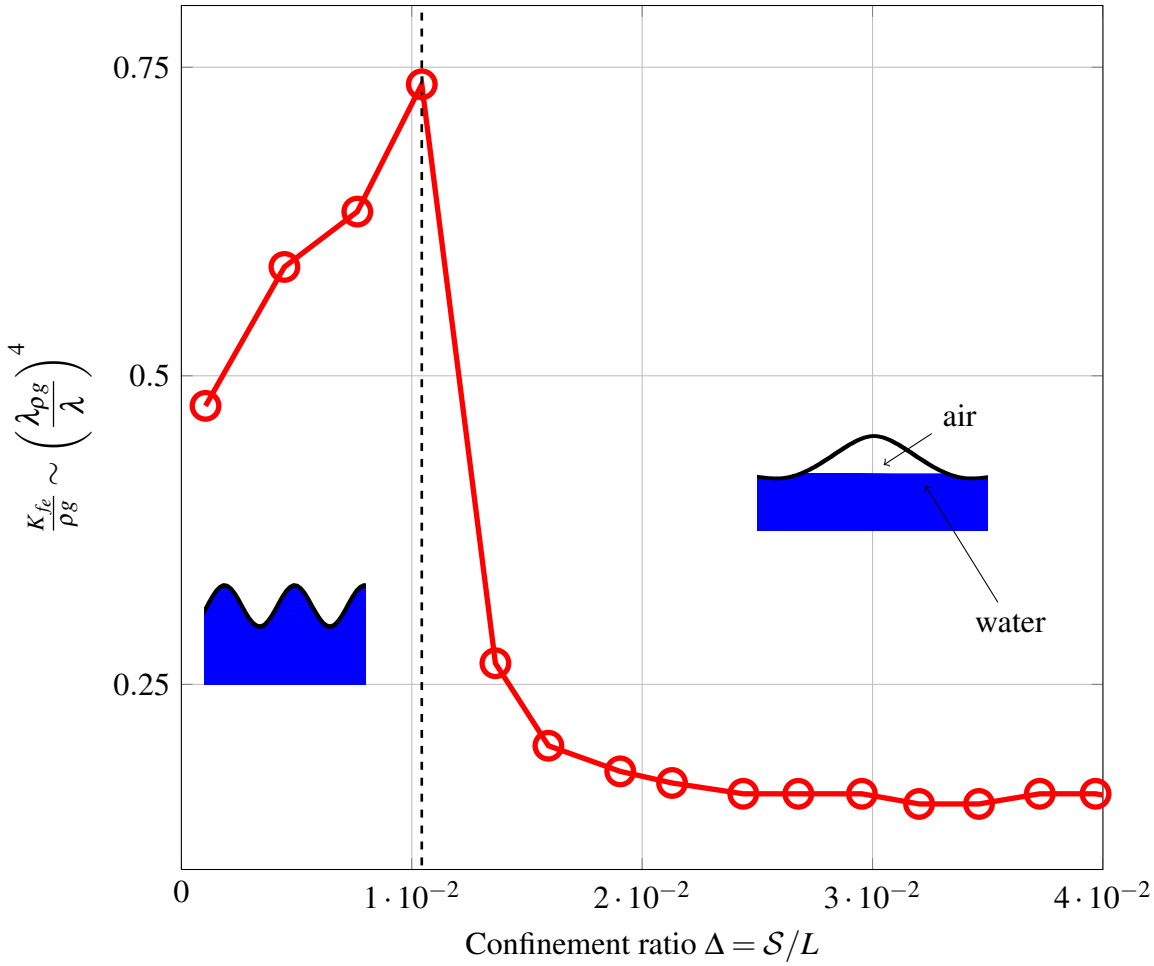

.

Figure 6.12 Effect of confinement ratio Δ on effective foundation stiffness (K_{f_e}) as inferred from buckling wavelength (λ) during *benchtop* experiment, Type-1 (HN), compliant seal material, system size $\eta_{\rho g} = 57$. ⊖, K_{f_e} is presented relative to hydrostatic stiffness $K_f = \rho g$. Notice rapid fall-off in (K_{f_e}) near $\Delta \approx 10^{-2}$. This Δ corresponds to the inception of blistering (see Figure 6.4). λ is estimated from the turning-point analysis.

out S gives,

$$\Pi_T = (\underbrace{\frac{\Pi_K + \Pi_D}{S}}_{F_{RQ}} - F)S. \tag{6.10}$$

The quantity $\frac{\Pi_K + \Pi_D}{S}$ is also known as the Rayleigh quotient (F_{RQ}) (Bažant and Cedolin, 2010). Both Π_K and Π_D are positive in nature, due to quadratic terms and positive bending rigidity D and the foundation stiffness K_f. The sign of Π_T is determined solely by the

magnitude of F relative to F_{RQ}. It can be shown that F_{RQ} represents an upper bound for the critical compressive load F_c (Bažant and Cedolin, 2010).

Per the scaling introduced in Section 5.3, the buckling load F_{RQ} is non-dimensionalized by $(DK_f^{0.5})$ to form f_{RQ}:

$$f_c \leq f_{RQ} = \frac{F_{RQ}}{(DK_f)^{0.5}} = \frac{\Pi_K + \Pi_D}{S(DK_f)^{0.5}}. \tag{6.11}$$

Let K_f be the hydrostatic stiffness ($K_f = \rho g$). According to linear theory (Section 5.4), for a beam of infinite length ($\eta \to \infty$), $f_c \leq 2$. In the case of a finite-length beam, $f_c \geq 2$. Now the buckling load versus deflection curve as estimated from Equation 6.11 for the isotropic nylon sample (N2) is shown in Figure 6.13. The system size, $\eta = 20.6$. The material shape has been fit with an amplitude modulated sinusoid (Equation 6.4) prior to computing the bending energy. Critical buckling loads for an infinite plate (- · - ·) and a clamped-clamped beam of size η (- - -) are also shown. Typical of post-buckling experiments, the system buckles before the linear critical buckling load can be reached (Singer et al., 1998).

Derivatives of the load-deflection curve such as presented in Figure 6.13 may provide clues as to the stiffness of the benchtop system with respect to end-loading[3]. Figure 6.15 shows three potential states for the load deflection curve based on the sign of $df/d\Delta$.

Case a) shows a system that is *stable* with respect to end-loading. Application of a constant load above f_c causes the system to buckle and follow the f_c post-buckling path, with the end-displacement increasing until the external load is balanced. This is typical of a finite-length Euler beam (no foundation), under an applied load of f_c. The behavior of the BoF should approach this *stable* behavior in the limit as system size $\eta \to 0$. This type of behavior was noted in the study of the foundation-less elastica in Section 5.3.1. Case c) represents the load-deflection behavior of a system that is *unstable* with respect to end-loading. Under the application of a constant load $f_c = 2$, the end-displacement is un-

[3]This is different than the stability of the system to perturbations.

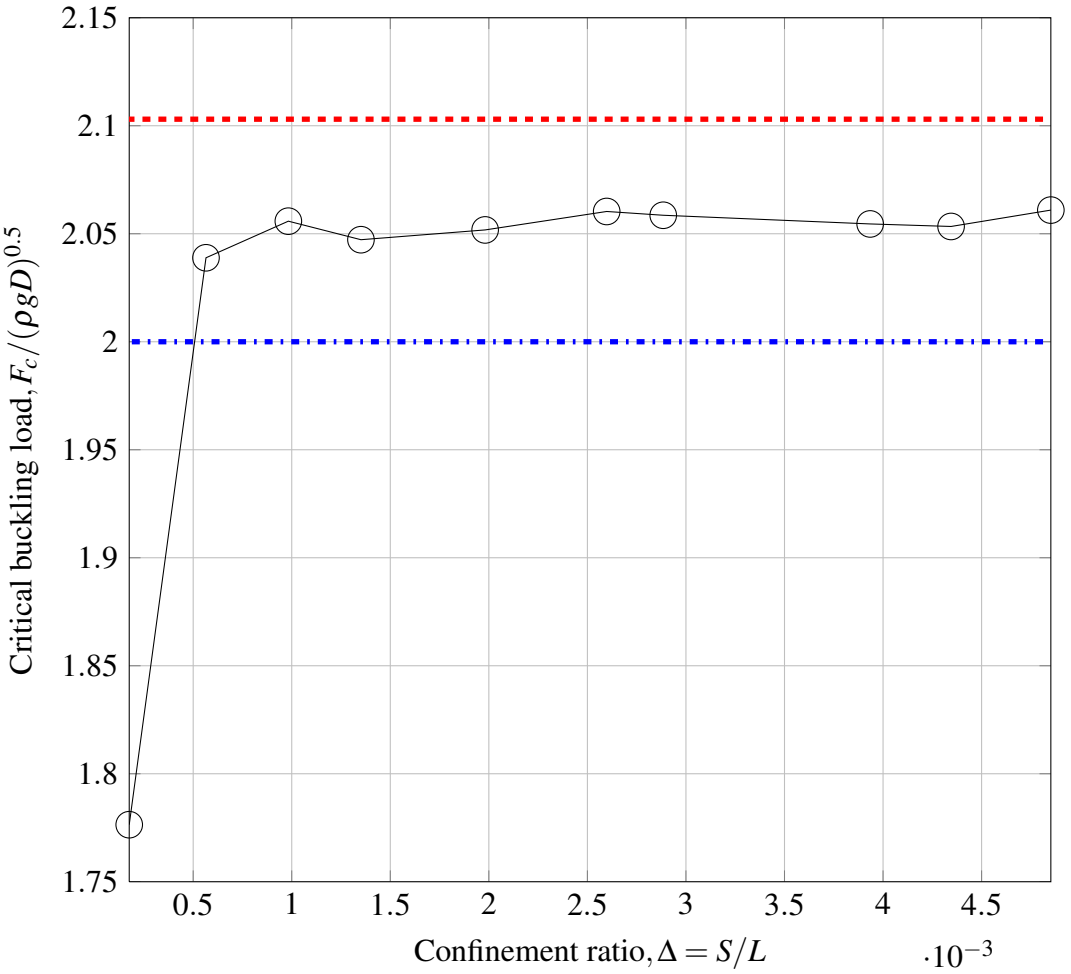

Figure 6.13 Upper bound on critical buckling load F_c as estimated from Rayleigh quotient (Bažant and Cedolin, 2010), isotropic nitrile (N2) sample, system size $\eta = 16$; ⊖, $F_{RQ} = \frac{\Pi_K + \Pi_D}{S} \geq F_C$, where S is the end-displacement, given by Equation 5.78. Potential energies Π_D and Π_K are calculated via Equations 5.54 and 5.55, which are valid for large slopes. For reference, critical buckling loads for an infinite plate (- · - ·) and a clamped-clamped beam of size η (- - - -) are shown. Slope of $F - \Delta$ curve indicates that sample may be *neutrally stable* with respect to end-loading.

bounded. This is typical of an infinite plate ($\eta \to \infty$) on an elastic foundation. For example, the load-deflection relation for the analytical solution (Diamant and Witten, 2011) presented in Section 5.3, reads $f = 2 - \frac{1}{16}\Delta^2$, with the restoring force decreasing quadratically with Δ.

Due to the sample sinking or detaching from the free-surface, it is not possible to fully map the post-buckling path from the benchtop experiments. Figure 6.13 shows $df/d\Delta \approx 0$ for the N2 sample at system size $\eta = 20.6$. This may be indicative of a system marginally stable with respect to end-loading. In contrast, consider Figure 6.14, the load-Δ curve

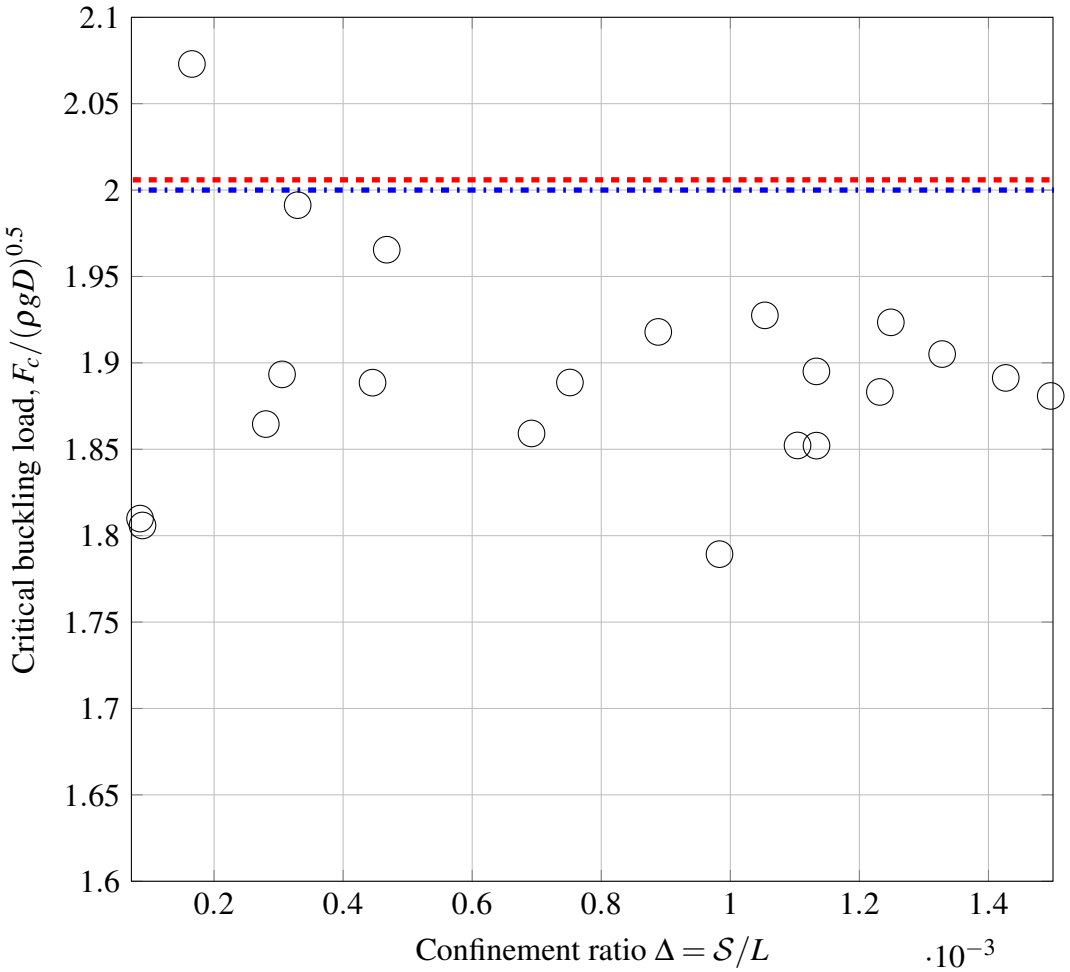

Figure 6.14 Upper bound on critical buckling load F_c as estimated from Rayleigh quotient (Bažant and Cedolin, 2010), silicone (S0) sample, system size $\eta = 83$; ◯, $F_{RQ} = \frac{\Pi_K + \Pi_D}{S} \geq F_C$, where S is the end-displacement, given by Equation 5.78. Potential energies Π_D and Π_K are calculated via Equations 5.54 and 5.55, which are valid for large slopes. For reference, critical buckling loads for an infinite plate (- · - ·) and a clamped-clamped beam of size η (- - -) are shown. System buckles prior to reach critical buckling load. Slope of $F - \Delta$ curve indicates that the large η sample may be *unstable* with respect to end-loading.

for the compliant S0 sample, $\eta = 83$. For this sample, $df/d\Delta < 0$, therefore, the large η system is unstable with respect to dead loading. As a result, under dead loading near f_c, the system offers little resistance to buckling and would eventually reach the limiting case of self-contact. This potentially has significance for the bow seal problem as hydrodynamic loads between adjacent fingers have a transverse or cross-flow component. Because once buckled the seal offers little resistance to lateral compression, gaps may form between

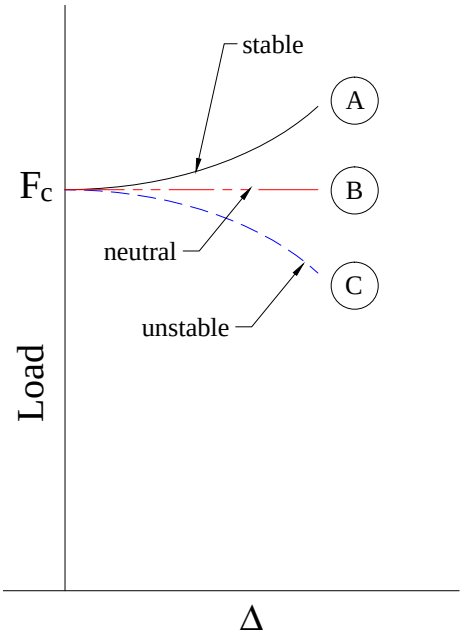

Figure 6.15 Load-displacement classification.

fingers leading to air leakage. An example of leakage between seals can be seen in Figure 4.2.

Fold Amplitude

In Section 5.4.4 a scaling for fold amplitude was presented on the basis of the inextensibility of the material as

$$\frac{A}{\lambda} \sim \left|\frac{dh}{dx}\right| \sim \sqrt{\Delta}. \tag{6.12}$$

The benchtop experiments provide an opportunity to test this fold amplitude scaling and determine whether higher order corrections are required. The amplitude for the N2 material under various compressions is shown in Figure 6.11. The scaling law presented in Section 5.4.4 relies on an estimate of

$$max\left|\frac{dh}{dx}\right| \approx 2\pi\frac{A}{\lambda}. \tag{6.13}$$

Looking at a buckling profile such as seen in Figure 6.5, there are a number of potential

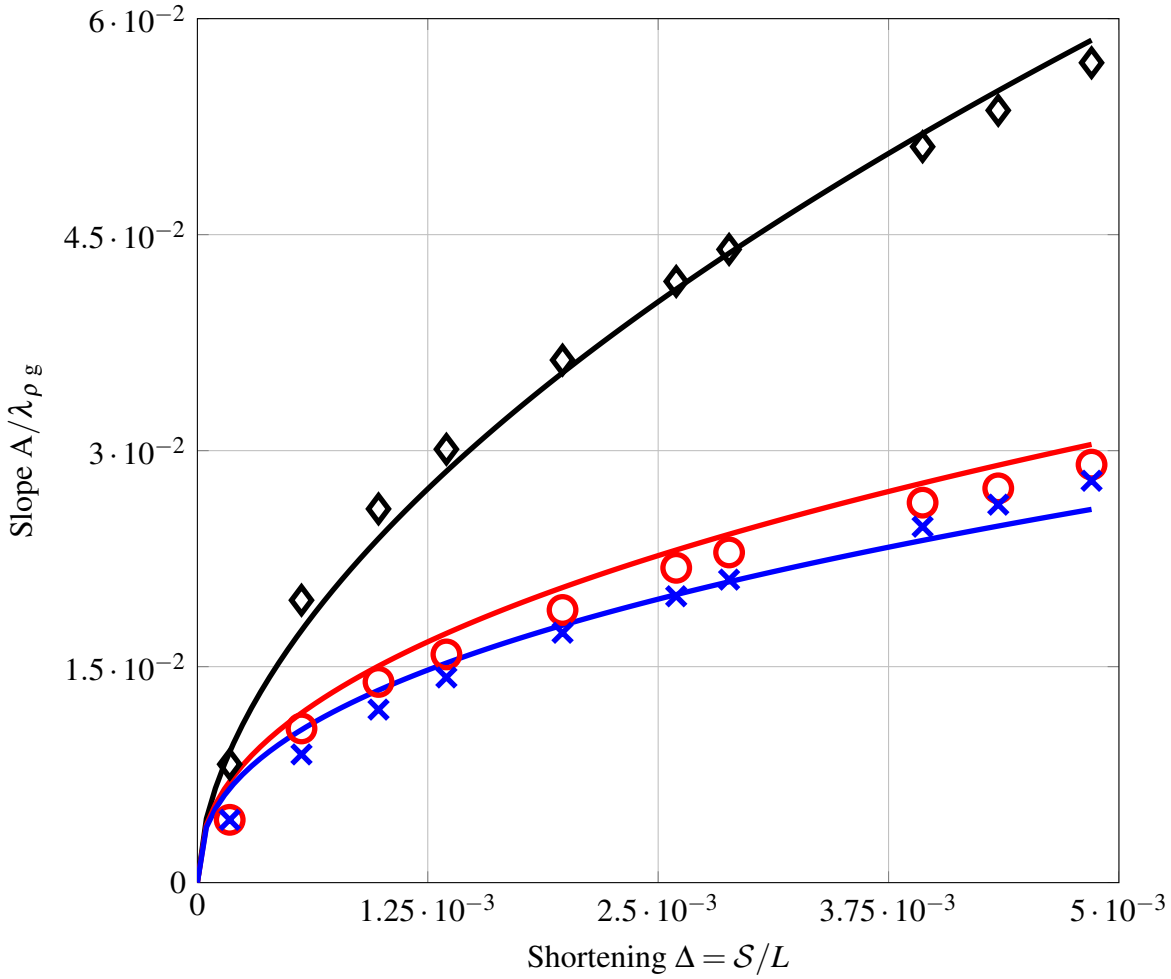

Figure 6.16 Fold slope (A/λ) as a function of confinement ratio (Δ). Fold amplitude (A) and wavelength (λ) estimated using non-linear curve fit. Three estimates of (A/λ) are shown(see Figure 3.15 for reference); ◇, largest crest-to-trough height, H_{C2T}; ○, largest crest-to-zero amplitude, A_{C2Z}, ×, largest trough-to-zero amplitude, A_{T2Z}. Power-law fits are also shown; —, $H_{C2T} \sim \Delta^{0.56}$; —, $A_{C2Z} \sim \Delta^{0.44}$; —, $A_{T2Z} \sim \Delta^{0.41}$.

approximations for the slope that can be used as a basis for comparison (see Figure 3.15 for nomenclature). The large-scale seal buckling data presented Chapter 4, employed the approximation:

$$\frac{A}{\lambda} \approx 2\pi \frac{H_{C2T}}{4L_{C2T}}, \tag{6.14}$$

where H_{C2T} is the crest-to-trough height and L_{C2T} is the crest-to-trough half wavelength. Both of these are found from a turning point analysis of the profile. An advantage of this

approach is that it can easily be applied to folds such as in Figure 4.13 (b) and (e) where the mean level is highly dependent on the window width. The magnitude of the slope for buckling profiles such as seen in Figure 6.5 can be approximated by the amplitude of the individual folds. Figure 6.16 presents three such representations, A_1 is the amplitude of the largest fold relative to the undisturbed fabric position. A_2 is the amplitude of the second largest fold. The largest crest-to-trough height H_{C2T} is also shown. For the case of Figure 6.16, H_{C2T} is the average of A_1 and A_2. Rather than use $\lambda \approx 2L_{C2T}$ as for the normalization, the wavelength, $\lambda_{fit} = 2\pi/\omega_{fit}$ from the curve fit (Equation 6.2), which seems to be less susceptible to noise is used.

The power-law fit confirms the $A/\lambda \sim \Delta^{0.5}$ scaling observed in large scale data for both the Type-1 and Type-0 seals. The relative coarseness of the test leads to significant uncertainty in the exponent of the power-law fit. Future work should compile data for the additional materials tested in order to generate a better fit. Higher order corrections to the scaling such as suggested by Brau et al. (2010) may also improve the fit.

Scaling in buckling problems

Figure 6.3 shows buckling profiles for two materials, Type-0 (NN) ($D_Y = 3.56 \cdot 10^{-3}$) and S0 ($D = 1.75 \cdot 10^{-6}$) with bending rigidities differing by three orders of magnitude; however, in terms of system size η the two profiles are roughly equivalent. It is observed that when η similitude is achieved, mode number and buckling characteristics of the two systems are similar. They both feature the same mode number and feature amplitude-modulated mode shapes. The side lobes and material slope is larger for the more compliant S0 sample. The difference in amplitude modulation is likely due to differences in the effective boundary conditions. The differences in material slope is due to differences in the relative confinement Δ between samples.

It is then reasonable to postulate that to match the buckling behavior (static stability) for physical model tests, $\eta = \frac{L}{(D/K_f)^{0.25}}$ of the small and large-scale seal needs to be matched

($\eta_m = \eta_f$). If this is the case, the balance of bending to restoring forces is maintained under a change in physical length scale. For the case of zero-speed, where $K_{f_m} = K_{f_f} = \rho g$, achieving similitude with η leads to the following relation between the model and full scale bending rigidity

$$D_m = \frac{D_f}{\lambda_{SF}^4}, \tag{6.15}$$

which is equivalent to the non-dimensionalization provided in Section 2.5.1 and which proved almost impossible to maintain given the bending rigidities of commercially available materials. For example, the geometric length scale factor λ_{SF} between a) and b) in Figure 6.3 is $\lambda_{SF} \approx 6.66$. In the case of large target vessels such as the proposed U.S. Navy's T-CRAFT, due to test facility limitations, much larger geometric length scales $\lambda_{SF} > 25$ are generally required. In addition, the S0 material is not viable for a physical model test at $\lambda_{SF} = 6.66$, as the material is unable to satisfy the hoop stress requirements.

Material property scaling is further complicated by the arguments presented in Section 5.6.4, which showed that the effective foundation stiffness K_{f_e} may be velocity and fold amplitude dependent, or in general $K_{f_e}(\Delta, Re, fn)$. In addition to the difficulties in material selection discussed previously, Reynolds number differences between full and model scale may lead to additional distortions. As is described in the Future Work, η may be used for designing geometrically-dissimilar experiments intended to isolate specific aspects of seal buckling.

Features of benchtop experiment not captured by the BoF model

The mechanical simplicity of the benchtop experiment belies the complexity of the material response. A number of interesting phenomena were observed that are not captured by the model and are briefly described. Many of these phenomena are artifacts of the setup, however they illustrate the sensitivity of the buckling response to factors such as wetting properties, imperfections and boundary conditions. Blistering, as shown in Figure 6.4, is

the tendency of the system to favor configurations separated from the free-surface. This phenomenon was observed for the Type-0 (NN), N1, and HN materials. The confinement Δ at which the material separates from the free-surface was found to be hysteretic and sensitive to the hydrophobicity of the material. Treating the surface with the hydrophobic coating led the system to separate from the free-surface earlier than it would otherwise. Unlike previous experiments (Vella et al., 2009), the blistering phenomenon was shown to exhibit significant hysteresis. Certain blistered configurations could only be reached by first increasing Δ, and then decreasing Δ, as the material would not reattach at the same displacement as the initial detachment.

Other phenomenon of note concern the character of the "wrinkle" to fold transition and the sensitivity of the system to imperfections. The literature (Pocivavsek et al., 2008), and geometrically non-linear model (Diamant and Witten, 2011) suggests that for large system sizes, near the initial bifurcation point, the material is characterized by a uniform distributed "wrinkled" state. As Δ is increased for a system of large size (η), previous studies indicate that this wrinkled state gives way to a series of localized folds (see Figure 5.11). In our experiments, all but the most compliant materials seem to be influenced by boundary conditions and formed amplitude modulated buckling packets such as seen in Figure 6.3. For compliant materials such as S0 (Figure 6.2), $\eta = 83.3$, fairly regular buckling patterns were observed; however these did not extend over the full domain and were localized near the boundaries. Folds were most likely to occur at the fixed boundary away from the moving backstop. Similar observations were made by Boucif et al. (1991) and Hunt et al. (1989), who attributed the behavior to a reaction moment at the support. As the backstop displacement was increased, rather than the waves compressing uniformly or localized folds occurring regularly, one of the folds seems to act as a point of local weakness. Additional material from the transverse displacement is absorbed by this single fold, leading to a dramatic increase in fold amplitude and eventual sinking of the sample. In the case of the composite samples (e.g. Type-0 (NN) and Type-1 (HN), it was observed that packets

would form in repeatable asymmetric (non-centered) locations even after remounting. This suggests that imperfections and prestress from the manufacturing process may be driving packet location. It was noted though, that folds could be relocated along the length of the sample with minimal effort, suggesting that the total energy was almost independent with respect to translation.

6.1.4 Conclusion

In conclusion, a small-scale benchtop experiment was designed and executed and is shown to capture many of features of the cross-flow buckling model developed in Chapter 5. Furthermore it is found to be qualitatively similar to the buckling of finger seals at large-scale. The experiments provide a concrete physical interpretation for the natural buckling length (L_n) introduced in Chapter 5. The experiments confirm that the buckling response of samples with different physical sizes but the same non-dimensional system size ($\eta = L/L_n$) exhibit similar buckling behavior. This suggests that (η) could be a useful quantity in material selection in future physical model tests.

Good agreement between the measured and predicted buckling wavelength was observed. Due to the clear relationship between buckling wavelength λ and bending rigidity D, an apparatus similar to the benchtop buckling experiment may have utility as a method for estimating the effective bending rigidity of materials. The bending rigidity estimated via the benchtop buckling experiment would likely have a clearer physical relationship to seal response than the bending length test described in Appendix A and would require minimal instrumentation (a scale).

Likewise, a similar approach may have application in estimating the bending rigidity of other materials in situ. For example, there is the potential to estimate the bending rigidity of ice sheets through remote-sensing surveys post-processed to identify spatial (buckling) wavelengths. Similar to benchtop experiment, the ice sheet, in the absence of significant currents, is supported by a foundation of known stiffness $K_f = \rho g$. On a much smaller

scale, it could be used to estimate the bending rigidity of biological membranes such as skin (Cerda and Mahadevan, 2003) which are supported by a supported by substrate.

Both mode shapes and buckling load estimates suggest that the boundary conditions realized during the experiment were closer to clamped-clamped than pinned-pinned. Similar to the large-scale experiments, symmetric, amplitude-modulated configurations are preferred for small system sizes, often over energetically favorable asymmetric configurations. Treating the system as clamped-clamped, the agreement between linear theory and experiment is quite favorable. This is likely due to the small-slopes achievable by the benchtop experiment. The clamped-clamped boundary conditions leads to amplitude modulation, which may also play an important role setting mode-shape at large-scale. Estimates of the buckling load are made indirectly using energy measures. These show that the material buckles before the linear buckling load is reached. As expected, the buckling loads for small system sizes are higher than for the infinite plate. For all system sizes, the material seems to be unstable or neutrally stable with respect to end load.

Refinements to the execution of the benchtop experiments as well as proposals for how the experiments can be modified to better capture seal physics are provided in the Future Work, Chapter 8.

Chapter 7
Conclusion

The present study makes a fundamental contribution to our understanding of finger seal physics. Using a large-scale test platform developed as part of the thesis, and described in Chapter 3, detailed observations of bow seal response are made. These high-resolution observations, presented in Chapter 5, show bow seal hydroelastic response to be characterized by complex post-buckling behavior. Under the action of hydrodynamic forces and confinement seals reconfigure, changing cross-flow wavelength, amplitude and often, stability. Analysis of Gaussian curvature from 3-dimensional seal shapes, indicates that in the Knuckle region of the seal, large pressure gradients and material confinement combine to create localized areas of strain. The Tail region, characterized by single curvature and largely inextensible, is more amenable to qualitative modeling. In this region, a model based on a beam-on-an-elastic foundation (BoF), a classical problem of elastic stability, is employed to investigate changes in cross-flow configuration. Within the BoF framework, described in Chapter 5, finger seal conformation is found to follow a series of scaling relationships. These scalings are confirmed across a range of bending rigidities through a small-scale experiment, described in Chapter 6. The work highlights the rich statics and dynamics of a buckled structure subject to fluid loading.

The study identifies a number of dimensionless parameters driving the cross-flow response of finger seals. Of particular importance is $\eta = L/L_n = L(K_f/D)^{0.25}$, the system size (L) as non-dimensionalized by the natural buckling length L_n. L_n is the natural length-scale at which bending (strain) and hydrodynamic restoring energies are balanced and is given by

$L_n = (D/K_f)^{0.25}$, where D is the bending rigidity and K_f is a foundation stiffness.

Using the beam-on-an-elastic foundation as an analogy for buckling behavior in the Tail region, the effect of system size η on mode shape is examined in Chapter 5. This work shows that mode shapes for small system sizes (η) are characterized by low mode numbers and are significantly influenced by boundary conditions (Heténi, 1979). Equilibrium configurations along the critical F_c buckling path (minimum potential energy) for small system sizes can be *stable* as $\eta \to 0$ (Koiter and van der Heijden, 2009). Small η response is typified in the large-scale data for the relatively *stiff* Type-0 (NN) material ($D_X = 4.10 \cdot 10^{-3}$ Nm, $\eta_{\rho g} = 8.6$); $\eta_{\rho g}$ is the zero-speed system size computed using $K_f = \rho g$. For this test case, mode number was observed to vary between $m = 1$ and $m = 7$, with a mode number of three typical for moderate immersions. Mode shapes for the Type-0 material are generally symmetric ("odd") featuring amplitude modulation and raised central folds. The analysis carried out in Chapter 5, shows that both amplitude modulation and the symmetry may be due to boundary conditions. However, it is not clear why Type-0 finger seals prefers symmetric configurations over asymmetric configurations that may be energetically favorable. Within the limited parameter space of the experiments, Type-0 seals are found to be stable for moderate immersions $\frac{\delta_s}{R_f} > 0.25$ and pressures $\frac{\delta_c}{\delta_s} > 0.6$. Future work should examine the stability of equilibrium configurations in the Tail region within the context of the BoF system. Preliminary work suggests the stability of bow seal at low-mode numbers is consistent with the BoF analogy. Type-0 seals are observed to lose stability at lower immersions $\frac{\delta_s}{R_f} < 0.25$ through a convective "mode-cycling" type instability. A similar instability was reported by Besch (1976) near the same non-dimensional immersion, $\frac{\delta_s}{R_f} > 0.25$.

In contrast, mode shapes for large system sizes η are characterized by high mode numbers, and may favor localized responses (Hunt et al., 1989). For large η, the structural boundary layer created by the supports extends over a relatively small portion of the domain, resulting in reduced effects due to boundary conditions. The critical buckling path for large η is *unstable* (Koiter and van der Heijden, 2009). Large η response is typified in

the large-scale data for the compliant Type-1 material ($D_X = 6.17 \cdot 10^{-5}$ Nm, $\eta_{\rho g} = 30.3$). Mode numbers for the Type-1 material are found to vary from $m = 3$ to $m = 11$, corresponding to significantly shorter wave-lengths and smaller amplitudes than the Type-0 material. Unlike the Type-0 seals, mode shapes for the Type-1 seals are generally localized rather than distributed in nature. At deeper immersions, these localized buckling packets merge to form a distributed-type response whose wavelength is well captured by the BoF model. Consistent with large η, Type-1 seals are unstable under all conditions. Instead of the mode-cycling instability found in the stiff Type-0 seals, where mode number is constant, seal constructed of the compliant Type-1 material are subject to a type of high-frequency mode-switching. The mode-cycling and mode-switching type instabilities observed during the experiments and partially examined in the stability analysis, are distinct from the flutter-type instabilities that previous researchers (Ryken, 1978; Yamakita and Itoh, 1998) have attempted to link to seal vibration and are likely important in understanding the persistent problem of seal wear.

The mean buckling wavelength for the Type-1 material, λ varies linearly with the local draft of the seal, δ_s and with the compression Δ. The measured wavelength approaches the hydrostatic buckling wavelength $\lambda_{\rho g} = 2\pi \left(\frac{D}{\rho g} \right)^{0.25}$ at large shortenings. This suggests that hydrodynamic components of the restoring force are relatively small at the laser plane for the velocities tested. It is hypothesized that at higher speeds, hydrodynamic contributions to the stiffness due to mechanisms such as flow-induced tension may dominate. Future work, discussed in Chapter 8, should explore how the foundation stiffness K_f is set and identify transitions between buoyancy and flow-induced tension driven regimes.

The benchtop experiments described in Chapter 6 confirm that the buckling response of samples with different physical sizes but the same non-dimensional system size (η) exhibit similar buckling behavior. This suggests that η, together with suitable estimates of the foundation stiffness K_f, is a useful quantity in material selection in future physical model tests. As will be discussed in Chapter 8, identification of the parameter η enables the use of cost-effective small-scale experiments to isolate specific aspects of seal physics and inform

future large-scale work. In addition, the scaling parameters identified in this study may govern buckling in other physical systems, such as ice sheets and biological membranes. For example, there is the potential to estimate the bending rigidity of ice sheets through remote-sensing surveys post-processed to identify spatial (buckling) wavelengths.

Another key parameter identified as part of the study is the seal confinement ratio Δ, a non-dimensional measure of seal compression. The confinement Δ acts as a constraint on fold amplitude. Due to the compliance of the seal material, Δ is set by free-surface hydrodynamics local to the bow seal. Δ is found to vary almost linearly with the local immersion $\frac{\delta_s}{R_f}$. The large-scale data suggest, based on an analysis of the kinematics, that *compliant* Type-1(HN) seals behave similarly to a hinge rotating about a local waterplane. The parameter Δ is influenced by the cushion pressure via wave-rise, which consistent with linear theory was found to vary linearly with the pressure. Large-scale data for the Type-1 (HN) and Type-0 (NN) materials indicate that cross-flow fold slope $\frac{A}{\lambda}$ follows a power-law, $\frac{A}{\lambda} \sim \Delta^{0.5}$, where A is the amplitude, and λ is the wavelength. In Section 5.4.4, this scaling is shown to follow from the near inextensibility of the seal material. Similar $\frac{A}{\lambda} \sim \Delta^{0.5}$ power-law type behavior is found in the benchtop experiments and is reported across a range of physical scales, encompassing diverse systems such as sea ice, biological membranes, curtains and nano-structures (Brau et al., 2010).

The SES bow seal system is a complex fluid-structure interaction problem and presents significant modeling challenges. State-of-the-art seal models, such as those proposed by Doctors (2012) neglect the 3-dimensional finger seal shape, seal material properties (Graham et al., 1983) and real fluid effects (Ryken, 1978). Curvature-based measures developed in Chapter 5 suggest that modeling assumptions such as the membrane hypothesis and 2-dimensionality should be re-examined in light of the large-scale data. Due to shortenings typical of finger seals at deep immersions, seal response is characterized by large-rotation; therefore geometric nonlinearities should also be incorporated. The present study provides much needed reference data for validation studies. Unlike previous experimental studies,

the data set possesses spatial and temporal resolution sufficient to determine whether a given model captures the relevant physics. Future work should focus on dissemination of the data set.

Finger seals add considerable risk to the future development of the Surface-Effect Ships. Problems such as the rapid degradation of seal components contribute significantly to life-cycle costs of these craft. Similarly, difficulties in predicting seal loads at the design stage adds risk to prime-mover selection: this is especially problematic as SES are weight sensitive. These are major reasons why adoption of SES technology, which has significant advantages in terms of transport efficiency, is limited to all but the most specialized of military applications. The present study, restricted in velocity range, and tied to a specific seal geometry, would seem to contribute little towards solving these practical problems. However, upon closer investigation, solutions to the difficult engineering problems posed by bow seals are contingent on a basic understanding of the response of finger seals to hydrodynamic loads. To this end, the present study provides some of the first detailed data on seal response. The unique, high-resolution data set acquired as part of this thesis should serve as a valuable reference for future designers and modelers. As is discussed in the Future Work, owing to the compliance of bow seals, the data set may even permit inverse methods to be applied to estimate seal forces from the seal shape. The study also provides some of the first clues as to physical mechanisms responsible for seal vibration and wear. Lastly, a flexible test platform and a suite of novel measurement techniques have been developed for observing the response of seals at large-scale. With this contribution, future designers and engineers have a new testing capability to evaluate and refine seal designs. More importantly, together with the scalings developed as part of this work, engineers can begin to interpret the data. The thesis provides a solid foundation for future development of SES.

Chapter 8
Future work

The thesis represents a first step in understanding the hydroelastic response of bow seals. A flexible test platform has been developed for observing the response of seals at large-scale and a number of important features of bow seal response have been identified. A unique, high-resolution data set has been acquired which serves as a valuable resource for follow-on studies and future researchers. Finally, a qualitative model for buckling of the seals in the Tail region has been introduced and confirmed for the case of buckling on a hydrostatic foundation.

Given the complexity of the bow seal fluid-structure interaction problem, it is not surprising that this work raises more questions than it answers and presents a number of avenues for future work. The future work promises to not only further our understanding of bow seals, but has applications to the buckling of ice sheets and the response of flexible structures on elastic foundations in general.

Four types of future work are briefly discussed in this chapter. In Section 8.1, ideas for further analysis of the data set collected during large-scale experiments are presented. In Section 8.2 additional experiments utilizing the large-scale test platform are proposed. Section 8.3 discusses modifications to the small-scale buckling experiment that could be made to isolate additional aspects of seal physics. Section 8.4 suggests refinements that could be made to the beam-on-an-elastic foundation model in order to more realistically capture bow seal behavior.

8.1 Detailed analysis of the large-scale data

Important outstanding questions concerning the vibrations and hydrodynamic forces experienced by bow seals remain. The rich data set collected during the large-scale experiments at the Large Cavitation Channel contains data pertinent to these questions. To further delve into this data requires robust approaches deriving hydrodynamic forces from the gross load measurements. Similarly, to understand the spatio-temporal evolution of the buckling packets requires specialized processing of the high-resolution distance maps and cross-flow profiles.

Estimate hydrodynamic loads from gross load measurements

Derived quantities such as the hydrodynamic drag, lift and pitch-moment are highly sensitive to measurement error and analysis method. At low immersions and pressures, the magnitude of the hydrodynamic forces is the same order as the resolution of the load cells, which are sized to handle the expected gross loads. Due to the size of the seal system and superstructure, gross loads, which include the effect of the cushion pressure acting on the seal system, are significantly larger than the hydrodynamic loads.

To minimize errors associated with deriving hydrodynamic forces from gross loads, calibration procedures such as fill tests and forced oscillation tests were developed for the large-scale experiments. These tests can be post-processed to empirically verify the geometry of the seal system. One such approach is provided Appendix C. Based on calibration runs, this method generates a look-up table of the projected area as a function of seal immersion. At each time step, this look-up table is called to remove the effect of the cushion pressure, or pressure tare, from the load data, leaving the hydrodynamic contribution. Data-driven approaches such as this should be further developed and validated in order to build confidence in hydrodynamic load estimates. Sensitivity studies should be performed to compare this method to other methods. The resulting hydrodynamic forces should be

non-dimensionalized and compared with the current seal models (Doctors and Zalek, 2010) and past experimental work (Ryken, 1978).

Estimate bounds on hydrodynamic forces from seal shape:

There is also the potential, given the compliance of the seal and the quality of the seal shape measurements that seal drag can be approached as an inverse problem and bounds on hydrodynamic forces can be estimated indirectly from the measured shape. These estimates can serve as a check on the drag and lift derived from the load cells which are highly susceptible to biases.

Both far-field control volume and near-field approaches to the inverse problem should be explored. As a starting point, if it can be shown that a majority of the hydrodynamic load is carried through stretching alone (Section 5.1), the membrane hypothesis can be applied to estimate the flow-induced tension and pressure differential across the seal. The equilibrium equations for the case of a membrane are equivalent to the Young-Laplace equation for surface tension, where for the bow seal the bi-axial tension T and pressure differential are unknown, and the curvatures κ are estimated from the 3-dimensional ToF measurement [1]. More sophisticated methods which incorporate bending effects (Lee et al., 2008) are currently being developed to study forces acting on cells captured using 3-dimensional confocal microscopes. Before these inverse force estimation methods are applied to the noisy seal data, they should first be trained on synthetic data where applied forces and shapes are known quantities.

8.1.1 Qualitative hydrodynamic force modeling

Hypotheses should be developed to begin to understand the mechanisms responsible for the trends and magnitudes observed in the hydrodynamic forces. In particular, the near

[1] Assumptions such as the following likely have to be made: in the small region where the pressure differential is largest (see Figure 4.4), the tension in the membrane is essentially constant.

linear dependence of drag and lift on cushion pressure may be amenable to modeling. For instance, expanding on an idea from Yamakita and Itoh (1998), the linear dependence on pressure may partially be explained by treating the seal as a flat plate of length L, hinged at the leading edge, with constant pressure p_c acting on the upper face and hydrodynamic forces acting on the lower.

8.1.2 Seal shape measurement processing

The experiments completed in July 2012 yielded a wealth of data on the complex shapes assumed by finger seals. These data are in a number of forms including high-speed videos, three-dimensional point clouds, stereo-tracking image pairs and high-resolution cross-flow profiles. A small subset of the collected data are presented in Chapter 4. As measurement techniques such as time-of-flight imaging are relative new, there exists many opportunities for refinement of the image-processing techniques and calibration methods associated with these cameras. Further development of this high-resolution measurement technique should be pursued, as it holds significant promise for not just the bow seal problem, but difficult measurement problems in the area of fluid-structure interaction and free-surface hydrodynamics.

Registration and smoothing of 3-dimensional point clouds

As described in Section 3.2 a series of post-processing steps are required to register and smooth the distance images returned by the time-of-flight cameras. Images need to be corrected for optical distortion and segmented to identify the seal edge. To calculate higher order quantities such as curvature, time-averaging and/or spatial smoothing is required. (Figure 3.13a shows a raw seal shape prior to smoothing.)

Before attempting to apply inverse methods for estimating forces on the seals, such as proposed in Section 8.1, each step in the processing stream should be evaluated and

potential noise sources identified. Calibration procedures for the ToF cameras should be re-examined. In particular, corner detectors utilized in standard automated procedures for camera calibration such as implemented in OpenCV (Zhang, 1999) have difficulty with the low-resolution intensity images from the ToF camera. Similarly, robust procedures for locating the ToF cameras in the global coordinate system should be developed. Current methods often require minor adjustment of the transformation matrices for the seal shapes to pass basic sanity checks. Similarly, methods for estimating the stereo transformation matrix between two time-of-flight cameras should be further developed.

An example of how problems with the processing stream manifest themselves for the bow seal problem can be seen in Figure 8.1, where distance images acquired simultaneously from the two calibrated time-of-flight cameras located are overlayed. After calibration and registration, a separation of 10 mm exists between the seal shapes as estimated by the two cameras. It also appears that there is a discrepancy in the seal diameter, a symptom of problems with the camera calibration. These problems are not unique to the bow seal problem. Significant developments in the areas of camera calibration, multiple-view geometry and data fusion are occurring in the computer vision community. Due to the unique potential of these imaging techniques such recent advancements in the use of these cameras should be evaluated and incorporated into the processing stream.

Free surface processing

Data acquired during the large-scale experiments suggest that the ToF imaging technique utilized for experiments may be capable of resolving free-surface shape, a measurement of interest in many naval and fluid mechanics testing applications. An examples of an ToF image that has been post-processed to yield free-surface profile is shown in Figure 3.12. The potential of ToF imaging as a free-surface measurement technique should be explored further. In particular, the uncertainty of the ToF measurement system needs to be better understood. Experiments should be conducted to compare free-surface elevation measurements using

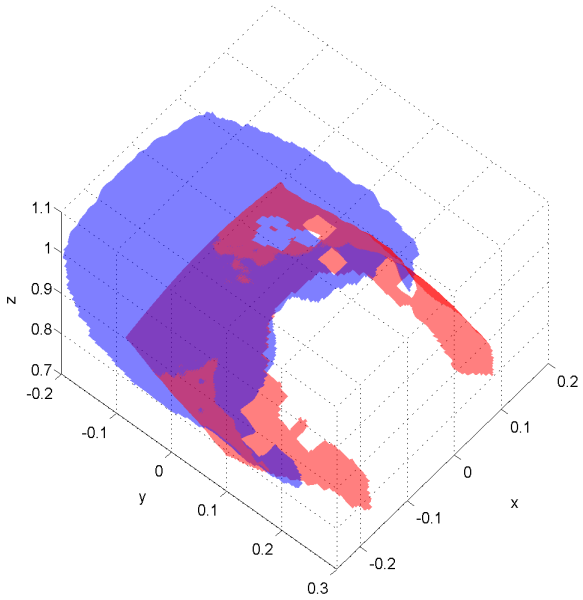

Figure 8.1 Seal 4, shape as measured by downward(red) and forward looking(blue) PMD cameras. Holes denote areas with poor return quality.

the ToF cameras to those made with reference channels. Free-surface data derived from the ToF camera during the large-scale experiments often feature a physically unrealizable drop-off in the free-surface elevation near the edge of the field-of-view. It should also be ascertained whether seeding or agitation of the free surface can improve the return.

Other measurement techniques

A number of measurement techniques developed for the large-scale tests merit further investigation for applications to hydrodynamics. The Tekscan® pressure mapping system utilized to measure pressure distributions on the Type-0 material should be further investigated. In particular, the calibration procedures and relatively low-resolution of this system require additional work. Naval applications of this technology are numerous and include problems such as measuring wave impact pressures and estimating measuring pressure drag in air-water mixtures where standard pressure ports have difficulties. Dense pressure arrays also have significant applications to the feedback and control of marine vehicles, where, similar to the lateral line in fish, pressure can be used to identify the disturbances caused by

bodies (Fernandez et al., 2011).

The ultra-violet sensitive dyes utilized as active markers during the large-scale experiments should also be investigated further. These were used to deploy a stereo-tracking system in parallel with the ToF camera. These dyes likely have applications in the area of digital image correlation and strain measurement and may have potential as color-coded tracers in fluids.

Fold descriptor estimation using continuous wavelet transform (CWT)

Presently, fold amplitude and wavelength are estimated using a zero-crossing analysis, where local minima and maxima are identified. Fourier analysis in the spatial domain has also been implemented, however it has proved difficult to reliably extract fold amplitudes using Fourier transforms due to the localized and low mode number shapes of the seal profiles. This is unfortunate as Fourier analysis is a particularly attractive method for understanding the unsteady behavior of bow seals, particularly for estimating the speed of transverse travelling waves, which can be found from the phase of the cross-spectrum of sequential frames (Jähne (1993)).

An alternative to Fourier methods that may be better suited to buckling profiles such as those seen in Figure 4.25 which contain a series of localized buckling packets, is the continuous wavelet transform (CWT). Wavelets allow spatial localization without manually tuning window sizes. Advanced signal processing methods such as wavelets should be investigated.

Depending on the wavelet family, the wavelet transform may also have a physical interpretation for the seal buckling problem. Analytical work (Budd and Peletier (2000)) has shown that localized buckling of a flexible membrane on a nonlinear foundation may take the form of a Gaussian-windowed sinusoid ($Ae^{-x^2\gamma}cos(x)$, where A and γ are constants. This approximate form of the post-buckled shape is advantageous for signal processing reasons, as it is identical to a continuous Morlet wavelet (Mallat, 1999), which is a standard

mother wavelet implemented in Matlab®. There is also the potential (see Chapa and Rao (2000) implemented as pat2cwav.m in Matlab®) to develop a custom wavelet family based on analytical solutions to the geometrically non-linear buckling problem such as presented by Diamant and Witten (2011).

Wavelets should be investigated as an alternative method for estimating the amplitudes, wavelength and mode numbers of localized buckling patterns. More importantly, when used in the complex form, wavelet analysis may facilitate calculation of wave speeds and aid in interpreting dynamic buckling events such as the complex fold splitting and spreading observed in Figure 4.25b. In particular, the coefficients from the wavelet decomposition can be used to estimate band-limited derivatives of the seal shape. From these derivatives the curvature and bending energy can be estimated. Changes in bending energy may provide an important indicator of work being performed by the fluid.

8.1.3 Quantitative identification of seal response regimes

A critical outcome of Chapter 4 is a classification of finger seal response regimes. Identification of potential stability boundaries provides insight into the dominant parameters influencing bow seal response and indicates transition regions that warrant further investigation. For instance, in the preliminary classification of response regimes for the Type-0 (NN) seal presented in Figure 4.26, a travelling-wave type instability is observed for immersion ratios $\delta_s/R_f < 0.2$. Above this immersion ratio, a portion of the seal lies parallel to the free-surface and the response changes dramatically. The physical mechanism responsible for this change in behavior[2] should be investigated.

Based on coding of still images acquired during the first round of experiments, seal response in Figure 4.26 is classified qualitatively in terms of pressure ratio, fold number, symmetry and instability type. The data used to generate Figure 4.26 are extremely subjec-

[2]One possible physical explanation is that the flow-induced tension from the presence of the "tail" suppresses the vibration (Morris-Thomas and Steen, 2009)

tive and rely on highlights on the wet seal surface to identify mode number. Because of this, the current classification scheme is not reproducible, and of limited use to numerical modelers trying to understanding whether a given approach begins to describe the observed range of material responses.

To reduce subjectivity, a classification similar to that of Figure 4.26 should be developed based on quantitative measures. As demonstrated in Chapter 4 and 6, when post-processed, the high-resolution cross-flow profiles acquired with the linescan camera yield sensitive quantitative descriptors of fold shape. These descriptors include estimates of fold amplitude, wavelength, vibration frequency and bending energy. This collection of post-processed data should be synthesized and if possible, compared to analytical predictions of stability boundaries. The quantitative measures should be chosen such that they are not biased by the width of the seal profile in the linescan measurement plane. Alternatively, if biased descriptors such as mode number are to be used, the time-synced high-speed video should be analyzed together with the linescan data to code seal behavior.

8.2 Large-scale experiments

The large-scale testing platform developed as part of this thesis and described in Chapter 3 provides the capability for making detailed observations of bow seals operating in a full-scale environment. In order to extend the results and scalings of the present study with confidence, additional experiments should be performed to address limitations of the present study such as the narrow velocity range. Modifications to the seal system presented below are also suggested that promise to dramatically increase the resolution of load measurements.

Repeat experiments to achieve variation of inflow velocity

A significant limitation of the present study is the narrow speed range. Past work (Besch, 1976) and the preliminary scaling laws introduced in Section 5.6.4 suggest that seal con-

figuration and stability may be highly dependent on inflow velocity particularly near the leading edge. To extend the speed range with the existing testing platform is a non-trivial task but should be attempted. The experiments on the high-speed carriage performed by Besch (1976) represent one method of augmenting the speed range.

Adapt measurement subsystems for sea trial use

Another potential avenue for increasing the speed range is to adapt the measurement subsystems from the large-scale experiment and conduct sea trials on a suitable ACV or SES. Due to the harsh operating environment at the LCC, systems for measuring seal loads and motions developed as part of this thesis are quite robust. In particular, it would be relatively straightforward to adapt the linescan camera utilized in this thesis for sea trial use.

Additional data to acquire during large-scale experiments

An interesting question that arises from the analytical work on seal buckling is how the buckling mode of the seal is set. It is hypothesized, based on underwater footage (see Figure 4.6a), that the mode is set by tension at the knuckle. The footage shows small, almost conical folds initiating at the knuckle; moving downstream, these folds are observed to spread at some rate eventually merging near the trailing edge. Recent work by Vandeparre et al. (2011) provides a framework for understanding the spatial evolution of these folds. In the case of Vandeparre et al. (2011), tension in the fabric is set by gravity and by the mass of the fabric below the point of interest. At this time, it is not possible to place the seal buckling problem within the hierarchy presented by Vandeparre et al.. This is due to the time-averaging process and limited spatial resolution of the ToF data. In Figure 4.22 there is evidence that spreading similar to Vandeparre et al. (2011) does occur and is well-resolved by the linescan camera. However, as the camera was positioned at a fixed streamwise location ${}^{s}X_{ivc}$ for all tests, comparisons to the scaling laws presented by Vandeparre et al. (2011) cannot be made. For further large-scale studies measurement of the buckling wavelength should be made at a

number of streamwise positions within a single test condition. The current mounting system on the large-scale test platform permits repositioning the camera longitudinally, however this requires draining the LCC test section. Methods for repositioning the camera while running and maintaining a given condition, should be investigated.

Truncated seal testing

A challenge in estimating hydrodynamic loads on bow seals is that the current test platform requires deriving hydrodynamic loads from gross load measurements - a calculation which is highly susceptible to error. The uncertainty in the hydrodynamic load calculation is closely linked to the projected area of the seal system (see Appendix C). It is therefore advantageous to reduce the projected area. This was partially accomplished in the large-scale experiments through the use of the 3-axis load cell system, which removed the support structure from the load path. Further reductions to the projected area should be implemented. As long as the height of the seal is greater than the immersion, the hydrodynamic performance of the seal should remain largely unchanged. A truncated seal will still develop the same hoop stress when inflated and will project the same geometry into the fluid as a taller seal. The advantages of a vertically truncated seal are three-fold: 1) smaller capacity load cells can be employed; 2) the load path does not include pressure barriers and support structure, therefore there is less uncertainty in projected area estimates; and 3) if desired, the size of the physical model can be reduced.

Testing a rigid model based on 3-dimensional mode shape acquired by ToF camera

Three-dimensional measurements of the seal shape and rapid-prototyping enable additional approaches for understanding local seal hydrodynamics. One idea that should be explored is whether the highly compliant bow seal, acted on by both internal pressure forces and hydrodynamic forces, can be replaced with a rigid body of the same shape acted on by solely hydrodynamic forces. The rigid model could be printed via rapid-prototyping techniques

to the shape as measured by the ToF camera for a stable configuration. This allows more conventional measurement techniques to be applied to measuring bow seal loads. As the body would now be solid, features such as pressure taps can also be introduced to the physical model. If hydrodynamic loads are of interest, load cells can be sized according to the hydrodynamic, not gross loads. The advantage being that hydrodynamic loads are measured directly for the solid model rather than derived from the pressure, gross force and free-surface elevation measurements as is the case for the compliant seal.

There are a number of challenges to a rigid seal approach. It is not clear how to fully match the test conditions of the compliant structure, in particular the waverise caused by the air cushion plays an important role in seal response. In addition, the technique is sensitive to the treatment of the trailing edge and how it fairs to the larger body. Despite these challenges, techniques such as this should be explored going forward, particulary if one is studying the detailed hydrodynamics in a small water tunnel and can avoid the large-scale test platform and challenges of running in the Large Cavitation Channel.

8.2.1 Testing in the presence of known disturbances

During the experiments it was observed that seal shapes featuring higher mode numbers, corresponding to larger system sizes η, were more susceptible to vibrations than those at lower mode numbers. This phenomenon should be investigated as a potential mechanism responsible for fatigue-causing vibration. To do this, one avenue of research is to perturb the bow seal system. As seen in Figure 4.25, when excited, the system momentarily moves to a higher energy state. A number of forms of excitation should be investigated, including pulses of various durations as well as regular waves. The excitation should be well characterized and small in amplitude so as not to drastically change the immersion. Particularly at high mode numbers, the system should require minimal excitation to change configuration. A challenge to be considered if excitation is to be performed at the LCC is that it is almost impossible to create a truly quiescent inflow, and that if the excitation is intended to simulate

ocean waves the frequency of encounter of a vessel travelling at the free-stream velocity should be matched.

8.2.2 Other large-scale experiments

Due to the complexity of bow seal structural response, the hydroelastic response of simplified "seal-like" geometries should be explored to isolate aspects of seal physics and to validate numerical techniques. In particular, the experimental set-up of Doctors and Zalek (2010), which features a 2-dimensional flexible bow seal, should be revisited. The seal shape of Doctors and Zalek (2010) is more amenable to analytical work than the full 3-dimensional bow seal, and features a balance of internal pressures, structural and hydrodynamic forces similar to the 3-dimensional finger at centerline. In addition, by varying the seal length, the experiments could provide an opportunity to develop inverse methods for estimating hydrodynamic forces.

Currently, there are significant differences between the 3-dimensional geometry of finger seals as tested and the geometry and Reynolds number of seal models such as developed by Doctors and Zalek (2010). In order to facilitate development of these models, experiments should be devised that enable direct comparisons with numerical simulations. For instance, the seal model by Doctors and Zalek (2010) treats the seal as a 2-dimensional plate assuming a certain form (linear/quadratic/cubic). As such, forms equivalent to those implemented in Doctors and Zalek (2010) model should be tested. A starting point for these experiments could be a first-order seal shape or a hinged flat plate. Differences between model and experiment for this direct comparison should be understood before proceeding to compare results to the complex geometries of a finger-seal.

Large-scale experiments should also be performed to isolate physics of the Tail region. One approach, inspired by Vandeparre et al. (2011) is to impose buckling at a given wavelength at the leading edge of a fluid-loaded sheet. This could be accomplished, rather than through displacement of the lateral edges, which only excites a single wavelength, through

clamps of a sinusoidal form. By varying properties such as the wavelength and amplitude of the clamps and the length of the sheet (tension), hydrodynamic effects on the spatial evolution of the buckling wavelength can be better understood. The persistence of wavelengths above and below the natural buckling wavelength may provide insight into the stability of certain buckling patterns. Experiments of this kind not only have the potential to shed light on seal physics but may also have application as an optical shear stress measurement technique, since the spreading rate of the buckling wavelength is set by the flow-induced tension in the sheet.

8.3 Small-scale experiments

Small-scale experiments provide a low-cost method of testing highly-compliant structures such as bow seals under simplified loadings. The current experimental set-up, as described in Chapter 6 is configured to evaluate the beam-on-an-elastic foundation model presented in Chapter 5, which corresponds to the bow seal operating at zero-speed where hydrostatic restoring forces dominate. These buckling experiments should be improved and extended to understand the influence of the flow-induced tensions, which may play an important role in seal response at higher velocities.

8.3.1 Understanding the role of boundary conditions in wavelength selection

One of the interesting observations from the benchtop experiments is the presence of amplitude modulation in the post-buckled shapes of the thicker samples (smaller system size η). The regular wave forms observed in Figure 6.2 for the silicone sample S0 (and predicted), are not observed for the NN, N1 and N2 samples. The post-buckled shape at the initial bifurcation of these materials is similar to that shown in Figure 6.3 for the Type-0 (NN) material. These amplitude modulated shapes are reminiscent of those observed during the

large-scale experiments (see Figure 4.13, (b,c,d)) for the Type-0 (NN). It is hypothesized that even for the largest physical sizes, the post-buckled shape of the thicker samples is influenced by boundaries. In particular, it is suspected that the knife-edge supports restrict rotation of the material. Experiments should be performed to better understand the source of this amplitude modulation and the role of boundary conditions. Boundary conditions may also explain why symmetric configurations are preferred at large-scale. Various experimental approaches should be investigated, including extending the length to allow for larger samples, and/or forcing the boundary condition to a clamped-clamped state. A purely clamped-clamped condition can be approximated better than pinned/pinned condition in an experimental setting (Singer et al., 1998).

8.3.2 Inclined cylinder under confinement

The results of the present study pertain to a relatively small portion of the experimental space tested at the LCC. In particular, the study is relevant to the response of the Type-1 material at deep immersions. The correspondence between the BoF theory and the Type-0 seal response was much poorer than the Type-1. Due to the small system size η of the Type-0 material, the effect of the foundation is expected to be fairly small in relation to the effect of boundary conditions. The proposed experiments look at the response of the Type-0 seal under the action of a solid boundary. There is evidence (see Cerda et al. (2005)), that similar to a confined cone, the wavelength of the post-buckled seal is set entirely by confinement and isometric bending of the material. The experiments would comprise inflating a seal and moving a ground plate vertically to simulate the hydrodynamic effect. The 3-dimensional shape of the seal would be acquired for various vertical positions of the ground plate. Further tests could examine the influence of the angle between the ground plate and seal. Proof of concept experiments conducted at the Marine Hydrodynamics Lab indicate that mode shapes in the Type-0 material similar to those observed at the LCC can be reproduced on the tabletop, in the absence of hydrodynamic forces.

8.3.3 Other small-scale experiments

Due to challenges measuring hydrodynamics forces on bow seals, the ability to use seal shape, which can be acquired reliably, as an indicator for hydrodynamic forces should be developed and validated. In order to build confidence in this approach, small-scale studies on simplified geometries should be conducted to evaluate solution methods for tackling this inverse problem. As a first step, ballasting the structure could be used to simulate the action of hydrodynamics forces.

The idea of ballasting the material to simulate the action of hydrodynamic force should also be employed to understand the role of flow-induced tension in seal buckling. It is hypothesized that the influence of hydrostatic restoring forces will decrease at higher velocities; in their place, restoring forces due to flow-induced tension may begin to dominate. The tension (set by velocity and wetted-length) at which this transition occurs should be investigated at small-scale.

8.3.4 Dynamic mechanical analysis of seal materials

As both the reinforcement and coating are constructed of polymers, which exhibit complex constitutive properties including nonlinear stress-strain behavior, hysteresis and viscoelasticity (Graham et al., 1983; Hertzberg et al., 1975), nonlinear behavior is expected to play a role in the behavior of SES seals. In addition, the presence of the woven fabric reinforcement adds a degree of orthotropy, with the fabric possessing principal directions due to the weaving process (Hu, 2004). An example of the viscoelastic behavior found in SES seal materials is seen in Figure 2.12. This shows that as strain rate is increased in the tensile mode, the seal material become more "glassy" or rigid, resulting in a 10-fold increase in elastic modulus. The situation is further complicated due to the fact that seal materials are composites, with different polymers-glass transition frequencies for the reinforcement and coating. When the material is excited in tension, the transition frequency may be set by the

reinforcement while in bending the transition frequency may be dependent on properties of the coating. To date, very little attention has been devoted to the constitutive modeling of seal materials. In order to support detailed modeling efforts, additional work on seal material characterization should be performed.

8.4 Refinement of post-buckling model

The beam-on-an-elastic-foundation (BoF) model presented in Chapter 5 provides a useful analogy for understanding the response of bow seals in the Tail region. In order to more realistically model bow seal behavior, the model should be refined to include factors such as non-linearities in the foundation stiffness, unsteadiness and 3-dimensionality.

8.4.1 Explore finite width effects for the elastica on a foundation

Per Diamant and Witten (2011), the geometrically non-linear model presented in Chapter 5 has a family of known solutions for a beam of infinite width. While this solution can be applied qualitatively to the Type-1 material, with a minimum system size of $\eta_\rho g = 40$, finite-width effects are expected to be significant for relatively stiff materials such as the Type-0 (NN) material. Solution techniques for the finite-width case should be explored. Starting points for approaching the nonlinear finite-width problem are provided by Rivetti and Neukirch (2014) and Walton (1999), who employ analytical continuation methods and perturbation analysis to solve the nonlinear differential equations. In addition, small-strain, large-rotation finite element methods should also be explored.

8.4.2 Discontinuous foundation

The free-surface is observed to detach from the seal in both the small and large-scale experiments. The current model does not capture the transition between these states (Vella et al., 2009). This phenomenon should be explored as it may play a role in air leakage and

hydrodynamic drag, the detachment representing a change in wetted area. It may also play a role in seal vibration as mechanisms for seal vibration may be dominated by fabric inertia without the free surface. One aspect of seal detachment that may be worth exploring (Crewe, 1971) is that the detached state may offer certain performance advantages such as decreased drag (air lubrication).

8.4.3 Dynamic buckling

The response regimes for the Type-0 material indicate that the seal response is generally unsteady, with traveling-wave or mode-switching type instabilities present for most conditions. Closer examination of time-series for the Type-1 seal (see Figure 4.25, shows that the seal shifts to a higher mode number when subjected to disturbances. Despite these features and the fact that bow seal operate in an unsteady wave environment, the model presented in Chapter 5, considers solely the quasi-static behavior of bow seals and cannot capture these effects. To begin to understand the problem of seal vibration, time-dependence should be introduced. To begin with, the linear buckling model could be modified Lindberg and Florence (1987). For an example of how time-dependence might be introduced to the geometrically-nonlinear model see Santillan (2007).

8.4.4 Panel flutter

Seal vibration in the Tail region has a number of correlates to the classical problem of shell and panel aeroelasticity Dowell (1975). As time-dependence is introduced, work should be performed to understand whether seal vibration can be viewed in the context of panel flutter, and whether changes in seal behavior such as seen in Figure 4.26 are due to a loss of static stability (divergence) or flutter. The panel flutter literature suggests that boundary conditions play a significant role in how the structure loses stability.

Introduce three-dimensional effects

The experiments showed that seal response is characterized by large-rotations and can only be adequately described in 3-dimensions. In Section 5.1, it was shown that for the cylindrical face of the seal, constrained by the neighboring seals, to buckle and conform to the free-surface, it must experience a non-zero Gaussian curvature and strain. There is no 2-dimensional analogue of the Gaussian curvature. Despite this 3-dimensionality, both the buckling model presented in Section 5 and models such as proposed by Doctors (2012) are 2-dimensional. Future work should examine the suitability of this assumption and explore ways to incorporate three-dimensional effects. One method, utilized extensively in the study of shell aeroelasticity is to treat the seal as a shallow or Donnell's type shell(**?**). In this case, the presence of curvature leads to a local stiffening of the structure and is most suitable to cases where the curvature due to buckling (A/λ^2 is much less than the curvature of the unbuckled structure (for instance $\kappa_f = \frac{1}{R_f}$). Ultimately, fully 3-dimensional descriptions and/or finite-element methods may need to be investigated.

Appendices

Appendix A
Bending rigidity of SES seal materials

A.1 Background

The bending rigidity D of materials utilized in the large and scale experiment is required for the post-buckling analysis conducted in Chapter 5. The results presented in this appendix provide estimates of this important parameter for each of the materials tested, fully covering the range of curvatures observed during the experiments.

There are a number of methods commonly adopted for estimating the bending rigidity of materials. The most straightforward method, applicable to an isotropic linearly elastic material with known Young's modulus, is to directly calculate the bending rigidity (via Equation A.1), where E is Young's modulus of elasticity, h is the fabric thickness and ν is Poisson's ratio. Owing to the presence of a relatively thin and stiff fabric core which drives the tensile modulus, it is expected that Equation A.1, if applied using the gross tensile modulus E_t, would significantly overestimate the rigidity of the material.

$$D = \frac{Eh^3}{12(1-\nu^2)} \tag{A.1}$$

However, as described in Section 2.5.1, it is feasible, given the geometry and stress-strain properties of the reinforcement and coating that Equation A.1 can be modified to account for the composite nature of seal materials.

Another method, commonly used in the fabric and seal testing community is the ASTM 1388 (ASTM, 2010) fabric stiffness test standard. Based on Peirce (1930), the ASTM

standard uses the equations of an heavy elastica to estimate the bending rigidity from the geometry of a cantilevered fabric sample. The method assumes that the bending rigidity is independent of the curvature.

$$D_{Peirce} = \rho_f g(\frac{L_b}{2})^3(\frac{cos(\phi/2)}{tan(\phi)}) \tag{A.2}$$

L_b is the bending length (described in the ASTM standard) and ϕ is a constant of the test setup, typically 43^o.

Using the ASTM method, proof-of-concept experiments for the present study were conducted. These showed significant variability in D, with disparities of an order of magnitude possible between repeat tests. It should be noted that all methods for estimating D discussed in this appendix, consider only the static behavior of the material and do not attempt to characterize the visco-elastic (Graham et al., 1983) or hysteretic (Culpin, 1974) behavior known to affect elastomers and fabrics such as seal materials.

A.2 Test Method

The test method implemented in this report, similar to Clapp et al. (1990), improves upon the ASTM/Peirce method by measuring the displaced shape of the cantilevered beam during a bending length test. This allows one to map the full bending moment (B_m) versus curvature relationship (κ) for the fabric, and to test the validity of the bending rigidities derived from the ASTM method (equation A.2) which is specific to a single curvature (Szablewski and Kobza, 2003). For the present study, D is found from the slope of the bending moment versus curvature diagram.

$$D = \frac{dB_m}{d\kappa} \tag{A.3}$$

The test setup is shown in Figure A.1. A laser linescan scan camera (IVC-3D, resolution

<0.5 mm) acquires the deformed shape of a cantilevered test sample acting under it's own weight.

The test procedure is as follows:

1. A series of calibration images are obtained of the reference plane alone. The reference plane has been aligned perpendicular to gravity to within the accuracy of a machinist's level (~0.01 deg). The reference plane can be seen in Figure A.2 . These calibration images enable one to determine the transformation between the camera coordinate system and global coordinate system. See Figure A.1 for the global coordinate system.

2. Next the fabric is installed on the reference plane such that there is no overhang and the thickness of the fabric can be verified.

3. Finally, using an acrylic push block, a portion of the sample is pushed over the edge and displaces downward due to gravity. The fabric shape is then acquired, together with scale measurements and still photos. The scale measurements provide a check on the arc-length, which can also estimated directly from the displacement measurement.

4. The process is repeated for three different arc-lengths, or until the fabric is hanging nearly vertically at which point the laser scanner (as presently set-up) cannot resolve the hanging shape. Testing at a number of arc-lengths enables one to obtain bending rigidity estimates for a range of curvatures.

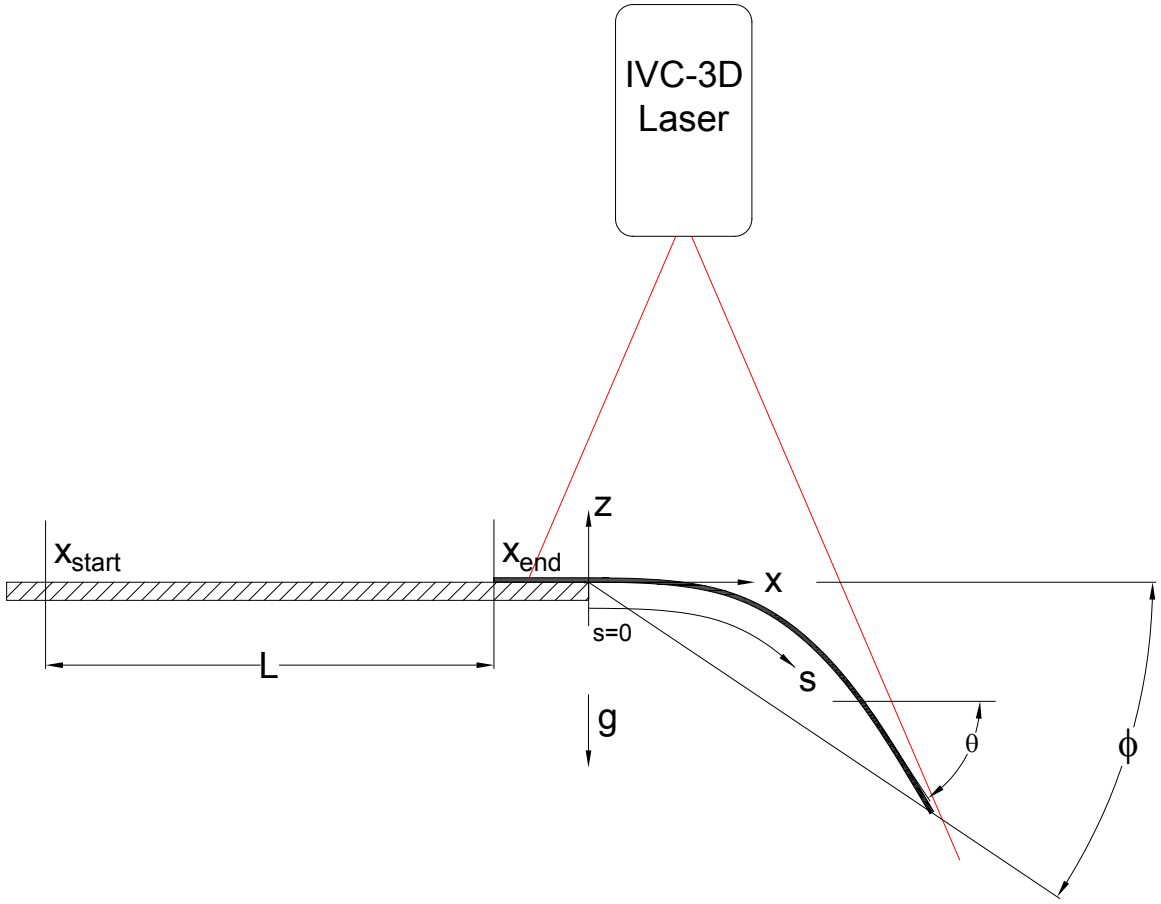

Figure A.1 Bending length test setup and coordinate system.

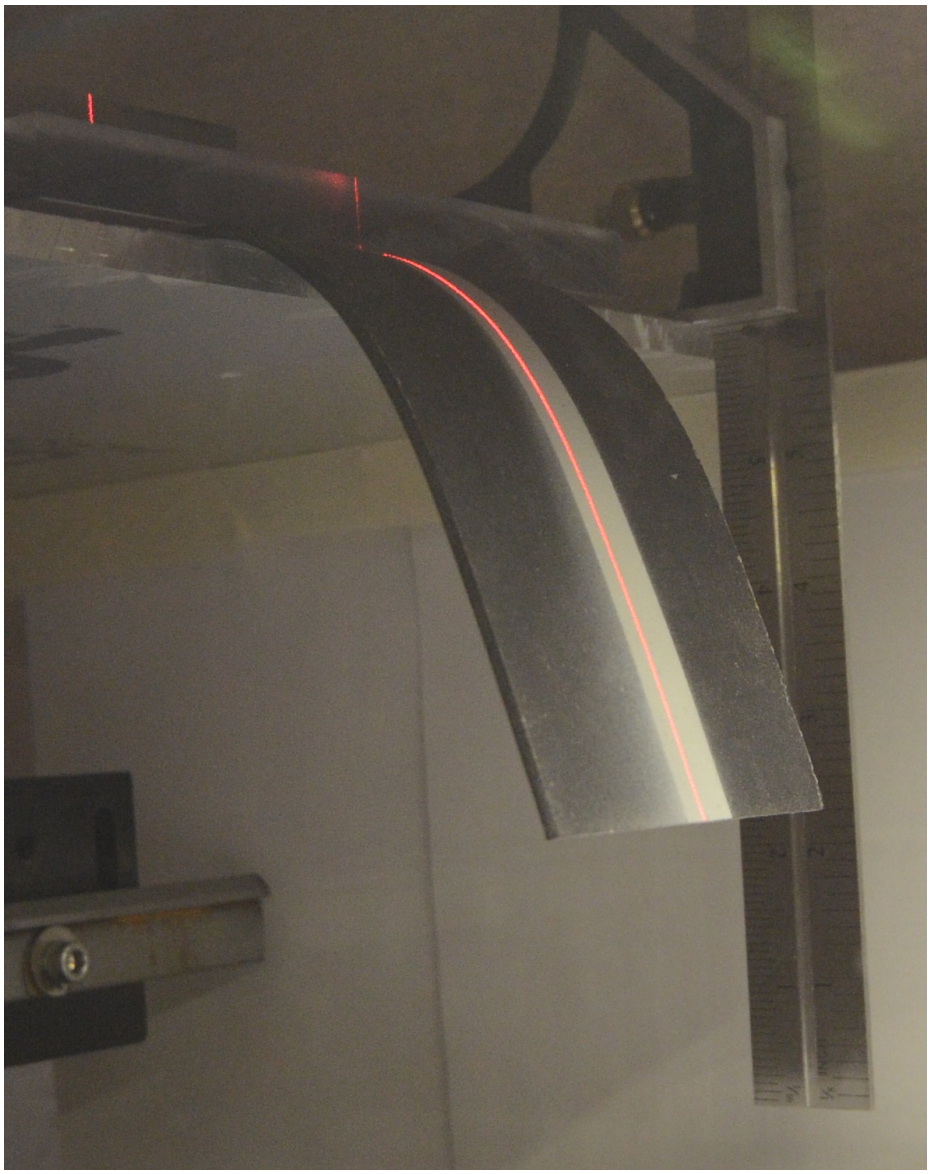

Figure A.2 Cantilever bending test - Sample N0, Side A.

A.3 Data Analysis

Once data are acquired, the raw displacement data are carefully curve-fit to determine both the curvature and bending moment. Even with accurate displacement data, because the equation for curvature (Equation A.4 (Frisch-Fay, 1962)) relies on the second derivative of the displacement, which tends to amplify noise, smoothing is required to avoid artifacts.

$$\kappa = \frac{d\theta}{ds} = \frac{\frac{\partial^2 \zeta}{dx^2}}{[(1+(\frac{\partial \zeta}{\partial x})^2]^{3/2}} \neq \frac{d^2\zeta}{dx^2} \tag{A.4}$$

Measurements must also be transformed from the camera coordinate system to the global coordinate system.

In Matlab®, a constrained least squares method (lsqlin) is used for the curve-fitting as it enables one to easily enforce realistic boundary conditions and constraints. The essential boundary conditions (Equations A.5, A.6) are similar to the canonical fixed-free beam and state that at the fixed end, the neutral axis must pass through the origin and lie parallel to the reference plane.

1. No slope at table end

$$\frac{d\zeta}{dx}(s=0) = tan(\theta_0) \tag{A.5}$$

2. Passes through origin at table end

$$\zeta(s=0) = 0 \tag{A.6}$$

Non-essential boundary conditions are also implemented and required in some cases. These conditions are applied to correct for curling at the edge of the sample which precludes realistic estimates of the bending rigidity at small curvatures. An example of curling can be seen at the free-edge of the HN sample in Figure A.3. A very powerful non-essential boundary condition is given in Equation A.8, which requires zero curvature at the free end.

1. Concave down

$$\frac{d^2\zeta}{dx^2}(s=0 \quad \text{to} \quad L) < 0 \tag{A.7}$$

2. No bending moment/curvature at free end,

$$\frac{d^2\zeta}{dx^2}(s=L) = 0 \tag{A.8}$$

The impact of this on a typical bending moment versus curvature plot can be seen in Figure A.8. A less stringent method of dealing with curl is to require that the deformed shape be concave-down over a selected interval (Equation A.7).

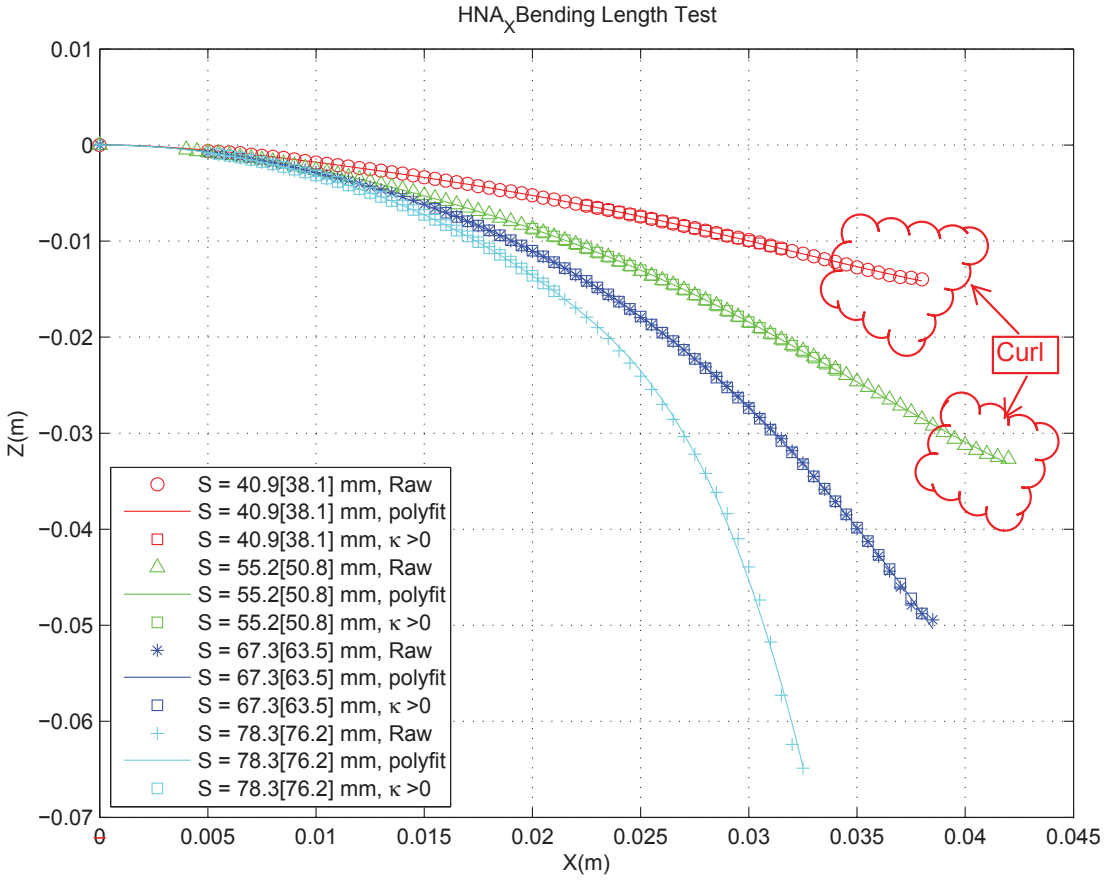

Figure A.3 Fabric displacement showing curl, raw data and after curve-fit, HN side A, Warp (X)

A number of different curve-fit types are implemented in the code. The choice of fit method depends on the behavior of the sample. Samples exhibiting curling at the ends

(curvature change) may require a higher order fit than other samples. In addition to the default continuous 5th-order polynomial fit, the user also has the option to use 6th order as well as quartic spline formulations. Lower order continuous fits are favored as they have fewer possible sign changes in the 2nd derivative. The default fit is sufficient for the majority of test cases, however it was found that the 6th-order or spline fits are required for the Hypalon (HN) material particularly near the clamped boundary. For spline fits, the number of segments is set as low as possible, typically 3 or 4 segments are sufficient even in the most extreme cases.

Once the data are curve fit, the curvature and bending moment can be estimated via Equations A.10 and A.4. Analytical derivatives of the polynomials are used to reduce noise. The data are also rotated (Equation A.9) such that at the clamped edge, θ, the angle of the clamped edge with respect to the gravity reference plane is zero.

$$\theta = tan^{-1}(\frac{d\zeta}{dx}) - \theta_0 \tag{A.9}$$

θ_0 is the roll correction from the calibration image. The bending moment is estimated by calculating the product $\rho_f(L-s^*)cos(\theta(L-s^*))$ at each site and integrating numerically with respect to the arc-length using the trapezoidal rule.

$$B_m(s) = \int_0^{L-s} \rho(L-s*)cos(\theta(L-s*))ds* \tag{A.10}$$

ρ_f is the areal weight of the fabric, L is the total arc length of the sample and s^* is a dummy variable for the arc length (s). Finally, the bending rigidity is calculated by taking the derivative of the bending moment with respect to curvature (Equation A.3). If non-essential B.C.'s are not used and the curl at the end of the sample is allowed to persist , the data are windowed to exclude points after this change in curvature (see Figure A.6). If these were allowed to be included the bending rigidity has the potential to be multi-valued for a given curvature (as in the $\kappa \neq 0$ case in Figure A.4). In addition, points near the fixed boundary

are also excluded; displacements at these locations lie in the shadow of the laser and have to be extrapolated making them highly sensitive to the curve-fitting method.

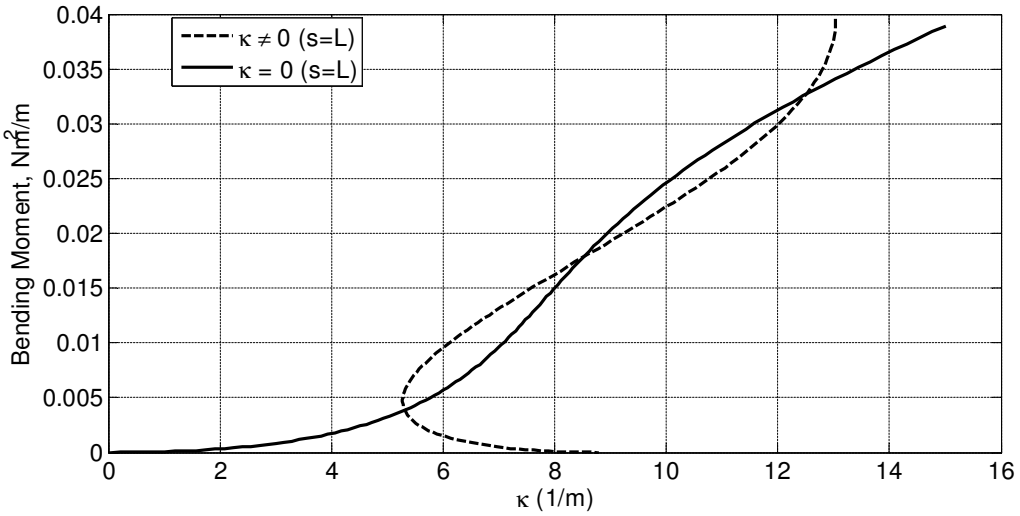

Figure A.4 Effect of $\frac{d^2\zeta}{dx^2}(s=L)=0$ constraint on B_m as function κ, NNA_X sample.

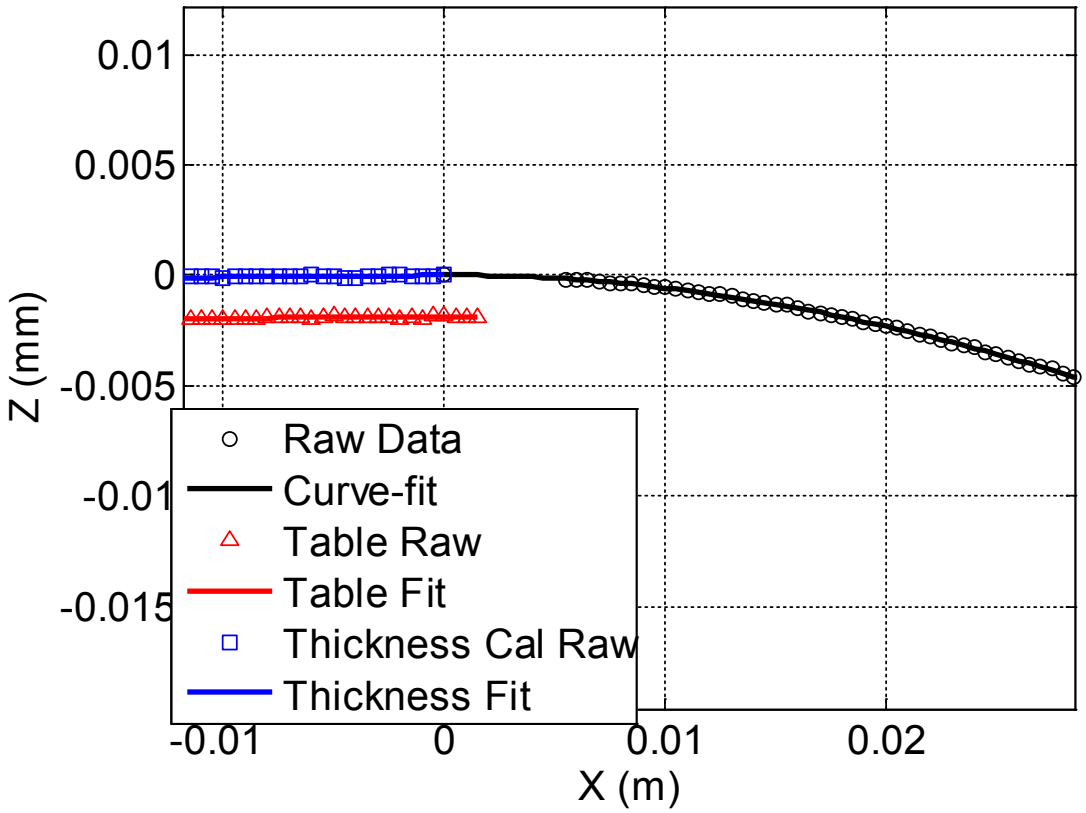

Figure A.5 Details of typical NNA_X curve-fit, showing table edge and thickness calibration data.

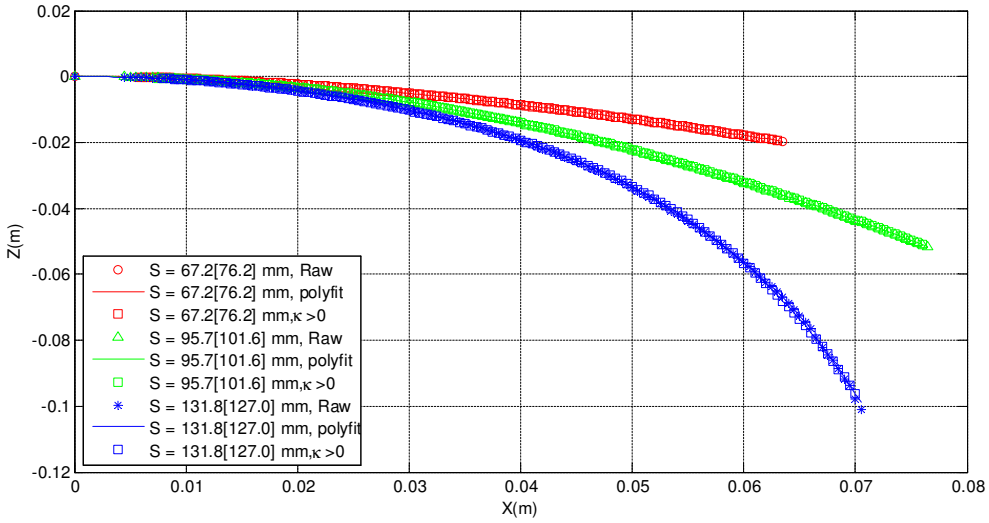

Figure A.6 Fabric displacement raw data and after curve-fit, NN side A, Warp (X) , squares indicate region of positive curvature. In the legend, the arc-length in brackets is based on the from ruler measurement. The arc-length outside the bracket is estimated from the data.

A.4 Results and Discussion

Results from the bending length experiments are shown in Table A.1 along with estimates of the bending rigidity calculated using ASTM/Peirce (Equation A.2) and a lamina model of the fabric (Equation A.11). The bending rigidity is calculated from the derivative of the bending moment with respect to curvature (Equation A.3). The bending moment versus curvature relationship for the Type-0 (NN) material in the warp (X) direction is shown in Figure A.7. Similarly, the bending moment versus curvature relationship for the Type-1 (HN) material in the warp (X) direction is shown in Figure A.8. This is calculated on a per test basis. Table A.1 consolidates these results by grouping all runs for a given material together and applying a linear regression, the slope of which is D. The results of the linear regression is compared with the local $\frac{dB_m}{d\kappa}$ for the Type-0 and Type-1 materials in Figures A.8 and A.10. These results indicate that in general, the bending rigidity in the warp (X) direction (samples NN and HN) is higher than in weft (Y), with the difference less pronounced for material NN. The order of magnitude for D ranges from $O(10^{-6})$ for S0 to $O(10^{-3})$ for NN and N0. The order of magnitude of D is captured by both the $D = \frac{dB_m}{d\kappa}$, D_{Peirce} (Equation A.2), and

$D_{||}$ with D_{Peirce} on average about 40% higher than $\frac{dB_m}{d\kappa}$.

It should be noted that the ruler measurement of the arc-length was used in calculating D_{Peirce}. The ruler measurement of arc length is more robust than that estimated from fabric displacement as identifying the free edge location at the larger overhangs often proved challenging. Disparities in the arc length estimates are shown in the legends of the figures such as Figure A.7, where the arc length in the brackets is from the scale measurement. The arc-length outside the bracket is calculate from the shape. The effect of this is seen most dramatically in plots of B_m versus κ where the difference manifests as vertical shifts in the bending moment. As we are interested in derivatives, the net effect of incorrectly identifying the fabric edge is believed to be fairly small. However this effect can be clearly seen by comparing B_m versus κ, for NNB_X where the arc lengths agree well, and the bending moment curves almost collapse, to those from the N2 sample where there are significant arc length disparities. Even when there is not a bias due to the arc-length, there is significant scatter in the bending rigidity estimates. This is likely due to measurement noise, and uncertainty from the curve fitting. There may also be problems difficulties properly resolving the higher curvatures. A final trend worth noting is the tendency for the bending rigidity to increase or "stiffen" at higher curvatures.

Considering the fabric reinforcement and coating to behave like three lamina in parallel, an estimate of the bending rigidity of the NN sample ($D_{||}$) was made lamination theory Vinson (2005). The model is shown in Figure 2.11. Starting with Equation 2.16 which is generalized for any number of the layers and is suitable for double-ply materials, the term $\frac{E_c}{12(1-\nu_c^2)}$ is factored. The resulting Equation (A.11), assumes no-slip between layers and a linearly elastic material.

$$D_{||} = \frac{E_c t_t^3}{12(1-\nu_c^2)} \left(1 + \frac{t_r^3}{t_t^3}\left(\frac{E_r(1-\nu_c^2)}{E_c(1-\nu_r^2)}\right)\right) \tag{A.11}$$

The tensile elastic modulus of the fabric reinforcement (E_r) used in this calculation was

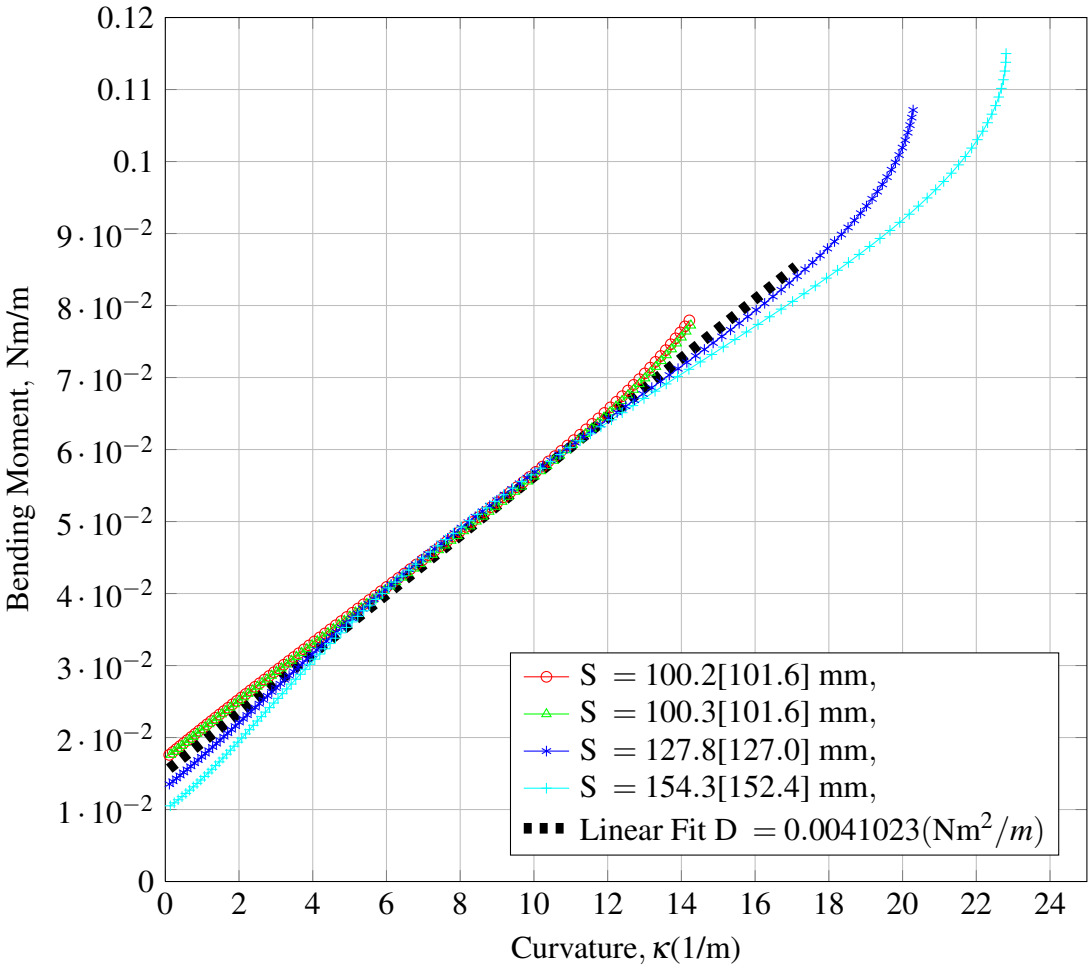

Figure A.7 Bending moment versus curvature relationship, Type-0 (NN) material, warp (X) direction, B side up.

estimated using Equation A.12, which the mixture rule applied to the stress-strain data obtained shown in Appendix B.1,

$$E_r \approx \frac{E_t t_t - E_c t_c}{t_r} \tag{A.12}$$

t_r is the thickness of the reinforcement, E_c is Young's modulus of the coating. t_t and t_c are the thickness and Young's modulus of the total composite including all layers. While stress-strain data is available for the coating of only the NN material, $D_{||}$ estimated in this manner compares favorably to that derived from the bending length data. This suggests, that the bending rigidity of the NN sample, with it's thin core and thick coating ($t_r \ll t_t$), is

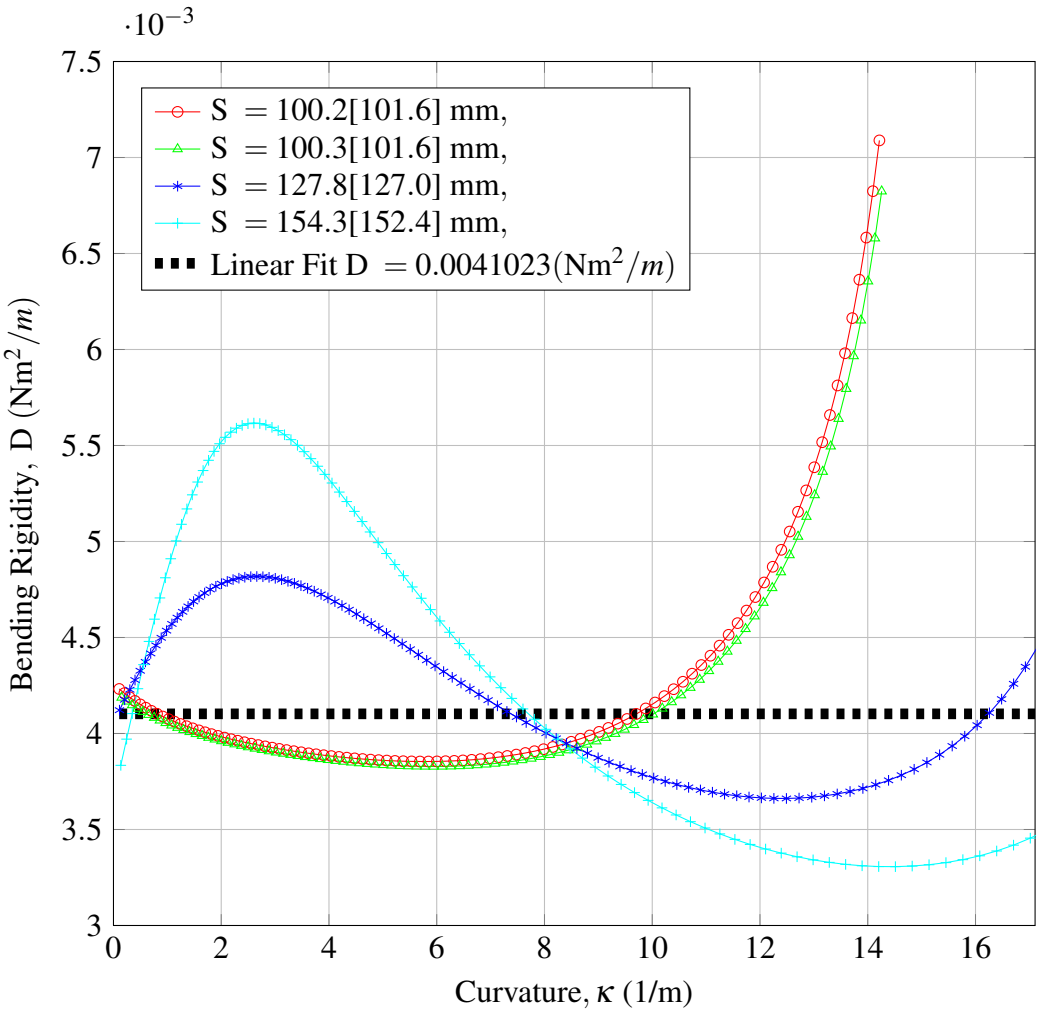

Figure A.8 Bending rigidity D versus curvature κ relationship, Type-0 (NN) material, warp (X) direction, B side up.

driven primarily by the properties of the coating. This can be seen in columns D_c and D_t which show the bending rigidities if the full thickness was comprised solely of coating (D_c) material, or with a material with the same modulus as was found for the composite NN (D_t). Comparison between the D_c and D_t suggests that as far as bending is concerned, one could almost assume that the composite material is composed entirely of elastomer coating.

Material Code	Side	Direction	$D = \frac{dB_m}{d\kappa}$(avg)	D_{ASTM}(avg)	$D_{\|\|}{}^a$	D_c(based on E_c)	D_t (based on E_t)
			Nm^2/m	Nm^2/m	Nm^2/m	Nm^2/m	
NN	A	X	0.003762	0.003243	0.006760	0.002153	0.1091
NN	B	X	0.004102	0.007391	0.006760	0.002153	0.1091
NN	A	Y	0.003564	0.003577	0.004241	0.002153	0.0506
HN	A	X	0.0000617	0.00006208			
HN	A	Y	0.0000338	0.00004978			
N0	AB	N/A (Isotropic)	0.0007204	0.0009466			
N1	AB	N/A	0.002759	0.003835			
N2	AB	N/A	0.003551	0.003789			
S0	A	N/A	1.706E-09	1.109E-09			

Table A.1 Bending rigidities derived from the modified bending length test.

[a] A Poisson's ratio of $\nu = 0.5$ (incompressible) was used

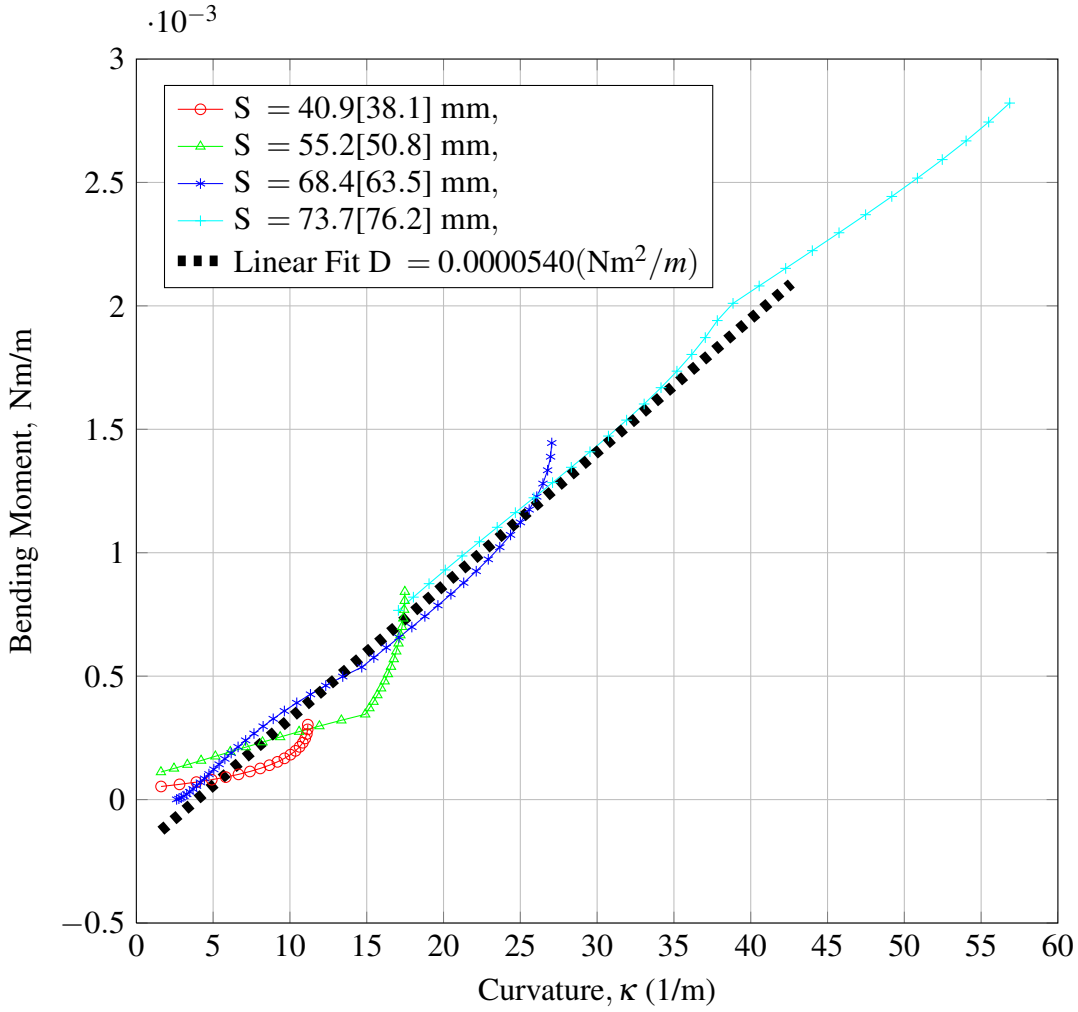

Figure A.9 Bending moment B_m versus curvature κ relationship, Type-1 (HN) material, warp (X) direction, A side up.

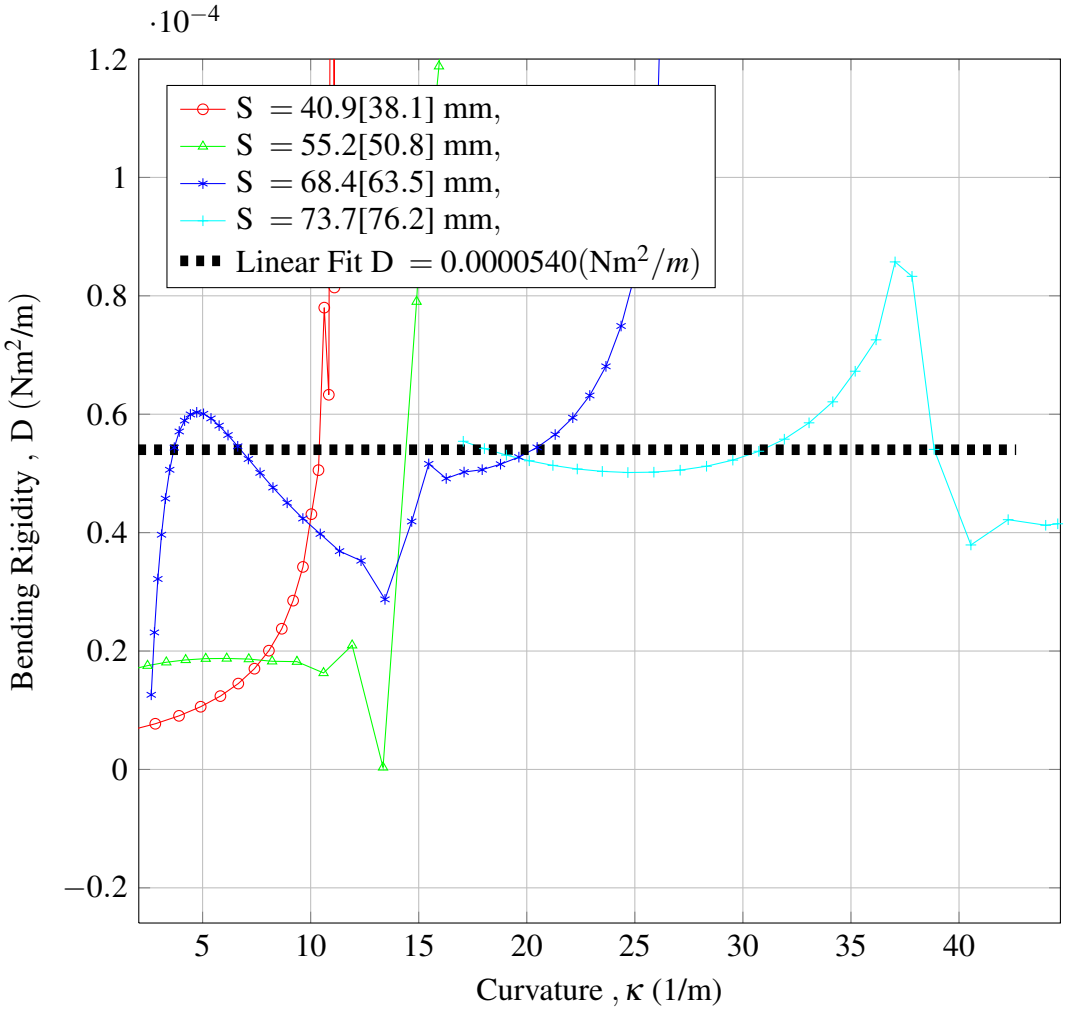

Figure A.10 Bending rigidity D versus curvature κ relationship, Type-1 (HN) material, warp (X) direction, A side up.

Appendix B

Areal weight and other properties of SES seal materials

Material	SampleID	Length (in)	Width (in)	Area (sq in)	Mass1 (g)	Mass2 (g)	Mass3 (g)	Avg. Mass (g)	ρ_f (kg/m^2)
N0	001	5.99	1.01	6.05	4.4	4.4	4.4	4.4	1.127
N1	002	5.99	1.01	6.05	8.3	8.4	8.4	8.37	2.144
N2	003	6.01	1.02	6.13	10.7	10.7	10.7	10.7	2.741
HN	007	12.10	4.02	48.64	9.5	9.4	9.4	9.43	0.300
NN	008	5.89	0.98	5.77	7.1	7.1	7.1	7.1	1.906

Table B.1 Fabric mass properties.

Material	Thickness, h (mm)
N0	0.79
N1	1.59
N2	2.38
HN	0.24
NN	1.59
NC [a]	0.63

Table B.2 Sample thicknesses.

[a]Coating from NN sample

B.1 Tensile modulus of material used in large-scale experiments

Material	Description	Direction	Modulus of Elasticity (MPa)
NN	Nitrile/Nylon	X	244.3
NN	Nitrile/Nylon	Y	113.4
HN	Hypalon/Nylon	X	741.8
HN	Hypalon/Nylon	Y	315.0
NC	Coating from NN Material	N/A	4.4763

Figure B.1 Modulus of elasticity, zero-strain.

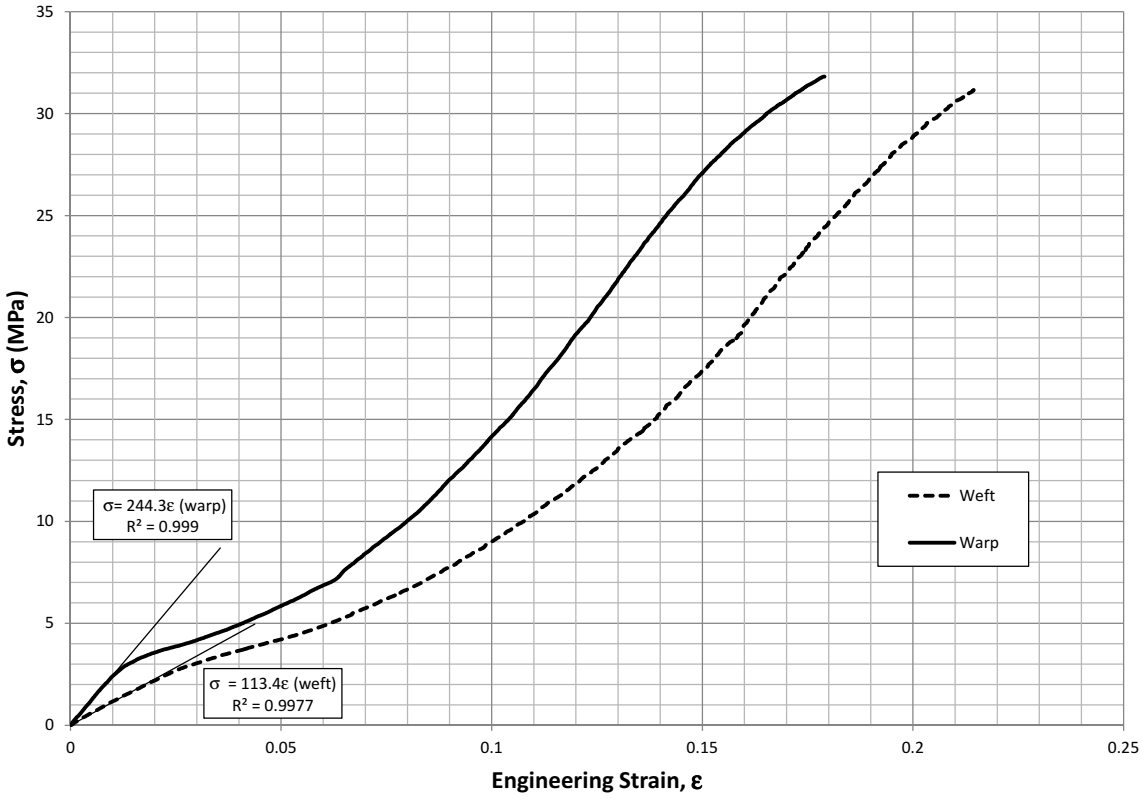

Figure B.2 Type-0 Nitrile-Nylon (NN) sample, uni-axial stress-strain relation, warp (X) and weft (Y) directions.

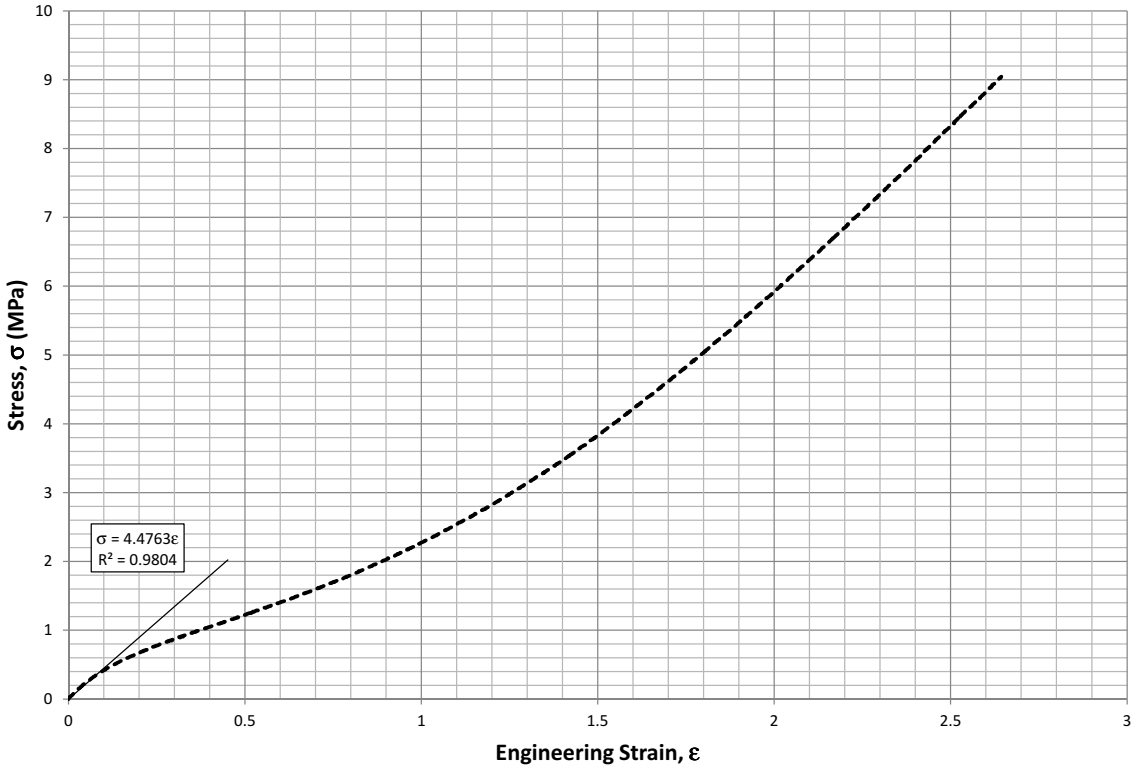

Figure B.3 Nitrile coating (NC) extracted from NN, uni-axial stress-strain relation.

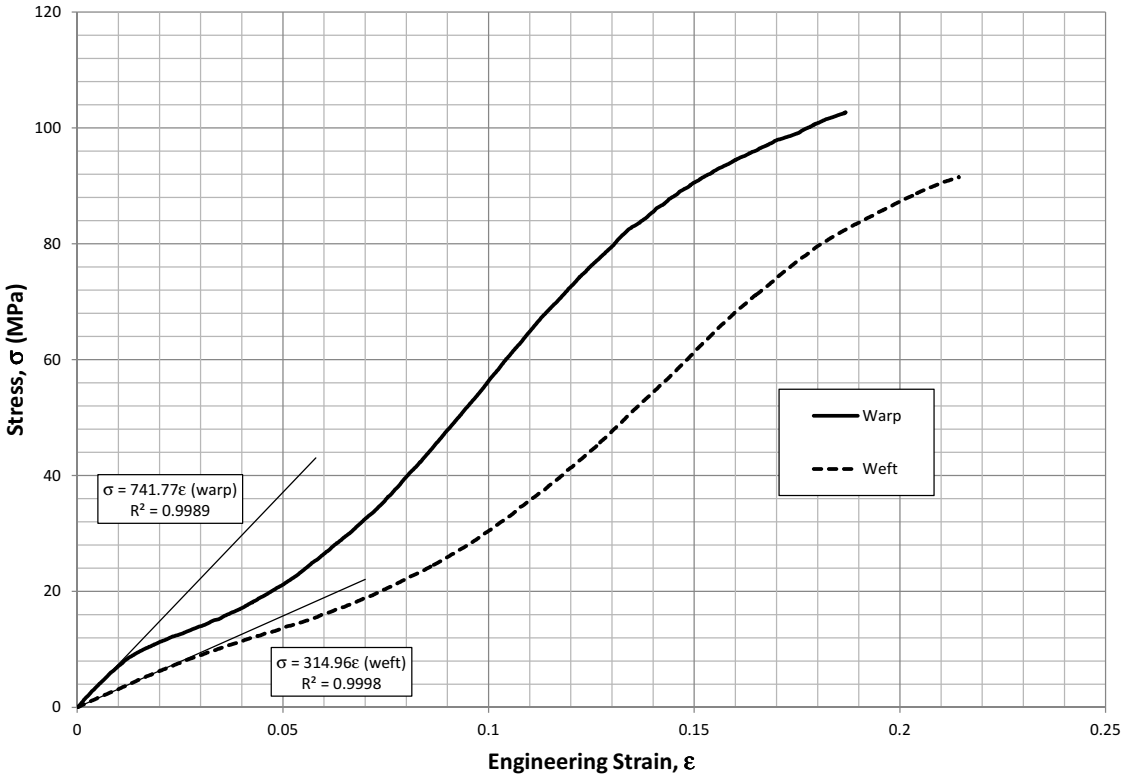

Figure B.4 Type-1 Hypalon-Nylon (NN) sample, uni-axial stress-strain relation, warp (X) and weft (Y) directions.

Appendix C
Pressure tare method

The forces acting on the bow seal force balance are shown in Figure C.1. Load cells register the gross load (F_{X_gross}) on the seal system, which is composed of a downstream-acting hydrodynamic force (F_{X_hydro}), the force due to internal cushion pressure ($F_{X\_p\_tare}$) as well as various mechanical losses (Equation C.1).

$$\begin{aligned} F_{X\_gross} &= F_{X\_fore} + F_{X\_aft} \\ F_{X\_hydro} &= F_{X\_gross} - \underbrace{F_{X\_p\_tare}}_{unknown} \end{aligned}$$

An exact calculation of the total force due to cushion pressure, or pressure tare, would require knowledge of the cushion pressure and surface normals everywhere on bow seal force balance (Equation C.1).

$$\begin{aligned} F_{X\_p\_tare} &= \int p(x,y,z) \cdot n_x dA \\ &\approx -k_{X\_p}(I)\overline{p_{int\_w}}A_{X\_p0} + k_{X\_p}(I)\overline{p_{int\_w}}D_{eff}(z_{g\_h\_int\_ref} - z_{g\_bs\_tip}) \end{aligned} \tag{C.1}$$

As this is not feasible, the pressure distribution is estimated through point measurements. To improve these estimates, during the latest round of testing, air pressure was acquired at 16 points on the inside face of the seal and floating beam structure. The locations of these measurements are shown in figure 3.10. The pressure measurements showed that the pressure tends to taper near the seal tip with maximum spatial variations of less than 2%. An

area-weighted average of the pressures (Equation C.2) is then used to compute the pressure tare.

$$\overline{p_{int\_w}} = \frac{\sum_{i=1}^{N\_p\_sensors} A_i p_i}{\sum_{i=1}^{N\_p\_sensors} A_i}$$

The surface normals and areas on which the internal pressure acts can be estimated directly through shape measurements and through auxiliary tests, where loads on the seal system force balance are simplified. For example, during zero immersion cases, there was no hydrodynamic force, meaning that the gross load on the seal system is composed mainly of the force due to internal pressure F_p, and to a lesser extent mechanical friction and flagellation loads due to air leakage.

Similarly, gross loads on the bow seal system were acquired as the test section was filled prior to testing with the pressure control system set to maintain constant cushion pressure. During these "fill tests", the gross load was composed of forces due to internal pressure, F_p

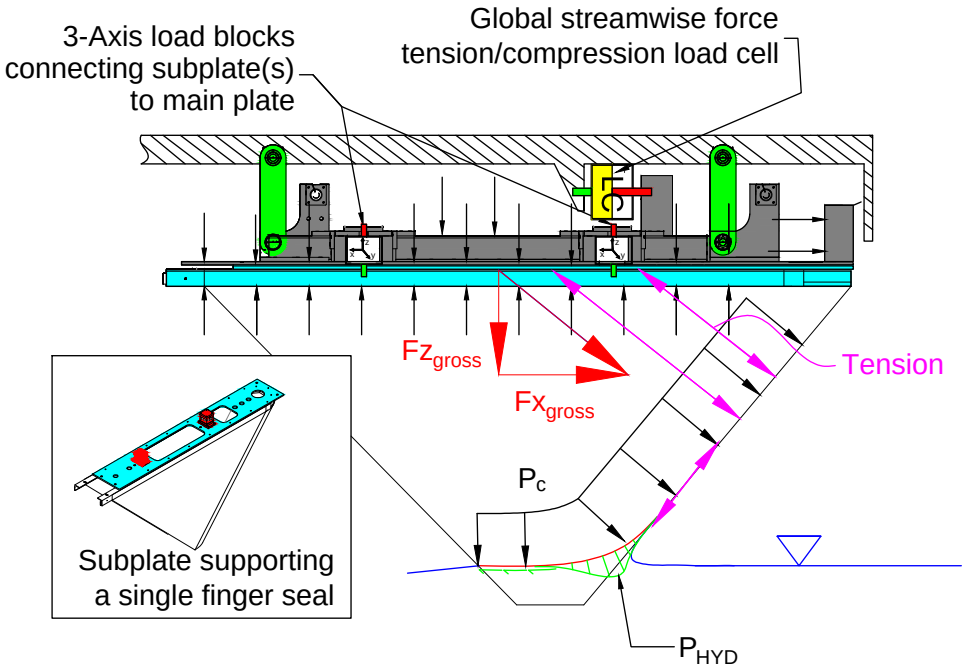

Figure C.1 Bow seal force measurement system with seal system load paths shown.

and hydrostatics $F_{X\_hydrostatic}$, which can be estimated reliably.

In fact, fill tests are particularly valuable. While the test section was filling, the projected area changed in a known manner with the fill height, allowing estimates of the seal diameter and projected area at zero immersion. Figure C.2 shows the change in the vertical projected area (gross force/pressure) during a fill test from 2011. As expected, the projected area varies linearly. Equation C shows the method presently employed to estimate $F_{X\_p\_tare}$. The projected area at zero immersion A_{X_p0} and the effective diameter D_{eff} are estimated from the fill tests. The correction factor $k_{X\_p}(I)$ is a function of the immersion and is close to one if, as expected, the projected area is a linear function of immersion.

$$\left[\frac{F_{X\_gross} - F_{X\_hydro\_fill}}{\overline{p_{int\_w}}}\right] = \underbrace{k_{X\_p}(I) D_{eff}}_{slope}(z_{g\_h\_int\_ref} - z_{g\_bs\_tip}) - \underbrace{k_{X\_p}(I) A_{X\_p0}}_{intercept}$$

$$\begin{aligned} p_{hydrostatic}|_{zg\_h\_int\_ref} &= p_{int\_tip} = \rho g(z_{g\_h\_int\_ref} - z_{g\_h\_ext\_ref}) \\ F_{X\_hydro\_fill} &= F_{X\_hydrostatic} = \int p(x,y,z) \cdot n_x dA \\ &= \frac{-p_{int\_tip} D_{eff}(z_{g\_h\_int\_ref} - z_{g\_h\_ext\_ref})}{2} \end{aligned}$$

To first order the error in this method is $\varepsilon^2 \approx (\frac{A_{X\_p0} p_e + \overline{p_{int\_w}} A_e}{F_{X\_hydro}})^2$, where p_e are A_e are the errors in the pressure and projected area. The diameter (D_{eff}) term can be ignored at small immersions, since $z_{g\_h\_int\_ref} - z_{g\_bs\_tip} \approx 0$. This shows that at low immersions, when F_{X_hydro} is small, the error can be unbounded. It also shows the benefit, in future experiments, of reducing the projected area A_{X_p0} of the seal system as it reduces the sensitivity to errors in pressure. Because A_{X_p0}/F_{X_hydro} of the 3-axis load cell system is estimated to be 20% less than the floating plate system, drag derived from the 3-axis system is expected to be more accurate. In addition, it shows that small errors in the pressure measurements and projected area estimates can lead to large errors in the derived hydrodynamic force.

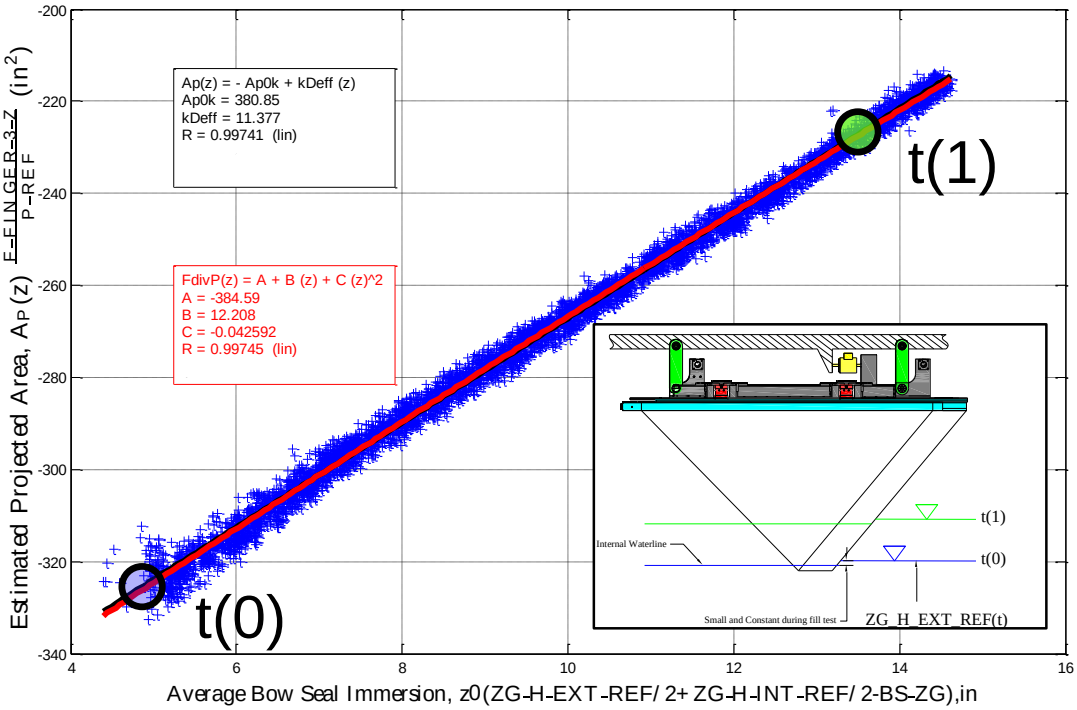

Figure C.2 Fill test results (2011) for vertical force on seal 3

Appendix D

Test-platform geometry and system

D.1 Test platform dimensions

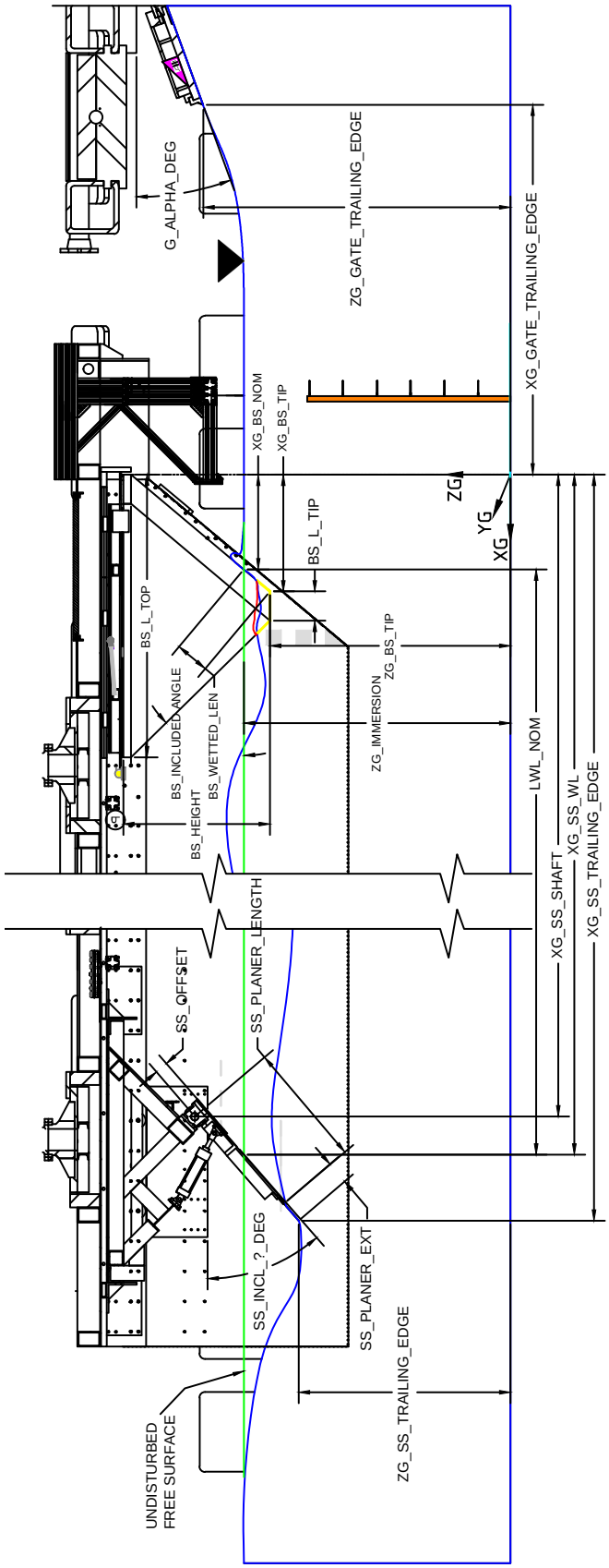

Figure D.1 Test platform geometry.

Dimension	Value	Units
BEAM_CUSHION	1.524	m
BEAM_MOLDED	1.5431	m
BS_HEIGHT	0.9906	m
BS_INCLUDED_ANGLE	45	deg
BS_L_AT_TIP	0.1979	m
BS_L_TOP	1.9083	m
BS_LEADING_ANGLE	50	deg
BS_NOM_A_0_ALL_FINGERS	0.2969	m
BS_NOM_A_0_ONE_FINGER	0.0594	m
BS_NOM_IMMERSION	0.1524	m
BS_WETTED_LEN	0.1989	m
BS_WIDTH	0.2985	m
GATE_FLAP_LENGTH	0.7303	m
GATE_FLAP_OFFSET	0.0572	m
LWL_NOM	5.8777	m
N_FINGERS	5	m
NOM_GATE_ANGLE	20	m
NOM_SS_ANGLE	30	m
PLANER_OFFSET	0.1461	m
SIDEWALL_HEIGHT	1.6828	m
SS_PLANER_EXT	0.4572	m
SS_PLANER_LENGTH	0.7557	m
XG_BS_NOM	0.6671	m
XG_BS_TIP	0.795	m
XG_BS_TOP	0	m
XG_GATE_PIVOT	-3.2957	m
XG_GATE_TRAILING_EDGE	-2.629	m
XG_SS_SHAFT	5.9658	m
XG_SS_WL	6.5448	m
XP_SS_SHAFT	5.9658	m
ZG_BS_TIP	1.5164	m
ZG_FLOATING_PLATE_WET	2.5305	m
ZG_GATE_PIVOT	2.396	m
ZG_GATE_TRAILING_EDGE	2.0925	m
ZG_NOM_IMMERSION	1.6688	m
ZG_SIDEWALL_LEADING_EDGE	1.124	m
ZG_SS_SHAFT	2.1717	m
ZG_SS_TRAILING_EDGE	1.4388	m
ZG_WET_DECK_AFT_CL_5	2.8194	m
ZG_WET_DECK_FORE_CL_1	2.8067	m
ZG_WIN_CLAMP_ABV_FLOOR	0.9406	m
ZP_FLOATING_PLATE_WET	0.2762	m
ZP_SS_SHAFT	0.6477	m

Table D.1 Test platform dimensions.

D.2 Lofted seal geometry

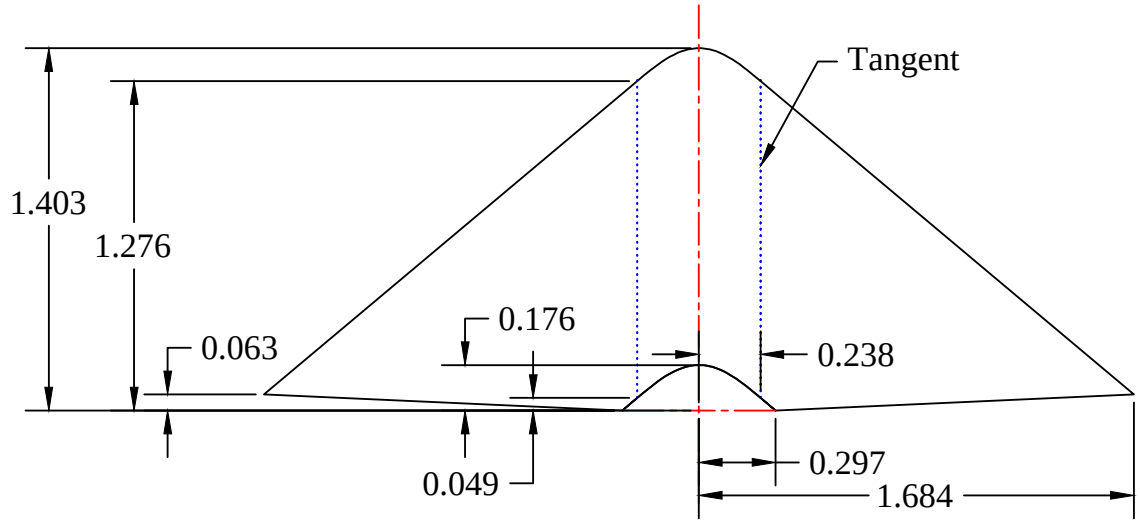

(a) Lofted finger seal geometry

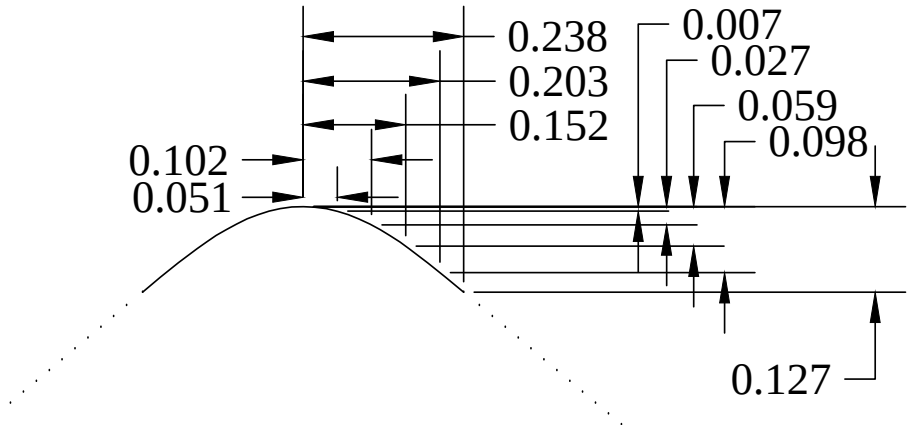

(b) Detail, lofted finger seal geometry

Figure D.2 Lofted finger seal geometry, as tested during Study 1

D.3 Sensor locations

Table D.2 Channel descriptions.

Channel	Units	Description
seal_type	N/A	parsed from filename preceded by T? type 0 (heavy finger seals) type 1 (lighter finger seals) type 3 (rigid 2D seal) type 4 (flexible 2D seal)
immersion	N/A	parsed from filename I? immersion inches x10
flow_speed	N/A	parsed from filename S? flowspeed m/s x100 as measured by LDV
pressure	N/A	parsed from filename P? pressure inches of water column
TEST_LOG_ENTRY_CREATION_DATESTR	N/A	Day that file was preprocessed used for debugging
Start_Time	N/A	Test Start Time derived from CRIO/SCAN TDMS file time_stamps
ATM_Pressure_mbar	mbar	Atmospheric Pressure (manually entered from barometer mounted on control room wall)
Chan_Avg_Temp_x_10	F	Channel water temperature as reported by LCC process control system

Table D.2 – continued from previous page

Name	Units	Description
Chan_Press_PSIA_x_100	psig	Pressure from pressure ring at entance to test section as reported by LCC PCS (of limitted use due to presence of gate)
Chan_Velocity_x100	N/A	Channel as reported by LCC ignore
H_2b	m	Free surface elevation at bay 2 downstream (b) window derived from ruler measurement see loc structure for X_G position
H_3a	m	Free surface elevation at bay 3 upstream (a) window derived from ruler measurement see loc structure for X_G position
H_4a	m	Free surface elevation at bay 4 upstream (a) window derived from ruler measurement see loc structure for X_G position
H_5a	m	Free surface elevation at bay 5 upstream (a) window derived from ruler measurement see loc structure for X_G position

Table D.2 – continued from previous page

Name	Units	Description
H_6a	m	Free surface elevation at bay 6 upstream (a) window derived from ruler measurement see loc structure for X_G position
Initial_Fill_Level_m	m	Fill level as measured by sight-glass
Iris_Damper_K_Value_Down	N/A	Orifice coefficient for downstream pressure control fan used in deriving flow rates from pressure drop
Iris_Damper_K_Value_Up	N/A	Orifice coefficient for upstream pressure control fan used in deriving flow rates from pressure drop
Motor_Speed_RPM_x_100	N/A	Impeller RPM as reported by LCC PCS
TEMP_C	C	Air Temperature/manually entered
BS_IMMERSION_derived_Mean	m	Estimated immersion of bow seal reference to upstream free-surface elevation typically H_FINGER_2_UP_ABV_FL is used
DP_VEL_1_derived_Mean	$\frac{m}{s}$	Upstream flow velocity via pitot rake

Table D.2 – continued from previous page

Name	Units	Description
DP_VEL_2_derived_Mean	$\frac{m}{s}$	Upstream flow velocity via pitot rake
DP_VEL_3_derived_Mean	$\frac{m}{s}$	Upstream flow velocity via pitot rake
DP_VEL_4_derived_Mean	$\frac{m}{s}$	Upstream flow velocity via pitot rake
DP_VEL_5_derived_Mean	$\frac{m}{s}$	Upstream flow velocity via pitot rake
FAN_1_HZ_scaled_Mean	hz	Fan rotation rate upstream centrifugal
FAN_2_HZ_scaled_Mean	hz	Fan rotation rate centrifugal
F_BOW_LC_X_HYD_0_derived_Mean	N	All seals streamwise (X) hydrodynamic force zero immersion (_0) P tare
F_BOW_LC_X_HYD_H_derived_Mean	N	All seals streamwise (X) hydrodynamic Force upstream bow seal immersion (_H) P tare
F_BOW_LC_X_P_TARE_0_derived_Mean	N	All seals streamwise (X) cushion pressure tare zero immersion (_0) P tare
F_BOW_LC_X_P_TARE_H_derived_Mean	N	All seals streamwise (X) cushion pressure tare corrected for bow seal immersion (_H)
F_BOW_LC_X_scaled_Mean	N	All seals streamwise (X) gross force (sum of fore and aft)

Table D.2 – continued from previous page

Name	Units	Description
F_FINGER_3_AFT_X_scaled_Mean	N	Finger 3 streamwise (X) gross force registered on aft load cell
F_FINGER_3_AFT_Y_scaled_Mean	N	Finger 3 spanwise (Y) gross force registered on aft load cell
F_FINGER_3_AFT_Z_scaled_Mean	N	Finger 3 vertical (Z) gross force registered on aft load cell
F_FINGER_3_DIR_derived_Mean	deg	Finger 3 (X Z) direction of gross force
F_FINGER_3_FORE_X_scaled_Mean	N	Finger 3 streamwise (X) gross force registered on forward load cell
F_FINGER_3_FORE_Y_scaled_Mean	N	Finger 3 spanwise (Y) gross force registered on forward load cell
F_FINGER_3_FORE_Z_scaled_Mean	N	Finger 3 vertical (Z) gross force registered on forward load cell
F_FINGER_3_HYD_DIR_H_derived_Mean	deg	Finger 3 (X Z) direction of hydrodynamic force
F_FINGER_3_HYD_MAG_0_derived_Mean	N	Finger 3 (X Z) magnitude of hydrodynamic force
F_FINGER_3_HYD_MAG_H_derived_Mean	N	Finger 3 (X Z) magnitude of hydrodynamic force
F_FINGER_3_MAG_derived_Mean	N	Finger 3 (X Z) magnitude of gross force

Table D.2 – continued from previous page

Name	Units	Description
F_FINGER_3_X_HYD_0_derived_Mean	N	Finger 3 streamwise (X) hydrodynamic force zero immersion (_0) P tare
F_FINGER_3_X_HYD_H_derived_Mean	N	Finger 3 streamwise (X) hydrodynamic upstream bow seal immersion (_H) P tare
F_FINGER_3_X_P_TARE_0_derived_Mean	N	Finger 3 streamwise (X) hydrodynamic force zero immersion (_0) P tare
F_FINGER_3_X_P_TARE_H_derived_Mean	N	Finger 3 streamwise (X) hydrodynamic force upstream bow seal immersion (_H) P tare
F_FINGER_3_X_derived_Mean	N	Finger 3 streamwise (X) gross force (sum of fore and aft)
F_FINGER_3_Y_derived_Mean	N	Finger 3 spanwise (Y) gross force (sum of fore and aft)
F_FINGER_3_Z_CF_derived_Mean	m	Finger 3 longitudinal center of gross force from FP
F_FINGER_3_Z_HYD_0_derived_Mean	N	Finger 3 vertical (Z) hydrodynamic force finger 3 (center)
F_FINGER_3_Z_HYD_CF_H_derived_Mean	m	Finger 3 longitudinal center of vertical hydrodynamic force

Table D.2 – continued from previous page

Name	Units	Description
F_FINGER_3_Z_HYD_H_derived_Mean	N	Finger 3 vertical (Z) hydrodynamic Force
F_FINGER_3_Z_P_TARE_0_derived_Mean	N	Finger 3 streamwise (X) hydrodynamic force zero immersion (_0) P tare
F_FINGER_3_Z_P_TARE_H_derived_Mean	N	Finger 3 streamwise (X) hydrodynamic Force upstream bow seal immersion (_H) P tare
F_FINGER_3_Z_derived_Mean	N	Finger 3 vertical (Z) gross force (from sum of fore and aft loads)
F_FINGER_4_AFT_Z_scaled_Mean	N	Finger 4 streamwise (X) gross force registered on aft load cell
F_FINGER_4_FORE_Z_scaled_Mean	N	Finger 4 streamwise (X) gross force registered on forward load cell
F_FINGER_4_Z_CF_derived_Mean	m	Finger 4 longitudinal center of gross force from FP
F_FINGER_4_Z_HYD_0_derived_Mean	N	Finger 4 vertical (Z) hydrodynamic force
F_FINGER_4_Z_HYD_H_derived_Mean	N	Finger 4 longitudinal center of vertical hydrodynamic force
F_FINGER_4_Z_P_TARE_0_derived_Mean	N	Finger 4 streamwise (X) hydrodynamic force zero immersion (_0) P tare

Table D.2 – continued from previous page

Name	Units	Description
F_FINGER_4_Z_P_TARE_H_derived_Mean	N	Finger 4 streamwise (X) hydrodynamic Force upstream bow seal immersion (_H) P tare
F_FINGER_4_Z_derived_Mean	N	Finger 4 vertical (Z) hydrodynamic Force
F_TC_AUX_1_scaled_Mean	N	Tension/Compression load cell used for calibrations ignore
G_ALPHA_DEG_derived_Mean	deg	Free-surface forming gate angle
H_CL_1_ABV_FL_derived_Mean	m	Centerline Water level derived from airgap referenced to floor see loc structure for position
H_CL_2_ABV_FL_derived_Mean	m	Centerline Water level derived from airgap referenced to floor see loc structure for position
H_CL_3_ABV_FL_derived_Mean	m	Centerline Water level derived from airgap referenced to floor see loc structure for position
H_CL_4_ABV_FL_derived_Mean	m	Centerline Water level derived from airgap referenced to floor see loc structure for position

Table D.2 – continued from previous page

Name	Units	Description
H_CL_5_ABV_FL_derived_Mean	m	Centerline Water level derived from airgap referenced to floor see loc structure for position
H_CL_FIP_1_ABV_FL_derived_Mean	m	Water level at fixed instrumentation platform (FIP) derived from airgap referenced to floor see loc structure for position
H_CL_FIP_2_ABV_FL_derived_Mean	m	Water level at fixed instrumentation platform (FIP) derived from airgap referenced to floor see loc structure for position
H_CL_FIP_3_ABV_FL_derived_Mean	m	Water level at fixed instrumentation platform (FIP) derived from airgap referenced to floor see loc structure for position
H_CL_FIP_4_ABV_FL_derived_Mean	m	Water level at fixed instrumentation platform (FIP) derived from airgap referenced to floor see loc structure for position

Table D.2 – continued from previous page

Name	Units	Description
H_FINGER_2_UP_ABV_FL_derived_Mean	m	Water level upstream of Finger 2 derived from airgap referenced to floor see loc structure for position
H_REF_ABV_FL_derived_Mean	m	Upstream water level finger 3 derived from airgap referenced to floor see loc structure for position
H_W_1_ABV_FL_derived_Mean	m	Water level outside cushion near tunnel wall referenced to floor
H_W_2_ABV_FL_derived_Mean	m	Water level outside cushion near tunnel wall referenced to floor
H_W_3_ABV_FL_derived_Mean	m	Water level outside cushion near tunnel wall referenced to floor
H_W_4_ABV_FL_derived_Mean	m	Water level outside cushion near tunnel wall referenced to floor
H_W_5_ABV_FL_derived_Mean	m	Water level outside cushion near tunnel wall referenced to floor
H_W_6_ABV_FL_derived_Mean	m	Water level outside cushion near tunnel wall referenced to floor
H_W_7_ABV_FL_derived_Mean	m	Water level outside cushion near tunnel wall referenced to floor

Table D.2 – continued from previous page

Name	Units	Description
IVC_STATE_scaled_Mean	Bool	Indicate whether IVC (linescan) camera is actively scanning
PMD_INCL_X_1_DEG_derived_Mean	deg	PMD 1 Time-of-Flight Camera Orientation about X axis
PMD_INCL_X_2_DEG_derived_Mean	deg	PMD 2 Time-of-Flight Camera Orientation about X axis
PMD_INCL_X_3_DEG_derived_Mean	deg	PMD 3 Time-of-Flight Camera Orientation about X axis
PMD_INCL_Y_1_DEG_derived_Mean	deg	PMD 1 Time-of-Flight Camera Orientation about X axis
PMD_INCL_Y_2_DEG_derived_Mean	deg	PMD 2 Time-of-Flight Camera Orientation about X axis
PMD_INCL_Y_3_DEG_derived_Mean	deg	PMD 3 Time-of-Flight Camera Orientation about X axis
P_11_SCAN_1_scaled_Mean	Pa	Pressure on face on seal 1 elevation 1 from scanivalve system (see loc structure for elevation)
P_12_SCAN_2_scaled_Mean	Pa	Pressure on face on seal 1 elevation 2 from scanivalve system (see loc structure for elevation)

Table D.2 – continued from previous page

Name	Units	Description
P_13_SCAN_3_scaled_Mean	Pa	Pressure on face on seal 1 elevation 3 from scanivalve system (see loc structure for elevation)
P_14_SCAN_4_scaled_Mean	Pa	Pressure on face on seal 1 elevation 4 from scanivalve system (see loc structure for elevation)
P_15_SCAN_5_scaled_Mean	Pa	Pressure on face on seal 1 elevation 5 from scanivalve system (see loc structure for elevation)
P_16_SCAN_6_scaled_Mean	Pa	Pressure on face on seal 1 elevation 6 from scanivalve system (see loc structure for elevation)
P_17_SCAN_7_scaled_Mean	Pa	Pressure on face on seal 1 elevation 7 from scanivalve system (see loc structure for elevation)
P_26_SCAN_8_scaled_Mean	Pa	Pressure on face on seal 2 elevation 6 from scanivalve system (see loc structure for elevation)
P_36_SCAN_9_scaled_Mean	Pa	Pressure on face on seal 3 elevation 6 from scanivalve system (see loc structure for elevation)

Table D.2 – continued from previous page

Name	Units	Description
P_46_SCAN_10_scaled_Mean	Pa	Pressure on face on seal 4 elevation 6 from scanivalve system (see loc structure for elevation)
P_56_SCAN_11_scaled_Mean	Pa	Pressure on face on seal 5 elevation 6 from scanivalve system (see loc structure for elevation)
P_BOW_LC_X_derived_Mean	Pa	Pressure all seals average weighted by projected arefloating plate system (F_BOW_LC_X)
P_CL_2_SCAN_14_scaled_Mean	Pa	Pressure at wetdeck CL location 2
P_CL_3_SCAN_15_scaled_Mean	Pa	Pressure at wetdeck CL location 3
P_CL_4_SCAN_16_scaled_Mean	Pa	Pressure at wetdeck CL location 4
P_FINGER_1_X_derived_Mean	Pa	Pressure Finger 1 average weighted by projected area in X
P_FINGER_1_Z_derived_Mean	Pa	Pressure Finger 1 average weighted by projected area in X
P_FINGER_3_X_derived_Mean	Pa	Pressure Finger 3 average weighted by projected area in Z

Table D.2 – continued from previous page

Name	Units	Description
P_FINGER_3_Z_derived_Mean	Pa	Pressure Finger 3 average weighted by projected area in Z
P_FLOATING_PL_CENTER_SCAN_12_scaled_Mean	Pa	Pressure centerline near center of floating plate
P_FLOATING_PL_FORE_SCAN_13_scaled_Mean	Pa	Pressure near forward pressure barrier
P_REF_BP_scaled_Mean	Pa	Pressure at pilot side of backpressure regulator (BP)
P_REF_SETRA_scaled_Mean	Pa	Reference pressure inside cushion wetdeck near floating plate
Q_SUPPLY_DN_derived_Mean	m^3/min	Downstream Flow Rate via DP at orifice
Q_SUPPLY_UP_derived_Mean	m^3/min	Upstream Flow Rate via DP at orifice
SS_INCL_1_DEG_derived_Mean	deg	Segment 1 Inclination
SS_INCL_2_DEG_derived_Mean	deg	Segment 2 Inclination
SS_INCL_3_DEG_derived_Mean	deg	Segment 3 Inclination (CL)
SS_INCL_4_DEG_derived_Mean	deg	Segment 4 Inclination
SS_INCL_5_DEG_derived_Mean	deg	Segment 5 Inclination
STEREO_START_scaled_Mean	Bool	Indicates status of stereo camera system
STEREO_STOP_scaled_Mean	Bool	Indicates status of stereo camera system
SYNC_SINE_IN_MASTER_scaled_Mean	V	Sync signal used to find delay between DAQ Master/Slave

Table D.2 – continued from previous page

Name	Units	Description
SYNC_SINE_IN_SLAVE_scaled_Mean	V	Sync signal used to find delay between DAQ Master/Slave
TUNNEL_ATM_P_scaled_Mean	inHg	Atmospheric pressure in tunnel (not scaled properly)
XG_BS_WL_derived_Mean	m	X coordinate of bow seal forward waterline
XG_GATE_TRAILING_EDGE_derived_Mean	m	X coordinate of gate trailing edge
XG_SS_TRAILING_EDGE_derived_Mean	m	Average X coordinate of stern seal trailing edge
ZG_GATE_TRAILING_EDGE_derived_Mean	m	Z coordinate of gate trailing edge
ZG_SS_TRAILING_EDGE_derived_Mean	m	Average Z coordinate of stern seal trailing edge

Table D.3 Sensor locations.

Channel	Units	X_G	Y_G	Z_G
flow_speed (LDV)	m	-0.152	0	1.27
DP_VEL_1	m	$5.715 \cdot 10^{-2}$	0	0.445
DP_VEL_2	m	$5.715 \cdot 10^{-2}$	0	0.673
DP_VEL_3	m	$5.715 \cdot 10^{-2}$	0	0.902
DP_VEL_4	m	$5.715 \cdot 10^{-2}$	0	1.13
F_BOW_LC_X	m	0.584	0	2.743
F_FINGER_3_AFT_X	m	1.445	0	2.565

Table D.3 – continued from previous page

Channel	Unit	X_G	Y_G	Z_G
F_FINGER_3_AFT_Y	m	1.445	0	2.565
F_FINGER_3_AFT_Z	m	1.445	0	2.565
F_FINGER_3_FORE_X	m	0.711	0	2.565
F_FINGER_3_FORE_Y	m	0.711	0	2.565
F_FINGER_3_FORE_Z	m	0.711	0	2.565
F_FINGER_4_AFT_Z	m	1.445	0.305	2.565
F_FINGER_4_FORE_Z	m	0.711	0.305	2.565
G_ALPHA	m	-2.629	0	1.905
H_CL_1	m	2.486	0	2.468
H_CL_2	m	3.096	0	2.469
H_CL_3	m	3.705	0	2.462
H_CL_4	m	4.315	0	2.464
H_CL_5	m	4.924	0	2.465
H_CL_FIP_1	m	1.153	-0.305	2.197
H_CL_FIP_2	m	1.382	-0.305	2.122
H_CL_FIP_3	m	1.687	0.305	2.214
H_CL_FIP_4	m	1.991	0.305	2.136
H_FINGER_2_UP	m	$2.54 \cdot 10^{-2}$	-0.305	2.046
H_REF	m	-1.168	0	2.565
H_W_1	m	1.267	1.102	2.301
H_W_2	m	1.876	1.102	2.361
H_W_3	m	2.486	1.102	2.364
H_W_4	m	3.096	1.102	2.358
H_W_5	m	3.705	1.102	2.365
H_W_6	m	4.315	1.102	2.365
H_W_7	m	4.924	1.102	2.356

Table D.3 – continued from previous page

Channel	Unit	X_G	Y_G	Z_G
PMD_INCL_X_1	m	0.794	0.305	0
PMD_INCL_X_2	m	1.429	0.305	0
PMD_INCL_X_4	m	1.581	0	0
PMD_INCL_Y_1	m	0.794	0.305	0
PMD_INCL_Y_2	m	1.429	0.305	0
PMD_INCL_Y_4	m	1.581	0	0
P_11_SCAN_1	m	0.774	−0.61	1.543
P_12_SCAN_2	m	0.731	−0.61	1.594
P_13_SCAN_3	m	0.667	−0.61	1.67
P_14_SCAN_4	m	0.603	−0.61	1.746
P_15_SCAN_5	m	0.539	−0.61	1.822
P_16_SCAN_6	m	0.466	−0.61	1.909
P_17_SCAN_7	m	0.247	−0.61	2.171
P_26_SCAN_8	m	0.466	−0.305	1.909
P_36_SCAN_9	m	0.466	0	1.909
P_46_SCAN_10	m	0.466	0.305	1.909
P_56_SCAN_11	m	0.466	0.61	1.909
P_CL_2_SCAN_14	m	3.096	0	2.731
P_CL_3_SCAN_15	m	3.705	0	2.731
P_CL_4_SCAN_16	m	4.315	0	2.731
P_FLOATING_PL_CENTER_SCAN_12	m	0.953	0	2.172
P_FLOATING_PL_FORE_SCAN_13	m	0.102	0	2.591
P_REF_SETRA	m	$7.863 \cdot 10^{-2}$	0	$6.935 \cdot 10^{-2}$
SS_INCL_1	m	6.401	−0.61	1.448
SS_INCL_2	m	6.401	−0.305	1.448
SS_INCL_3	m	6.401	0	1.448

Table D.3 – continued from previous page

Channel	Unit	X_G	Y_G	Z_G
SS_INCL_4	m	6.401	0.305	1.448
SS_INCL_5	m	6.401	0.61	1.448
H_2B	m	−0.305	1.524	0.941
H_3A	m	1.08	1.524	0.941
H_4A	m	3.073	1.524	0.941
H_5A	m	5.067	1.524	0.941
H_6A	m	7.061	1.524	0.941

D.4 Pressure control system

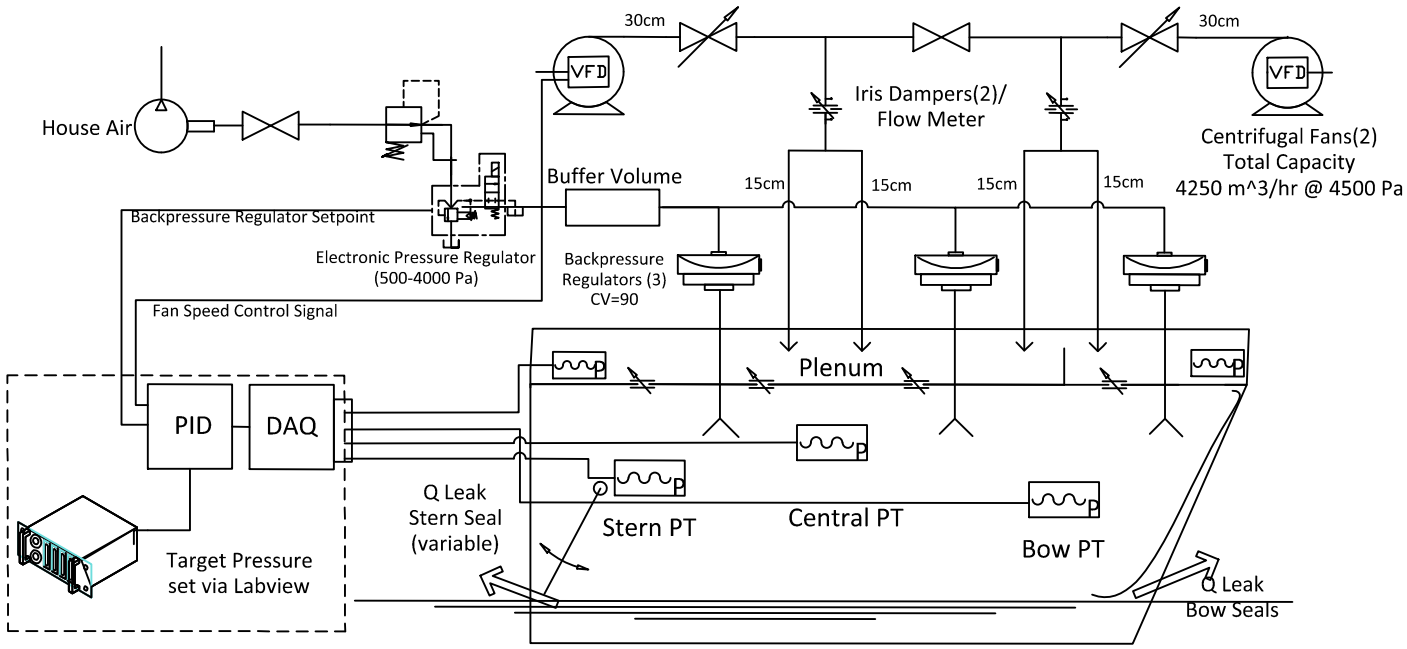

Figure D.3 Low pressure control system, large-scale test platform

Bibliography

Antman, Stuart S. 2005. *Nonlinear Problems of Elasticity Second Edition*, vol. 107, Springer Verlag, 2nd edn.

Ashton, George D. 1986. *River and lake ice engineering*, Water Resources Publication.

ASTM. 2010. ASTM D1388: Standard Test Method for Stiffness of Fabrics.

Audoly, B. 2010. *Elasticity and Geometry: From hair curls to the non-linear response of shells*, Oxford University Press.

Bažant, ZP and L Cedolin. 2010. *Stability of structures: elastic, inelastic, fracture and damage theories*, World Scientific.

Benya, Yu. 1971. *Basic Theories of Air Cushion Vehicles*, U.S. Army Foreign Science Technology Center, Army Materiel Command.

Besch, P K. 1976. Motions of Bow Fingers in a Surface Effect Ship Flexible Seal, Ship Performance Department Research and Development Report 76-0026, David W. Taylor Naval Ship Research and Development Center, Bethesda, MD 20084.

Biot, Maurice a. 1964. *Mechanics of Incremental Deformations*, vol. 18, New York: John Wiley & Sons, 1st edn.

Bliss, DS. 1969. Means for bounding a space for receiving pressurized gas, *US Patent 3,420,330*.

Boucif, M, JE Wesfreid, and E Guyon. 1991. Experimental study of wavelength selection in the elastic buckling instability of thin plates, *European journal of mechanics. A. Solids*, 641–661.

Brau, Fabian, Hugues Vandeparre, and Abbas Sabbah. 2010. Multiple-length-scale elastic instability mimics parametric resonance of nonlinear oscillators:supplementary information, *Nature Physics*, 3(2), 1–6.

Brodtkorb, P A, P Johannesson, G Lindgren, I Rychlik, J Rydén, and E Sjö. 2000. WAFO - a Matlab Toolbox for the Analysis of Random Waves and Loads, in *Proc. 10'th Int. Offshore and Polar Eng. Conf., ISOPE, Seattle, USA*, vol. 3, 343–350.

Budd, Chris J. and Mark a. Peletier. 2000. Approximate Self-Similarity in Models of Geological Folding, *SIAM Journal on Applied Mathematics*, 60(3), 990–1016.

Butler, E A. 1985. The surface effect ship, *Naval Engineers Journal*, 97(2), 200–253.

Calladine, C.R. 1983. *Theory of Shell Structures*, Cambridge Univ Press, 1st edn.

Cerda, E. and L. Mahadevan. 2003. Geometry and Physics of Wrinkling, *Physical Review Letters*, 90(7), 1–4.

Cerda, E, L Mahadevan, and Proc R Soc A. 2005. Confined developable elastic surfaces : cylinders , cones and the Elastica Confined developable elastic surfaces : cylinders , cones and the Elastica, 671–700.

Cerda, E, L Mahadevan, and J M Pasini. 2004. The elements of draping., *Proceedings of the National Academy of Sciences of the United States of America*, 101(7), 1806–10.

Champneys, A R, G W Hunt, and J M T Thompson. 1999. *Localization and solitary waves in solid mechanics*, vol. 12, World Scientific.

Chang, YB, SJ Fox, DG Lilley, and PM Moretti. 1991. Aerodynamics of moving belts, tapes and webs, in *DE-Vol. 36 Machinery Dynamics and Element Vibrations*, Miami, FL, 33–40.

Chapa, Joseph O and Raghuveer M Rao. 2000. Algorithms for designing wavelets to match a specified signal, *Signal Processing, IEEE Transactions on*, 48(12), 3395–3406.

Chapin, J. B. 1977. Study of Large ACV Skirt Design Concepts: Report 7588-950048, Tech. rep., Bell Textron, Bethesda, MD 20084.

Clapp, T.G., H. Peng, T.K. Ghosh, and J.W. Eischen. 1990. Indirect Measurement of the Moment-Curvature Relationship for Fabrics, *Textile Research Journal*, 60(9), 525–533.

Colquhoun, L R. 1971. Aerodynamics of Air Cushion Vehicles: Operation and Technical Aspects of Amphibious Hovercraft, in *von Karman Institute for Fluid Dynamics, Lecture Series 33*, 1–35.

Crago, WA. 1968. Problems associated with the use of skirts on hovercraft, *Hovering Craft and Hydrofoil*.

Crewe, P.R. 1971. Aerodynamics of Air Cushion Vehicles: Skirt Design, in *von Karman Institute for Fluid Dynamics, Lecture Series 33*, 1–35.

Culpin, M F. 1974. The Flexural Rigidity of Thin Fabrics, *Journal of the Society of Naval Architects of Japan*, 65(7), 218.

Da Vinci, Leonardo. 2008. *Notebooks*, Oxford University Press.

Das, Moumita, Ashkan Vaziri, Arshad Kudrolli, and L. Mahadevan. 2007. Curvature Condensation and Bifurcation in an Elastic Shell, *Physical Review Letters*, 98(1), 014301.

Den Hartog, Jacob P. 1956. *Mechanical Vibrations*, New York: McGraw-Hill, 4th edn.

Diamant, Haim and Thomas Witten. 2011. Compression Induced Folding of a Sheet: An Integrable System, *Physical Review Letters*, 107(16), 164302.

Doctors, Lawrence J. 2012. Near-Field Hydrodynamics of a Surface-Effect Ship, *Journal of Ship Research*, 56(3), 183–196.

Doctors, Lawrence J. and Steven F. Zalek. 2010. Experimental Study of the Resistance of Surface-Effect-Ship Seals, in *28th Symposium on Naval Hydrodynamics*, Pasadena, CA.

Dowell, Earl H. 1975. *Aeroelasticity of plates and shells*, 1, Leyden: Noordhoff.

Dyke, Raymond. 1976. The design and operating features of Vosper Thornycroft skirts, in *International Hovering Craft, Hydrofoil and Advanced Transit Systems Conference*, vol. 15, 129–147.

Everall, P. R. and G. W. Hunt. 1999. Quasi-periodic buckling of an elastic structure under the influence of changing boundary conditions, *Proceedings of the Royal Society A: Mathematical, Physical and Engineering Sciences*, 455(1988), 3041–3051.

Fernandez, Vicente I, Audrey Maertens, Frank M Yaul, Jason Dahl, Jeffrey H Lang, and Michael S Triantafyllou. 2011. Lateral-line-inspired sensor arrays for navigation and object identification, *Marine Technology Society Journal*, 45(4), 130–146.

Foix, Sergi, G Alenya, and C Torras. 2011. Lock-in time-of-flight (ToF) cameras: a survey, *Sensors Journal, IEEE*, 11(3), 1–11.

Fridsma, Gerard and Robert L. Van Dyck. 1979. Report SIT-DL-79-1861: The contribution of seals and sidewalls to the force and moment characteristics of an SES, Tech. rep., Stevens Institute of Technology, Hoboken, NJ.

Frisch-Fay, R. 1962. *Flexible bars*, Butterworth Scientific Publications, 1st edn.

Graham, T A, P A Sullivan, and M J Hinchey. 1983. Material effects on the dynamic stability of a flexible skirted air cushion, in *American Institute of Aeronautics and Astronautics, Aerospace Sciences Meeting, 21st, Reno, NV*.

Heber, Charles E. 1977. An Analysis of Seal Loads and their effect on the performance of a Surface Effect Ship in Calm Water, Aviation and Surface Effects Department Research and Development Report 77-0056, David W. Taylor Naval Ship Research and Development Center, Bethesda, MD 20084.

Hertzberg, R. W., J. a. Manson, and M. Skibo. 1975. Frequency sensitivity of fatigue processes in polymeric solids, *Polymer Engineering and Science*, 15(4), 252–260.

Hetényi, M. 1979. *Beams on elastic foundation*, Ann Arbor, MI: University of Michigan Press, 11 edn.

Hilbert, D and S Cohn-Vossen. 1952. *Geometry and the Imagination*, New York: Chelsea Publishing.

Hu, J. 2004. *Structure and mechanics of woven fabrics*, CRC.

Huang, Jiangshui, Benny Davidovitch, Christian D. CD Santangelo, Thomas P. Russell, and Narayanan Menon. 2010. Smooth Cascade of Wrinkles at the Edge of a Floating Elastic Film, *Physical Review Letters*, 105(3), 038302.

Hunt, G. W., H. M. Bolt, and J. M. T. Thompson. 1989. Structural Localization Phenomena and the Dynamical Phase-Space Analogy, *Proceedings of the Royal Society A: Mathematical, Physical and Engineering Sciences*, 425(1869), 245–267.

Hunt, GW, MK Wadee, and N Shiacolas. 1993. Localized elasticae for the strut on the linear foundation, *Journal of applied mechanics*, 60(December).

Inch, P., M.E. Prentice, and C. Jean Lewis. 1989. Development in skirt systems for air cushion vehicles, *AIAA Advanced Marine Vehicles Conference*.

Jähne, B. 1993. Spatio-temporal image processing: theory and scientific applications, *Springer Verlag*.

Jones, Robert M. 2006. *Buckling of bars, plates, and shells*, Bull Ridge Publishing.

Kapsenberg, Geert K and R. Compton. 1996. The High-Speed Marine Vehicles Committee, in *Internation Towing Tank Conference*, Trondheim: ITTC, 117.

Kármán, T Von. 1929. Report 321: The impact on seaplane floats during landing, Tech. rep., NACA, Washington DC.

Klichko, VV. 1991. Basic principles of choosing the skirt arrangement of amphibious ACV's, in *Fast Sea Transportation Conference*, Trondheim, 1315–1329.

Koiter, W.T. and AMA van der Heijden. 2009. *W.T. Koiter's elastic stability of solids and structures*, Cambridge Univ Press, 1st edn.

Kornecki, A. 1976. On the aeroelastic instability of two-dimensional panels in uniform incompressible flow, *Sound And Vibration*, 47.

Kramer, M.R., K.J. Maki, and Y.L. Young. 2013. Numerical prediction of the flow past a 2-D planing plate at low Froude number, *Ocean Engineering*, 70, 110–117.

Lamb, Horace. 1932. *Hydrodynamics*, Cambridge Univ Pr, 6th edn.

Langhaar, H. L. 1962. *Energy Methods in applied mechanics*, New York: John Wiley & Sons, 1st edn.

Lavis, D. R. 2009. Fifty years and more of hovercraft development, in *Internation Conference on Air Cushion Vehicles and Surface Effectr Craft*, London: Royal Institution of Naval Architects, May.

Lavis, D. R., R. J. Bartholomew, and J. C. Jones. 1974. Response of Air Cushion Vehicles to Random Seaways and the Inherent Distortion in Scale Models, *Journal of Hydronautics*, 8(3), 83–94.

Lee, H., E. Peterson, R. Phillips, W. Klug, and P. A. Wiggins. 2008. Membrane shape as a reporter for applied forces., *Proceedings of the National Academy of Sciences of the United States of America*, 105(49), 19253–7.

Lee, Myung Hoon and Jong Min Park. 2004. Flexural stiffness of selected corrugated structures, *Packaging Technology and Science*, 17(5), 275–286.

Lindberg, Herbert E and Alexander L Florence. 1987. *Dynamic pulse buckling: theory and experiment*, vol. 12, Springer.

Lisle, R J. 1994. Detection of zones of abnormal strains in structures using Gaussian curvature analysis, *AAPG Bulletin*, 78(12).

Little, M. A. and N. S. Jones. 2011. Generalized methods and solvers for noise removal from piecewise constant signals. I. Background theory., *Proceedings of the Royal Society A: Mathematical, Physical and Engineering Sciences*, 467(2135), 3088–3114.

Longuet-Higgins, MS. 1957. The statistical analysis of a random, moving surface, *Philosophical Transactions of the Royal Society of London. Series A, Mathematical and Physical Sciences*.

Mäkiharju, SA and BR Elbing. 2013. On the scaling of air entrainment from a ventilated partial cavity, *Journal of Fluid Mechanics*, 732(October), 47–76.

Malakhoff, A and S Davis. 1981. Dynamics of SES bow seal fingers, in *American Institute of Aeronautics and Astronautics, Marine Systems Conference, 6 th, Seattle, WA*, 1981.

Mallat, Stephane. 1999. *A Wavelet Tour of Signal Processing*, Elsevier.

Manela, A. and M.S. Howe. 2009. The forced motion of a flag, *Journal of Fluid Mechanics*, 635, 439–454.

Morris-Thomas, M T and S Steen. 2009. Experiments on the stability and drag of a flexible sheet under in-plane tension in uniform flow, *Journal of Fluids and Structures*, 25(5), 815–830.

Moulijn, J C. 2000. *Added Resistance due to Waves of Surface Effect Ships*, Ph.D. thesis, Delft University of Technology.

Newman, J N. 1977. *Marine Hydrodynamics*, Cambridge, MA: Mit Press, 1st edn.

NMAB. 1978. NMAB-340: Skirts and Seals for Surface Effect Vehicles, Tech. rep., National Materials Advisory Board, National Academy of Sciences, Washington DC.

Peirce, FT. 1930. The handle of cloth as a measurable quantity, *Journal of the Textile Institute Transactions*.

Pocivavsek, Luka, Robert Dellsy, Andrew Kern, Sebastián Johnson, Binhua Lin, Ka Yee C Lee, and Enrique Cerda. 2008. Stress and fold localization in thin elastic membranes., *Science (New York, N.Y.)*, 320(5878), 912–6.

Potier-Ferry, M. 1987. Foundations of elastic postbuckling theory, in *Buckling and Postbuckling: Four Lectures in Experimental, Numerical and Theoretical Solid Mechanics Based on Talks Given at the CISM-Meeting Held in Udine, Italy, September*, Berlin / Heidelberg: Springer-Verlag, chap. 288, 1–82.

Prokhorov, Sergei D. 1981. Status of Hydrodynamic Technology as Related to Model Tests of High-Speed Marine Vehicles: Air Cushion Vehicles, in *16th International Towing Tank Conference*.

Rapp, H and M Frank. 2008. A theoretical and experimental investigation of the systematic errors and statistical uncertainties of Time-Of-Flight-cameras, *International Journal of Intelligent Systems Technologies and Applications*, 5, 402–413.

Ratzersdorfer, Julius. 1936. *Die knickfestigkeit von stäben und stabwerken*, J. Springer.

Rayleigh, Lord. 1883. The Form of Standing Waves on the Surface of Running Water, *Proceedings of the London Mathematical Society*, s1-15(1), 69–78.

Rice, SO. 1944. Mathematical analysis of random noise, *Bell System Technical Journal*.

Rijken, O, M Spillane, and SJ Leverette. 2010. Vibration Absorber Technology and Conceptual Design of Vibration Absorber for TLP in Ultradeep Water, in *29th International Conference on Ocean, Offshore and Arctic Engineering*, Shanghai, China: ASME.

Rivetti, Marco and Sébastien Neukirch. 2014. The mode branching route to localization of the finite-length floating elastica, *Preprint*, 1–16.

Ryken, J. 1978. Test Data Analysis and Correlation Report: SES-100B Finger Motions and Finger Drag, Test Data Analysis and Correlation Report 7593-925003, Bell Aerospace/Textron, New Orleans.

Santillan, ST. 2007. *Analysis of the elastica with applications to vibration isolation*, Thesis, Duke.

Singer, J, J Arboz, and T Weller. 1998. *Buckling Experiments: Experimental Methods in Buckling of Thin Walled Structures. Volume 1 Basic Concepts, Columns, Beam and Plates*, vol. 1, John Wiley & Sons.

Steen, S. 2004. Experiences with Seakeeping Capabilities of SES Ships.

Stein, M. 1959. The phenomenon of change in buckle pattern in elastic structures, *NASA*.

Strutt, John William (Baron Rayleigh). 1877. *The theory of sound, vol. 1*, New York: Dover Publications.

Sullivan, P A, J E Byrne, and M J Hinchey. 1985. Non-linear oscillations of a simple flexible skirt air cushion, *Journal of Sound and Vibration*, 102(2), 269–283.

Sullivan, PA and TA Graham. 1989. Scaling of cushion capacitance in air cushion vehicle model testing, *Journal of Aircraft*, 26(8), 1987–1989.

Swallow, JE, J.H. Cadwell, M. Webb, R.A. Establishment, and G. Britain. 1971. *Fabric Properties and the Wear of Hovercraft Fingers*, Defense Technical Information Center.

Szablewski, Piotr and Waldemar Kobza. 2003. Numerical Analysis of Peirce Cantilever Test for the Bending Rigidity of Textiles, *Fibres and Textiles in Eastern Europe*, 11(4), 54–57.

Timoshenko, S, S Woinowsky-Krieger, and S Woinowsky. 1959. *Theory of plates and shells*, McGraw-Hill, 2nd edn.

Timoshenko, SP. 1961. *Theory of elastic stability*, McGraw-Hill, 2nd edn.

Tovstik, P. E. and Smirnov Andrei. 2001. *Asymptotic Methods in the Buckling Theory of Elastic Shells*, Singapore: World Scientific.

Tsutsumi, Atsuhiro and Minoru Naito. 1991. Water-Jet Flagellator and Test Results on Seal Materials for SES, Seal Vibration Test Results of 30 ton Type SES Test Craft, *Journal of the Society of Naval Architects of Japan*, 169, 319–336.

Vandeparre, Hugues, Miguel Piñeirua, Fabian Brau, Benoit Roman, José Bico, Cyprien Gay, Wenzhong Bao, Chun Ning Lau, Pedro M. Reis, and Pascal Damman. 2011. Wrinkling Hierarchy in Constrained Thin Sheets from Suspended Graphene to Curtains, *Physical Review Letters*, 106(22), 224301.

Vella, Dominic, Arezki Boudaoud, and Mokhtar Adda-bedia. 2009. Statics and Inertial Dynamics of a Ruck in a Rug, *Physical Review Letters*, 3(2), 6–9.

Vinson, JR. 2005. *Plate and panel structures of isotropic, composite and piezoelectric materials, including sandwich construction*, Springer Netherlands.

Wadee, M. K., G. W. Hunt, and a. I. M. Whiting. 1997. Asymptotic and Rayleigh-Ritz routes to localized buckling solutions in an elastic instability problem, *Proceedings of the Royal Society A: Mathematical, Physical and Engineering Sciences*, 453(1965), 2085–2107.

Wagner, Till and Dominic Vella. 2011. Floating Carpets and the Delamination of Elastic Sheets, *Physical Review Letters*, 107(4), 044301.

Waldo, RD. 1968. Some Special Problems in Surface Effect Ships, *Journal of Hydronautics*, 2(3), 152–159.

Walton, DB. 1999. Analysis of Localized Buckling by Multiple Scale Analysis, *The Nonlinear journal*, 1, 18–28.

Wang, CY. 1984. On symmetric buckling of a finite flat-lying heavy sheet, *Journal of applied mechanics*.

Wellman, Larry K. 1981. Summary of Surface Effect Ship Testcraft, Tech. rep., DTNSRDC Aviation and Surface Effects Department.

Wiggins, Andrew D, Steven F Zalek, Marc Perlin, Steven L Ceccio, Lawrence J Doctors, and Robert J Etter. 2013. Development of a Large-scale Surface Effect Ship Bow Seal Testing Platform, *Journal of Ship Production and Design (from FAST 2011 Proceedings)*, 29(4), 1–8.

Winkler, E. 1868. *Die Lehre von der elasticitaet und festigkeit*, Prague: Dominicus, H.

Witten, T. 2007. Stress focusing in elastic sheets, *Reviews of Modern Physics*, 79(2), 643–675.

Yamakita, K and H Itoh. 1998. Sea trial test results of the wear characteristics of SES bow seal finger, *Hydroelasticity in Marine Technology, Fukuoka, Japan*.

Yamakita, Kazuyuki. 1985. Tank Experiments on Various Types of SES Bow Seal Models, *Journal of the Society of Naval Architects of Japan*, 157, 126–130.

Yeung, RW, MV Makasyeyev, and C Matte. 2011. On Wave Elevations Under a Moving Pressure Distribution In Minimum-Resistance Conditions, *Proc. of the 26th IWWWFB*, (1), 17–20.

Yun, L and A Bliault. 2000. *Theory and design of air cushion craft*, Butterworth-Heinemann.

Zhang, Zhengyou. 1999. Flexible camera calibration by viewing a plane from unknown orientations, in IEEE, (Ed.) *The Proceedings of the Seventh IEEE International Conference on Computer Vision*, Kerkyra, vol. 00, 666–673.